University of Cambridge

Department of Biochemistry

Fitzwilliam College

PRESERVING HYPERPOLARISED NUCLEAR SPIN ORDER TO STUDY CANCER METABOLISM

by

Irene Marco-Rius

M.Sc.

This dissertation is submitted for the degree of

Doctor of Philosophy

February, 2014

SUMMARY

PRESERVING HYPERPOLARISED NUCLEAR SPIN ORDER TO STUDY CANCER METABOLISM
by Irene Marco-Rius

Monitoring the early responses of tumours to treatment is a crucial element in guiding therapy and increasing patient survival. To achieve this, we are using magnetic resonance imaging (MRI), which can provide detailed physiological information with relatively high temporal and spatial resolution. In combination with the dynamic nuclear polarisation (DNP) technique, high signal-to-noise is obtained, resulting in a powerful tool for *in vivo* ^{13}C metabolic imaging. However, detection of hyperpolarised substrates is limited to a few seconds due to the exponential decay of the polarisation with the longitudinal relaxation time constant T_1.

This work aimed to improve the combination of hyperpolarisation and metabolic NMR/ MRI by extending the observation timescale of the technique. Working with quantum mechanical properties of the detected substrates, long lifetimes might be accessible by using the nuclear singlet configuration of two coupled nuclei. The singlet state is immune to intramolecular dipole-dipole relaxation processes, which is one of the main sources of signal decay in MRI. In favourable situations, the singlet relaxation time constant can be much longer than T_1, so transfer of the polarisation into the singlet state may allow one to extend the usable time period of the nuclear hyperpolarisation.

Here we studied the relaxation of hyperpolarised metabolites, including those found in the TCA cycle, and examined the possibility of extending their observation timescale by storing the polarisation in the long-lived singlet state. The polarisation remains in this state until it is eventually required for imaging. We also investigate how one may track polarised metabolites after injection into a subject due to the transfer of polarisation to the solvent by Overhauser cross-relaxation, so that the ^{13}C polarisation remains untouched until imaging is required. In this way we should be able to interrogate slower metabolic processes than have been examined hitherto using hyperpolarised ^{13}C MRS, and better understand metabolic changes induced in tumours by treatment.

Preserving hyperpolarised nuclear spin order to study cancer metabolism

Copyright 2014

by

Irene Marco-Rius

This dissertation is my own work and contains nothing which is the outcome of work done in collaboration with others, except as specified in the text and Acknowledgements. Published parts of this work are detailed on the next page.

This dissertation does not exceed the word limit for the Biology Degree Committee.

Signed   _____   Date   _____

LIST OF PAPERS

Material in this thesis is published or being prepared for publication in the following papers:

1. **'Direct enhancement of nuclear singlet order via dissolution DNP'**,
   M. C. D. Tayler, <u>**I. Marco-Rius**</u>, M. I. Kettunen, K. M. Brindle, M. H. Levitt and
   G. Pileio. *J. Am. Chem. Soc.*, vol. 134, 18, pp. 7668-7671, 2012.

2. **'Hyperpolarized singlet lifetimes of pyruvate in human blood and in the
   mouse'**, <u>**I. Marco-Rius**</u>, M. C. D. Tayler, M. I. Kettunen, T. J. Larkin, K. N.
   Timm, E. M. Serrao, T. B. Rodrigues, G. Pileio, J. H. Ardenkjaer-Larsen, M. H.
   Levitt and K. M. Brindle. *NMR Biomed.*, vol. 26, 12, pp. 1696-1704, 2013.

3. **'Quantitation of a spin polarization-induced Overhauser effect (SPINOE)
   between a hyperpolarized ^{13}C-labeled cell metabolite and water protons'**,
   <u>**I. Marco-Rius**</u>, S. E. Bohndiek, M. I. Kettunen, T. J. Larkin, M. Basharat, C.
   Seeley and K. M. Brindle. *Contrast Media Mol. I.* , vol. 9, 2, pp. 182-186, 2014.

4. **'*In vivo* single-shot ^{13}C spectroscopic imaging of hyperpolarized
   metabolites by spatiotemporal encoding'**, R. Schmidt, C. Laustsen, J-N. Dumez,
   M. I. Kettunen, E. Serrao, <u>**I. Marco-Rius**</u>, K. M. Brindle, J. H. Ardenkjaer-Larsen
   and L. Frydman. *J. Magn. Reson.*, 2014./ epub

5. **'^{13}C magnetic resonance spectroscopic imaging of hyperpolarized
   [1-^{13}C, U-^{2}H$_5$]ethanol oxidation *in vivo* can be used to assess aldehyde de-
   hydrogenase activity'**, P. Dzien, M. I. Kettunen, <u>**I. Marco-Rius**</u>,
   E. M. Serrao, T. B. Rodrigues, T. J. Larkin, K. N. Timm, K. M. and Brindle.
   Magn. Reson. Med., 2014./ *accepted*

6. **'Singlet NMR of [1,4-^{13}C$_2$]fumarate'**, <u>**I. Marco-Rius**</u>, M. C. D. Tayler, T. J.
   Larkin and K. M. Brindle. 2014./ *manuscript in preparation*

ACKNOWLEDGEMENTS

Contents

List of Figures

List of Tables

List of main abbreviations

- NMR: Nuclear Magnetic Resonance
- MRS/MRI: Magnetic Resonance Spectroscopy/Imaging
- NOE : Nuclear Overahauser Effect
- SPINOE: Spin Polarisation-Induced NOE
- PET: Positron Emission Tomography
- SPECT: Single-Photon Emission Tomography
- SNR: Signal-to-Noise Ratio
- CT: Computed Tomography
- DNP : Dynamic Nuclear Polarisation
- BSA: Bovine Serum Albumin
- PBS: Phosphate-Buffered Saline
- CSA: Chemical Shit Anisotropy
- T_1: Longitudinal relaxation time constant (in seconds). The superscripts HF or LF indicate the field strength at which the relaxation takes place
- T_2: Transverse relaxation time constant (in seconds)
- T_S: Singlet relaxation time constant (in seconds)
- J: J-coupling constant (in Hz)
- γ: Gyromagnetic ratio of the nucleus of interest (in rad/Ts)
- δ: Chemical shift of the nucleus of interest (in ppm)
- B_0: Magnetic field strength (in Tesla)

- ω_0: Larmor frequency of the nucleus of interest (in rad/s); $\omega_0 = -\gamma B_0$

- I: Spin quantum number

- P: Longitudinal polarisation

- κ_B: Boltmann constant; $\kappa_B \approx 1.38 \times 10^{-23}$ m^2 kg s^{-2} K^{-1}

- $\hbar$: reduced Planck's constant; $\hbar \approx 1.05 \times 10^{-34}$ Js

Introduction

<div align="right">1</div>

Magnetic resonance (MR) has traditionally been used to image water protons, although other nuclei can be studied, and provides spatial, temporal and chemical information. Upon application of a magnetic field, atomic nuclei precess around the axis defined by the direction of the magnetic field. The precession frequency, termed the Larmor frequency, is characteristic of the electronic environment of each atomic nucleus and makes it possible to distinguish signals from different nuclear spins. Faster precession frequencies provide higher sensitivity of detection.

Proton MR imaging (^{1}H-MRI) is a non-invasive technique that provides good contrast between soft tissues in the body without exposing the patient to ionising radiation and has been used in the clinic as a diagnostic tool since the 1980s. Other atomic nuclei have too low sensitivity for imaging at comparable resolution to the proton, due not only to their lower natural abundance but also to their lower precessional frequency. This drawback can be overcome by perturbing the equilibrium of the spin system by increasing the nuclear spin alignment with hyperpolarisation techniques, such as dynamic nuclear polarisation (DNP). These techniques achieve an increase in signal to noise ratio (SNR) of more than 10^4-fold (Ardenkjaer-Larsen *et al.*, 2003). Therefore, injection of hyperpolarised ^{13}C-labelled metabolites may be used to improve detection and allow for ^{13}C-MRI. This in turn has allowed monitoring of metabolic changes *in vivo*, for example to monitor the response of tumours to therapy in real time.

For all its value in boosting signal intensity, the non-equilibrium high level of polarisation achieved with hyperpolarisation techniques still decays exponentially with a relaxation time constant known as longitudinal relaxation time constant or T_1. The detection time is

therefore restricted by T_1, and current tracers relax with time constants between a few seconds and a minute, placing a limit on the length of time that metabolic processes can be followed. This thesis describes work that aimed to evaluate some approaches to preserve the polarisation until it is required for imaging, with an emphasis on 'long lived singlet states'. These states represent an energy configuration of the spin system that experiences a slower relaxation time constant. Although many groups have successfully demonstrated long lifetimes for the singlet state, no studies using endogenous metabolites have been previously reported (Levitt, 2012a, Levitt, 2012b). In this work I assess the possibility of preserving the polarisation of hyperpolarised ^{13}C-labelled endogenous metabolites by bringing the spin system into the singlet state. I then evaluate the applicability of this polarisation preservation method to metabolic studies *in vivo*. Slow decay of the polarisation would make it possible to manipulate the hyperpolarised metabolite of interest in the imaging room (next to the patient), inject it into the patient, and then acquire MRI images over a long enough period to obtain meaningful information about tumour metabolism.

This chapter introduces the key concepts of molecular imaging, magnetic resonance, hyperpolarisation and relaxation. Section 1.6 summarises the important properties of nuclear spin-1/2 pairs that lead to the existence of states that outlast T_1, introducing concepts such as eigenstates and magnetic equivalence. This provides a useful foundation for understanding Chapters 3 and 4. The last section summarises the scope of this thesis.

1.1   Molecular imaging

Obtaining information from a biological system at a molecular level is potentially a useful diagnostic tool. This would allow screening for abnormalities, determine risk of disease development or even guide treatment. Molecular imaging techniques, such as positron emission tomography (PET) and magnetic resonance spectroscopy (MRS), have provided novel approaches for detecting disease and response to treatment, as well as improving our knowledge of cancer biology (Brindle, 2008, Brindle *et al.*, 2011b, Day *et al.*, 2011, Day *et al.*, 2007, Kurhanewicz *et al.*, 2011, Witney *et al.*, 2009, Witney *et al.*, 2010).

1.1.1 Molecular imaging techniques

PET and SPECT

Both positron emission tomography (PET) and single-photon emission computed tomography (SPECT) require administration of radio-nuclides to the patient.

PET uses positron emitting isotopes, such as ^{15}O, ^{13}N, ^{18}F or ^{124}I. The most widely used probe in PET is ^{18}F-fluorodeoxyglucose (FDG), which allows detection of metabolically active tumours by detecting the areas where sugars accumulate (Menzel *et al.*, 2013).

SPECT uses gamma-emitting nuclides, such as ^{99m}Tc, ^{111}In, ^{123}I and ^{131}I. Currently, the detection efficiency and sensitivity of SPECT is lower than that of PET. However, whilst PET cannot distinguish different isotopes, SPECT allows detection of multiple probes simultaneously.

These methods show the activity of the probe but a complementary imaging technique, such as computed tomography or magnetic resonance imaging, is necessary to provide the anatomical information regarding the site where the nuclei have accumulated (Figure 1.1b, d and f).

CT

Computed tomography (CT) images are acquired from the different absorption of x-ray by different tissues. CT has good hard tissue contrast (Figure 1.1e), which makes it ideal for imaging bone structures. However, the kilovoltage-energy x-rays used in the clinical setting deliver ionising radiation to the patient. Minimising the amount of radiation that the patient receives for diagnostics is desirable.

Optical imaging

Optical imaging techniques include bioluminescence, fluorescence and near-infrared (NIR) tomography. In general, bioluminescence and fluorescence suffer the problem that tissues absorb and scatter the light, and are therefore only suitable for areas of the body that are readily accessible, such as the skin (Oppelt, 2005). With NIR tomography, however, detection of signal at depth within ~ 10 cm becomes feasible (Hielscher *et al.*, 2002).

Ultrasound

Ultrasound permits real-time monitoring of anatomical processes. Upon delivery of an ultrasound wave (1-5 MHz frequency), it travels into the body until it hits a boundary between tissues and
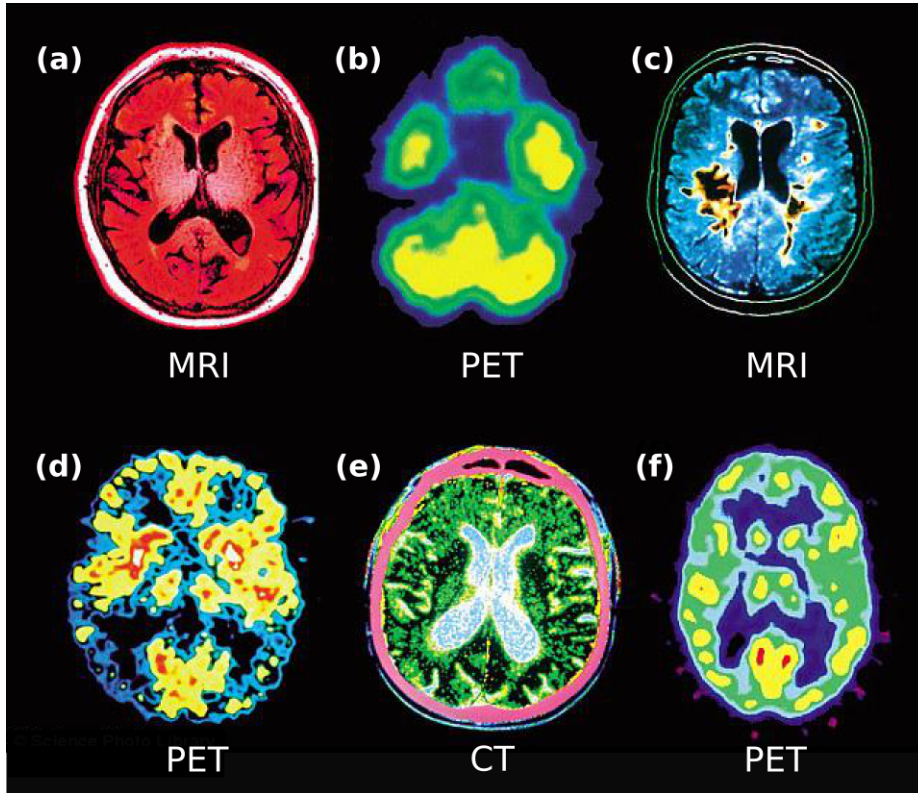
Figure 1.1: Brain scans using magnetic resonance imaging (MRI), positron emission tomography (PET) and computed tomography (CT) of people affected by (a) alcoholism, (b) marijuana use, (c) multiple sclerosis, (d) cocaine use, (e) Parkinson's disease and (f) Alzheimer's disease. Whilst MRI and CT scans provide anatomical information from the brain, PET highlights FDG uptake, displaying highly metabolically active regions. Adapted from Preston (2010).

the sound wave is reflected into the probe. Every tissue has different reflective properties, known as echogenicity. By sampling the frequency and intensity of the echoes it is possible to determine the distance and tissue characteristics. In its traditional form, it allows monitoring cardiac, abdominal, vascular and foetal motion, as well as providing guidance during invasive procedures. Contrast agents based on micro-bubbles bring ultrasound closer to the molecular level, although their development is still at an early stage (Unnikrishnan *et al.*, 2012).

MRS and polarisation-enhanced MRS

Magnetic resonance spectroscopy (MRS) or imaging (MRI) has a relatively high spatial resolution (e.g. *in vitro* resolutions down to tens of μm are possible (Petiet and Johnson, 2010), is not limited

by depth penetration and offers good soft tissue contrast (Figure 1.1a and c). It also provides anatomical information from the ^{1}H-MRI along with information on the injected molecular probe (e.g. ^{13}C-labelled substrate). The principal drawback of MRI is its low sensitivity, this being of the order of milli- to micromoles per voxel, which is at best 10^3 times less sensitive than other imaging modalities.

High temporal and spatial resolution measurements of enzyme-catalysed reactions *in vivo* are possible using dissolution-dynamic nuclear polarisation (dissolution-DNP) enhanced MRS. This technique allows the full nuclear spin magnetisation to be exploited, providing signals strong enough to detect nuclei other than protons. Several ^{13}C-labelled molecules have been successfully hyperpolarised and their metabolism imaged *in vivo* (Kurhanewicz *et al.*, 2011, Brindle *et al.*, 2011a). Moreover, since magnetic resonance does not make use of ionising radiation, MRI would be the ideal imaging modality for patients who need to be scanned regularly. This thesis focuses on hyperpolarisation-enhanced magnetic resonance.

1.2 NMR and cancer metabolism

Nuclear Magnetic Resonance (NMR) is a technique that makes use of the microscopic properties of matter to obtain molecular information on the system of interest. The magnetic fields employed in NMR interact with the 'intrinsic' angular momentum of some nuclei and electrons, known as spin, $\vec{I}$. Only nuclei with non-zero spin quantum number can be detected with NMR, the most common ones having total angular momentum or spin quantum number $I = 1/2$. ^{1}H, ^{13}C, ^{15}N, ^{3}H and ^{129}Xe are among the spin-1/2 nuclei used in NMR studies of cancer. ^{23}Na and ^{39}K, with spin quantum number $I > 1/2$, are also interesting NMR-active nuclei since they are involved in many biological processes and may provide information on heart and brain diseases or tumour progression (Ouwerkerk, 2007, Augath *et al.*, 2009).

The first observation of the NMR phenomenon is attributed to Felix Bloch *et al.* (1946) at Stanford University in California and Edward Mills Purcell *et al.* (1946) in Cambridge, Massachussetts, in 1945. Both groups were awarded with the Nobel Prize for physics in 1952. A couple of decades later, Damadian (1971) pointed out that NMR could be used for the detection of cancer, claiming that the relaxation time constants of protons in tumours are longer than in healthy tissue. In the clinical setting magnetic resonance images are usually from ^{1}H, due to the high natural abundance of protons and the high concentration of water in the human body. However, hyperpolarisation techniques compensate for the low natural abundance of other spin-1/2

nuclei and can facilitate their detection (Section 1.3). For example, hyperpolarised ^{13}C-MRI has allowed for observation of the Warburg effect *in vivo*, i.e. the increase of glucose metabolism in tumours, which is a key feature of cancerous tissue (Section 1.3.3).

1.2.1   Notation and basic concepts

The magnetic moment, $\vec{\mu}$, indicates that a particle can interact with an external magnetic field and is defined as the product of the gyromagnetic ratio of the isotope, γ, with its spin:

$$\vec{\mu} = \gamma \vec{I}. \tag{1.1}$$

The gyromagnetic ratio can be either positive or negative. If $\gamma > 0$, the magnetic moment is parallel to the spin angular momentum. If $\gamma < 0$, the magnetic moment and the spin angular momentum are antiparallel to one another.

The angular momentum projection onto a fixed axis, m, indicates the angular momentum alignment with respect to the quantisation axis of choice. Generally, this quantisation axis is chosen to be the one defined by the external magnetic field, and is arbitrarily denoted as the z-axis. For a spin quantum number I, there are $(2I + 1)$ values of m. For instance, for a nuclear spin-1/2 ($I = 1/2$), $m = -1/2$ or $+1/2$. For a nuclear spin with $I = 1$, $m = -1$, 0 or $+1$. The magnetic moment for each spin in the state m is then

$$\mu_m = m\hbar\gamma. \tag{1.2}$$

The macroscopic quantity detectable with the NMR receiver coil is the magnetisation, which arises from the contribution of magnetic moments from all the nuclear spins in the sample. Since the spins align with the external magnetic field, $\vec{B}_0$, along the z-axis, magnetisation along this axis is proportional to the number of nuclear spins in the sample, N, and the ensemble average of magnetic dipole moments along the longitudinal axis, $\langle \mu_z \rangle$:

$$M_z = N\langle \mu_z \rangle. \tag{1.3}$$

The frequency of the spin precession, known as the Larmor frequency, $\vec{\omega}_0$, is defined as:

$$\vec{\omega}_0 = -\gamma \vec{B}_0. \tag{1.4}$$

In a right-handed coordinate system, looking down the axis from above, a positive ω_0 (spin with $\gamma < 0$) corresponds to anti-clockwise precession of the nucleus around the rotation axis defined by the static external magnetic field (Levitt, 1997).

Energy and eigenstates

The energy levels of a spin system are quantised, i.e. the values of the energy of the system are restricted to a discrete and finite range characteristic of the system. A nuclear spin with spin quantum number I has $(2I + 1)$ possible energy levels, one corresponding to each projection quantum number m. However, when no magnetic field is applied, all the energy levels coincide, i.e. the system is degenerate. Upon application of a magnetic field, the degeneracy is broken and the distinct energy levels can be distinguished. This energy splitting is known as Zeeman splitting. The energy of each spin in the state m is defined by the product of its magnetic moment with the external magnetic field:

$$E_m = -\mu_m B_0. \tag{1.5}$$

The spin system has the least energy if the magnetic moment is parallel to the external magnetic field.

The eigenstates of the spin system, namely $|A_m\rangle$, satisfy the time independent Schrodinger equation:

$$\hat{H} |A_m\rangle = E_m |A_m\rangle, \tag{1.6}$$

where $\hat{H}$ is the Hamiltonian operator of the system and E_m are its eigenvalues or quantised energy values. The eigenstates are stationary states and do not mix with the other states under free evolution, only a complex factor $\mathrm{e}^{-iE_m t}$ is acquired.

A spin-1/2 has two eigenstates, either the low-energy state aligned with the magnetic field ($m = +1/2$), $|\alpha\rangle$, or the high-energy state antiparallel to the magnetic field ($m = -1/2$), $|\beta\rangle$:

$$
\begin{aligned}
E_\alpha &= -\frac{1}{2}\hbar\gamma B_0, \\
E_\beta &= +\frac{1}{2}\hbar\gamma B_0.
\end{aligned}
\tag{1.7}
$$

However, any nuclear spin may be in any nuclear state that is a superposition of the energy eigenstates:

$$|\varphi\rangle = a |\alpha\rangle + b |\beta\rangle. \tag{1.8}$$

a and b are complex numbers that characterise the probability of finding the state in the energy level corresponding to $|\alpha\rangle$ or $|\beta\rangle$ after a measurement, respectively:

$$
\begin{aligned}
p_\alpha &= |a|^2 = |\langle\alpha|\varphi\rangle|^2, \\
p_\beta &= |b|^2 = |\langle\beta|\varphi\rangle|^2.
\end{aligned}
\tag{1.9}
$$

Populations and coherences

The quantum state of an entire ensemble of spins may be described by the spin density operator, $\hat{\rho}$, which is a matrix whose diagonal elements are the populations and the off diagonal elements are the coherences.

For instance, the density matrix of an ensemble of spins-$1/2$ is the following:

$$
\hat{\rho} = \overline{|\varphi\rangle\langle\varphi|} = \begin{pmatrix} \rho_{\alpha\alpha} & \rho_{\alpha\beta} \\ \rho_{\beta\alpha} & \rho_{\beta\beta} \end{pmatrix}.
\tag{1.10}
$$

The difference in spin state populations indicates the net longitudinal spin polarisation,

$$
P = \rho_{\alpha\alpha} - \rho_{\beta\beta} = |\alpha\rangle\langle\alpha| - |\beta\rangle\langle\beta| \neq 0 \Leftrightarrow M_z \neq 0,
\tag{1.11}
$$

while the presence of coherences indicates the existence of transverse magnetisation,

$$
\left.\begin{aligned}
\rho_{\alpha\beta} &= |\alpha\rangle\langle\beta| \neq 0 \\
\rho_{\beta\alpha} &= |\beta\rangle\langle\alpha| \neq 0
\end{aligned}\right\} \Leftrightarrow M_{xy} \neq 0.
\tag{1.12}
$$

1.2.2   What determines NMR sensitivity?

The signal-to-noise ratio (SNR) compares the desired signal on the NMR spectra with the background noise. Higher SNR provides better signal contrast and allows detection of lower concentration substrates. SNR depends on:

- **The nuclear gyromagnetic ratio.** Larger gyromagnetic ratios give higher SNR. For instance, ^{1}H is more sensitive in NMR because $\gamma_\mathrm{H} \approx 4 \times \gamma_\mathrm{C}$.

- **The concentration of spins detected by the receiver coil.** High concentration of the nuclei under investigation improves the SNR. ^{1}H is found in natural abundance at levels 90 times higher than ^{13}C (^{1}H is found in 99.98%, while ^{13}C is only found in 1.11%), and therefore ^{1}H-NMR is in general more sensitive. In *in vivo* hyperpolarisation experiments, the concentration of the nuclei influencing the SNR is the final concentration after the dilution of the substrate upon injection into the subject. A large volume of sample seen by the radiofrequency coil increases the amount of signal arising from the nuclear spins, but it also increases the noise.

- **The filling factor.** It is defined as the ratio of the volume of sample to the volume of coil. Using a coil that matches the volume of the sample, i.e. increasing the filling factor, improves the SNR.

- **The polarisation level and the magnetic field strength.** Polarisation, i.e. imbalance between the lowest and the highest energy levels of a spin system, may be raised by increasing the magnetic field strength or by using external hyperpolarisation techniques. High polarisation levels provide better SNR.

- **The acquisition time.** This has to be optimised to guarantee the highest SNR: it has to be long enough to capture the whole decay of the FID, but short enough not to include unnecessary noise. However, this could be avoided by better filtering.

- **The width of the signal/shimming.** Higher B_0 field homogeneity makes the peak narrower and therefore easier to distinguish from the background noise.

- **The relaxation time constants T_1 and T_2.** These parameters will also affect the acquisition. Nuclei with fast T_2 relaxation present broader spectral peaks; fast T_1 relaxation allows fast repetition of the signal acquisition to increase the number of scans and improving the SNR.

- **The radiofrequency pulse sequence used for acquisition.** For example, the highest SNR achievable with a single scan is obtained with a radio frequency flip angle pulse of 90°.

At high magnetic fields, the main source of noise is the sample itself. In this case, the SNR dependence upon concentration of the nucleus under investigation, c, the magnetic field strength, B_0, and the gyromagnetic ratio of the nucleus, γ, is given by (Ardenkjaer-Larsen *et al.*, 2011):

$$\text{SNR} \propto c\gamma^2 B_0. \tag{1.13}$$

^{13}C-NMR involves detection of ^{13}C-labelled metabolites. ^{12}C is the more abundant carbon isotope found at 98.89% in natural abundance but has spin quantum number $I = 0$, making it NMR-invisible. The NMR active carbon isotope ^{13}C ($I = 1/2$) accounts only for 1.11% of the carbon found in normal conditions. Using ^{13}C-labelled material compensates for the low concentration of nuclei, but since its gyromagnetic ratio is one fourth of the gyromagnetic ratio of the proton, the sensitivity of a ^{13}C-NMR experiment is 16 times lower than ^{1}H-NMR at the same field. However, ^{13}C-NMR has a larger spectral range, provides information on the position of the label within the substrate and its metabolic products, and its signal is minimally disturbed by the natural abundance signal in the background.

In the following sections I present some strategies to improve the sensitivity of ^{13}C-NMR experiments for the study of cancer metabolism. First, those which boost the nuclear spin polarisation, including the dissolution-DNP technique. Then, those which efficiently preserve the nuclear spin polarisation until it is required for imaging or spectroscopy. Finally, some high-sensitivity approaches to signal acquisition.

1.3   Boosting sensitivity with hyperpolarisation

The spin ensemble is said to be 'hyperpolarised' if the nuclear population distribution is far above the thermal equilibrium. These techniques may increase the population difference more than 10^4 times, and correspondingly improve SNR (Ardenkjaer-Larsen *et al.*, 2003). Therefore, injection of hyperpolarised ^{13}C-labelled metabolites may be used to improve detection and monitoring of tumour metabolic changes after therapy.

1.3.1   Polarisation of an ensemble of non-interacting spin-1/2 nuclei

The longitudinal polarisation, P, of an ensemble of non-interacting spin-1/2 nuclei is defined as the difference in the state populations $|\alpha\rangle$ and $|\beta\rangle$ normalised by the total number of spins (Abragam and Goldman, 1978):

$$P = \left| \frac{N_\alpha - N_\beta}{N_\alpha + N_\beta} \right| = |n_\alpha - n_\beta|. \tag{1.14}$$

where n_α and n_β are the normalised populations so that $n_\alpha + n_\beta = 1$. This has been shown in terms of the density operator in Eq. (1.11).

An expression for the normalised populations in terms of the polarisation level arising from

Eq. (1.14) is given by:

$$\begin{cases} n_\alpha &= \frac{1}{2}(1+P), \\ n_\beta &= \frac{1}{2}(1-P). \end{cases} \tag{1.15}$$

The normalised populations lie between 0 and 1 ($0 \leq n_{\alpha(\beta)} \leq 1$), and therefore polarisation also ranges from $P = -1$ if all the ensemble spins are in the high-energy state $|\beta\rangle$ to $P = +1$ corresponding to the entire ensemble spins being in the low-energy state $|\alpha\rangle$.

Polarisation may also be defined as the projection of the density operator onto the longitudinal angular momentum operator

$$P = \frac{\mathrm{Tr}(I_z|\bar{\rho})}{\mathrm{Tr}(I_z|I_z)}. \tag{1.16}$$

For an ensemble of molecules with spin-1/2, in the absence of an external magnetic field, all energy states are equally populated. In contrast, when an external magnetic field is applied, at a temperature T, the spins reach thermal equilibrium and distribute with a biased spin orientation parallel to the field. Thermal equilibrium polarisation is then given by the high temperature approximation of the Boltzmann model:

$$P_0 = \tanh\left(\frac{\hbar\gamma B_0}{2\kappa_B T}\right) \approx \frac{\hbar\gamma B_0}{2\kappa_B T}, \tag{1.17}$$

where $\hbar$ is the reduced Planck's constant ($\hbar = h/2\pi \approx 1.05 \times 10^{-34}$ J s), γ is the gyromagnetic ratio of the nucleus, B_0 is the magnetic field strength, κ_B is the Boltzmann constant ($\kappa_B \approx 1.38 \times 10^{-23}$ m^2 kg s^{-2} K^{-1}) and T is the temperature of the sample.

For samples with polarisation levels different to P_0, Eq. (1.13) does not hold true. SNR depends then upon the polarisation level:

$$\mathrm{SNR} \propto c\gamma P. \tag{1.18}$$

1.3.2 Experimental determination of polarisation

The longitudinal spin angular momentum I_z of an ensemble of spin-1/2 nuclei, which gives rise to longitudinal magnetisation ($M_z = N\gamma I_z$), and therefore to NMR signal, is proportional to polarisation,

$$I_z = \frac{\hbar}{2}P. \tag{1.19}$$

Consequently, the ratio between the NMR signal S at any time when the polarisation is measured ($t = t_{\text{pol}}$) and its thermal equilibrium value is the same as the ratio between the polarisation (P) at the same time t_{pol} and the thermal equilibrium polarisation (P_0):

$$\frac{S(t_{\text{pol}})}{S_0} = \frac{P(t_{\text{pol}})}{P_0}. \tag{1.20}$$

In hyperpolarisation experiments, polarisation is often determined by dividing the signal intensity of a spectral peak at the beginning of a hyperpolarised experiment by the signal intensity of the same spectral peak acquired at thermal equilibrium (both acquired with the same flip-angle pulse), and multiplied by the calculated P_0 appropriate for the nucleus, magnetic field strength and temperature of the experiments:

$$P(\%) = \frac{S}{S_0} P_0(\%). \tag{1.21}$$

At 9.4 T and 293 K, P_0 is $\sim 0.0032\%$ for ^{1}H and $\sim 0.0008\%$ for ^{13}C [Eq. (1.17)]. With hyperpolarisation techniques, the theoretical limit is set to $P = 100\%$. This would imply that all the spins in the ensemble are in the same state.

1.3.3   Dynamic nuclear polarisation (DNP)

Dynamic nuclear polarisation (DNP) is a hyperpolarisation technique based on the cross-polarisation between electrons and atomic nuclei or the Overhauser effect.

The electron gyromagnetic ratio, γ_{e}, is 660 times larger than γ_{H} and, therefore, the thermal polarisation of electrons is much higher than that of nuclear spins. For example, in the presence of an external magnetic field of 3.35 T operating at 1.2 K, the electron polarisation is close to 100%, whilst the ^{1}H spin polarisation is $\sim 0.3\%$ and the ^{13}C is 0.08%.

The DNP process starts by doping a sample containing the nuclei of interest with a source of unpaired electrons (free radicals). Then, irradiating the sample with a microwave source operating at a frequency close to the resonance frequency of the electron spins drives the nucleus-electron transitions. This causes one of the nuclear spin states to become overpopulated, while the other is depleted, i.e. increases the nuclear polarisation (Figure 1.2). The sources of unpaired electrons are typically radicals such as nitroxide or trityl species. Whilst nitroxides have a broad electron resonance frequency range and cover the Larmor frequency of all nuclei, trityls present a narrow resonance band and the microwave irradiation frequency has to be selected to drive polarisation
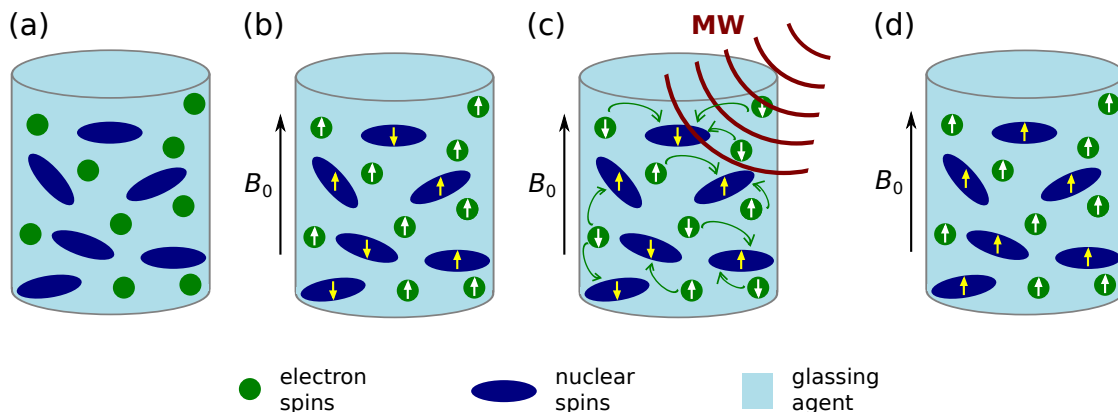
Figure 1.2: Scheme of the dynamic nuclear polarisation (DNP) process. (a) The sample is prepared with the substrate containing the nucleus to be polarised, the source of unpaired electrons (and the glass-forming agent in solid-state DNP). (b) Once inside the DNP magnet, the spins in the sample reach their thermal equilibrium polarisation. The electrons are polarised to $\sim 100\%$. (c) The polarisation transfer between electron spins and nuclear spins is driven by irradiating the sample with microwaves at a frequency close to the resonance frequency of the electrons. (d) The sample is hyperpolarised: there is a larger population imbalance between the nuclear spin states.

transfer with the nucleus of interest.

Nuclear polarisation of molecules in solution may be enhanced by doing Overhauser cross-relaxation between electrons and nuclei, known as **Overhauser-DNP**. However, efficient transfer relies upon low magnetic fields ($<$ fewer tesla) and small molecules, since the transfer relies on fast molecular diffusion with respect to the electron Larmor frequency. Much higher polarisation can be obtained for solutions by polarising in the solid state, followed by melting to a liquid state. This is known as **dissolution-DNP**.

To date, metabolism studies using hyperpolarisation by DNP have relied on dissolution-DNP, which provides greater signal enhancement and larger sample volumes.

Overhauser-DNP

Overhauser-DNP (O-DNP) operates at room temperature and is based on the Overhauser cross-polarisation between the free electrons from the doped radical and the nuclei of interest in the sample. Although the nuclear hyperpolarisation achievable at room-temperature with O-DNP is at best 100 times lower than using a dissolution-DNP setup, it may be suitable for fast-screening of metabolites with ^{1}H-NMR (van Bentum *et al.*, 2011). Some of the features of O-DNP include

the following:

- **Fast turnaround:** Much faster repetition time between successive sample polarisations, which may lead to higher resolution images or prolonged measurements to study the effect of drug treatment.

- **Small volumes:** O-DNP is the most suitable DNP method for sub-microlitre NMR samples (volumes of $\sim$100 nl).

- **Delicacy:** It allows one to hyperpolarise delicate samples, those that would not survive the harsh conditions of freezing and the temperature jump in dissolution-DNP.

- **Fast transport:** The transport from the hyperpolarisation cavity to the location where the NMR spectrum is to be acquired may be faster. This is desirable for nuclei with especially short values of T_1.

Drawbacks of O-DNP Proton signal in glucose has been previously increased using a microfluidic chip and O-DNP (Bart *et al.*, 2009, Krahn *et al.*, 2010). This may be a helpful tool for the study of cell metabolism *in vitro*. However, O-DNP has several features that make it incompatible with hyperpolarised *in vivo*-MRS:

- Very small sample volumes, since the microwaves penetration depth in water is poor.

- Heating in aqueous solutions, which limits the sample size.

- Currently limited to small molecules of three or four atoms.

- Relatively large concentrations of radicals required, which shorten T_1.

Dissolution DNP

An alternative to the liquid-state driven DNP is its solid-state counterpart. Dissolution-DNP is typically performed using two magnets: one used to polarise the sample in the solid state (usually at 3.4 or 5.0 T), the other as a dedicated NMR/MRI instrument (Figure 1.3). For pre-clinical work, the NMR spectrometer operates at magnetic field strengths much higher than the DNP magnet. However, current clinical magnets are typically in the range of 1.5-3 T, although higher fields up to 7 T are now available (Duchin *et al.*, 2012).

The dissolution-DNP process starts with pre-polarising the sample in the solid state at liquid helium temperature. In addition to the free radical, a glassing agent must be incorporated into

the sample. Glassing agents, such as glycerol or DMSO, are used to prevent crystallisation of the sample. This ensures a uniform distribution of the radicals in the sample and good microwave penetration.

After sample preparation, it is rapidly inserted into the DNP magnet and irradiated with microwaves to drive the electron-nucleus polarisation transfer. The polarisation build-up in the solid state depends on the radical and the substrate, electron and nuclear relaxation rates, and composition of the frozen mixture. For the nuclear polarisation to reach a maximum it may take several hours. When polarising ^{13}C, the regular DNP enhancement is performed by directly irradiating the frozen sample with the appropriate MW frequency for ^{13}C. Jannin *et al.* (2012) presented a faster alternative: polarise the protons in the sample, which build-up polarisation much faster, and transfer the ^{1}H polarisation to ^{13}C via cross-polarisation under Hartmann-Hahn irradiation. Using a 6.7 T-DNP magnet at 1.2 K, they report 70% ^{13}C polarisation before dissolution, built up in 20 minutes using this technique.

Once the polarisation build up reaches its maximum value, the sample is dissolved. 'Dissolution' refers to the practice of ejecting the polarised material from the DNP apparatus. This involves first carefully removing the sample chamber from its immersion in the cryostat and then injecting a hot liquid heated to 10 bar and 180°C to melt the frozen sample.
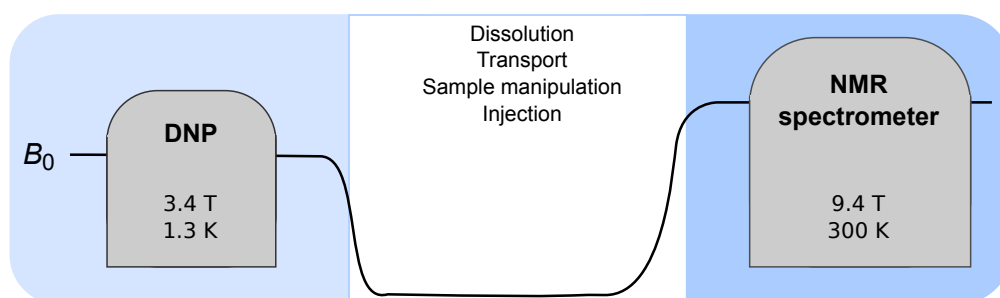
Figure 1.3: Scheme of a typical dissolution-DNP experiment. From left to right, the experiment starts with preparing the sample to be hyperpolarised and doping it with free radicals and then inserting it into the DNP magnet. The DNP magnet that we work with operates at 3.4 T and 1.3 K. The sample is irradiated with microwaves at the right frequency to build up the polarisation (Figure 1.2). Upon dissolution, the sample goes through the low field of the room for a variable interval of time depending on sample manipulation, transfer time and injection time. Once in the NMR spectrometer, which is at a magnetic field of 9.4 T and at room or body temperature for pre-clinical work, the pre-polarised ^{13}C-metabolite signal may be detected for spectral or image acquisition.

The jet of liquid forces the dissolved hyperpolarised material into a vial outside the DNP magnet (at approximately room temperature), where separation of gas and liquid phase occurs. The substrate must therefore tolerate the rapid temperature jump from ~ 1 K to ~ 300 K.

The hyperpolarised material is then taken to the NMR spectrometer within a few seconds from dissolution, where the ^{13}C signal is then acquired (either upon injection into an animal or a test tube). Faster transport times may be achieved with setups that allow automatic transfer and injection into the NMR spectrometer within 3 s (Bowen and Hilty, 2010, Cheng *et al.*, 2013). The delay between dissolution and acquisition may be longer in a clinical setting, taking up to 60 s, since radical filtration and quality control tests have to be performed before injection into the patient (Nelson *et al.*, 2013). Recent work from Reynolds *et al.* (2014) shows that it is feasible to automate the injection process while controlling the dose delivered, monitoring the pH and minimising the dead time.

It has been reported that irradiation of a neat pyruvic acid preparation with UV light generates photo-induced radicals, which can be used to catalyse solid-state DNP without addition of excess radicals. They report ^{13}C polarisations of about 10% (Eichhorn *et al.*, 2013). The advantage of this method is that no potentially toxic radicals need to be included in the preparation of the sample. The photo-induced radicals recombine upon dissolution and the liquid sample is composed exclusively of endogenous metabolites, excluding the need of filtration before injection into the subject and reducing steps in the quality control process.

^{13}C-labelled substrates to study metabolism   Glucose metabolism plays a very important role in the study of cancer biology. A well-known feature of tumour progression is the Warburg effect: glucose uptake and lactate production increase in tumourous tissue (Le *et al.*, 2012, Tennant *et al.*, 2010). Imaging of glucose and its metabolic products (Figure 1.4a) may therefore provide useful information on cancer cell metabolism.

Current studies involve performing metabolomic NMR experiments on extracts of cells cultured with ^{13}C-glucose. Due to the low concentration at which the label is present in the cell suspension, NMR spectrum acquisition requires large numbers of scans that may require hours or even days to complete (de Graaf *et al.*, 2009, Fan and Lane, 2008, Jeffries *et al.*, 2012, Le *et al.*, 2012). DNP may reduce this time and improve MR image resolution, since by boosting the signal the detection voxel size may be reduced.

The most widely used substrate for the study of cancer metabolism with dissolution-DNP is ^{13}C-pyruvate because the polarisation decay is slow compared to other substrates ($T_1 \sim 60$ s), it is

well-tolerated by the biological system and it provides useful metabolic information. Pyruvate has been used to detect response after cancer treatment (Day *et al.*, 2007, Chen *et al.*, 2013); the ratio of the lactate exchanged with the hyperpolarised pyruvate with the injected pyruvate provides information on the loss of LDH and coenzyme concentrations. Dissolution-DNP, in particular hyperpolarised [1-^{13}C]pyruvate, has taken the first steps towards translation into a clinical setting with the conclusion of a clinical trial in patients with prostate cancer at University of Calfornia San Francisco, US (Nelson *et al.*, 2013). Further clinical trials will soon take place at the University of Cambridge, UK.

^{13}C-fumarate is another marker of response after cancer treatment (Gallagher *et al.*, 2009). A high conversion of fumarate into malate indicates cell necrosis, when fumarate comes into contact with the enzyme fumarase responsible for the hydration reaction that converts it into malate.

The administration of ^{13}C-glutamine and its conversion into glutamate may be a probe of tumour cells proliferation (Gallagher *et al.*, 2008b).

^{13}C-bicarbonate has been used to determine extracellular pH, which in turn is a marker of disease and response to treatment (Gallagher *et al.*, 2008a).

The substrates used in DNP are not limited to the glycolytic pathway and the Krebs cycle. The oxidation reaction of ^{13}C-ascorbate into ^{13}C-dehydroascorbate (Figure 1.4b) provides valuable information on oxidative stress; reactive oxygen species increase in mitochondria during apoptosis (Keshari *et al.*, 2011, Bohndiek *et al.*, 2011).

Recently, a new substrate has been used to assess aldehyde dehydrogenase (ALDH2) activity in liver *in vivo* and in real time (Dzien *et al.*, 2014). ^{13}C-ethanol is oxidised to ^{13}C-acetate via acetaldehyde. Suppression of ALDH2 activity leads to lower acetate production. Since ALDH2 is an emerging drug target for treatment of cardiovascular diseases, cocaine and alcohol dependence, being able to monitor its activity *in vivo* would provide information on the success of the drug (Levin *et al.*, 2007, Mayer *et al.*, 2006, Reeder *et al.*, 2007).

Table 1.1 summarises most of the ^{13}C-labelled substrates used to study cancer metabolism using dissolution-DNP and their approximate longitudinal relaxation time constants, which have a direct effect on the decay rate of the hyperpolarisation. After a time $t = 3 \times T_1$, polarisation decays to 5% of its initial value, and by a time $t = 5 \times T_1$ only 0.7% of the initial polarisation is left. Therefore, hyperpolarisation of substrates with T_1 less than 20 s are unlikely to make it into a clinical setting, where the transport time from dissolution to patient is currently ~ 60 s (Nelson *et al.*, 2013).

(a)

(b)
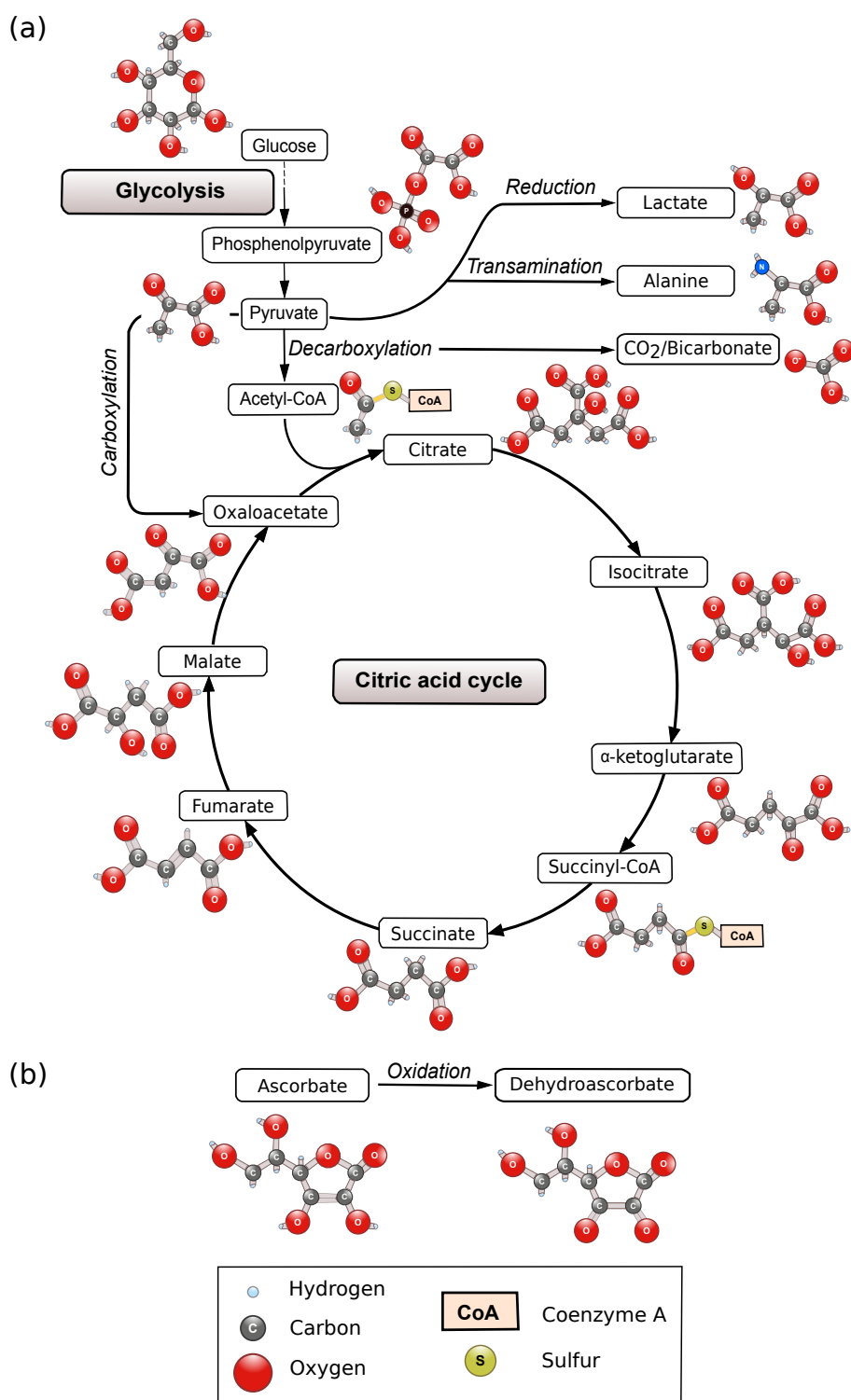
Figure 1.4: (a) Krebs cycle and (b) oxidation reaction of ascorbate.

Substrate	Products	P[%]	T_1 [s]
[1-^{13}C]pyruvate (Ardenkjaer-Larsen *et al.*, 2003, Hurd *et al.*, 2010, Albers *et al.*, 2008)	[1-^{13}C]lactate, [1-^{13}C]alanine, [^{13}C]bicarbonate, $^{13}CO_2$	20-25	65
[2-^{13}C]pyruvate (Schroeder *et al.*, 2009)	[^{13}C]bicarbonate, $^{13}CO_2$ [2-^{13}C]lactate, [2-^{13}C]alanine, 1 ^{13}C]acetyl-carnitine, [1-^{13}C]citrate, [5-^{13}C]glutamate	27	55
[1,2-$^{13}C_2$]pyruvate (Tayler *et al.*, 2012)	1 ^{13}C]acetyl-carnitine, [1-^{13}C]citrate, [5-^{13}C]glutamate [1,2-$^{13}C_2$]lactate, [1,2-$^{13}C_2$]alanine, [1-^{13}C]acetyl-carnitine, [1-^{13}C]citrate, [5-^{13}C]glutamate, [1-^{13}C]acetyl-carnitine, [^{13}C]bicarbonate, $^{13}CO_2$	26	30-50
[1-^{13}C]lactate (Kennedy *et al.*, 2012)	[1-^{13}C]lactate, [1-^{13}C]alanine, [^{13}C]bicarbonate, $^{13}CO_2$	20	40-50
^{13}C-bicarbonate (Gallagher *et al.*, 2008a, Wilson *et al.*, 2010)	$^{13}CO_2$	10-16	10-50
[1,4-$^{13}C_2$]fumarate (Gallagher *et al.*, 2009, Wilson *et al.*, 2010)	[1,4-$^{13}C_2$]malate	26-35	25-30
[1-^{13}C]acetyl-methionine (Chen *et al.*, 2011)	[1-^{13}C]methionine	4	28
[2-^{13}C]fructose (Keshari *et al.*, 2009)	[1-^{13}C]fructose-6-phosphate	12	16
[1-^{13}C]glutamate (Gallagher *et al.*, 2011)	[1-^{13}C]α-keto glutarate	28	34
[5-^{13}C]glutamine (Gallagher *et al.*, 2008b)	[5-^{13}C]glutamate	5	16
[1-^{13}C]ethyl pyruvate (Hurd *et al.*, 2010)	[1-^{13}C]pyruvate, [1-^{13}C]lactate, [1-^{13}C]alanine, [^{13}C]bicarbonate, $^{13}CO_2$	28-35	25
[1,1-$^{13}C_2$]acetic anhydride (Wilson *et al.*, 2009)	Multiple depending on reactant	6	34
[1-^{13}C]acetate (Bastiaansen *et al.*, 2013, Comment *et al.*, 2007, Mishkovsky *et al.*, 2012)	[1-^{13}C]acetylcarnitine, [5-^{13}C]2 oxoglutarate	10-13	15-30
[^{13}C]urea (Golman *et al.*, 2003, Wilson *et al.*, 2010)	None	10-13	20-45
HP001 (Johansson *et al.*, 2004)	None	15	40-80
α-keto-[1-^{13}C]isocaproate (Karlsson *et al.*, 2010)	[1-^{13}C]leucine	32	55
[1-^{13}C]dehydro ascorbic acid (Keshari *et al.*, 2011, Bohndiek *et al.*, 2011)	[1-^{13}C]ascorbic acid	6-10	20-50
[1-^{13}C]alanine (Jensen *et al.*, 2009)	[1-^{13}C]pyruvate, [1-^{13}C]lactate, [^{13}C]bicarbonate	26	29
[U-$^{13}C_6$-U-^{2}H]glucose (Allouche-Arnon *et al.*, 2013, Rodrigues *et al.*, 2014)		4	10
[1-^{13}C-U-^{2}H]ethanol (Dzien *et al.*, 2014)	[1-^{13}C]acetate	14	50

Table 1.1: ^{13}C-agents hyperpolarised with dissolution-DNP and their ^{13}C-metabolic products. HP001 stands for bis-1,1-(hydroxymethyl)-[1-^{13}C]cyclopropane-d8. Polarisation levels and T_1 s are presented here as estimates, but may vary depending on the magnetic field strength, temperature and solvent in which the measurement was taken. Adapted from Hurd *et al.* (2012).

Drawbacks of dissolution-DNP   The main drawbacks of dissolution-DNP in the context of cell and *in vivo* metabolic studies are summarised in the following:

- **Reproducibility:** Some commercial dissolution-DNP instruments, such as the Oxford Instruments HyperSense (Abingdon, Oxfordshire, UK), produce consistent initial levels of polarisation by using an automated dissolution process. However, dissolution-DNP experiments are difficult to reproduce because the signals finally acquired depend on several factors, including transport time, injection time, dilution post injection and uptake of the substrate. In general, there is no easy way to correlate signal intensity with polarisation and metabolite concentration.

- **Low throughput:** The build up of high polarisation levels in the frozen sample is a time consuming process, which may take several hours to achieve. This adds to the time taken in sample preparation and pre-cooling of the polariser.

- **Strict sample requirements:** The substrate of interest will only polarise well as a glass. This limits the method to systems where glass formation is feasible, and where the substrate does not precipitate from solution during the rapid temperature cycling involved in the dissolution-DNP process. Furthermore, the substrate needs to to be very soluble, so that it is concentrated in the solid state sample and still at high concentration after dissolution, and that its metabolism is very fast.

- **Polarisation loss:** Although dissolution-DNP may provide substrates with a larger initial polarisation before dissolving the frozen sample, the T_1 lifetimes of ^{13}C nuclei in solution are short and those for ^{1}H nuclei are even shorter (e.g. the lifetimes for glucose are $T_1(^{13}$C$)$ $\sim$ 10 s and $T_1(^1$H$) <$ 1 s). This prevents one from fully exploiting dissolution-DNP, since most of the hyperpolarisation is lost during the transport to the acquisition magnet. Section 1.4.3 suggests strategies to overcome the problem of fast polarisation decay.

1.3.4   Other hyperpolarisation techniques

Aside from DNP, there are many alternatives to increase the SNR of a sample. There are methods such as those using very strong magnetic fields and low temperatures (brute force) to achieve high thermal polarisations, and more sophisticated hyperpolarisation techniques that boost the initial polarisation to values much higher than thermal equilibrium: para-hydrogen induced polarisation (PHIP), chemically induced DNP (CIDNP), optical pumping (OP) or quantum tunnelling. Of

those, only DNP, PHIP and brute force have been used with molecules in solution (Ardenkjaer-Larsen *et al.*, 2011). In particular DNP is the most practical method within the metabolic and *in vivo* context.

1.4   Boosting sensitivity by preserving polarisation

Any perturbation of the thermal equilibrium population, caused either by radiofrequency pulses or hyperpolarisation, will drive the spin system to dissipate or absorb energy to return to equilibrium. This process is known as relaxation (Levitt, 2008). Hyperpolarisation experiments involve perturbing the spin system to achieve large signal enhancements. Nevertheless, the signal will decay with the longitudinal relaxation time constant, T_1, as soon as the source of polarisation enhancement ceases. Discussing ways to slow down the decay of the hyperpolarisation and minimise polarisation loss during transport between the DNP magnet and the acquisition spectrometer is the focus of this section.

1.4.1   Longitudinal and transverse relaxation

If the thermal equilibrium polarisation of a sample is perturbed, the spins will tend to return to the equilibrium state as soon as the source of the perturbation ceases. An example of such a perturbation is the rotation of the magnetisation with a radiofrequency pulse applied at the Larmor frequency of the nuclear spin of interest. While there is a component of the magnetisation in the transverse plane, the magnetisation will precess around the axis of the magnetic field. Arising from these observations, the Bloch equations were introduced by Felix Bloch (1946). The Bloch equations are phenomenological equations used to predict the macroscopic change of magnetisation with time, $M(t) = (M_x(t), M_y(t), M_z(t))$:

$$\frac{dM_x(t)}{dt} = \gamma(M_y(t)B_0 - M_z(t)B_1 \sin \omega t) - \frac{M_x(t)}{T_2}, \tag{1.22}$$

$$\frac{dM_y(t)}{dt} = -\gamma(M_x(t)B_0 - M_z(t)B_1 \cos \omega t) - \frac{M_y(t)}{T_2}, \tag{1.23}$$

$$\frac{dM_z(t)}{dt} = \gamma(M_x(t)B_1 \sin \omega t - M_y(t)B_1 \cos \omega t) - \frac{M_z(t) - M_0}{T_1}, \tag{1.24}$$

where M_0 is the thermal equilibrium magnetisation, B_0 is the static magnetic field along z-axis, B_1 is the radiofrequency field amplitude with components on the plane perpendicular to B_0, $\vec{B}_1 = (B_1 \cos \omega t, B_1 \sin \omega t)$, and T_1 and T_2 are the relaxation time constants of the magnetisation.

T_1 relaxation is defined as the transition between energy levels to re-establish the Boltzmann distribution after any perturbation of the equilibrium. It involves energy exchange between one spin and the spin system. In contrast, T_2 relaxation is the loss of coherence in spins precessing around the external magnetic field.

Relaxation after perturbation by a radiofrequency pulse

The solution of the above differential equations after a 90°_y radiofrequency pulse application, i.e. initial conditions $M_z(0) = 0$, $M_x(0) = M_0$, $M_y(0) = 0$ and $B_1 = 0$, is the following:

$$M_x(t) \quad = \quad M_0 \cos(\omega_0 t) \mathrm{e}^{-t/T_2}, \tag{1.25}$$

$$M_y(t) \quad = \quad -M_0 \sin(\omega_0 t) \mathrm{e}^{-t/T_2}, \tag{1.26}$$

$$M_z(t) \quad = \quad M_0(1 - \mathrm{e}^{-t/T_1}). \tag{1.27}$$

The longitudinal magnetisation recovers with T_1 (Figure 1.5a), whereas the transverse magnetisation decays exponentially with T_2 (Figure 1.5b).

Polarisation decay

Polarisation decay immediately after dissolution of hyperpolarised material is analogous to the longitudinal magnetisation recovery after perturbation by a radiofrequency pulse. Solving the Bloch equations [Eqs (1.22)-(1.24)] with the initial conditions appropriate for a hyperpolarisation experiment ($M_z(0) >> M_0$, $M_{x,y}(0) = 0$), the longitudinal component of the magnetisation relaxes with T_1 while the transverse magnetisation remains unchanged:

$$M_x(t) \quad = \quad 0, \tag{1.28}$$

$$M_y(t) \quad = \quad 0, \tag{1.29}$$

$$M_z(t) \quad = \quad M_0 + \mathrm{e}^{-t/T_1}(M_z(0) - M_0). \tag{1.30}$$

Figure 1.5c illustrates the return to the thermal equilibrium, which obeys a mono-exponential decay function with the time constant T_1 independently of the sign of the perturbation of M_z.

Relaxation at two different magnetic field strengths

If the sample is moved between two magnetic field strengths, for instance from a low magnetic field to a high magnetic field, the time the hyperpolarised material spends in each of the magnetic fields affects the decay of the polarisation. This will be discussed in more detail in Chapter 2.
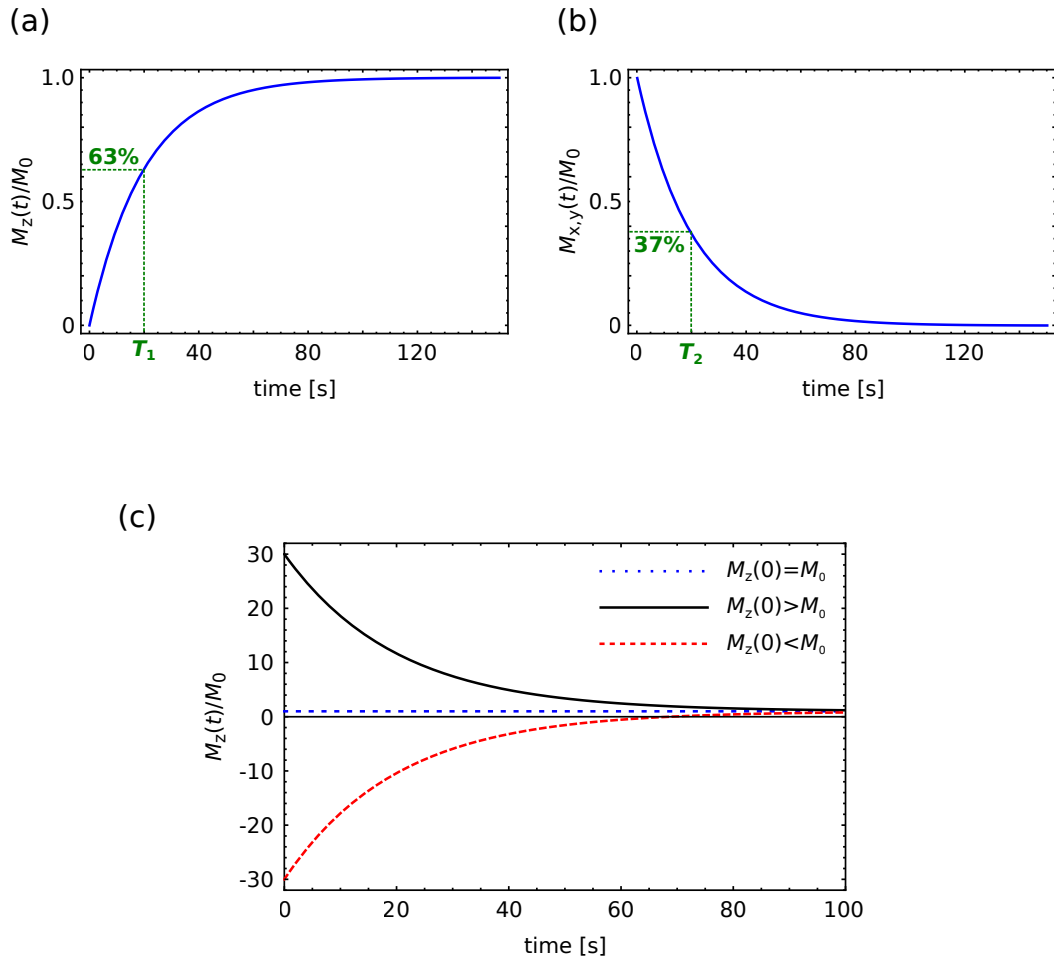
Figure 1.5: **Top:** Relaxation after perturbation by a radiofrequency pulse. a) Magnetisation along the magnetic field axis, M_z, recovers to 63% of the thermal magnetisation, M_0, after a time T_1 while b) the transverse magnetisation decays to 37% after a time T_2. **Bottom:** c) Longitudinal relaxation of M_z with $T_1 = 20$ s after hyperpolarisation. Three cases are presented: if $M_z(0) = M_0$, magnetisation is already in thermal equilibrium and no relaxation occurs (blue); if $M_z(0) > M_0$, as for positive polarisation, magnetisation decays exponentially to M_0 (black); and if $M_z(0) < M_0$, as for negative polarisation, magnetisation grows exponentially to M_0 (red).

1.4.2 Relaxation mechanisms

The spin ensemble tends to thermodynamic equilibrium via gradual loss of coherence of spins caused by microscopic fluctuations in the spins' magnetic environment under Brownian motion. A basic picture of relaxation, therefore, is given by the second order time-dependent perturbation theory. The transition rate between two states, $|p\rangle$ and $|q\rangle$, due to a fluctuating, random field characterised by a Hamiltonian, H, is

$$|\langle p|H|q\rangle|^2 j(\omega_{pq}), \tag{1.31}$$

where j is the spectral density of the fluctuation at the energy difference of the two states (ω_{pq} in angular units). Sometimes this formula is called 'Fermi's golden rule'.

For the states of a single spin-1/2 nucleus, $|\alpha\rangle$ and $|\beta\rangle$, the transition rate can be expressed as

$$\text{rate} = 1/T_1 = |\langle \alpha|H|\beta\rangle|^2 j(\omega_0). \tag{1.32}$$

In liquids, the fluctuation is caused by molecular reorientation and tumbling, and intermolecular spin-spin interactions. For a random isotropic tumbling, the spectral density is

$$j(\omega_0) = \frac{\tau_C}{1 + (\omega_0 \tau_C)^2} \approx \tau_C. \tag{1.33}$$

$j(\omega_0)$ simplifies to τ_C in the limit of fast correlation times relative to the nuclear Larmor frequency ($|\omega_0 \tau_C| << 1$), which is the regime satisfied by most small molecules in solution, and relaxation at low magnetic fields. For historical reasons, this is called extreme narrowing.

- **Direct dipole-dipole coupling** is the direct magnetic interaction of nuclear spins with each other. The spins separation distance, r, plays an important role in the contribution of this interaction to relaxation. Under the extreme narrowing limit, this is:

$$1/T_1^{\text{dd}} \propto \gamma_1^2 \gamma_2^2 \frac{\tau_C}{r^6}. \tag{1.34}$$

  Protons in molecules are a strong source of dipolar relaxation of ^{13}C (Moreno *et al.*, 2011), which is often avoided by replacing some (or all) of the ^{1}H by ^{2}H.

- **Chemical shift anisotropy (CSA)** may be an efficient relaxation mechanism where the electronic surroundings of the nucleus, i.e. distribution of the electron density, is highly

anisotropic. The CSA is the traceless component of the chemical shift tensor, being the part that averages to zero under fast molecular tumbling in solution, leaving only the isotropic (rotationally invariant) part visible in the spectrum. In general, the CSA contribution to the spins relaxation increases with the square of the magnetic field strength, therefore, it becomes an important relaxation mechanism at high fields (Jannin *et al.*, 2011):

$$1/T_1^{\mathrm{CSA}} \propto \gamma^2 B_0^2 \frac{\tau_C}{1 + \omega_0^2 \tau_C^2}. \tag{1.35}$$

For instance, T_1 of [1-^{13}C]pyruvate is $\sim 20\%$ larger at 7.0 T than at 9.4 T due to a strong CSA relaxation (Ardenkjaer-Larsen *et al.*, 2011). Although CSA relaxation is proportional to the gyromagnetic ratio, the number of electrons contributing to the anisotropy is a key factor too. For this reason, CSA relaxation is usually stronger for ^{13}C than ^{1}H. The symmetry of the molecule also plays an important role in anisotropy; near spherical, symmetric configurations, such as tetrahedral usually experience minimal CSA relaxation.

- **Scalar or *J*-coupling** is the interaction between nuclear spins and electrons in chemical bonds. It is position and field-independent, but depends on the *J*-coupling constant value, the difference in Larmor frequencies of the two spins and the T_2 relaxation time constant of the coupled spin (Noggle and Schirmer, 1971):

$$1/T_1^{\mathrm{J}(1)} \propto J^2 \frac{\tau_C T_2^{(2)}}{1 + \left[(\omega_{0(1)} - \omega_{0(2)}) T_2^{(2)} \right]^2}. \tag{1.36}$$

Scalar coupling is an important relaxation mechanism for spins with equal gyromagnetic ratios (very small Larmor frequencies difference) and very rapid transverse relaxation.

- **Quadrupolar coupling** is an electric interaction of $I > 1/2$ nuclei with the surrounding electric fields. Since we work mainly with spin-1/2 nuclei, this relaxation mechanism does not affect the nuclear spin systems that we study.

1.4.3   Preserving polarisation

Polarisation preservation strategies may be divided in two subgroups: (i) saving the ^{13}C polarisation until it is required for imaging and (ii) slowing polarisation decay, i.e. slowing relaxation.

Saving polarisation until required

Low flip angle pulses Detection of magnetisation involves application of a radiofrequency pulse. A 90°-flip angle pulse brings all the longitudinal magnetisation into the transverse plane. In this way, the maximum amount of signal is obtained, but since all the magnetisation has been used in a single acquisition, no further sampling can be performed until the polarisation is built up again. In thermally polarised experiments the delay between two acquisitions may be of the order of five times T_1 if fully relaxed spectra are required; for DNP experiments, polarising another sample would take at least 1 hour. Since DNP experiments provide very intense NMR signals, there is no need to apply 90°-radiofrequency pulses. Sampling with low-flip angle pulses of $\sim 5°$ allow detection of the ^{13}C-label without destroying much of the polarisation, and NMR spectra of the same sample can be acquired rapidly to monitor chemical reactions.

Indirect bolus tracking If a water-based solvent is used, polarisation transfer between hyperpolarised ^{13}C nuclei and the protons in the solvent occurs at expense of ^{13}C relaxation. This unavoidable loss of ^{13}C polarisation may be turned in our favour. The enhancement of the solvent proton signals may indicate the spatial location of the ^{13}C-label inside the subject without the need for acquiring ^{13}C-NMR spectra. This would allow saving the remaining ^{13}C-signal until the substrate has reached its target and imaging is required. Chapter 2 develops this idea further and shows an empirical demonstration using hyperpolarised [1,4-^{13}C$_2$]fumarate.

Slowing relaxation

Deuteration Simple ways of extending the relaxation lifetime of the polarisation *in vitro* include perdeuterating the ^{13}C-labelled substrate and using ^{2}H$_2$O solvents. For instance, perdeuterating [1-^{13}C]fumarate (pH = 7) elongates T_1 from 6 s to 27 s, and diluting it in ^{2}H$_2$O instead of H$_2$O raises it to 56 s (Chekmenev *et al.*, 2008). Using deuterated material made it possible to detect hyperpolarised glucose *in vivo* (Rodrigues *et al.*, 2014). Since protonated glucose has a T_1 of less than a second, signal was lost even before injection into the subject. However, perdeuterated fully ^{13}C-labelled glucose decays with $T_1 \sim 10$ s.

Radical and oxygen removal Relaxation rates increase in the presence of dissolved oxygen and free radicals in the sample, such as the ones used in DNP. To obtain a hyperpolarised sample free of paramagnetic species, radical scavengers may be used. For instance, the nitroxide radical TEMPOL may be scavenged with the incorporation of ascorbate in the dissolution buffer (Cheng *et*

al., 2013) or even to the DNP sample in frozen beads that will melt during the dissolution process (Mieville *et al.*, 2010), leaving the sample free of paramagnetic impurities. Degassing the sample removes the dissolved molecular oxygen in the solvent. If gadolinium were used in the sample preparation, addition of EDTA to the dissolution buffer could be used to scavenge it.

Optimal magnetic field strength The magnetic field strength that the sample experiences plays an important role in the spin interactions dominating relaxation. CSA increases as the square of the field, becoming the main relaxation mechanism as B_0 increases. At lower fields (< 1 T), the influence of slowly fluctuating interactions becomes dominant, such as those involving chemical exchange or intermolecular contact. The relaxation of each metabolite has to be studied individually to determine the optimal B_0 at which T_1 relaxation is longer for that particular substrate. For instance, while the ^{13}C T_1 of pyruvate increases at higher fields (Chattergoon *et al.*, 2013), ^{13}C T_1 of fumarate is longer at lower fields (Chapter 4).

Long-lived states For substrates that include two homonuclear spins-1/2, there is the possibility of exploiting an energy quantum state that decays with a relaxation time constant, T_S, much longer than T_1. This potentially longer-lived state is known as the 'singlet state'. An example of $T_S >> T_1$ is the singlet relaxation time for the protons of a partially deuterated saccharide with a similar molecular structure of that of glucose, which is 37 times slower than T_1 (Sarkar *et al.*, 2007). The discussion of this matter is expanded in Section 1.6 and Chapters 3 and 4.

1.5 Boosting sensitivity by improving signal detection

1.5.1 Micro-coil NMR probes

NMR probes are designed to deliver the best sensitivity for specific amounts of sample and nuclei. The most widely used NMR probes require sample volumes of at least 0.6 mL (5-mm inner diameter probe) or 3 mL (10-mm inner diameter probe). *In vitro* experiments may be limited by the amount of sample available for signal sampling, and dilution of the concentration of the nuclei of interest may be necessary to reach the minimum values required for spectral acquisition. When diluting the sample is not an option, or to speed-up experiments by reducing the number of scans, micro-coils may be an alternative. Several types of micro-coils have been reported, including solenoid coils, flat helical coils and striplines (Kentgens *et al.*, 2008).

DNP-*in vitro* experiments could benefit from micro-detection coils by reducing the amount of

dissolution buffer and hyperpolarised sample, reducing the unnecessary waste of labelled material. It would be particularly useful for those volume-limited biological samples, such as biopsy cells or finger-prick blood tests. Micro-coils can also deliver high decoupling power. This use of micro-coils is explored in section 3.6 to access and lock the singlet state of $[1,2\text{-}^{13}C_2]$pyruvate in a strong magnetic field.

1.5.2   SPEN

Pulse sequences for hyperpolarised MRI need to provide as much spectral information as possible in the short amount of time before the polarisation decays. Traditional pulse sequences, such as echo planar imaging (EPI) acquire all the necessary information to reconstruct the image in a single shot, but no spectral information can be obtained. Echo planar spectroscopic imaging (EPSI) allows one to distinguish nuclei precessing at different chemical shifts, but since each shot acquires partial information only, multiple shots are required (Du *et al.*, 2004, Sarkar *et al.*, 1999). Chemical shift imaging (CSI) provides 2D spatial information and a third dimension that is the spectral information for each voxel; multiple shots are needed (Levin *et al.*, 2007, Mayer *et al.*, 2006, Reeder *et al.*, 2007). Recently, single shot NMR and imaging techniques, such as spatiotemporal encoding (SPEN), allow chemical shift discrimination in a single acquisition (Tal and Frydman, 2010). Two versions of this pulse sequences would be useful in hyperpolarised ^{13}C experiments. One option involves performing localised spectroscopy by exciting a region with the shape of interest (Dumez and Frydman, 2013). From this selected area, NMR signal is acquired to get a spectrum that contains all the chemical shifts of the nuclei in the excited region of the sample. Another idea would be to obtain spatial information of a selected chemical shift with a single shot. Following the kinetics of a hyperpolarised substrate and its metabolic conversion into its products *in vivo* in a localised manner with SPEN-based pulse sequences is currently a hot topic in the field. First results showing the robustness and advantages of SPEN over EPI *in vivo* have been presented recently (Schmidt *et al.*, 2013, Schmidt and Frydman, 2013).

1.6   Characteristics of a two spins-1/2 system

Carravetta and Levitt (2005) elegantly demonstrated how the choice of the eigenbasis of a spin operator of the z-component of the angular momentum, I_z, can be important to demonstrate theoretically the long-lived non-equilibrium state of a pair of spins-1/2 that belong to the same molecule. Usually, for magnetically inequivalent spins in high magnetic field, the operator basis is

chosen to show the longitudinal magnetisation of each nucleus. However, for the long-lived state, it is necessary to choose a basis of $|S_0\rangle$ and $|T_i\rangle$ known as singlet and triplet eigenstates. Details on the correlation between the Zeeman and the triplet-singlet states are given in Chapter 3.

1.6.1   Zeeman eigenstates

If there is no external magnetic field, a quantum system has degenerate states. However, if an external magnetic field is applied, this degeneracy is broken and a separation between energy levels is established (Figure 1.6). From this phenomenon, called 'Zeeman splitting', the term Zeeman eigenbasis is derived. Considering a two-spin-1/2 system, the Zeeman energy eigenstates of the system are $|\alpha_1\alpha_2\rangle, |\alpha_1\beta_2\rangle, |\beta_1\alpha_2\rangle$ and $|\beta_1\beta_2\rangle$, which are composed of the product of the eigenstates of each spin-1/2 nucleus of the pair (e.g. $|\alpha_1\alpha_2\rangle = |\alpha_1\rangle \otimes |\alpha_2\rangle$). As previously mentioned, α denotes spin parallel to the magnetic field and β antiparallel, with angular momenta $\mu_\alpha = +\hbar/2$ and $\mu_\beta = -\hbar/2$, respectively.

Figure 1.6 illustrates the energy level diagram and transitions of a pair of spins-1/2. The probability per unit time that a transition will occur is denoted by W. There are four types of transitions: single quantum transitions ($W_1^{(1)}$ or $W_1^{(2)}$) in which only one of the two spins changes its state while the other one remains unchanged, double quantum transitions (W_2) when both spins are in the same state and relax simultaneously (e.g. $|\alpha_1\alpha_2\rangle \rightarrow |\beta_1\beta_2\rangle$) and zero quantum transitions (W_0) when the two spins are in opposite states and relax simultaneously (e.g. $|\alpha_1\beta_2\rangle \rightarrow |\beta_1\alpha_2\rangle$). Although NMR signal arises solely from single quantum transitions, all of them contribute to the spin system relaxation.

The spin-lattice relaxation rates of both spins may be defined in terms of the transition probabilities:

$$1/T_1^{(1)} \quad = \quad 2W_1^{(1)}, \tag{1.37}$$

$$1/T_1^{(2)} \quad = \quad 2W_1^{(2)}. \tag{1.38}$$

If there is dipole-dipole coupling between the two spins, cross-relaxation terms play a role in the relaxation of the spin system. Then, the selective T_1 values, i.e. when only the indicated spin is inverted while the other remains unaffected, are:

$$1/T_1^{(1)} \quad = \quad 2W_1^{(1)} + W_0 + W_2, \tag{1.39}$$

$$1/T_1^{(2)} \quad = \quad 2W_1^{(2)} + W_0 + W_2. \tag{1.40}$$
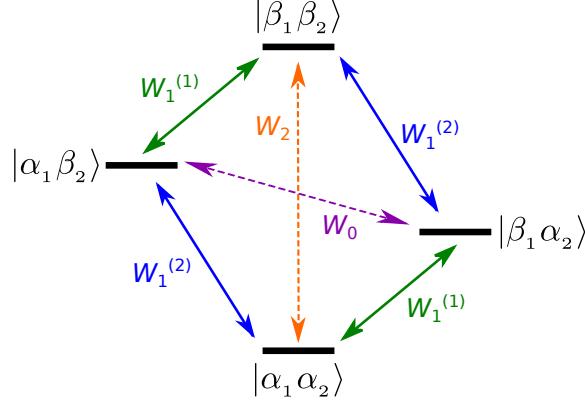
Figure 1.6: Energy level diagram for two spins-1/2, such as an electron spin and a nuclear spin. The transition probabilities are denoted with W. The transitions depicted with a solid line are the single-quantum transitions, in which only one of the two spins is involved.

Similarly, for a non-selective experiment, in which both spins are simultaneously inverted, Eqs (1.37) and (1.38) become:

$$1/T_1^{(1)} = 2W_1^{(1)} + 2W_2, \tag{1.41}$$

$$1/T_1^{(2)} = 2W_1^{(2)} + 2W_2. \tag{1.42}$$

The cross-relaxation rate constant, σ_{12}, is defined as

$$\sigma_{12} = \sigma_{21} = W_2 - W_0. \tag{1.43}$$

1.6.2 Singlet and triplet eigenstates

The singlet and the three triplet states of a pair of spins-1/2 are quantum states constructed from the superposition of the Zeeman eigenstates,

$$
\begin{aligned}
|T_{-1}\rangle &= |\alpha_1\alpha_2\rangle, \\
|T_0\rangle &= (|\alpha_1\beta_2\rangle + |\beta_1\alpha_2\rangle)/\sqrt{2}, \\
|T_{+1}\rangle &= |\beta_1\beta_2\rangle, \\
|S_0\rangle &= (|\alpha_1\beta_2\rangle - |\beta_1\alpha_2\rangle)/\sqrt{2}.
\end{aligned}
\tag{1.44}
$$

The subscripts correspond to the total nuclear spin of the system and the subindexes 1, 2 denote the two different spins. The singlet state $|S_0\rangle$ behaves like a single non-magnetic particle, while the triplet states $|T_m\rangle$ behave as the three states of a spin-1 particle. As mentioned previously, for an isolated pair of spin-1/2 nuclei, intrapair dipole-dipole interactions are the dominant relaxation mechanism. However, these interactions are symmetric and therefore do not affect $|S_0\rangle$, which is anti-symmetric. Hence, the relaxation time for $|S_0\rangle$ is longer than the longitudinal relaxation time. The populations of $|T_{-1}\rangle$, $|T_0\rangle$ and $|T_{+1}\rangle$ equilibrate with each other but are isolated from the singlet population and from singlet-triplet coherences. See Carravetta and Levitt (2005) for a detailed matrix description.

1.6.3 Transformation matrix

The transformation matrix U, which allows the expression of any state $|a\rangle$ or operator A that is initially expressed in the Zeeman basis (superscript *Zeeman*) into the triplet-singlet basis (superscript *S-T*), is constructed with the coefficients of the superposition of the Zeeman states.

$$|\varphi\rangle^{S-T} = U^{-1}|\varphi\rangle^{Zeeman}, \tag{1.45}$$

$$A^{S-T} = U^{-1}A^{Zeeman}U. \tag{1.46}$$

The vectors and the matrix are normalised, i.e. the matrix is unitary $UU^{-1} = U^{-1}U = \mathbb{1}$.

The representation of the Hamiltonian as a matrix in the triplet-singlet basis can be calculated in two different ways that lead to the same result:

$$1)\ H^{S-T} = U^{-1}H^{Zeeman}U, \tag{1.47}$$

$$2)\ H^{S-T} = \begin{pmatrix} \langle\varphi_1^{S-T}|H^{Zeeman}|\varphi_1^{S-T}\rangle & \langle\varphi_1^{S-T}|H^{Zeeman}|\varphi_2^{S-T}\rangle & ... \\ \langle\varphi_2^{S-T}|H^{Zeeman}|\varphi_1^{S-T}\rangle & \langle\varphi_2^{S-T}|H^{Zeeman}|\varphi_2^{S-T}\rangle & ... \\ ... & ... & ... \end{pmatrix}. \tag{1.48}$$

with

$$\langle\varphi_i|H|\varphi_j\rangle = \text{Tr}\left[(|\varphi_i\rangle\langle\varphi_j|)^t H\right] = \text{Tr}\left[(H|\varphi_i\rangle\langle\varphi_j|)\right]. \tag{1.49}$$

1.6.4   Magnetic equivalence

Two spins-1/2

Considering a two-spin system in a fixed magnetic field, each spin of the pair will precess with a Larmor frequency proportional to the local magnetic field it experiences. Depending on the molecular and spin environment, the magnetic field that each spin experiences may be different. This variable magnetic field, i.e. the external magnetic field modified by the molecular environment, is usually called the *local magnetic field*.

If the two spins of a pair experience different local magnetic fields, they have different chemical shifts and they precess at different frequencies. These spins are in ***magnetically inequivalent*** nuclear sites (AX) (Figure 1.7a). In this situation, the spin exchange symmetry of the Hamiltonian is broken, i.e. the permutation operator that swaps labels 1 and 2 does not commute with the Hamiltonian ($P(12)H - P(21)H \neq 0$), and the Zeeman states are the eigenstates of the system. Such systems are also called weakly coupled because their J-coupling constant is much smaller than their chemical shift difference ($|2\pi J| << |\Delta\omega_0|$).

On the other hand, if both spins have the same molecular environment, they experience the same local magnetic field. In this case, the spins are in ***magnetically equivalent*** nuclear sites (A_2) and there is no chemical shift difference between them, giving rise to a single peak in an NMR spectrum (Figure 1.7b). The singlet and the triplet states are eigenstates of A_2 spin systems and do not mix under free evolution.

Strongly coupled spin pairs, also called ***nearly-equivalent*** spins, are the ideal systems to study singlet relaxation. The chemical shift difference of a nearly-equivalent spin pair is much smaller than their J-coupling constant ($|2\pi J| >> |\Delta\omega_0|$). In such systems, the eigenstates of the Hamiltonian are close enough to the singlet-triplet eigenstates to experience longer relaxation times but also to allow for mixing of states. This may allow population migration from the triplet states to the slower relaxing singlet states.

The environment of the nuclear spin pair may be manipulated to obtain magnetically equivalence/inequivalence-behaviour. For instance, by changing the external magnetic field strength. A pair of spins in magnetically inequivalent sites may be weakly coupled at high B_0 and the Zeeman states are its eigenstates. However, at B_0 close to zero, the pair behaves like a strongly coupled system. An example of singlet order observed by bringing a spin pair with chemically inequivalent sites into a low field is detailed in Chapter 3 with [1,2-$^{13}C_2$]pyruvate.
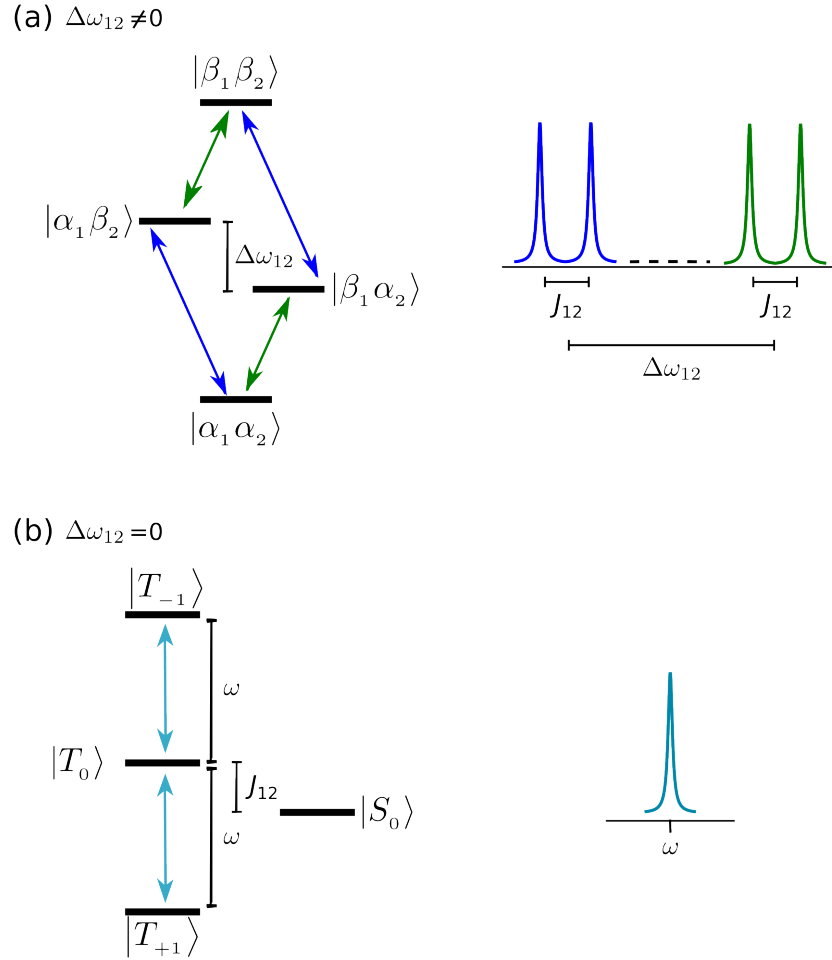
Figure 1.7: Representation of the energy eigenstates of a two-spins-1/2 system. (a) Inequivalent spins experience the Zeeman splitting, whilst (b) equivalent spins show the singlet triplet energy levels. J_{12} is the J-coupling constant and $\Delta\omega$ the chemical shift difference. The NMR observable transitions are displayed on the right of each energy diagram. Adapted from Brindle *et al.* (2011a).
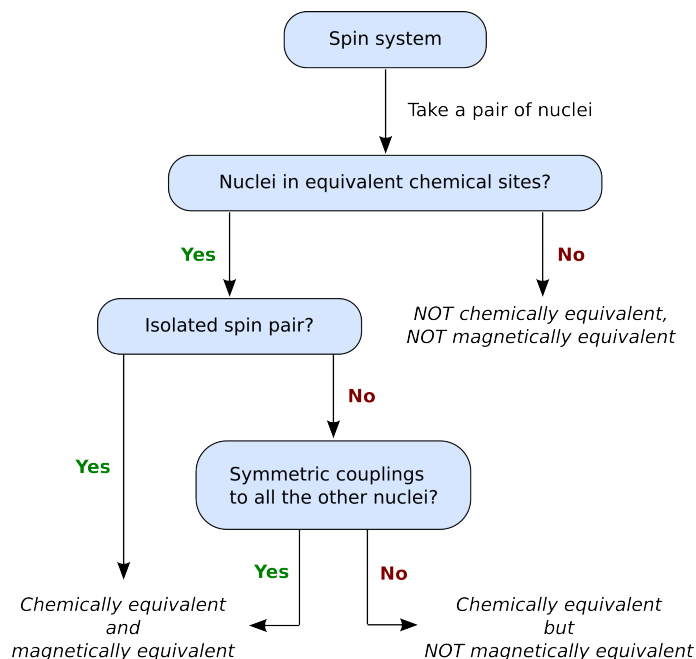
Figure 1.8: Diagram discerning between magnetic equivalence/inequivalence for a pair of nuclear spins.

More than two spins-1/2

For an isolated pair of spins-1/2, chemical equivalence implies magnetic equivalence. However, spin systems composed of three or more spins-1/2 may be magnetically inequivalent despite being chemically equivalent. Here, the equivalence of two nuclear sites may be broken by the out-of-pair J-couplings. The nuclear sites of a spin pair will only be both chemically and magnetically equivalent if the couplings to all the other nuclei are symmetric. Figure 1.8 illustrates the conditions for which chemical and/or magnetic equivalence are established.

For instance, the three nuclear sites of a spin system with three spins-1/2 will only be magnetically equivalent if the three spins are chemically equivalent and all the J-couplings are equal:

$$|J_{12}| = |J_{13}| = |J_{23}|. \tag{1.50}$$

Otherwise, the spin-exchange symmetry is broken.

An example of singlet order accessed through a slight inequivalence produced by asymmetric J-couplings is shown in Chapter 4 with $[1,4\text{-}^{13}C_2]$fumarate.

1.6.5 Singlet relaxation

T_S is the singlet-triplet relaxation time, that is the decay time of the population imbalance between the singlet state and the triplet states. Singlet order is immune to intra-pair dipole-dipole relaxation, which is the main relaxation mechanism for T_1, and is two to three times less sensitive than T_1 to paramagnetic relaxation agents (Tayler and Levitt, 2011a). The main sources of singlet relaxation include:

- coherent leakage, such as chemical shift difference and intramolecular couplings,
- chemical shift anisotropy (CSA),
- spin rotation and
- intermolecular couplings (such as couplings between the nuclei and the solvent, or the nuclei and the electrons in the dissolved oxygen, radicals or metals).

1.6.6 Requirements for the singlet state

The ideal candidate for a long-lived singlet state would be a molecule with two isolated spins with $I = 1/2$, low gyromagnetic ratio, rigid and rapidly tumbling. To access the singlet state in order to preserve and retrieve the signal, the spin pair should be nearly-magnetically equivalent, with a small isotropic chemical shift difference or inequivalent J-couplings. The singlet relaxation time constant will be longer lived for spin-pairs with small, or well-correlated, CSA tensors and spin rotation tensors (Levitt, 2012).

Furthermore, to exploit the long-lived singlet states for metabolically relevant experiments the molecule with the above characteristics should also be soluble in water, biocompatible, easily polarised with dissolution DNP and involved in metabolism.

1.6.7 Experimental demonstrations of the singlet state

Longer relaxation times can be achieved by manipulating the magnetic equivalence of a spin system during the course of an experiment: the signal can be trapped in the singlet state of the magnetically equivalent system and then returned to the corresponding Zeeman eigenstate of the magnetically inequivalent system, where the signal can be measured (Levitt, 2010). Several methods have been presented in the literature:

1. Field cycling By moving the sample from one magnetic field to another, chemical equivalence/inequivalence is obtained. Carravetta and Levitt demonstrated T_S experimentally for the

first time using a field cycling method (Carravetta *et al.*, 2004, Carravetta and Levitt, 2004). Using ^{1}H-NMR of the two protons in 2,3-dibromothiophene, they pre-polarised the sample in the high field of the spectrometer, moved it outside the spectrometer to trap the signal in the singlet state at low magnetic field (where $|S_0\rangle$ is an eigenstate of the system) and then acquired the remaining signal upon insertion of the sample back into the high field of the spectrometer (where the Zeeman states are the natural energy levels of the spin system). They measured relaxation times T_S up to 10 times longer than T_1. Nuclei other than protons, such as the coupled nitrogen spins in ^{15}N$_2$ nitrous oxide, have also been used recently to prove the long-lived singlet state (Pileio *et al.*, 2008).

2.   Radiofrequency spin-locking   Given two spins with very similar chemical shifts, a radiofrequency field may be used to temporarily suppress the chemical inequivalence (Pileio and Levitt, 2009). This requires the radiofrequency field to be applied very close to the Larmor resonance frequency of the spins.

3.   Heteronuclear symmetry-switching   Manipulating spin-spin couplings to nuclei of different isotopic species changes the symmetry of the spin Hamiltonian. This makes it feasible to study long-lived states in symmetric molecules (Feng *et al.*, 2012, Tayler, 2012).

4. Chemical reactions   By using chemical reactions, the symmetry of a molecule can be made or broken, establishing or destroying magnetic equivalence. Warren *et al.* exemplified this situation by changing the magnetic equivalence of hyperpolarised [2,3-^{13}C$_2$]diacetyl upon an hydration reaction (Warren *et al.*, 2009).

5.   Magnetisation-To-Singlet pulse sequence for nearly-equivalent spins   The pulse sequence known as M2S (Magnetisation-To-Singlet) allows transfer of the population from the zero-quantum triplet state to the singlet state. Since the spins involved are nearly-equivalent, long relaxation times may be measured without the need for additional symmetry-making methods. This has been proved for nearly magnetically equivalent spins, in which the spin symmetry is broken either by the difference in the chemical shifts (Tayler and Levitt, 2011b) or the heteronuclear couplings (Feng *et al.*, 2012). The M2S pulse sequence is discussed in more detail in Chapters 3 and 4.

6.   Level anti-crossing   In some cases, there are magnetic field strengths where the energy levels of a spin system with two or more spins cross. However, if the spin-exchange symmetry of

the molecule is broken, for example with long-range out-of-pair J-couplings, the energy states do not cross but mix (Buljubasich *et al.*, 2012, Franzoni *et al.*, 2012). Keeping the sample at the magnetic field strength where the level anti-crossing occurs allows population migration from the triplet states to the singlet state, and *vice versa*.

1.7   About this thesis

Dissolution-DNP has revolutionised metabolic MRI by allowing real-time monitoring of hyperpolarised ^{13}C-labelled substrates and their metabolic reactions *in vivo*. However, the fast decay of the high levels of polarisation that allow this ^{13}C detection limits the observation window of the reaction.

This work explores strategies to preserve ^{13}C polarisation in dissolution DNP experiments beyond solvent and substrate deuteration or radical scavenging. Trapping the polarisation in the slow-relaxing singlet state is a promising technique that would provide longer imaging times. The possibility of increasing the lifetime of a spin-system has been discussed extensively, both theoretically and has been demonstrated experimentally *in vitro* (Carravetta *et al.*, 2004, Carravetta and Levitt, 2004, Pileio *et al.*, 2010, Tayler and Levitt, 2011a, Bornet *et al.*, 2011, Feng *et al.*, 2012, Franzoni *et al.*, 2012, Laustsen *et al.*, 2012, Warren *et al.*, 2009). Taking this idea further, the aim was to combine the power of the enhanced NMR signal and longer relaxation times, namely DNP and the singlet state, to pursue *in vivo* MRI of tumour metabolic changes. A complementary option involves following the injected hyperpolarised ^{13}C bolus by sampling the protons in the solvent, whose signal is enhanced due to polarisation transfer via cross relaxation. This would allow tracking the bolus without any additional ^{13}C polarisation loss and performing ^{13}C-NMR only once the substrate has reached the site of interest.

This thesis is structured as follows.

Chapter 2 discusses intermolecular polarisation transfer between hyperpolarised ^{13}C and ^{1}H in the solvent water via cross-relaxation. The term used to refer to such phenomenon is spin polarisation induced nuclear Overhauser effect (SPINOE). Theory and experiments are shown using a typical *in vitro* dissolution-DNP experiment with [1,4-^{13}C$_2$]fumarate.

Chapters 3 and 4 explore singlet order relaxation in endogenous metabolites. Chapter 3 deals with the chemically inequivalent ^{13}C spin-pair of [1,2-^{13}C$_2$]pyruvate. The theory of adiabatic conversion between Zeeman states and triplet-singlet eigenstates is presented. Longer-lived singlet

order is demonstrated at the millitesla field of the laboratory in several solvents *in vitro* (^{2}H$_2$O, aqueous solutions with bovine serum albumin and whole human blood) and in mice *in vivo*.

Chapter 4 exemplifies accessing the singlet state of the chemically equivalent ^{1}H-pairs and ^{13}C-pairs in [1,4-^{13}C$_2$]fumarate, where magnetic equivalence is broken by the hetereonuclear *J*-couplings between ^{13}C and the intramolecular ^{1}H. This is studied as a four-spin-1/2 system and the singlet state is accessed using a pulse sequence. Longitudinal and transverse relaxation time constants of [1,4-^{13}C$_2$]fumarate are presented and compared with the singlet relaxation time constant.

Each chapter concludes with a summary of the topics discussed and the main outcomes. A general discussion is also presented in Chapter 5 with future prospectives of the work.

SPINOE between cell metabolites and solvent

<div style="text-align: right">2</div>

2.1 Introduction

The sensitivity of NMR of low gyromagnetic ratio nuclei, such as ^{13}C, has been improved by hyperpolarisation techniques. However, regardless of the technique employed to boost the initial polarisation from thermal equilibrium to a hyperpolarised state, once the hyperpolarised nucleus is in the liquid state and the source perturbing the equilibrium is off, the polarisation decays according to the longitudinal spin-lattice relaxation time, T_1. One of the pathways that contributes to the loss of polarisation is cross-relaxation between two spins, e.g. hyperpolarised ^{13}C dissolved in water relaxes due to dipole-dipole interactions with ^{1}H in the solvent. The Nuclear Overhauser Effect (NOE) describes polarisation transfer by cross-relaxation from one nuclear spin population to another following perturbation of one of the spins (for example by application of radiofrequency pulses). An extension of this idea is the so-called 'Spin Polarisation-Induced NOE' or 'SPINOE', which describes the enhancement of spin polarisation of solvent nuclei by the hyperpolarised spins of a solute.

Although the loss of polarisation due to cross-relaxation is unavoidable, SPINOE may be used to obtain indirect information about the hyperpolarised nucleus without the further destruction of the polarisation that direct sampling would cause. For instance, tracking the passage of a bolus of a hyperpolarised ^{13}C-fumarate in the body by detecting the SPINOE enhancement of the protons of the solvent water would prevent the loss of polarisation that would result from ^{13}C signal acqui-

sition, saving the hyperpolarisation until it reached the tissue of interest. The focus of this chapter is the change in the solvent proton NMR signal after the addition of ^{13}C-labeled cell metabolites that have been hyperpolarised using the dissolution DNP technique. A theoretical expression for the expected ^{1}H signal enhancement is derived and an experimental demonstration is given using hyperpolarised [1,4-^{13}C$_2$]fumarate.

The chapter is organised as follows.

First, a brief introduction to the concept and equations that describe NOE is given to link it with the theoretical derivation of the specific expressions for SPINOE. Then, intermolecular SPINOE is introduced and a method to calculate the intermolecular contribution of the spin-lattice relaxation rate constant from T_1 measurements is given. The theory is matched with the experiments performed on hyperpolarised [1,4-^{13}C$_2$]fumarate dissolved in an aqueous buffer. Finally, ideas on how to increase the change in signal that arises from the SPINOE are suggested.

2.2   Nuclear Overhauser Effect

The Nuclear Overhauser Effect (NOE) is the change of population for spins of one signal caused by cross-relaxation with those of another. The cross-relaxation may have a number of sources, the major ones being dipole-dipole coupling or a time-fluctuating J-coupling. J-modulation usually only takes place under chemical exchange, intramolecular motion (e.g. internal rotation) or rapid relaxation of one of the spins (Noggle and Schirmer, 1971). In the following sections I will focus on NOE produced by dipole-dipole relaxation. The NOE may involve heteronuclear or chemically inequivalent homonuclear spins, and can only take place when at least one of the nuclear spins is in a perturbed state, i.e. has a polarisation level that departs from the thermal equilibrium polarisation.

The NOE is widely used by chemists as a tool to study chemical kinetics and nuclear relaxation, assign complex NMR spectra, increase signal-to-noise in NMR experiments and obtain detailed qualitative and quantitative information on molecular configuration and conformation (Neuhaus and Williamson, 2000). To name one, the two-dimensional NMR pulse sequence known as Nuclear Overhauser Effect Spectroscopy (NOESY) is an example of an experimental technique that exploits NOE to obtain information on proximity between homonuclear spins.

Moreover, since NOE is a through space phenomenon and not only through chemical bonds, both intra- and intermolecular NOEs may occur.

2.2.1 Solomon equations

Following perturbation of one of the spins, the time dependence of the longitudinal spin angular momentum of two spins I and S that are weakly coupled (i.e. $2\pi J << \Delta\omega_0$, which is always the case for heteronuclear spins with $\gamma_I \neq \gamma_S$) or belong to different molecules (such as a ^{13}C-labeled molecule in water) is given by Solomon's equations (Solomon, 1955):

$$\frac{dI_z(t)}{dt} = -\rho_I(I_z(t) - I_0) - \sigma_{IS}(S_z(t) - S_0), \tag{2.1}$$

$$\frac{dS_z(t)}{dt} = -\rho_S(S_z(t) - S_0) - \sigma_{SI}(I_z(t) - I_0), \tag{2.2}$$

where I_z and S_z are the ensemble averages of the longitudinal spin angular momenta, I_0 and S_0 are the thermal equilibrium longitudinal spin angular momenta values, ρ_I and ρ_S are their spin-lattice relaxation rate constants and σ_{IS} and σ_{SI} are the cross-relaxation rate constants, which differ provided that the concentrations of spins I and S are not the same.

Relaxation rate constants

Since small molecules in non-viscous liquids, such as water at room temperature or hyperpolarised metabolites in solution, satisfy the condition $\omega_{I(S)}\tau << 1$, the relaxation rate constants presented here assume extreme narrowing limit conditions (Kowalewski and Maler, 2006). τ is the characteristic correlation time of the motion causing relaxation.

Cross-relaxation due to intermolecular dipole-dipole interactions is caused by the translational diffusion, D, of water and solute molecules as observed in $\tau^{\mathrm{xd}} = d^2(2D_{I(S)})^{-1}$. In the absence of molecular binding, the intermolecular cross-relaxation rate constant for spins-1/2 is (Song, 2000):

$$\sigma_{IS}^{\mathrm{xd}} = \hbar^2\gamma_I^2\gamma_S^2 \frac{\pi N_S}{15dD_{IS}}. \tag{2.3}$$

Here $\hbar$ is the reduced Planck's constant, γ_I and γ_S the gyromagnetic ratios, N_S is the concentration of nuclear spins in the sample, D_{IS} the mean translational diffusion coefficient of the two species $[(D_I + D_S)/2]$, and d is the minimum distance between the two spins.

$\sigma_{SI}^{\mathrm{xd}}$ is obtained similarly by exchanging N_S with N_I in Eq. (2.3). Therefore, the detailed balance condition is satisfied, ensuring that the matrix given by Eqs (2.1) and (2.2) is self consistent. The intermolecular contribution to the spin-lattice relaxation rate constant $\rho_{I,S}^{\mathrm{xd}}$ is twice the intermolecular cross-relaxation rate constant, i.e. $\rho_{I,S}^{\mathrm{xd}} = 2\sigma_{IS}^{\mathrm{xd}}$ (Noggle and Schirmer, 1971). Then, the

relationship between $\sigma_{IS}^{\mathrm{xd}}$ and $\rho_{S,I}^{\mathrm{xd}}$ is given by:

$$\sigma_{IS}^{\mathrm{xd}} = \frac{1}{2}\frac{N_S}{N_I}\rho_{S,I}^{\mathrm{xd}}. \tag{2.4}$$

Similarly, the intramolecular contribution to the spin-lattice relaxation rate constant is twice the intramolecular cross-relaxation rate constant: $\rho_{I,S}^{\mathrm{dd}} = 2\sigma_{IS}^{\mathrm{dd}}$. The cross-relaxation rate constant due to intramolecular dipole-dipole interactions is given by (Noggle and Schirmer, 1971):

$$\sigma_{IS}^{\mathrm{dd}} = \hbar^2\gamma_I^2\gamma_S^2\frac{\tau}{2d^6}, \tag{2.5}$$

which depends on the rotation correlation time constant of the spins in the molecule.

Note that the contribution of the proximity between the spins plays a more important role in the intramolecular relaxation ($\sigma_{IS}^{\mathrm{dd}} \sim d^{-6}$) than in the intermolecular one ($\sigma_{IS}^{\mathrm{xd}} \propto d^{-1}$) .

2.2.2 NOE enhancement factor

The NOE enhancement factor, η, is defined as the fractional change in the ensemble average longitudinal spin angular momentum of spin I from thermal equilibrium (MacNamara *et al.*, 2000):

$$\eta(t) \equiv \frac{I_z(t) - I_0}{I_0}. \tag{2.6}$$

Since signal intensity is proportional to I_z, η can also be calculated from the measured spectral signal. The profiles of $I_z(t)$ and $S_z(t)$, and here $\eta(t)$, depend on the NMR experiment and the values of $I_z(0)$ and $S_z(0)$, and on the spin system for the showing cross-relaxation behaviour. Traditionally, NOE has been used in two different types of experiments:

1. In the case shown in Figure 2.1a, the initial conditions are $I_z(0) = I_0$ and $S_z(0) = S(t) = 0$, which correspond to NOE obtained by saturating one of the nuclear spins to create a non-equilibrium system, i.e. applying a radiofrequency field to one of the nuclear spins throughout the duration of the experiment. This is known as a ***steady-state NOE***. One example is Overhauser DNP (Section 1.3.3).

2. In Figure 2.1b, the initial conditions are $I_z(0) = I_0$ and $S_z(0) = -S_0$, representing inversion of one of the nuclear spins with a selective 180°-pulse to perturb the system at the beginning of the experiment and letting it recover back to the equilibrium. This is known as a ***transient NOE***.
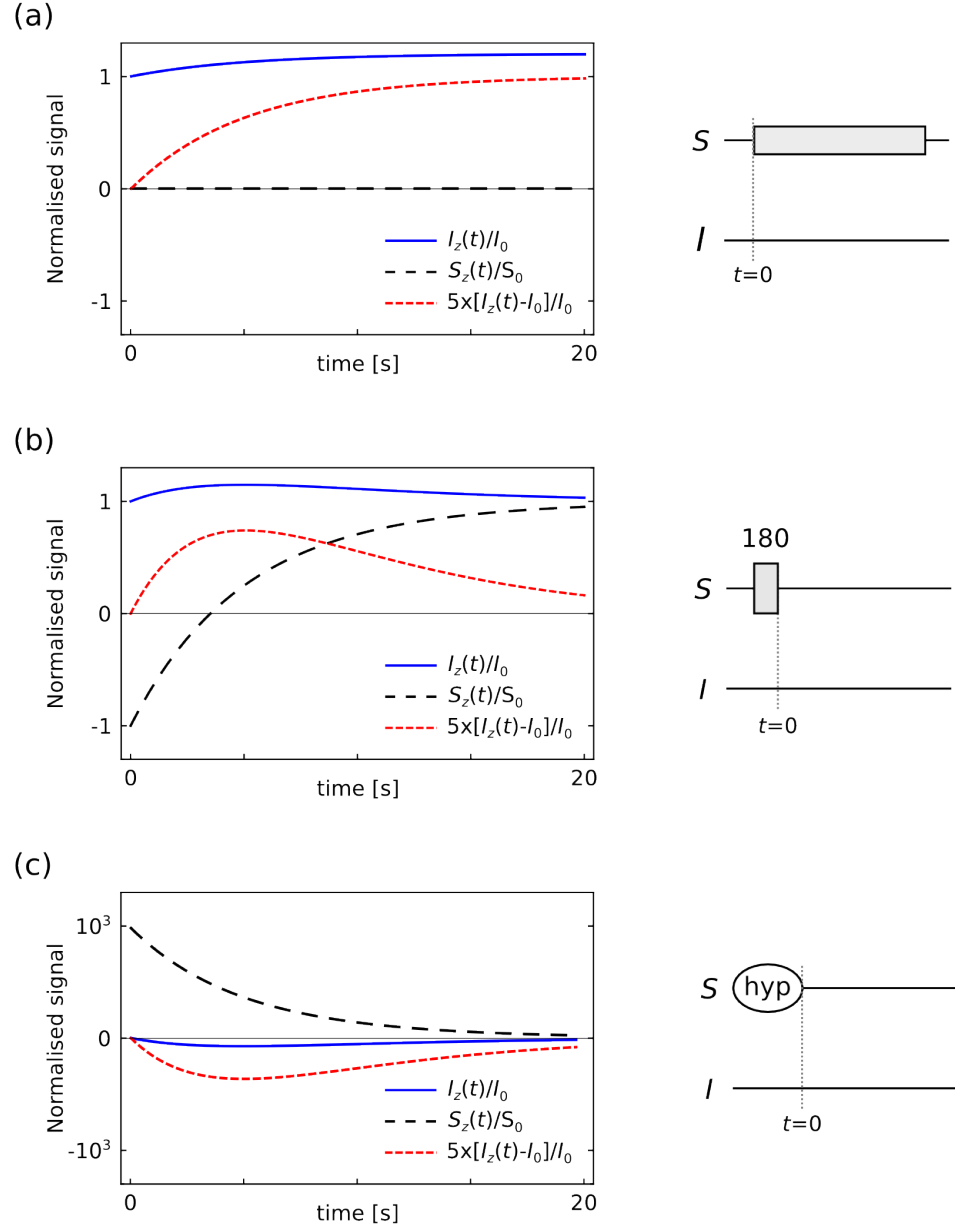
Figure 2.1: Demonstration of (a) steady-state NOE, (b) transient NOE with selective inversion of spin S, and (c) spin-polarisation induced NOE with hyperpolarisation of spin S. Simulation parameters used for the visualisation of the NOEs in Eqs (2.1), (2.2) and (2.6) were $N_S = N_I$, $\rho_I = \rho_S = 0.2$ s^{-1} and $\sigma_{IS} = \rho_I/5$.

2.2.3   Maximum NOE enhancement

From Eqs (2.1) and (2.6), the maximum enhancement is found when the time derivative of the spin I signal is zero, at $t = t_{\max}$:

$$\frac{dI_z(t)}{dt} = 0 \Leftrightarrow I_z(t_{\max}) - I_0 = -\frac{\sigma_{IS}}{\rho_I}(S_z(t_{\max}) - S_0). \tag{2.7}$$

The ratio of thermal equilibrium spin angular momenta of two spins I and S with the same spin quantum number, defined under the high temperature approximation, is related to the ratio of their gyromagnetic ratios, i.e. $S_0/I_0 = \gamma_S/\gamma_I$ (Navon *et al.*, 1996). It follows, therefore, that

$$\eta_{\max} = \eta(t_{\max}) = -\frac{\sigma_{IS}}{\rho_I}\frac{\gamma_S}{\gamma_I}\frac{(S_z(t_{\max}) - S_0)}{S_0}. \tag{2.8}$$

Since $\eta_{\max} \propto \sigma_{IS}/\rho_I$, the highest enhancement occurs when a fast cross-relaxation rate constant is combined with a slow spin lattice relaxation rate constant of spin I.

Upper limit of the NOE enhancement

Let us assume that spin I relaxes solely due to dipole-dipole coupling with spin S, such that $\rho_{I,S}^{\mathrm{xd(dd)}} = \rho_I$. The maximum NOE enhancement observable in any case using a steady-state NOE experiment, in which the S-spin is saturated by application of a radiofrequency pulse [$S_z(t_{\max}) = 0$], is given by the ratio of gyromagnetic ratios of the two spins:

$$\eta_{\max}^{\mathrm{SS-NOE}} \leq \frac{\gamma_S}{2\gamma_I}. \tag{2.9}$$

The enhancement is most favourable when saturating the spin with the largest gyromagnetic ratio. For the case of ^{1}H-^{13}C, proton saturation may double ^{13}C polarisation ($\eta_{\max}^{\mathrm{SS-NOE}} \approx 2$), whereas ^{13}C saturation only enhances the proton polarisation by a factor of 12.5% ($\eta_{\max}^{\mathrm{SS-NOE}} \approx 0.125$). Another example is the case of Overhauser DNP, i.e. electron-^{1}H cross-relaxation, which reaches a theoretical enhancement of

$$\eta_{\max}^{\mathrm{O-NOE}} \leq \frac{\gamma_e}{2\gamma_H} \approx 300. \tag{2.10}$$

Likewise, assuming that $-S_0 \leq S_z(t_{\max}) \leq S_0$, the upper limit for the enhancement produced

by an experiment using a transient NOE would be:

$$\eta_{\max}^{\text{t-NOE}} \leq \frac{\gamma_S}{\gamma_I} \tag{2.11}$$

This shows again the dependence of the enhancement factor on the ratio of the gyromagnetic ratios.

2.2.4 NOE vs SPINOE

The **SPINOE** is a transient NOE phenomenon that follows perturbation of the equilibrium by hyperpolarisation of one of the spins. The SPINOE is characterised by the initial conditions $I_z(0) = I_0$ and $S_z(0) >> S_0$, and in this case it can be assumed that $S_z(t)$ decays only due to ρ_S. The Solomon equations presented in Eqs (2.1) and (2.2) can then be solved, yielding

$$\begin{aligned} I_z(t) &= I_0 - \frac{\sigma_{IS}}{\rho_I - \rho_S}(\mathrm{e}^{-t\rho_S} - \mathrm{e}^{-t\rho_I})(S_z(0) - S_0), & (2.12) \\ S_z(t) &= S_0 + \mathrm{e}^{-t\rho_S}(S_z(0) - S_0). & (2.13) \end{aligned}$$

Figure 2.1c displays the time evolution of the magnetisation of spins I and S, as well as the SPINOE enhancement for $S_z(0)$ being 10^3 times larger than S_0. As in a transient NOE experiment, I_z departs from its equilibrium value to relax back to it while S_z decays exponentially.

2.3 Theoretical SPINOE enhancement

This chapter is concerned with the polarisation transferred from hyperpolarised ^{13}C nuclei to ^{1}H (both with spin quantum number 1/2). The term SPINOE will be used from this point on and expressions that apply to spin quantum number 1/2 will be given. The notation $I \equiv {}^1$H and $S \equiv {}^{13}$C will be used.

2.3.1 Maximum SPINOE enhancement

Determination of $\eta_{\max}$ for spin I using Eq. (2.8) requires knowledge of $S_z(t_{\max})$. One can express this in terms of the measurable polarisation as follows:

$$\eta_{\max} = -\frac{\sigma_{IS}}{\rho_I}\frac{\gamma_S}{\gamma_I}(\mathrm{e}^{(t_{\mathrm{pol}} - t_{\max})\rho_S}\frac{P(t_{\mathrm{pol}})}{P_0}. \tag{2.14}$$

The time t_{max} is the time-point at which the absolute value of the enhancement is at a maximum. Its value depends on the relaxation rate constants of the two species I and S, as the stationary state of the Solomon equations predicts:

$$t_{max} = \frac{\ln(\rho_I/\rho_S)}{\rho_I - \rho_S}. \tag{2.15}$$

The time $(t_{pol} - t_{max})$ is the delay between the time when the polarisation P is measured and when the maximum enhancement is reached. The polarisation at thermal equilibrium, P_0, is calculated from the Boltzmann approximation [Eq. (1.17)]. One should recognise that $\rho = T_1^{-1}$ for each nucleus, and therefore the spin-lattice relaxation rate constants can be determined by measuring T_1 of spins I and S (e.g. with an inversion recovery experiment), and the cross-relaxation rate constant can also be expressed in terms of measurable parameters (an expression for intermolecular cross-relaxation is given in Eq. (2.18)). Eq. (2.14) was obtained by modifying Eq. (2.8) under the following assumptions:

- $S_z(t)/S_0 = P(t)/P_0$: Taking into account that the longitudinal spin angular momentum is proportional to polarisation, i.e. $S_z(t) = P(t)\hbar/2$, the ratio between the longitudinal spin magnetisation in the sample at any time and its thermal equilibrium value is the same as the ratio between the polarisation at the same time and the thermal equilibrium polarisation.

- $S_z(t_{max}) >> S_0$: Hyperpolarisation of the spin S. This means that its spin angular momentum decays mono-exponentially from the moment it is measured to the time of maximum enhancement and that $(S_z(t_{max}) - S_0) \approx S_z(t_{max})$.

Upper limit of the SPINOE enhancement

The upper limit of the SPINOE enhancement factor is given under the assumption that the relaxation of spin I is only due to dipole-dipole coupling, $\rho_{I,S}^{dd(xd)} = \rho_I$:

$$\eta_{max}^{SPINOE} \leq -\frac{\gamma_S}{2\gamma_I}\left(e^{(t_{pol}-t_{max})\rho_S}\frac{P(t_{pol})}{P_0}\right). \tag{2.16}$$

This expression differs from the ones presented for the steady-state NOE and the traditional transient NOE in that the maximum enhancement observable depends on the initial polarisation level and its sign. As an example, for $P(t_{pol}) = 0.36$ at 9.4 T and 293 K, $\eta_{max}^{SPINOE} \approx -4230$. As shown in the following sections, the intermolecular dipole-dipole coupling is usually not the sole

relaxation mechanism of the system. The SPINOE enhancement predicted from experimental relaxation time constants of [1,4-^{13}C]fumarate polarised to $P(t_{\text{pol}}) = 0.36$ is on the order of $\eta_{\max}^{\text{SPINOE}} \approx -0.02$.

2.3.2 Intermolecular SPINOE enhancement

Dissolution DNP should be a classic example of an intermolecular SPINOE between hyperpolarised solute spins (^{13}C) and spins in the solvent (^{1}H). The cross-relaxation between solute and solvent spins is inefficient due to the relatively low concentration of the solute spins and the unfavourable ratio γ_C/γ_H; however, this is counterbalanced by the high levels of polarisation of the solute spins. In addition, since the polarisation of the solute spins is already perturbed from thermal equilibrium it does not require the application of radiofrequency pulses. Navon *et al.* (1996) were the first to demonstrate transfer of hyperpolarisation from optically pumped ^{129}Xe gas to solution phase proton spins in benzene without the need for radiofrequency irradiation, observing an enhancement factor of about 50% for $P/P_0 \sim 6000$. They found that the magnitude of the SPINOE enhancement was dependent on the magnitude of the initial polarisation and the proximity and relative motion of the molecules, and therefore was concentration, diffusion and field dependent.

The equations presented so far do not assume any mechanism for cross-relaxation. For polarisation transferred between hyperpolarised ^{13}C nuclei and ^{1}H nuclei in the solvent, cross-relaxation may be assumed predominantly to be due to intermolecular dipole-dipole interactions. By inserting Eq. (2.4) into (2.14), the SPINOE enhancement of the solvent proton spins due to hyperpolarised solute ^{13}C spins is given by:

$$\eta_{\max} = -\frac{\rho_{S,I}^{\text{xd}}}{\rho_I} \frac{N_S}{2N_I} \frac{\gamma_S}{\gamma_I} \left(e^{(t_{\text{pol}}-t_{\max})\rho_S} \frac{P(t_{\text{pol}})}{P_0} \right). \tag{2.17}$$

The intermolecular contribution of the longitudinal relaxation time constant of the hyperpolarised spin S, $\rho_{S,I}^{\text{xd}}$, is in this case expressed in terms of its total spin-lattice relaxation time constant in water with 10% ^{2}H$_2$O for the lock (90% H$_2$O, 10% ^{2}H$_2$O), and in heavy water (100% ^{2}H$_2$O), with D_I and D_S being the translational diffusion coefficient of the two species:

$$\rho_{S,I}^{\text{xd}} = \frac{\rho_S(90\%\text{H}_2\text{O}, 10\%^{2}\text{H}_2\text{O}) - \rho_S(100\%^{2}\text{H}_2\text{O})}{0.9 \left(1 - \frac{D_S+D_I}{D_S+D_K} \frac{8\gamma_K^2}{3\gamma_I^2} \right)}. \tag{2.18}$$

Given that spin S is dissolved in 90% H$_2$O and 10% ^{2}H$_2$O, the relaxation rate constant of S is influenced by intermolecular dipole-dipole interactions with solvent protons ($\rho_{S,I}^{\text{xd}}$) and deuterons

($\rho_{S,K}^{\text{xd}}$), but also by other relaxation mechanisms that contribute to ρ_S (ρ_S^0), such as intramolecular interactions with other spins-1/2 in the molecule [Eq. (2.19)] (Fitzgerald *et al.*, 1998). If spin S is dissolved in 100% ^{2}H$_2$O, the relaxation of the S spins is dependent only on intermolecular relaxation with solvent deuterons ($\rho_{S,K}^{\text{xd}}$) and on ρ_S^0 [Eq. (2.20)].

The relaxation rate constants due to the different mechanisms add linearly, resulting in relaxation rate constants that one can measure:

$$\rho_S(90\%\text{H}_2\text{O}, 10\%{}^2\text{H}_2\text{O}) = \rho_S^0 + 0.9\rho_{S,I}^{\text{xd}} + 0.1\rho_{S,K}^{\text{xd}}, \qquad (2.19)$$

$$\rho_S(100\%{}^2\text{H}_2\text{O}) = \rho_S^0 + \rho_{S,K}^{\text{xd}}. \qquad (2.20)$$

Then, Eq. (2.18) is obtained by subtracting the two relaxation rate constants in Eqs (2.19) and (2.20), and using Eqs (2.3) and (2.4). The assumptions made are that in the same volume of solution there are the same number of protons plus deuterons in a 90%/10% ^{1}H$_2$O/^{2}H$_2$O solution as deuterons in a 100% ^{2}H$_2$O solution, $N_I = N_K$, and that the minimum approach distance between these nuclei and the ^{13}C spins is the same, $d_I = d_K$. For this calculation the ratio $\frac{D_S + D_I}{D_S + D_K} = 1.125$ was used, which was obtained by using the known values of the diffusion coefficients of H$_2$O and ^{2}H$_2$O at 30°C (2.6 10^{-9} m^2/s and 2.1 10^{-9} m^2/s, respectively) (Yoshida *et al.*, 2005) and, as D_S is unknown, the average value of the ratio in the limit when $D_S << D_{I(K)}$ and the limit when $D_S >> D_{I(K)}$ was taken. The degree of enhancement was shown to be relatively insensitive to the value used for D_S, with a maximum difference of 2% in the results obtained between these two extreme cases.

2.3.3   Time dependence of the enhancement

Eq. (2.6) together with Eq. (2.13) predicts that η evolves with time as a bi-exponential function. Following the same reasoning as presented above, a time-dependent expression for η is expressed in terms of η_{max} as defined in Eq. (2.17). Here the assumptions that $S_z(0) >> S_0$ and $S_z(t_{\text{max}}) >> S_0$ are used:

$$\eta(t) = \eta_{\text{max}}\frac{\rho_I}{\rho_I - \rho_S}\frac{S_z(0)}{S_z(t_{\text{max}})}(\text{e}^{-t\rho_S} - \text{e}^{-t\rho_I}). \qquad (2.21)$$

An exact result without taking into account any approximations is shown by Song (2000).

Replacing $S_z(0)/S_z(t_{\text{max}})$ with $P(0)/P(t_{\text{max}}) = \text{e}^{t_{\text{max}}\rho_S}$ as shown in Eq. (2.14), an alternative equation for the SPINOE enhancement is obtained:

$$\eta(t) = \eta_{\text{max}}\frac{\rho_I}{\rho_I - \rho_S}(\text{e}^{-t\rho_S} - \text{e}^{-t\rho_I})\text{e}^{t_{\text{max}}\rho_S}. \qquad (2.22)$$

This is a bi-exponential function of the type

$$\eta(t) = A(\mathrm{e}^{-Bt} - \mathrm{e}^{-Ct}), \tag{2.23}$$

where $A = \eta_{\max}\frac{\rho_I}{\rho_I - \rho_S}\mathrm{e}^{t_{\max}\rho_S}$, $B = \rho_S$ and $C = \rho_I$.

Eqs (2.17) and (2.22) show that when intermolecular relaxation does not dominate the relaxation of the spin S, a lower enhancement will be observed (Figure 2.2a). This occurs when the difference $|\rho_S(\mathrm{H_2O}) - \rho_S(^2\mathrm{H_2O})|$ in the $^{13}\mathrm{C}$ relaxation rate constants in $\mathrm{H_2O}$ and $^2\mathrm{H_2O}$ is small. Moreover, the sign of the enhancement depends on the sign of γ_I and γ_S; if they are both positive (as for $^{13}\mathrm{C}$ and $^1\mathrm{H}$), then the sign of $\eta(t)$ is opposite to that of the polarisation of S (Figure 2.2a). The magnitude of η will have the largest values in molecules in which the spin S has a very long T_1 (small ρ_S) compared to the T_1 of spin I. Conversely, η will be small for molecules with fast relaxing S-spins. As an example of this, Figure 2.2b displays the enhancement curves in the cases in which the relaxation time constant of the spins S is twice, five times and ten times larger than $T_{1,I}$. The time to reach maximum enhancement $\eta(t_{\max})$ also depends on $T_{1,S}$. The faster the S-spins relax, the earlier the maximum enhancement will be reached.

Two-field effect on SPINOE

The above models predict the SPINOE enhancement within a constant external magnetic field. In the dissolution DNP context, this is perhaps an oversimplification, as the real experiment involves transport of the sample through regions of vastly different magnetic fields (Figure 2.3):

1. The hyperpolarised nuclei S are in contact with the solvent nuclei I as soon as the dissolution takes place (low field).

2. During the transport of the sample into the high-field spectrometer magnet, the nuclei will experience a field that changes with time.

3. Finally, once in the spectrometer, the sample remains at a stable field in which the signal acquisition takes place.

Accurate information about the magnetic field that the sample experiences at each time point is difficult to obtain, however it is worthwhile: the evolution of the measured SPINOE with time can give information on whether the polarisation transfer by SPINOE started during transport to the high-field magnet.
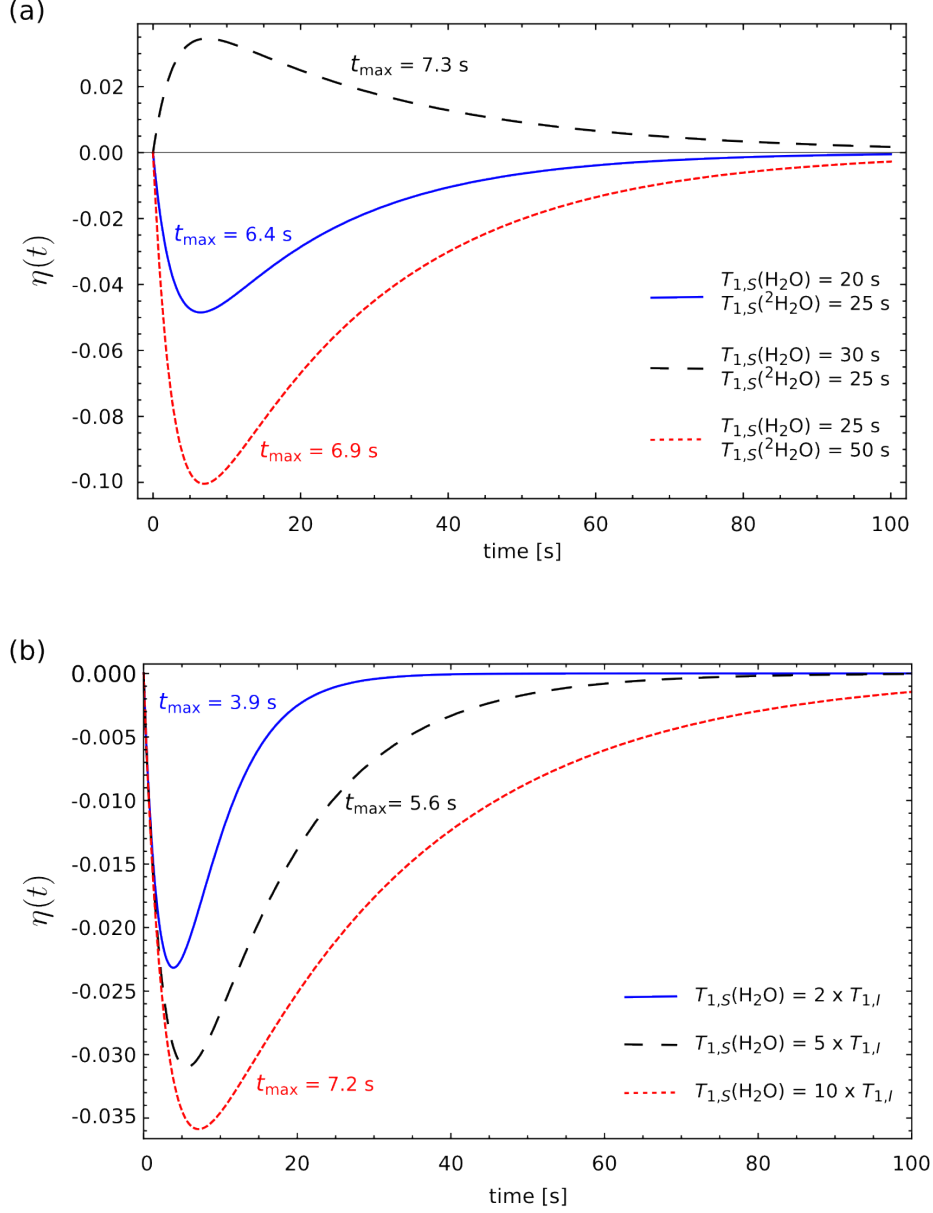
Figure 2.2: Calculated SPINOE enhancement profiles $\eta(t)$ of the ^{1}H signal with ^{13}C polarised to 36%, based on the model of Eq. 2.22. The parameters used in the simulation were $P(t_{\text{pol}}) = 0.36$, $T_{1,I} = \rho_I^{-1} = 2.8$ s, $N_S/N_I = 3.6 \times 10^4$, $B_0 = 9.4$ T, $T = 293$ K, and different $T_{1,S} = \rho_S^{-1}$ as shown. (a) Variation of $\eta(t)$ against $|\rho_S(\text{H}_2\text{O}) - \rho_S(^2\text{H}_2\text{O})|$. $T_{1,S}(\text{H}_2\text{O}) > T_{1,S}(^2\text{H}_2\text{O})$ is shown here for illustration purposes, although it does not happen in practice. (b) Variation of $\eta(t)$ against $T_{1,S}$ keeping the intermolecular relaxation constant fixed at $|\rho_S(\text{H}_2\text{O}) - \rho_S(^2\text{H}_2\text{O})| = 0.007$ s^{-1} for the calculation of the three curves.

The longitudinal relaxation time constants play a role on the SPINOE enhancement, and those of different molecules behave differently depending on the magnetic field strength. While some molecules relax faster at lower fields (e.g. ^{13}C pyruvate), others may relax more slowly (e.g. ^{13}C-fumarate). The fact that the thermal equilibrium signal increases with the magnetic field strength has also has an effect on the predicted enhancement: since the ratio P/P_0 becomes larger as the magnetic field gets weaker, i.e. the background signal gets weaker while the high pre-polarisation level remains unchanged, larger enhancements are expected at lower magnetic fields.

In the first field, when the contact between S and I-nuclei takes place for the first time, the evolution of the longitudinal angular momentum with time follows Eqs (2.12) and (2.13). After a time τ_1 in which the sample has been at the first magnetic field, if it then experiences a second field, the longitudinal angular momentum will be affected by the spin angular momentum present at the moment of exiting 'field 1'. The following stepwise functions represent the two-field transition described above, with the superscripts 'field 1' and 'field 2' indicating the first and the second magnetic field that the sample experiences, respectively (Figure 2.3).

$$I_z(t) \quad = \quad \begin{cases} I_z^{\text{field1}}(t), & \text{if } t \leq \tau_1 \\ I_z^{\text{field2}}(t), & \text{if } t > \tau_1 \end{cases} \tag{2.24}$$

$$S_z(t) \quad = \quad \begin{cases} S_z^{\text{field1}}(t), & \text{if } t \leq \tau_1 \\ S_z^{\text{field2}}(t), & \text{if } t > \tau_1 \end{cases} \tag{2.25}$$
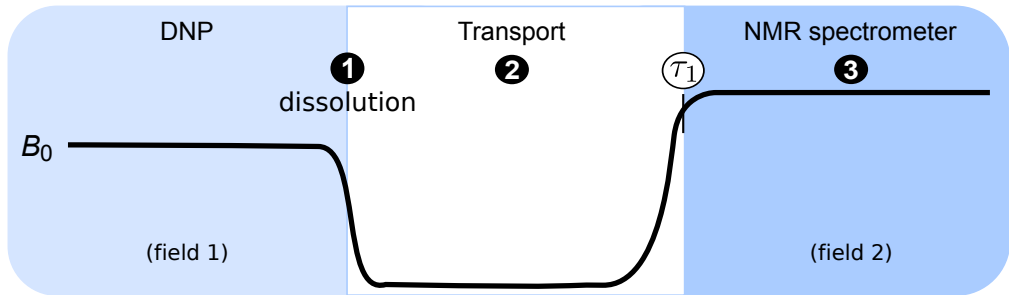
Figure 2.3: Scheme of the magnetic field strengths experienced by a sample during transfer from the polariser to the NMR spectrometer magnet. τ_1 is the time that the sample has remained at the first magnetic field.

where for the I spins,

$$I_z^{\text{field1}}(t) = I_0^{\text{field1}} - \frac{\sigma_{IS}^{\text{field1}}}{\rho_I^{\text{field1}} - \rho_S^{\text{field1}}} \left(e^{-t\rho_S^{\text{field1}}} - e^{-t\rho_I^{\text{field1}}} \right) \left(S_z(0) - S_0^{\text{field1}} \right), \quad (2.26)$$

$$I_z^{\text{field2}}(t) = I_0^{\text{field2}} + e^{(\tau_1-t)\rho_I^{\text{field2}}}(I_z^{\text{field1}}(\tau_1) - I_0^{\text{field2}}) -$$
$$\frac{\sigma_{IS}^{\text{field2}}}{\rho_I^{\text{field2}} - \rho_S^{\text{field2}}} \left(e^{(\tau_1-t)\rho_S^{\text{field2}}} - e^{(\tau_1-t)\rho_I^{\text{field2}}} \right) \left(S_z^{\text{field1}}(\tau_1) - S_0^{\text{field2}} \right), \quad (2.27)$$

and for the S spins

$$S_z^{\text{field1}}(t) = S_0^{\text{field1}} + e^{-t\rho_S^{\text{field1}}} \left(S_z(0) - S_0^{\text{field1}} \right), \quad (2.28)$$

$$S_z^{\text{field2}}(t) = S_0^{\text{field2}} +$$
$$e^{(\tau_1-t)\rho_S^{\text{field2}}} \left(S_0^{\text{field1}} - S_0^{\text{field2}} + e^{-\tau_1\rho_S^{\text{field1}}} (S_z(0) - S_0^{\text{field1}}) \right). \quad (2.29)$$

Since the thermal equilibrium spin angular momentum is field dependent, when the sample experiences a sudden change of magnetic field strength, there is evolution of the S- and I-spins angular momenta due to this field jump, which is independent of the cross-relaxation between spins, and that would take place even in the case of non-hyperpolarised samples (Figure 2.4 and Figure 2.5, black dashed line). I label this change of spin angular momentum attributed to the field jump with the subscript 'MWoff', as it is the background change in polarisation that one would detect for experiments in which the sample sits in the DNP magnet ('field 1') but the MW source is not switched on, i.e. no polarisation other than thermal occurs, before being dissolved and transferred to the acquisition magnet ('field 2').

$$I_{z,\text{MWoff}}(t) = \begin{cases} I_{z,\text{MWoff}}^{\text{field1}}(t), & \text{if } t \leq \tau_1 \\ I_{z,\text{MWoff}}^{\text{field2}}(t), & \text{if } t > \tau_1 \end{cases} \quad (2.30)$$

$$S_{z,\text{MWoff}}(t) = \begin{cases} S_{z,\text{MWoff}}^{\text{field1}}(t), & \text{if } t \leq \tau_1 \\ S_{z,\text{MWoff}}^{\text{field2}}(t), & \text{if } t > \tau_1 \end{cases} \quad (2.31)$$

where for the I spins,

$$I_{z,\text{MWoff}}^{\text{field1}}(t) = I_0^{\text{field1}}, \quad (2.32)$$

$$I_{z,\text{MWoff}}^{\text{field2}}(t) = I_0^{\text{field2}} + e^{(\tau_1-t)\rho_I^{\text{field2}}} \left(I_0^{\text{field1}} - I_0^{\text{field2}} \right), \quad (2.33)$$

and for the S spins

$$S_{z,\mathrm{MWoff}}^{\mathrm{field1}}(t) \quad = \quad S_0^{\mathrm{field1}}, \tag{2.34}$$

$$S_{z,\mathrm{MWoff}}^{\mathrm{field2}}(t) \quad = \quad S_0^{\mathrm{field2}} + \mathrm{e}^{(\tau_1 - t)\rho_S^{\mathrm{field2}}} \left(S_0^{\mathrm{field1}} - S_0^{\mathrm{field2}} \right). \tag{2.35}$$

Obviously, this is a simplistic representation in which the change in magnetic field is adiabatic but sudden. However, during the dissolution and transfer to the spectrometer the sample experiences a constant adiabatic change of the magnetic field.

Figure 2.4 and Figure 2.5 display the time evolution of the angular momenta considering hyperpolarisation of the spin S as shown in Eqs (2.24) - (2.29); the background change of polarisation due to the field jump, $S_{z,\mathrm{MWoff}}(t)$ and $I_{z,\mathrm{MWoff}}(t)$ as in Eqs (2.30) - (2.35); and the curves $[S_z(t) - S_{z,\mathrm{MWoff}}(t)]$ and $[I_z(t) - I_{z,\mathrm{MWoff}}(t)]$. If the intermolecular relaxation rate constant is the same in both fields and the relaxation time constants are also the same, the curve $[I_z(t) - I_{z,\mathrm{MWoff}}(t)]$ is the same if the sample moves from the low magnetic field strength to the high one (Figure 1.4a, left), or *vice versa* (Figure 2.4b, left). It can also be noted that due to the high initial polarisation, $S_z(t)$ remains effectively unaffected by the background signal change due to the field jump (Figure 2.4, right).

Similar to the case of the sample resting in one field during the whole experiment (Figure 2.2), the intermolecular relaxation rate constant $\rho_{S,I}^{\mathrm{xd}}$ at each magnetic field strength has an important effect on the curve $[I_z(t) - I_{z,\mathrm{MWoff}}(t)]$ (Figure 2.5), and therefore on $\eta(t)$. If $\rho_{S,I}^{\mathrm{xd}}$ in the first field is larger than $\rho_{S,I}^{\mathrm{xd}}$ of the second field, i.e. $\rho_{S,I}^{\mathrm{xd,field1}} > \rho_{S,I}^{\mathrm{xd,field2}}$, the curve reaches the maximum while the sample is at 'field 1' (Figure 2.5a). Conversely, if $\rho_{S,I}^{\mathrm{xd,field1}} < \rho_{S,I}^{\mathrm{xd,field2}}$, upon insertion of the sample into the second field, the curve reaches another maximum (Figure 2.5b). Figure 2.5c shows the curve when $\rho_{S,I}^{\mathrm{xd,field1}} = 0$, which means that the intermolecular component of the spin-lattice relaxation in the first magnetic field is zero. It is as if there had been no contact between S-spins and I-spins until they reach the second field. However, the maximum enhancement in the second field will be smaller for longer delays in the first field because of polarisation decay during τ_1 (compare maximum enhancement in Figure 2.5a and Figure 2.5c). Furthermore, the shape of the curve depends not only on $\rho_{S,I}^{\mathrm{xd}}$ but also on $\rho_S(\mathrm{H_2O})$ at each field and how much time the sample spends experiencing each magnetic field.

(a)

(b)
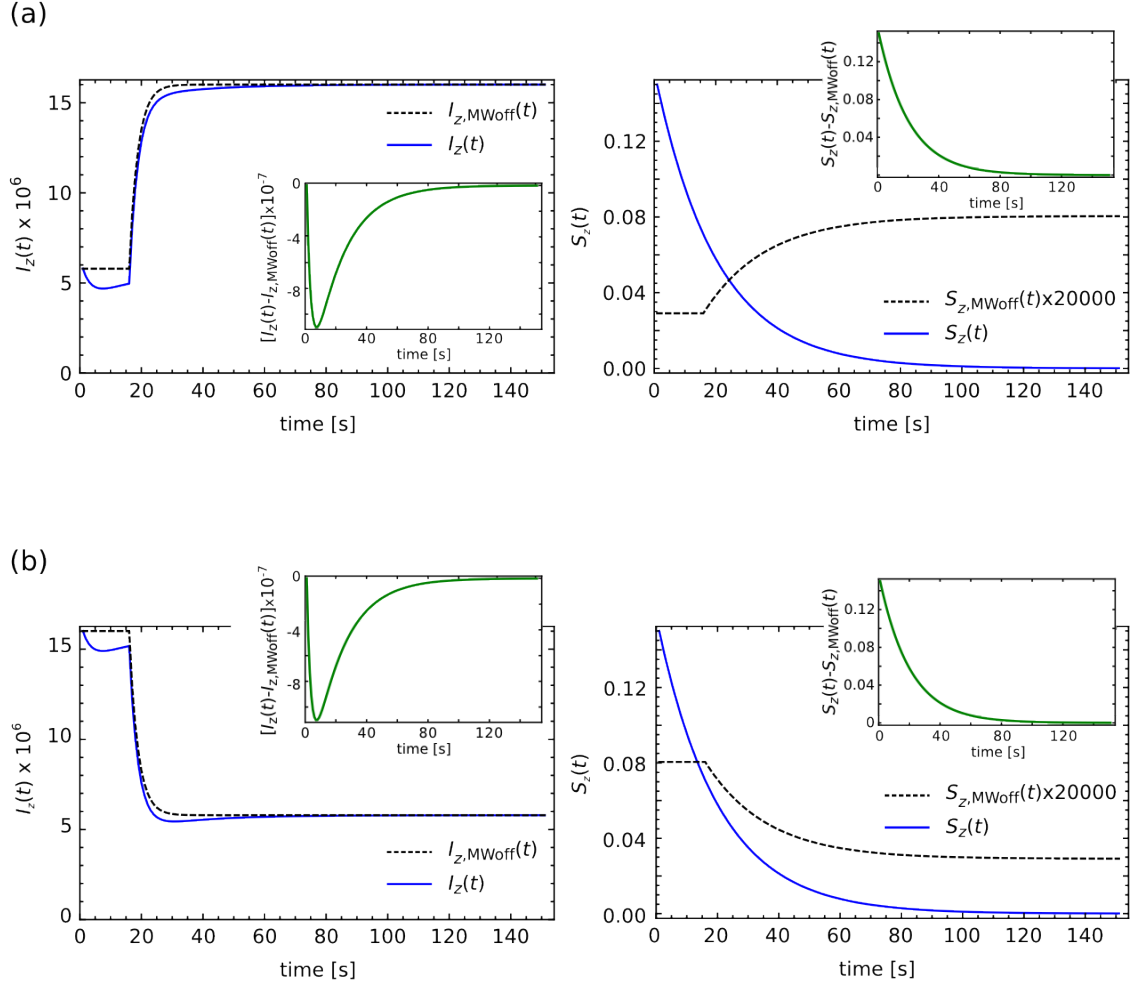
Figure 2.4: Simulation of longitudinal magnetisation of spins I and S of a sample experiencing two different magnetic field strengths with time. $P(0) = 0.3$ and the relaxation time constants used for the plots were $T_{1,I}^{\text{field1}} = T_{1,I}^{\text{field2}} = 2.83$ s, $T_{1,S}^{\text{field1}}(\text{H}_2\text{O}) = T_{1,S}^{\text{field2}}(\text{H}_2\text{O}) = 20$ s, $T_{1,S}^{\text{field1}}(^2\text{H}_2\text{O}) = T_{1,S}^{\text{field2}}(^2\text{H}_2\text{O}) = 30$ s. τ_1 is the time the sample experienced the magnetic field '1' before being moved to a magnetic field '2', and it was set to 15 s here. The magnetic field strengths experienced in each case were (a) $B_0^{\text{field1}} = 3.4$ T, $B_0^{\text{field2}} = 9.4$ T; and (b) $B_0^{\text{field1}} = 9.4$ T, $B_0^{\text{field2}} = 3.4$ T. The magnitude of $S_{z,\text{MWoff}}(t)$ has been plotted multiplied by a factor of 2×10^4.
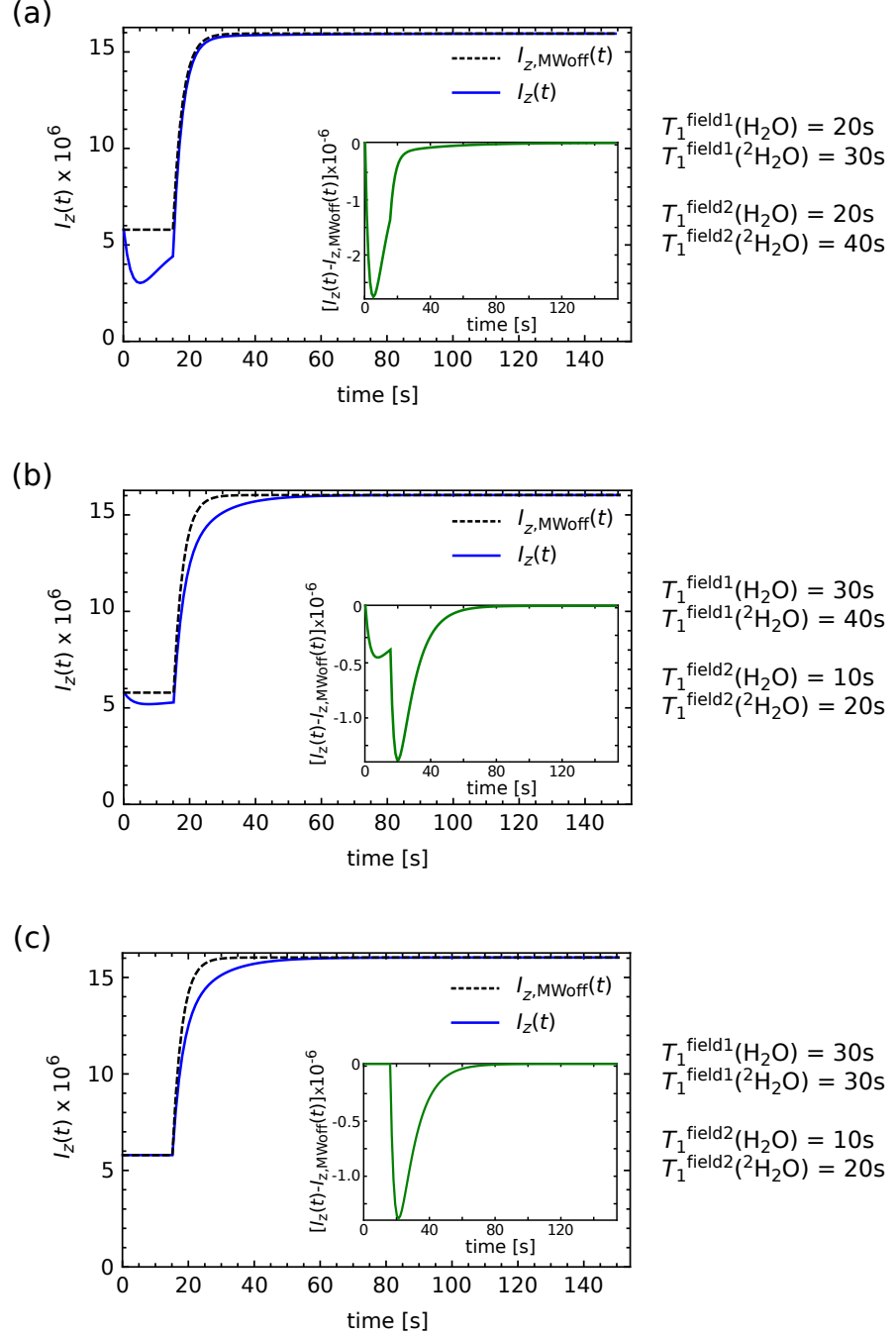
Figure 2.5: Simulated longitudinal magnetisation of spin I of a sample experiencing two different magnetic field strengths with time under different relaxation time constants of spin S. The relaxation time constants of the spin S used in each case are detailed on the plot. The constants used for the three plots were $P(0) = 0.3$, $T_{1,I}^{\text{field1}} = T_{1,I}^{\text{field2}} = 2.83$ s, $\tau_1 = 15$ s, $B_0^{\text{field1}} = 3.4$ T and $B_0^{\text{field2}} = 9.4$ T.

The SPINOE enhancement should then be calculated accounting for the field jump effect as:

$$\eta(t) = \begin{cases} \frac{I_z(t) - I_{z,\text{MWoff}}(t)}{I_0^{\text{field1}}}, & \text{if } t \leq \tau_1 \\ \frac{I_z(t) - I_{z,\text{MWoff}}(t)}{I_0^{\text{field2}}}, & \text{if } t > \tau_1 \end{cases} \qquad (2.36)$$

Since the fractional enhancement is calculated dividing $[I_z(t) - I_{z,\text{MWoff}}(t)]$ by the thermal angular momentum at the magnetic field strength at each time point t, on top of the effects shown in Figure 2.5, $\eta(t)$ will experience a sudden decrease when moving the sample from a low field to a high field. If the sample is moved from high to low field, $\eta(t)$ will increase suddenly.

2.4   Experimental SPINOE enhancement using $^{13}\text{C}_2$-fumarate

2.4.1   Choice of the metabolite

Using Eqs (2.17) and (2.18), the maximum SPINOE enhancement can be estimated. When selecting the metabolite that is the source of spins S, the parameters to take into account are: the concentration of hyperpolarised ^{13}C in the sample after dissolution, the spin-lattice relaxation time constants and the level of polarisation that can be achieved.

The accuracy of the prediction is influenced by the standard deviation of measurements of the longitudinal relaxation time constants; the better T_1s can be determined, the better the prediction will be. Moreover, it is important to keep in mind that each DNP protocol results in different metabolite concentrations after dissolution and also achieves different levels of polarisation, which would have a direct effect on the calculated value of η_{max}. For instance, [1-^{13}C]pyruvate polarises to $P \approx 30\%$ and the dissolved sample has 82 mM ^{13}C-pyruvate (Witney *et al.*, 2011) whilst [1-^{13}C]ascorbate reaches $\sim 5\%$ polarisation at neutral pH and contains 40 mM ^{13}C-ascorbate (Bohndiek *et al.*, 2011). With these polarisation and concentration values, and the relaxation time constants shown in Table 2.1, at 7.0 T and 37°C, η_{max} is predicted to be around 7% for [1-^{13}C]pyruvate; and around -4% for [1-^{13}C]ascorbate. At a low field of 4 mT, the value of η_{max} is calculated to be around -120% for [1-^{13}C]pyruvate; and -50% for [1-^{13}C]ascorbate. These results show that although the maximum polarisation achievable with DNP is important, so it is the cross-relaxation time constant. [1-^{13}C]pyruvate polarises six times more than [1-^{13}C]ascorbate, but its $\rho_{S,I}^{\text{xd}}$ is between five and six times smaller. Consequently, accounting for the fact that a solution of [1-^{13}C]pyruvate has twice the concentration of ^{13}C after DNP, η_{max} of pyruvate and ascorbate are on the same order of magnitude.

	$T_{1,S}$ (in H_2O) [s]	$T_{1,S}$ (in ^2H_2O) [s]	B_0 [T]
[1-^{13}C]pyruvate	54.3 ± 3	79.4 ± 4	7.0
	50 ± 4	64 ± 7	0.004
[1-^{13}C]ascorbate	12 ± 1	22 ± 2	7.0
	17 ± 3	28 ± 4	0.004

Table 2.1: Measured spin-lattice relaxation times for ^{13}C in solutions of 82 mM [1-^{13}C]pyruvate and 40 mM [1-^{13}C]ascorbate dissolved in 90%/10% H_2O/^2H_2O or 100% ^2H_2O at a magnetic field strength of 7.0 T and 4 mT. The measurement of the relaxation time constants was done at the University of Southampton using a home-built field cycling setup (average of n=2 experiments).

The magnets used currently in the clinic are mainly 1.5 T or 3 T (although higher fields up to 7 T are recently available), therefore, a substrate that has a strong cross-relaxation at those field strengths would be preferred as it would give rise to a higher SPINOE enhancement.

To test the theory presented in the previous sections, the SPINOE of water protons in contact with hyperpolarised [1,4-^{13}C$_2$]fumaric acid was measured. Fumarate appeared to be the best candidate to test the SPINOE enhancement of solvent protons from hyperpolarised ^{13}C, not only because the cross-relaxation term of the spin-lattice relaxation is higher at 3.4 T than at 9.4 T (Table 2.2), but also because of the information that it provides about cell death. In studies performed using hyperpolarised ^{13}C fumarate, the ratio of malate produced to fumarate injected is indicative of the level of cell necrosis (Bohndiek *et al.*, 2010, Gallagher *et al.*, 2009, Gallagher *et al.*, 2011).

2.4.2 Materials and methods

T_1 measurements

To determine $\rho_{S,I}^{xd}$, the longitudinal relaxation time constant of [1,4-^{13}C$_2$]fumarate in water and heavy water was measured. For this purpose, samples of 20 mM [1,4-^{13}C$_2$]fumaric acid (99% ^{13}C, Cambridge Isotope Laboratories Inc, Ibstock, UK) were prepared in 40 mM phosphate buffer (pH 7.4) containing 50 mM NaCl, 40 mM NaOH, 100 mg/L EDTA and 4 mM sodium 3-trimethyl- silylpropionate-d4 (TSP), as a chemical shift and intensity standard. The buffer solution was made with both 90%/10% H_2O/^2H_2O and 100% ^2H_2O.

The spin-lattice relaxation time constants of ^{13}C and ^{1}H were measured at room tempera-

ture using an inversion-recovery pulse sequence in a 9.4 T vertical wide-bore magnet (100 MHz
^{13}C, Oxford Instruments, Oxford, UK) interfaced with a Varian UnityInova spectrometer console
(Varian Inc., Palo Alto, CA). Additional ^{13}C T_1 measurements were carried out (i) in a 3.4 T
vertical wide-bore magnet (36 MHz ^{13}C, Oxford Instruments, Oxford, UK) interfaced with a Varian
Chemagnetics SpinSight spectrometer console (Varian Inc., Palo Alto, CA) using an inversion-
recovery pulse sequence, and (ii) in the stray field of the magnet room (1 mT). For the latter
measurement, 0.5 mL of hyperpolarised sample dissolved in buffer made with either 90% H$_2$O/10%
^{2}H$_2$O or 100% ^{2}H$_2$O, were injected into eight 10-mm NMR tubes containing 2 mL of buffer made
with either 90%/10% H$_2$O/^{2}H$_2$O or 100% ^{2}H$_2$O respectively, that were maintained in the NMR
laboratory background field of $\sim$ 1 mT at room temperature and then inserted sequentially into
the 9.4 T spectrometer magnet at intervals of $\sim$ 30 s. The first spectrum of each tube was
acquired using a flip angle of 6°. The area under the fumarate peak (from both the ^{13}C1 and ^{13}C4
resonances) was integrated and fitted to a mono-exponential decay function to determine T_1. The
stray field of the magnet room was measured with a transverse Hall probe attached to a hand-held
gaussmeter (HIRST GM04, Magnetic Instruments Ltd).

The T_1 values were then substituted into Eq. (2.18) to calculate $\rho_{S,I}^{\mathrm{xd}}$, and were subsequently
substituted in Eq. (2.17) for prediction of enhancement values in solvent water protons. The error
in the prediction was determined using propagation of errors,

$$u^2 = \sum_i \left(\frac{\partial \eta}{\partial x_i} \right)^2 u_{x_i}^2, \tag{2.37}$$

taking into account the error, u_{x_i}, on each of the parameters employed in Eq. (2.17).

Hyperpolarisation of [1,4-^{13}C$_2$]fumaric acid

^{13}C-labeled fumaric acid was hyperpolarised using the DNP technique (Section 1.3.3). A sample
consisting of 3.23 mmol of [1,4-^{13}C$_2$]fumaric acid was dissolved in 8.74 mmol dimethyl sulfoxide
(DMSO) containing 11.48 μmol of a trityl radical ($\sim$ 18.5 mM; AH111501; GE Healthcare, Amer-
sham, UK) and 0.48 μmol of a gadolinium chelate ($\sim$ 0.8 mM; Gd-3; GE Healthcare, Amersham,
UK). The solution was sonicated and centrifuged, and a 40 mg aliquot was hyperpolarised at 3.35 T
and $\sim$ 1.2 K, with sample irradiation with a 94 GHz microwave source operating at 100 mW. For
some samples no microwave irradiation was used as a control.

SPINOE enhancement detection

The solid sample was then rapidly dissolved in 6 mL of the phosphate buffer described above, which had been pressurized to 10 bar at 180°C. Half of the sample was injected into a 10 mm o.d. NMR tube inside the magnet via a transfer line. The other half was used to determine the level of the polarisation with a polarimeter at the time of injection. Proton signal was acquired with 6°-flip-angle pulses every second. The zero time point was taken to be the moment of injection of the material into the NMR tube.

The enhancement $\eta(t)$ was determined by measuring changes in the proton signal integral following injection of a hyperpolarised sample of [1,4-^{13}C$_2$]fumarate into H$_2$O and was plotted, with correction for the background change of the signal due to the field jump as:

$$\eta(t) = \frac{I_z(t) - I_{z,\text{MWoff}}(t)}{I_{z,\text{MWoff}}(t \to \infty)}, \tag{2.38}$$

where $I_{z,\text{MWoff}}(t)$ was measured in an experiment using a non-hyperpolarised solution of fumarate. Experimental data on the SPINOE enhancement detection was kindly made available to me by Dr. Sarah E. Bohndiek.

2.4.3 Results and discussion

Measurements of ^{13}C spin lattice relaxation time constant, $T_{1,S}$, for [1,4-^{13}C$_2$]fumarate showed that the ^{13}C nuclei relaxed faster in 90%/10% H$_2$O/^{2}H$_2$O than in 100% ^{2}H$_2$O, i.e. the intermolecular dipole-dipole interaction is a strong relaxation mechanism for this molecule (Table 2.2).

With these T_1s the maximum enhancement of the water proton signal with 20 mM [1,4-^{13}C$_2$]fumarate hyperpolarised to 36% and dissolved in H$_2$O, was calculated to be $\sim 2\%$ at 9.4 T and greater than 14% at lower fields (calculated using Eqs (2.17) and (2.18)) (Figure 2.6). The water proton, $T_{1,I}$, used for the predicted enhancement was ~ 2.8 s, which was measured at 9.4 T. Since water protons have a very short correlation time constant ($\sim 10^{-11}$ s) their spin-lattice relaxation time is independent of the magnetic field strength (Gore and Kennan, 1999). In tissue, the T_1 of water protons decreases with increasing magnetic field strength (de Graaf *et al.*, 2006) and would need to be accounted for in calculation of the SPINOE in tissue. However, in an injected bolus, the T_1 is expected to be approximately the same as that in pure water. Although a gadolinium chelate was used in the DNP process, the concentration of this paramagnetic ion after dissolution was too small (~ 8 μM) to have an effect on the water proton T_1 (Tayler and Levitt, 2011, Waldner *et al.*, 2010).

$T_{1,S}$ (in H_2O) [s]	$T_{1,S}$ (in ^2H_2O) [s]	$\eta_{\max}$	$t_{\max}$ [s]	B_0 [T]
27.6 ± 0.3	30.8 ± 0.8	-0.020 ± 0.005	7.2	9.4
41.0 ± 1.3	66.6 ± 7.5	-0.14 ± 0.03	8.1	3.4
34.3 ± 5.5	49.5 ± 1.2	-450 ± 238	7.7	0.001

Table 2.2: Measured ^{13}C spin-lattice relaxation times (S spins) in solutions of 20 mM [1,4-$^{13}C_2$]fumarate dissolved in 90%/10% H_2O/^2H_2O or 100% ^2H_2O at a magnetic field strength of 9.4 T (average of n=6 experiments), 3.4 T (n=3) and 1 mT (n=3), the predicted enhancement in the water signal with fumarate polarised to (0.36 ± 0.02) s at t_{pol}=0, and the calculated time point when the maximum enhancement takes place, $t_{\max}$. The spin-lattice relaxation time of the water protons ($T_{1,I}$) used for calculation of the predicted enhancement was (2.83 ± 0.02) s, which was measured at 9.4 T (n=6). Quoted errors are the standard deviation of the mean for T_1s and the propagated errors for $\eta_{\max}$.
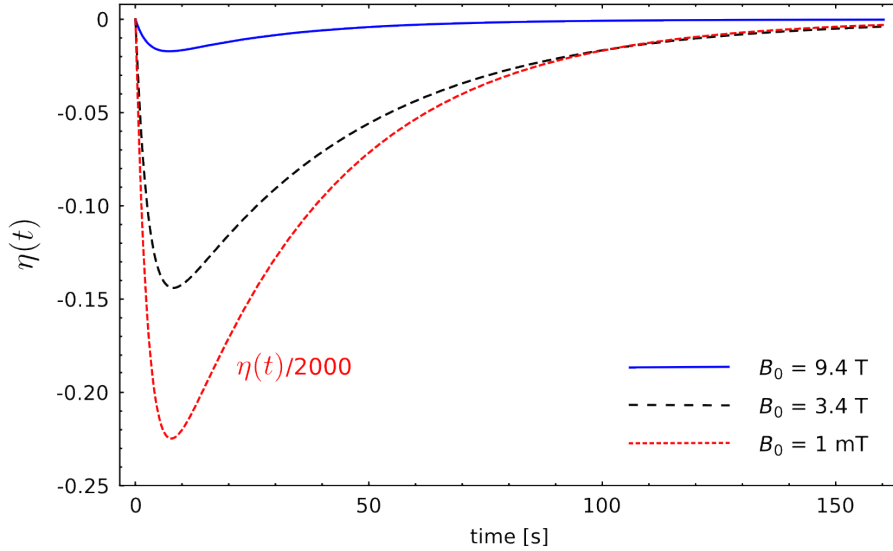
Figure 2.6: SPINOE enhancement curve calculated with Eq. 2.17 using the spin-lattice relaxation data from Table 2.2. The magnitude of $\eta(t)$ at 1 mT has been plotted divided by 2000 for ease of visualisation.
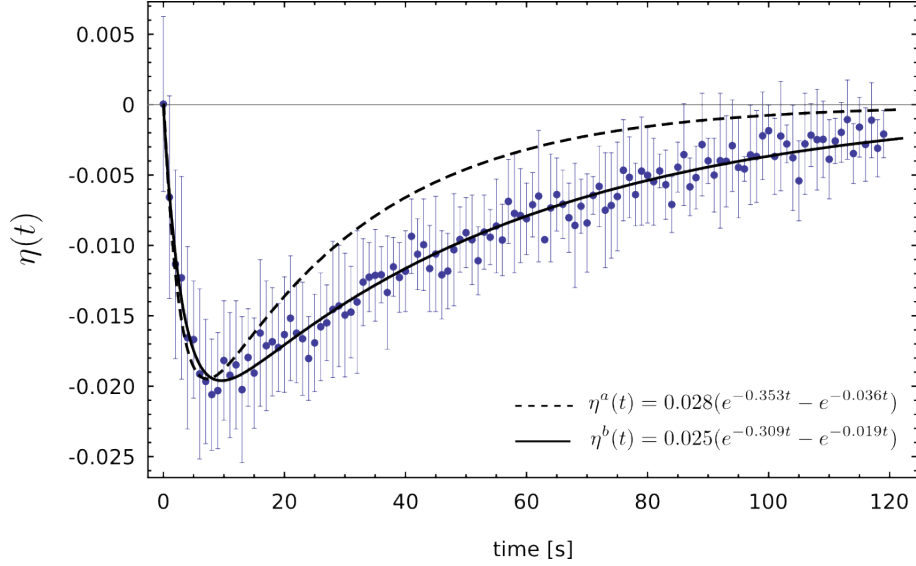
Figure 2.7: Measured SPINOE effect curve for solvent protons (water) at 9.4 T following the addition of 20 mM [1,4-^{13}C$_2$]fumarate that had been hyperpolarised to 36% at the time of injection (n=2). Error bars are the standard deviation on the mean. $\eta^a(t)$ was calculated using Eq. 2.22 and the experimental values shown in Table 2.2 (dashed line). $\eta^b(t)$ is the best fit to the experimental data (solid line).

Figure 2.7 shows the observed enhancement in water protons at 9.4 T after the addition of 20 mM [1,4-^{13}C$_2$]fumarate that had been hyperpolarised to 36%. The enhancement curves shown in Figure 2.7 were either calculated using the bi-exponential function in Eq. (2.22) and the relaxation rate constants reported in Table 2.2 (dotted line) or the measured enhancements were fit to Eq. (2.23) (solid line). There was reasonably good agreement between the water proton T_1 estimated from the fit to the experimentally determined enhancement curve [(3.3 $\pm$ 0.2)s] and that measured directly [(2.83 $\pm$ 0.02)s; Table 2.2], and between the calculated maximum SPINOE value [$\eta^a_{\max}$=(0.020 $\pm$ 0.005) at $t_{\max}$=(7 $\pm$ 1)s] and that determined from the fit to the experimental data [(0.0196 $\pm$ 0.0002) at $t_{\max}$=(9 $\pm$ 1)s]. However, the ^{13}C T_1 estimated from the enhancement [(51.9 $\pm$ 1.2) s] curve was $\sim$1.7 $\times$ longer than the ^{13}C T_1 measured directly [(27.6 $\pm$ 0.3) s; Table 2.2]. Addition of noise to the simulation did not bring the results closer. A possible explanation of the discrepancy of T_1s could be a mixing effect. The hyperpolarised [1,4-^{13}C$_2$]fumarate was injected, via a transfer line, into a water-containing 10 mm o.d. NMR tube, that had already been placed in the magnet. Progressive mixing in the seconds after injection could have led to increasing contact of the bulk of the water protons with the ^{13}C in the injected bolus of hyperpolarised [1,4-^{13}C$_2$]fumarate, leading to an increased SPINOE at later time points, which would have been

modulated by the decay of the ^{13}C polarisation.

The SPINOE enhancement displayed in Figure 2.7 gives information about how much SPINOE took place during transport from the DNP magnet to the acquisition spectrometer. As shown in Figure 2.5, if the sample experiences two magnetic field strengths during the experiment, the curve of $\eta(t)$ depends on the time spent in each field and the corresponding relaxation time constants. Although no NMR spectra were acquired for the first seconds of the experiment, during which the frozen hyperpolarised [1,4-^{13}C$_2$]fumarate was rapidly dissolved in water and transported to the acquisition magnet, the fact that the initial value of $\eta(t)$ at 9.4 T is almost zero indicates that little SPINOE occurred before the sample was inserted into the spectrometer. If $|\rho_S(\mathrm{H_2O}) - \rho_S(^2\mathrm{H_2O})| = 0$, the intermolecular component of the spin-lattice relaxation is zero and no SPINOE takes place (Figure 2.6c). In the dissolution-DNP experiment performed, stating that the sample experienced two fields is a simplistic approximation. The *low* millitesla magnetic field strength of the room where the experiments were carried out, which is mainly given by the stray fields of the DNP and the spectrometer magnet, is position dependent: the closer to the spectrometer magnet, the higher the field. During dissolution and transport, the sample was not kept at a fixed magnetic field strength but was moved through the room. Consequently, the sample experienced a magnetic field that changed as it approached the spectrometer. This may result in $|\rho_S(\mathrm{H_2O}) - \rho_S(^2\mathrm{H_2O})|$ averaging to zero for the time the sample is at low field.

2.5   Summary and potential applications

The magnitude of the SPINOE effect in a typical dissolution DNP experiment using 20 mM [1,4-^{13}C$_2$]fumarate hyperpolarised to 36% at 9.4 T has been measured to be of the order $\eta_{\max} \approx 2\%$. This is roughly in agreement with the predictions of cross-relaxation using Solomon's equations. The SPINOE depends on the ratio of the cross-relaxation rate constant between solute (^{13}C) and solvent spins to the longitudinal relaxation time constant of solvent protons, itself dependent on the magnetic field strength. SPINOE increases at lower field strengths, the calculated enhancement using [1,4-^{13}C$_2$]fumarate reaching $\eta_{\max} \approx 14\%$ at 3.4 T, which is close to the field strengths used in the clinic (1.5-3 T). The effect will be higher at lower magnetic field strengths (Table 2.2). The SPINOE effect offers the possibility of following the progress of a bolus of hyperpolarised ^{13}C-labeled material in the bloodstream by acquiring signal from solvent protons, rather than from the ^{13}C, which is preserved for its principal purpose - to probe the metabolic reaction pathway. Detection of the enhancement in signal from solvent water protons in effect turns the inevitable

loss of ^{13}C polarisation, due to relaxation, into a detectable and potentially useful ^{1}H signal that could be used for bolus tracking. This would offer new challenges and opportunities with respect to pharmacokinetic modelling.

2.5.1 Ideas to increase the SPINOE-derived signal

Distant dipolar fields (DDF)

Intermolecular dipolar interactions over distances beyond 10 μm apart are known as distant dipolar fields (DDF). DDF was first observed in the early 1990s with the use of pulse sequences that incorporated magnetic field gradients, such as CRAZED and HOMOGENIZED, which allow detection of multiple quantum coherences (Richter *et al.*, 2000). Warren *et al.* (1998) applied DDF as an alternative contrast for MRI to the traditional T_1, T_2 or T_2^* contrasts. In their experiments, they showed that two water molecules that are separated between 10 μm and 1 mm give rise to zero quantum coherences whose NMR signal is 5-10% larger than the signal due to thermal equilibrium magnetisation. DDF has been shown to amplify the weak solvent proton signal during an experiment of indirect detection of ^{13}C (Zhao *et al.*, 2013). However, DDF would not be a useful technique to boost the weak SPINOE signal at high fields. The pulse sequence that employs DDF is based on the acquisition of a single-shot echo, which would not allow monitoring the time-course of the proton signal. Furthermore, DDF relies on perturbation of the transverse magnetisation of ^{13}C, while in hyperpolarisation experiments one wishes to preserve the longitudinal magnetisation of ^{13}C. The advantage of indirectly tracking the bolus of hyperpolarised material with SPINOE is that no radiofrequency pulse or perturbation of the hyperpolarised ^{13}C magnetisation is required. Hence, a method that does not interfere with ^{13}C magnetisation is desirable to boost the SPINOE signal.

Further ideas

A simpler alternative to amplify the change in the proton signal that arises from the SPINOE would be to use a partially deuterated solvent, so as to increase the concentration of hyperpolarised ^{13}C spins relative to solvent ^{1}H spins (MacNamara *et al.*, 2000). However, this would translate into fewer proton spins to detect.

Moreover, as it has been pointed out for SPINOE from hyperpolarised ^{129}Xe, large flip-angle radiofrequency pulses can be applied to ^{1}H to increase the SNR because the hyperpolarised nuclei will continuously restore the ^{1}H polarisation (Fitzgerald *et al.*, 1998). However, care has

to be taken when using flip-angle radiofrequency pulses close to $90°$. The interaction of the large bulk magnetisation with the radiofrequency coil may lead to radiation feedback, causing a loss of longitudinal magnetisation that is faster than T_1, and affecting the intermolecular cross-relaxation exchange (Krishnan and Murali, 2013). This phenomenon is known as radiation damping (RD). Due to the inhomogeneous B_0 magnetic fields in MR experiments *in vivo*, RD has no effect on the NMR signal. For experiments *in vitro*, RD can be avoided by applying a constant very small gradient along the longitudinal axis (Lin *et al.*, 2000).

Detection of the SPINOE signal could be made more effective by pre-suppressing the signal from the protons in the background by saturating the protons already in the test tube before injection of the hyperpolarised material (*in vitro*) or applying pulse sequences to cancel the signal from stationary protons (*in vivo*) (Wen, 2001). In either case, the radiofrequency coil would detect only the signal from the protons in the bolus.

2.5.2   Intramolecular SPINOE

The formulae presented up to Eq. (2.14) are general and do not assume any specific cross-relaxation mechanism. Although from Section 2.3.2 onwards the intermolecular cross-relaxation pathway is considered for the particular case of polarisation transfer from hyperpolarised solute to the solvent, intramolecular SPINOE could be analysed in a similar way.

Intramolecular SPINOE may also prove useful to monitor dynamic biomolecular processes such as protein folding. It has recently been reported that the protons of hyperpolarised water in contact with proteins undergo rapid exchange with the protons in the amide group, and that SPINOE between the hyperpolarised protons now in the amide group and the ^{15}N gives experimental enhancement values of $\eta_{\max} \approx 200$ at $B_0 = 11.7$ T (Harris *et al.*, 2013). The expressions in this chapter may be used to predict the intramolecular SPINOE between two neighbouring spins. Nevertheless, sequences like reverse INEPT may be more efficient to transfer polarisation in coupled spin systems (Petit and Lee, 2014).

3

Prolonging spin relaxation of [1,2-^{13}C$_2$]pyruvate

In the field of hyperpolarisation with DNP, the most widely used substrate to date to study cancer metabolism has been [1-^{13}C]pyruvate, due to the high polarisation that can be obtained and the long T_1 of the carboxyl carbon relative to its rates of cellular uptake and subsequent metabolism ($T_1 \sim 30$ s *in vivo* in magnetic fields above 1 T) (Brindle *et al.*, 2011). Pyruvate is the end product of the glycolytic pathway and may be reversibly converted to lactate and alanine in the reactions catalysed by lactate dehydrogenase and alanine aminotransferase, respectively. Measurements of the interconversion of pyruvate and lactate, which is fast relative to the T_1 of the hyperpolarised ^{13}C label, have been used for tumour grading and detection of treatment response (Albers *et al.*, 2008, Day *et al.*, 2007).

Pyruvate is well-tolerated when injected intravenously and a clinical trial of hyperpolarised [1-^{13}C]pyruvate in prostate cancer has been completed recently (Nelson *et al.*, 2012). However, the relatively short lifetime of the hyperpolarised signal remains a significant limitation and compounds in which the hyperpolarised ^{13}C label has a longer lifetime would be of great value in the clinical setting. For instance, this would provide more time for handling the substrate prior to injection into a patient and reduce relaxation-induced signal losses during circulation in the blood stream.

Here we investigate extending the time window for observing metabolism by preserving the hyperpolarisation of [1,2-^{13}C$_2$]pyruvate in long-lived states.

This chapter is structured as follows.

First, the eigenstates of the Hamiltonian for two weakly coupled spins $1/2$ are introduced, both at low and high magnetic field. Following this, definitions of longitudinal polarisation and singlet order polarisation are given. Then, three methods to demonstrate the singlet order of [1,2-^{13}C$_2$]pyruvate are presented: (i) direct enhancement of nuclear singlet order at low field after dissolution DNP, (ii) longitudinal magnetisation to singlet order pulse sequences at low field and (iii) chemical shift difference suppression with decoupling at high field. Each method is developed in greater detail as separate subsections. Finally, there is a short summary of the concepts and results at the end of the chapter.

3.1   Eigenstates of a pair of spins-1/2

The upper limit of the spin polarisation lifetime of an isolated spin-$1/2$ nucleus (such as the carboxyl carbon in [1-^{13}C]pyruvate) is the longitudinal relaxation time T_1. In spin-$1/2$ pairs, however, longer relaxation times may be possible.

The four eigenstates of the Hamiltonian of a two spins-$1/2$ system in an arbitrary magnetic field B_0 are the following (Carravetta and Levitt, 2005):

$$
\begin{aligned}
\left|T'_{-1}\right\rangle &= \left|T_{-1}\right\rangle, \\
\left|T'_0\right\rangle &= \left|T_0\right\rangle\cos(\theta/2) - \left|S_0\right\rangle\sin(\theta/2), \\
\left|T'_{+1}\right\rangle &= \left|T_{+1}\right\rangle, \\
\left|S'_0\right\rangle &= \left|S_0\right\rangle\cos(\theta/2) + \left|T_0\right\rangle\sin(\theta/2).
\end{aligned}
\tag{3.1}
$$

With the mixing of states given by

$$
\theta = \arctan\left(\frac{\Delta\omega_0}{2\pi J}\right),
\tag{3.2}
$$

where $\Delta\omega_0 = -\gamma B_0(\delta_2 - \delta_1)$.

A direct observation is that $\theta = 0$ in the strong coupling limit ($|\Delta\omega_0| << |2\pi J|$), which is true if the magnetic field is zero ($B_0 = 0$) or the two spins are magnetically equivalent ($\Delta\omega_0 = 0$). Then, the eigenstates of the Hamiltonian are the ***triplet-singlet eigenstates*** $\{\left|T_{-1}\right\rangle, \left|T_0\right\rangle, \left|T_{+1}\right\rangle, \left|S_0\right\rangle\}$. The ***Zeeman states*** are eigenstates of the Hamiltonian ($\theta = \pi/2$) if the two spins are magnetically inequivalent and they experience a strong B_0 magnetic field ($|\Delta\omega_0| >> |2\pi J|$). The relationship between triplet-singlet states and Zeeman states is shown in Eq. (1.44).

The population of $|S_0\rangle$ decays with a time constant denoted T_S, which may exceed T_1 by an order of magnitude. In general, $T_S > T_1$ arises only in the regime of near magnetic equivalence between the spin pair, where (i) the singlet and triplet spin states of the pair are stationary with respect to coherent evolution (triplet-singlet eigenstates), and (ii) symmetric relaxation mechanisms are symmetry-forbidden (Section 1.6).

3.1.1 Adiabatic correlation of eigenstates

For a weakly coupled spin pair, the population from a state in the Zeeman eigenbasis may be adiabatically transferred to a state in the triplet-singlet eigenbasis by, for instance, moving the sample from a high magnetic field to a low one. The condition of adiabaticity is that the transport time is slow compared to $|J^{-1}|$, which ensures that the change in the spin Hamiltonian is always slower than the smallest difference in energy eigenvalues of the system (Carravetta, Johannessen and Levitt, 2004). Given that the scalar coupling constant between C1 and C2 in pyruvate is $J = 60$ Hz ($J^{-1} = 0.02$ s), and that the transport time through the magnetic fields is on the order of seconds, then the adiabatic condition is satisfied.

From Eq. (3.1), the Zeeman and triplet-singlet eigenstates of a spin pair with positive gyromagnetic ratio, γ, positive chemical shift difference, $(\delta_2 - \delta_1)$, and positive intra-pair scalar coupling, J, correlate as follows:

$$
\begin{aligned}
|\beta_1\beta_2\rangle &\leftrightarrow |T_{-1}\rangle, \\
|\alpha_1\beta_2\rangle &\leftrightarrow |T_0\rangle, \\
|\alpha_1\alpha_2\rangle &\leftrightarrow |T_{+1}\rangle, \\
|\beta_1\alpha_2\rangle &\leftrightarrow |S_0\rangle.
\end{aligned}
\tag{3.3}
$$

For a reversed sign in any of the parameters γ, $(\delta_2 - \delta_1)$ and J the states $|\alpha_1\beta_2\rangle$ and $|\beta_1\alpha_2\rangle$ correlate the opposite way around:

$$
\begin{aligned}
|\beta_1\beta_2\rangle &\leftrightarrow |T_{+1}\rangle, \\
|\alpha_1\beta_2\rangle &\leftrightarrow |S_0\rangle, \\
|\alpha_1\alpha_2\rangle &\leftrightarrow |T_{-1}\rangle, \\
|\beta_1\alpha_2\rangle &\leftrightarrow |T_0\rangle.
\end{aligned}
\tag{3.4}
$$

3.2   Polarisation of an ensemble of coupled spin-1/2 pairs

For a pair of nearly equivalent spins-1/2 in a strong magnetic field, the populations in each energy level are the products of the populations of each nucleus of the pair. The following is an extension of Eq. (1.15) for a pair of spins-1/2:

$$\begin{cases} n_{\alpha_1\alpha_2} = n_{\alpha_1}n_{\alpha_2} = \tfrac{1}{4}(1+P_1)(1+P_2), \\[4pt] n_{\alpha_1\beta_2} = n_{\alpha_1}n_{\beta_2} = \tfrac{1}{4}(1+P_1)(1-P_2), \\[4pt] n_{\beta_1\alpha_2} = n_{\beta_1}n_{\alpha_2} = \tfrac{1}{4}(1-P_1)(1+P_2), \\[4pt] n_{\beta_1\beta_2} = n_{\beta_1}n_{\beta_2} = \tfrac{1}{4}(1-P_1)(1-P_2). \end{cases} \qquad (3.5)$$

Analogously to the longitudinal polarisation defined for an ensemble of isolated spins-1/2 in Eq. (1.14), the longitudinal polarisation of an ensemble of pairs of spins-1/2 is defined as the population difference between the states $|\alpha_1\alpha_2\rangle$ and $|\beta_1\beta_2\rangle$,

$$P \equiv n_{\alpha_1\alpha_2} - n_{\beta_1\beta_2}, \qquad (3.6)$$

and, therefore,

$$P = (P_1 + P_2)/2, \qquad (3.7)$$

i.e. the longitudinal polarisation of the two-spin system is the average of the longitudinal polarisation of each spin in the pair.

3.2.1   Singlet polarisation

There are several well-established methods available for preparing hyperpolarised singlet order starting from longitudinal spin order, both at low and high magnetic fields (Bornet *et al.*, 2011, Levitt, 2012, Pileio *et al.*, 2010, Sarkar *et al.*, 2007, Tayler and Levitt, 2011b).

In the triplet-singlet regime, longitudinal polarisation is defined as in Eq. (3.6), using here the difference between the states $|T_{+1}\rangle$ and $|T_{-1}\rangle$:

$$P \equiv n_{T_{+1}} - n_{T_{-1}}. \qquad (3.8)$$

The polarisation of the singlet order is defined as the mean singlet-triplet population difference:

$$P_{\text{singlet}} \equiv n_{S_0} - \frac{1}{3}(n_{T_{+1}} + n_{T_0} + n_{T_{-1}}). \tag{3.9}$$

During a field-cycle experiment in which the initial longitudinal magnetisation under the Zeeman regime is transferred adiabatically into the triplet-singlet eigenstates, the expected singlet polarisation can be calculated similarly as:

$$P_{\text{singlet}} = n_{\beta_1 \alpha_2} - \frac{1}{3}(n_{\alpha_1 \alpha_2} + n_{\alpha_1 \beta_2} + n_{\beta_1 \beta_2}). \tag{3.10}$$

And in terms of longitudinal polarisation, inserting Eq. (3.5) into Eq. (3.10), this is:

$$P_{\text{singlet}} = \frac{1}{3}(P_2 - P_1 - P_1 P_2). \tag{3.11}$$

Assuming that the polarisation of two spins of the pair is the same, i.e. $P_1 = P_2$,

$$P_{\text{singlet}} = \frac{-P^2}{3}. \tag{3.12}$$

For instance, for longitudinal polarisation $P = 30\%$, P_{singlet} is $\sim 3\%$, which is 10 times less than P but yet more than 10^4-fold the ^{13}C thermal polarisation at 9.4 T and 25°C ($P_0^C \approx 8 \times 10^{-4}\%$).

3.3 Options to access the singlet in pyruvate

The two ^{13}C nuclei of [1,2-^{13}C$_2$]pyruvate are chemically inequivalent; the C1 carbon signal appears at 171 ppm whilst the C2 signal appears at 207 ppm. As explained in section 3.1, the singlet state of a pair of spins-1/2 is nearly an eigenstate of the Hamiltonian of the system only under the condition of near-equivalence. The chemical shift difference may be suppressed by keeping the sample in a near-zero field, where the Larmor frequencies of the two nuclei become similar, or in high field by applying a decoupling field. Using these ideas, to exploit the singlet state of a magnetically inequivalent spin pair, three different approaches may be considered:

1. Hyperpolarise the spin pair, transport it adiabatically to a low field ($|B_0| << |2\pi J|/|\gamma\Delta\delta|$) and keep it at this low field until the moment of acquisition, when it will be inserted into the spectrometer. This method has been termed 'direct enhancement of nuclear singlet order by dissolution DNP' (Tayler *et al.*, 2012), and instead of populating the singlet state, it provides a spectrum characteristic of the depletion of the singlet state. However, the relaxation time constant of the singlet order is the same regardless of the sign. Other methods that rely on

adiabatic correlations of the eigenstates would fall into this category, e.g. adiabatic switching of a radiofrequency spin lock (Kiryutin *et al.*, 2013).

2. Apply a pulse sequence to populate the singlet state in the near-equivalence regime (low magnetic field) or populate a singlet pre-cursor in a high magnetic field. The singlet could be then isolated using a decoupling radiofrequency pulse or moving the sample to $|B_0| << |2\pi J|/|\gamma\Delta\delta|$. In both cases, some extra hardware would be required to apply the pulse sequences. Strategies for this method have been discussed extensively in the literature (Levitt, 2012, Pileio *et al.*, 2010, Bornet *et al.*, 2011).

3. Access the singlet at high field by means of a pulse sequence and locking the singlet state by either taking the sample to a low field or by applying a strong decoupling field whilst in the high-field of the spectrometer. The latter may require some extra hardware capable of delivering high power input. For instance, a decoupling field of at least 40 kHz would be required to lock the singlet state in [1,2-^{13}C$_2$]pyruvate. Micro-coils are particularly useful to test such approach, as the smaller the size of the coil, the less power required and heat produced (Kentgens *et al.*, 2008).

3.4   Direct enhancement of nuclear singlet order at low field

The work described in this section was done in collaboration with Malcolm Levitt's laboratory (University of Southampton, School of Chemistry) and is an extension of the material published in (Tayler *et al.*, 2012, Marco-Rius *et al.*, 2013).

Singlet order is observed in the hyperpolarised state immediately after dissolution-DNP, without the need to apply any pulse sequence, simply due to adiabatic transfer of the spin populations between the Zeeman eigenstates and the triplet-singlet eigenstates of the spin pair. This approach is illustrated in Figure 3.1, where frozen hyperpolarised material is dissolved and transported adiabatically into a region of low magnetic field. This procedure leads to a depletion in the population of $|S_0\rangle$, creating singlet order proportional to the square of the longitudinal polarisation [Eq. (3.12)].

The population difference between the triplet states tends to thermal equilibrium with the longitudinal relaxation time constant T_1^{LF} of the low field. Meanwhile, the depleted singlet population equalises with the time constant T_S, which in favourable circumstances may be longer (Figure 3.2). Figure 3.1b (middle panel) shows the system configuration assuming $T_S > T_1^{LF}$ after the triplet populations have reached equilibrium.
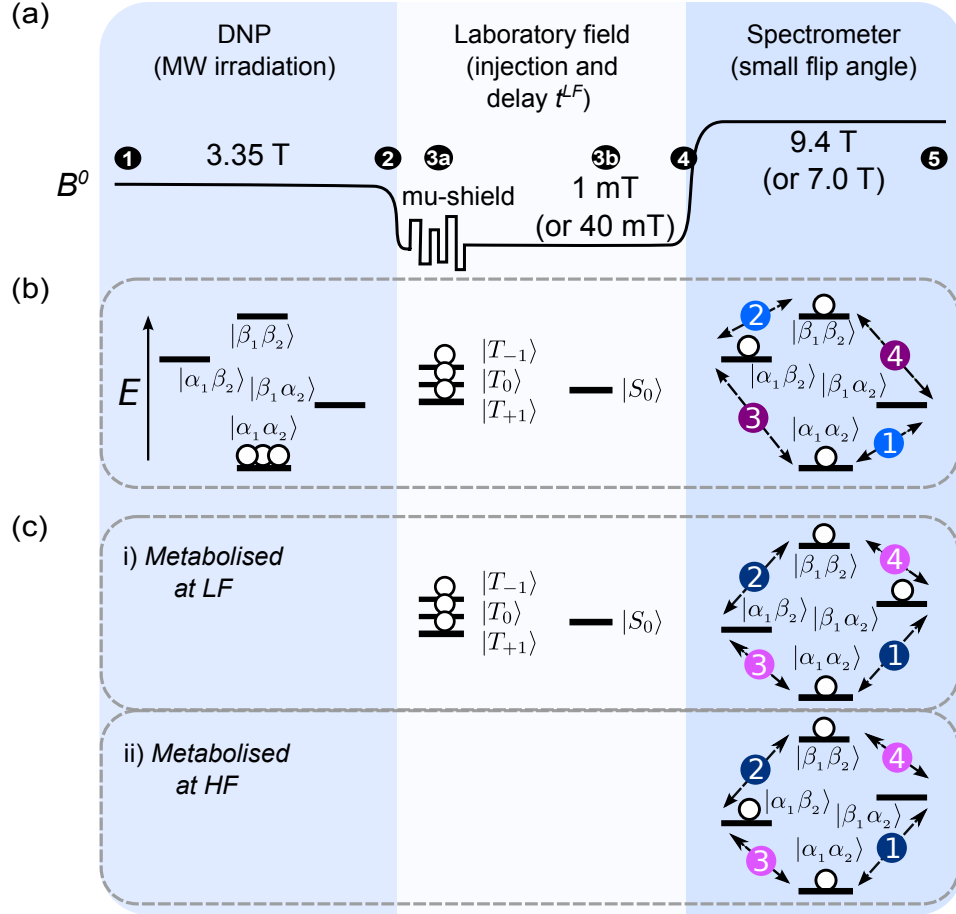
Figure 3.1: (a) Experimental sequence for hyperpolarised singlet NMR of [1,2-^{13}C$_2$]pyruvate. Dissolution DNP (1 and 2) of the sample is followed by manipulations in low magnetic field: (3a) shaking the sample inside a magnetically shielded chamber, which rapidly dephases non-singlet spin order; (3b) injection into the biological system at low field. After waiting in the low field, the sample is then shuttled into a high-field spectrometer for NMR signal readout (4 and 5). (b) Illustration of the excess population in $|\alpha_1\alpha_2\rangle$ of the hyperpolarised substrate, which generates singlet depletion order upon dissolution and transfer to low magnetic field. Pure singlet order remains after the triplet states equilibrate via rapid T_1 relaxation in the low field, or are dephased using a mu-metal chamber. The resulting spectrum contains a pair of peaks in anti-phase. (c) Fate of the singlet order in [1,2-^{13}C$_2$]pyruvate after metabolism to [1,2-^{13}C$_2$]lactate. Different outcomes are predicted depending on whether metabolism takes place at high or low magnetic field, since the chemical shift difference has opposite sign in the two molecules.
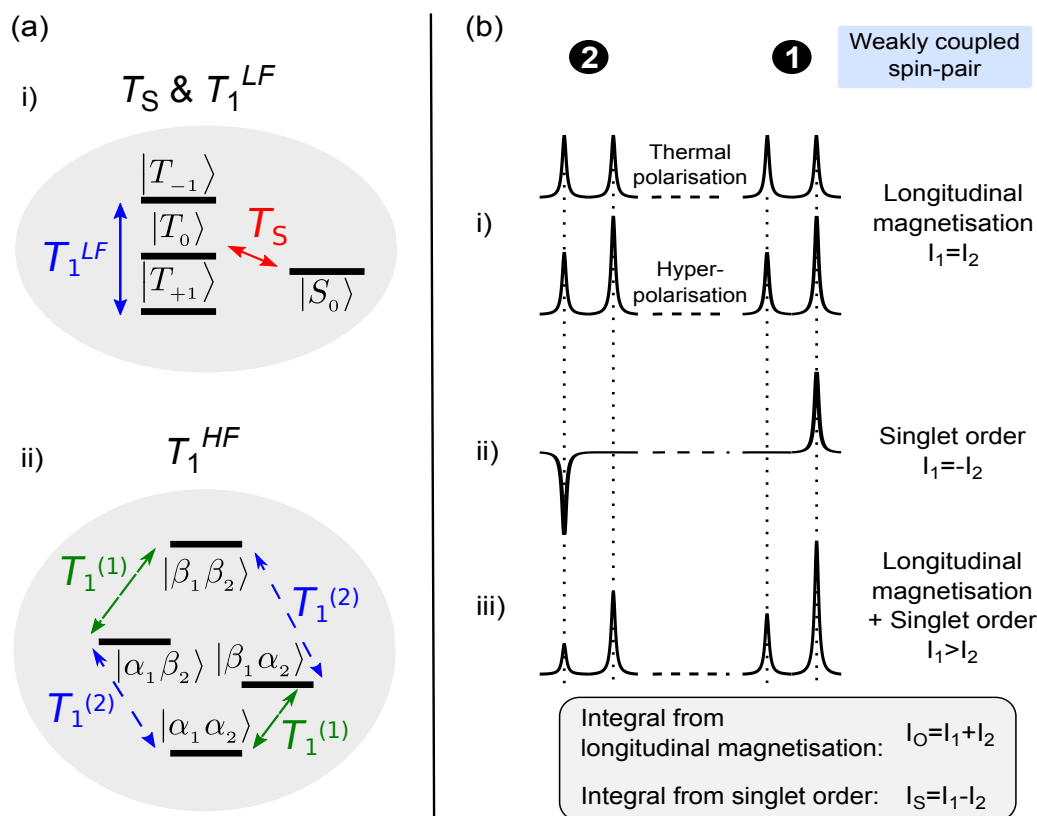
Figure 3.2: (a) Relaxation of a spin-1/2 pair at high and low magnetic fields. (i) At low field (triplet-singlet configuration, or near-magnetic-equivalence regime), the triplet populations relax with a single exponential time constant T_1^{LF}, while the singlet population relaxes with a potentially slower time constant T_S. At high magnetic field, as shown in (ii) (Zeeman configuration, or weak-coupling regime), each nucleus of the pair relaxes with its own distinct T_1. (b) Illustration of the spectral signatures obtained after placing the system in high field, arising from (i) longitudinal magnetisation, (ii) singlet order or (iii) both. By adding or subtracting the peak integrals I$_1$ and I$_2$, one may distinguish the contribution of each of (i) and (ii) to the spectrum (see text).

3.4.1 Singlet order filtration

A simple yet effective procedure that allows one to selectively observe NMR signals resulting from singlet spin order is to shake the sample in and out a magnetically shielded chamber, which rapidly dephases all other spin order (Figure 3.1a). The mu-metal cylinder distorts magnetic flux lines to its surface, resulting in an extremely inhomogeneous and weak fluctuating magnetic field in the neighbouring space (Tayler *et al.*, 2012). Shaking the sample modulates this field, the result of which is to rapidly dephase non-rotation invariant spin order, such as longitudinal magnetisation, which averages out and leaves only rotation invariant spin order, which for a coupled spin-1/2 pair is equal only to the singlet order.

3.4.2 Spectral information on magnetisation and singlet order

The characteristic spectrum of a spin system with singlet order in which the triplet populations are equilibrated at low field, or are filtered out by using the magnetically shielded chamber, contains two outer transitions when acquired with a small flip angle radiofrequency pulse, as shown in Figure 3.2b(ii). The two peaks have equal area but are opposite in sign. This contrasts with all four transitions being in-phase (same sign) following a small flip angle pulse applied to pure longitudinal spin order (Figure 3.2b(i)). If the sample is inserted into the spectrometer before the triplet populations have equilibrated and a small flip-angle spectrum is acquired, two asymmetric doublets will be obtained (Figure 3.2b(iii)). The two contributions to the spectrum can be separated from one another: the total area under the spectrum is proportional to the longitudinal magnetisation present,

$$I_O = I_1 + I_2, \tag{3.13}$$

while the difference in the areas under each doublet is characteristic of the singlet order,

$$I_S = I_1 - I_2. \tag{3.14}$$

Table 3.1 and Table 3.2 display the longitudinal magnetisation and singlet order contributions to the NMR spectra for the two extreme cases in which the spin population is (i) pure Zeeman order and (ii) pure singlet depletion order (the triplet states have equilibrated leaving the singlet state population depleted). Before normalisation, signal from Zeeman order is $3P^{-1}$ times higher than signal from singlet order.

Population distribution	Polarisation level of each nuclear spin	$I_O = I_1 + I_2$	$I_S = I_1 - I_2$
Zeeman order	Any	$\propto (P_1 + P_2)$	$\propto (P_1 - P_2)$
	$P_1 = P_2 = P$	$\propto (2P)$	0
Negative singlet order *(triplet states equilibrated)*	Any	0	$\propto 2/3(P_1 - P_2 + P_1 P_2)$
	$P_1 = P_2 = P$	0	$\propto (2/3P^2)$

Table 3.1: Contribution of longitudinal and singlet order to the NMR spectrum. $I_O = I_1 + I_2$ and $I_S = I_1 - I_2$. P, P_1 and P_2 are the polarisation values at the moment of adiabatic transfer.

Population distribution	Polarisation level of each nuclear spin	$I_O/(I_O + I_S)$	$I_S/(I_O + I_S)$
Zeeman order	Any	$\propto (P_1 + P_2)/(2P_1)$	$\propto (P_1 - P_2)/(2P_1)$
	$P_1 = P_2 = P$	$\propto 1$	0
Negative singlet order *(triplet states equilibrated)*	Any	0	1
	$P_1 = P_2 = P$	0	1

Table 3.2: Normalised I_O and I_S values of Table 3.1.

Nuclear spin evolution at low field

Starting from high levels of Zeeman polarisation, i.e. highly-populated ground state, when the sample is placed in a low magnetic field, the population imbalance between the triplet states equilibrates mono-exponentially with T_1^{LF}. Therefore, keeping the sample in the low field for an interval t^{LF} and then moving it into the spectrometer for signal sampling would show that:

$$I_O \propto P e^{-t^{LF}/T_1^{LF}}. \tag{3.15}$$

On the other hand, the population difference between singlet state and mean population of the triplet states equalises with the relaxation time constant T_S. The evolution of the singlet order-derived signal, I_S, detected in the high field of the spectrometer is a combination of the triplet states populations equilibrating with T_1^{LF} and singlet-triplet populations equilibrating with T_S:

$$I_S \propto \frac{2P^2}{3} e^{-t^{LF}/T_S^{LF}} (1 - e^{-t^{LF}/T_1^{LF}}). \tag{3.16}$$

Figure 3.3 illustrates how the intensity of I_S increases with T_1^{LF} as the triplet state population imbalance decreases and then decays with T_S, reaching its maximum value

$$I_S(t_{max}^{LF}) \propto \frac{2P^2}{3} \left(\frac{T_1^{LF} + T_S}{T_1^{LF}} \right)^{-T_1^{LF}/T_S} \left(1 - \frac{T_1^{LF}}{T_1^{LF} + T_S} \right) \tag{3.17}$$

after remaining in the low field a time $t = t_{max}$:

$$t_{max}^{LF} = T_1^{LF} \ln \left(\frac{T_1^{LF} + T_S}{T_1^{LF}} \right). \tag{3.18}$$

If the triplet states were fully equilibrated or $T_1^{LF} = 0$, the maximum value of I_S at $t_{max} = 0$ would be proportional to $2P^2/3$.

To measure T_S, a simple mono-exponential function may be fitted to the singlet-triplet relaxation decay after t_{max}. Best results are obtained when the function is fitted after $2 \times t_{max}$. For example, for relaxation time constant values of $T_1^{LF} = 4$ s and $T_S = 20$ s, $t_{max} = 7.2$ s. If an exponential decay is fitted to Eq. (3.16) from $t = t_{max}$ onwards, T_S is given with 12% error; if the exponential decay is fitted from $t = 2 \times t_{max}$ onwards, as in Figure 3.3, T_S is given with 1% error (with the error being calculated as $(T_S^{fit} - T_S)/T_S$). The discrepancy between fitted and I_S curve decreases as the ratio T_S/T_1^{LF} increases and for larger values of T_S and T_1^{LF}.
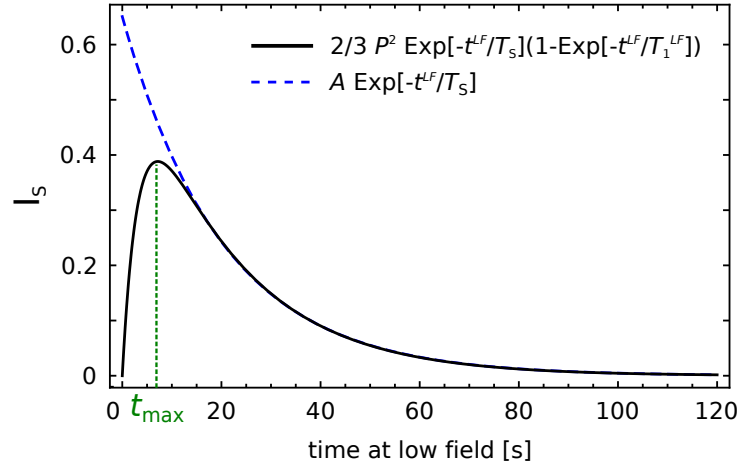
Figure 3.3: Evolution of the signal intensity of $I_S = I_1 - I_2$ at a low magnetic field strength, as described by Eq. (3.16) (solid black line). The intensity increases with T_1^{LF} as the triplet states populations equilibrate. After reaching a maximum at t_{max}, it decays due to singlet-triplet relaxation with T_S. T_S decay is mono-exponential (dashed blue line). The values used for the calculations presented here were $T_1^{LF} = 4$ s and $T_S = 20$ s, with $t_{max} = 7.2$ s and $A = 0.65$.

3.4.3   Spectral signal evolution at high field

The sum of the integrals of the two peaks in each J-doublet decays mono-exponentially with the longitudinal relaxation time constant of each carbon site. However, analysis of each peak within the doublet reveals that they evolve differently with time (Figure 3.4). The relaxation of each peak depends on the population distribution at the moment of insertion of the sample into the high field magnet of the spectrometer:

- If $P = 1$ at the moment of insertion, 100% of the population is in the state $|\alpha_1\alpha_2\rangle$. The transitions observed in the first spectrum acquired with a small flip-angle radiofrequency pulse immediately after insertion of the sample are $|\alpha_1\alpha_2\rangle \to |\beta_1\alpha_2\rangle$ for C1 and $|\alpha_1\alpha_2\rangle \to |\alpha_1\beta_2\rangle$ for C2 (Figure 3.4a, bottom). The spectral peaks arising from these two transitions decay with time, whilst the peaks of the other two transitions grow with a curve characteristic of the cross-relaxation between C1 and C2 (Figure 3.4a, top).

- If the sample has been left at low field for an interval of time larger than T_1^{LF} but shorter than T_S, the triplet states will have equilibrated while the singlet state remains deficient in population. The transitions observed in the first spectrum acquired with a small flip-angle radiofrequency pulse immediately after insertion of the sample are $|\alpha_1\alpha_2\rangle \to |\beta_1\alpha_2\rangle$ for C1 and $|\beta_1\beta_2\rangle \to |\beta_1\alpha_2\rangle$ for C2 (Figure 3.4b, bottom). Again, these spectral peaks decay with time, whilst the peaks for the other two transitions grow as a result of cross relaxation between C1 and C2 (Figure 3.4b, top).

These observations indicate that measurements of polarisation for each carbon site have to be performed by adding the integrals of the two peaks at each site.

3.4.4   Predicted singlet-MRS spectra following metabolism of pyruvate

Following injection of hyperpolarised [1,2-^{13}C$_2$]pyruvate into a mouse, the pair of ^{13}C nuclei of the product of any metabolic reaction will also be expected to be in singlet order configuration, provided that the chemical bond between the two ^{13}C nuclei is preserved and that the field is sufficiently low to satisfy the near-equivalence condition ($|\Delta\omega_0| \ll |\pi J_{CC}|$). Hyperpolarised [1,2-^{13}C$_2$]pyruvate can be converted into [1,2-^{13}C$_2$]lactate. There are different spectral outcomes for [1,2-^{13}C$_2$]lactate depending on whether the enzymatic reaction occurs at low or high magnetic field, since the chemical shift difference ($\delta_2 - \delta_1$) for [1,2-^{13}C$_2$]lactate has opposite sign to that for [1,2-^{13}C$_2$]pyruvate:
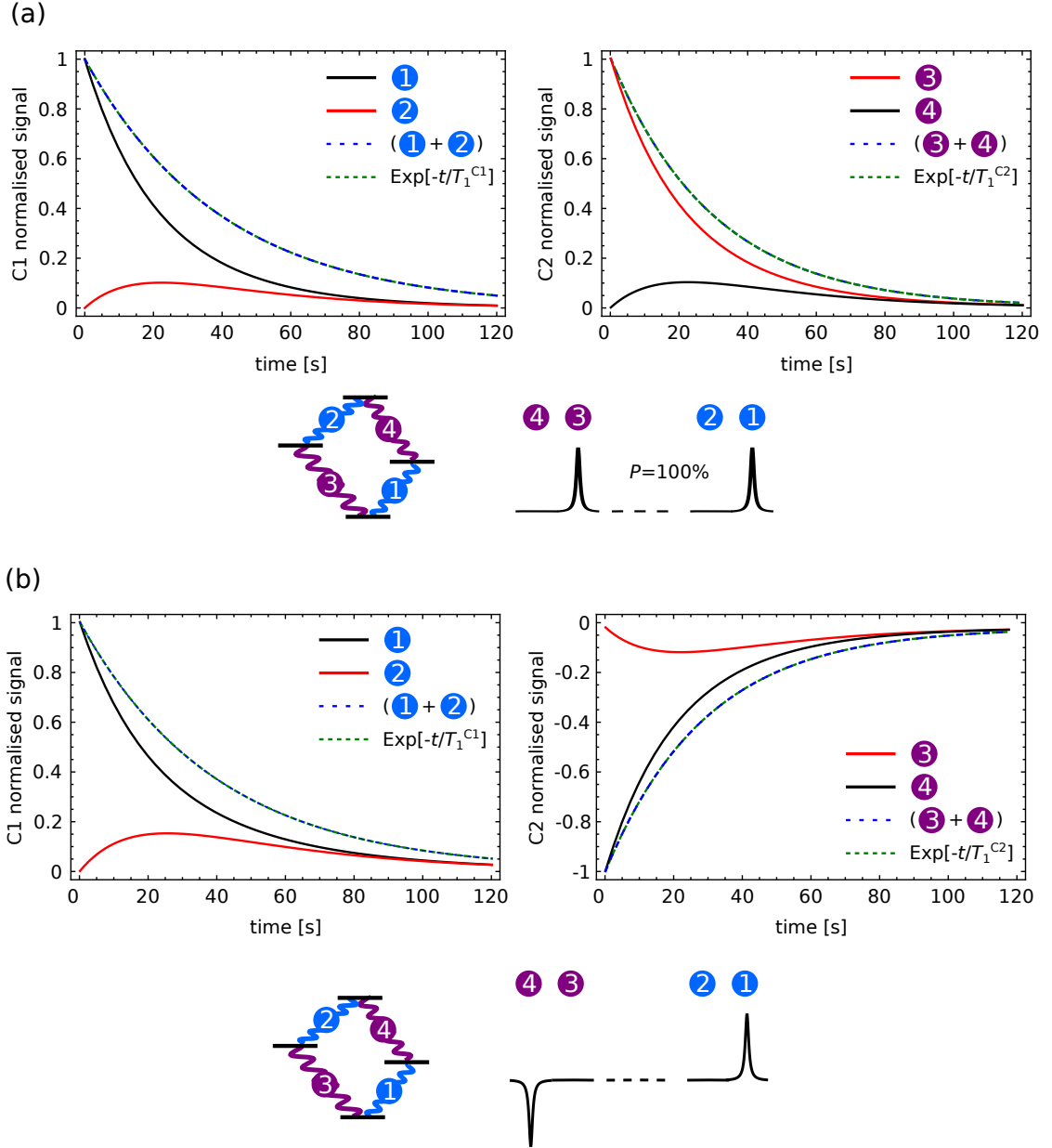
Figure 3.4: Evolution of C1 and C2 *J*-doublet signals from [1,2-^{13}C$_2$]pyruvate in the high field of the spectrometer assuming (a) 100% population of the state $|\alpha_1\alpha_2\rangle$ and (b) depletion of $|S_0\rangle$ with an equilibrated population in the triplet states. The dashed lines illustrate that the sum of each *J*-doublet decays mono-exponentially with the T_1 of the corresponding carbon site. The peak pattern representation displays the expected spectra acquired with a small flip angle radiofrequency pulse at $t = 0$ for (a) and (b). The simulation values used here were $T_1^{C1} = 40$ s and $T_1^{C2} = 30$ s.

1. Metabolic conversion at low field (Figure 3.1c(i)) generates singlet-depleted ^{13}C$_2$ lactate. According to Eq. (3.4) the state after transfer into high magnetic field corresponds to a depleted population of $|\alpha_1\beta_2\rangle$ (since for lactate ($\delta_2 - \delta_1 < 0$). The small-flip-angle spectrum contains one positive peak from the $|\alpha_1\alpha_2\rangle$ to $|\alpha_1\beta_2\rangle$ transition and one negative peak from the $|\beta_1\beta_2\rangle$ to $|\alpha_1\beta_2\rangle$ transition. This should be contrasted with the singlet-derived NMR signal from [1,2-^{13}C$_2$]pyruvate, which gives a positive peak for the $|\alpha_1\alpha_2\rangle$ to $|\beta_1\alpha_2\rangle$ transition and a negative peak for the $|\beta_1\beta_2\rangle$ to $|\beta_1\alpha_2\rangle$ transition, under the same circumstances.

2. During adiabatic transport from a low to a high magnetic field, the singlet order of [1,2-^{13}C$_2$]pyruvate is transferred into a population depletion of $|\beta_1\alpha_2\rangle$ (Figure 3.1b). Subsequent metabolic conversion then results in [1,2-^{13}C$_2$]lactate depleted in $|\beta_1\alpha_2\rangle$, in contrast to the low field metabolic post-cursor (Figure 3.1c(ii)). The small-flip-angle spectrum contains one positive peak for the $|\alpha_1\alpha_2\rangle$ to $|\beta_1\alpha_2\rangle$ transition and a negative peak for the $|\beta_1\beta_2\rangle$ to $|\beta_1\alpha_2\rangle$ transition (Figure 3.5a(ii)).
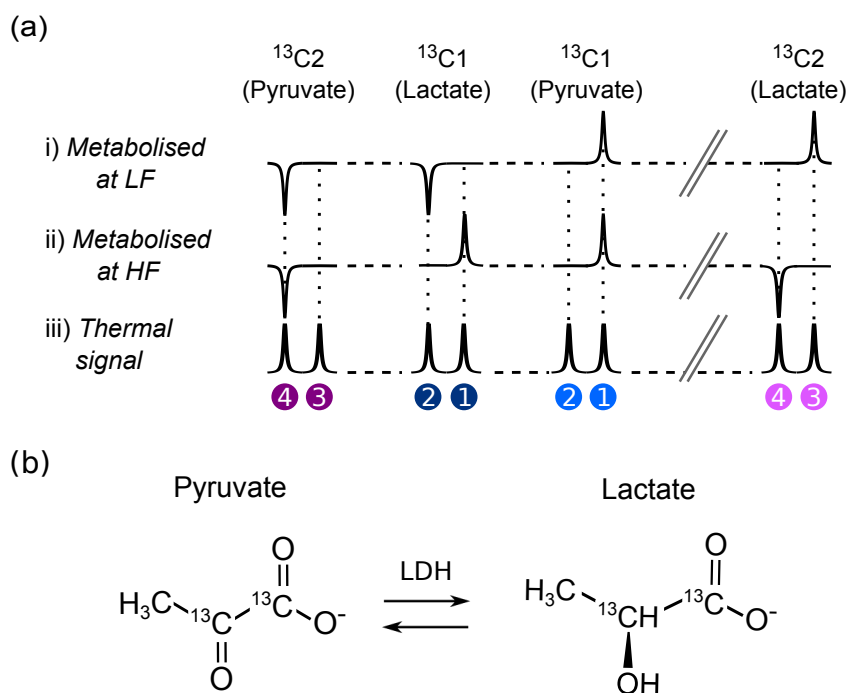
Figure 3.5: (a) Resulting spectral patterns for the experiment described in Figure 3.1. For reference, the peak pattern of a sample at thermal equilibrium is shown in (iii). (b) Schematic pyruvate-lactate exchange reaction. LDH stands for the enzyme lactate dehydrogenase.

Similar reasoning explains the expected peak pattern from [1,2-^{13}C$_2$]pyruvate hydrate, which has also a chemical shift difference ($\delta_2 - \delta_1$) with opposite sign to that for [1,2-^{13}C$_2$]pyruvate. However, if the bond is broken, for example as occurs during the decarboxylation of pyruvate to form carbon dioxide in the reaction catalysed by pyruvate dehydrogenase, the product metabolite will display zero NMR signal, since the correlation of its angular momentum is lost entirely.

3.4.5   Methods

Sample preparation and hyperpolarisation

[1,2-^{13}C$_2$]pyruvic acid (99% purum) and [1-^{13}C]pyruvic acid (95% purum) were purchased from Sigma (Sigma-Aldrich Company Ltd, Dorset, UK). Samples were prepared using 43.5 mg of pyruvic acid, 0.7 mg of trityl radical OX063 (GE Healthcare, Little Chalfont, UK) and 1.2 mg of a 1:10 gadolinium chelate solution (Gadoteric acid, Dotarem; Guerbet, Roissy, France), and were placed in a GE Healthcare DNP prototype hyperpolariser working at 3.35 T and $\sim$ 1.2 K. The frozen sample was irradiated for 1 hour with 100 mW microwaves at 93.972 GHz. The material was then dissolved using 6 mL of a superheated buffer solution ($\sim$ 180°C, $\sim$ 1 MPa) containing 100 mg/L ethylenediaminetetraacetic acid (EDTA), 30 mM NaCl, 94 mM NaOH and 40 mM 4-(2-hydroxyethyl)-1-piperazineethanesulfonic acid (HEPES) dissolved in ^{2}H$_2$O (pH 7.0).

For *in vivo* experiments, the hyperpolarisation step was carried out using a Hypersense instrument (Oxford BioTools, Oxford, UK), otherwise following the same procedure as that described above.

MRS of hyperpolarised pyruvate in ^{2}H$_2$O

To estimate the amplitudes of P and P_{singlet}, 0.4 mL of hyperpolarised material were injected into each of two identical 10 mm o.d. NMR tubes already containing 2 mL of ^{2}H$_2$O (final concentration of pyruvate in solution was $\sim$ 13.5 mM). The first tube was immediately inserted into a 9.4 T vertical wide-bore magnet (100 MHz ^{13}C, Oxford Instruments, Oxford, UK) interfaced with a Varian UnityInova spectrometer console (Varian Inc., Palo Alto, CA) and a ^{13}C-NMR spectrum acquired with a 6°-flip angle pulse. The second tube was shaken in a mu-metal chamber for $\sim$ 5 s to filter the singlet order and then inserted into the 9.4 T magnet for spectrum acquisition using the same 6°-flip angle pulse as previously. Polarisation of the sample was measured to be $\sim$ 26% at the moment of insertion into the spectrometer ($\sim$ 10 s after dissolution).

To estimate singlet relaxation time at low field, the hyperpolarised material was shaken in

the mu-metal chamber immediately after dissolution-DNP. A 3 mL portion of the shaken hyperpolarised pyruvate solution was injected into 15 mL of ^{2}H$_2$O contained in a 50 mL Falcon tube, giving a final pyruvate concentration of $\sim$ 13.5 mM. Aliquots (3 mL) of the solution were added to six 10 mm o.d. NMR tubes. The tubes were then inserted sequentially into the 9.4 T magnet at 30 s intervals, when a 6°-flip angle ^{13}C NMR spectrum was acquired.

The measurement of T_1 at low field was performed using a field-cycling setup, in which the sample was thermally polarised in the high-field spectrometer, shuttled outside the magnet to an $\sim$ 1 mT magnetic field for a resting time and then reinserted into the spectrometer magnet for signal acquisition. Spectra were acquired with a 90° pulse for different resting times at low field, and peak integrals were fit to a mono-exponential decay function.

MRS of hyperpolarised pyruvate in whole blood

Immediately after dissolution, 2 mL of the hyperpolarised pyruvate solution were injected into 10 mL of whole human blood contained in a 50 mL Falcon tube, giving a final pyruvate concentration of $\sim$ 13.5 mM. An optional step of oxygenating the blood was performed prior to this mixing by passing O$_2$ gas through the void space of the Falcon tube whilst gently swirling to encourage the gas to dissolve. Oxygen was flushed for approximately 2.5 minutes, until no further change in the colour of the blood was observed (Figure 3.6a). The sigmoid oxygen-binding curve for haemoglobin indicates that once oxygen has bound to one site in haemoglobin, it is more likely that the other sites will be occupied subsequently (Figure 3.6b) (Berg *et al.*, 2007).
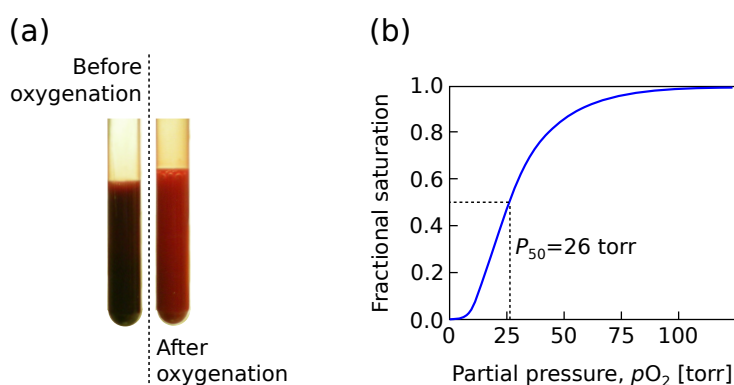
Figure 3.6: (a) NMR tubes filled with whole human blood before and after oxygenation (see text). (b) Oxygen-binding curve for haemoglobin in red blood cells (adapted from Berg *et al.* (2007)). The fractional saturation is the fraction of possible binding sites that contain oxygen.

For measurement of T_1 and T_S at low field, 3 mL aliquots of the blood-pyruvate solution were transferred into three 10 mm o.d. NMR tubes. These were placed to rest in a water bath at 37°C in the laboratory field (~ 1 mT). At intervals of approximately 20 s the tubes were inserted sequentially into the 9.4 T spectrometer magnet. Spectra were acquired using a ^{13}C flip angle of 6° with the probe maintained at 37°C. T_S^{LF} and T_1^{LF} were determined by fitting to the sum and difference of the spectrum integrals, as outlined below (Section 3.4.5).

To measure T_1^{HF}, a 0.5 mL aliquot of the dissolved pyruvate sample was injected via a transfer line into a tube containing 2.5 mL blood inside the 9.4 T magnet (resulting in a 3 mL sample volume with the same final pyruvate concentration, 13.5 mM, as the low-field experiments). Polarisation decay was determined by measuring 6°-flip angle spectra at intervals of 1 s and fitting an exponential to the spectrum integrals.

The ^{13}C nuclear polarisation was determined by comparing the hyperpolarised NMR signals with a spectrum of one of the tubes after complete decay of the hyperpolarisation. This thermal equilibrium spectrum was acquired using a 6°-flip angle pulse, and 128 transients with a repetition time of 60 s. The polarisation was estimated to be approximately $\sim 20\%$ at the time of injection, approximately 10 s after dissolution.

MRS of hyperpolarised pyruvate in BSA solutions

Hyperpolarised [1,2-^{13}C$_2$]pyruvate was added to phosphate-buffered saline (PBS) solutions containing 0%, 1%, 2%, 3% or 5% (w/v) bovine serum albumin (BSA) to give a final pyruvate concentration of 13.5 mM. The pH of each BSA solution was 7.0 ± 0.1 after addition of the hyperpolarised pyruvate. Aliquots (2.5 mL) of each BSA solution were added to five 10 mm o.d. NMR tubes and maintained at 37°C. The tubes were then inserted sequentially into the 9.4 T magnet at 30 s intervals to measure T_1^{LF} and T_S^{LF}. For each tube, fourteen 6°-flip angle ^{13}C spectra were acquired at intervals of 1 s, with the tubes maintained at 37°C, to measure T_1^{HF}.

Measurements of the stray field of the 9.4 T and the 7.0 T magnets

The magnetic field at the locations where the hyperpolarised samples were stored was measured using a transverse Hall probe in combination with a hand-held gaussmeter (HIRST GM04, Magnetic Instruments Ltd, UK).

Cell culture and tumour implantation

EL-4 murine lymphoma cells were grown to a density of circa 5×10^7 cells/mL in RPMI 1640 medium supplemented with 10% (v/v) foetal-calf serum and 2 mM glutamine.

C57/Blk6 female mice (6 - 8 weeks old) were injected subcutaneously with 100 μL of a suspension of 5×10^6 EL-4 cells in the left flank and tumours were allowed to grow for 11 days, by which time they were ~ 2 cm^3 in volume. Tumour development and mouse well being were assessed by regular measurements of tumour size and by visual inspection respectively. All experiments were performed under the Animals (Scientific Procedures) Act of 1986 and were approved by local ethical review committees.

Preparation and performance of *in vivo* experiments were carried out at the Cambridge Institute, Cancer Research UK, with assistance from Eva M. Serrao and Dr. Tiago B. Rodrigues.

Nuclear magnetic resonance spectroscopy *in vivo*

Animals were anaesthetized prior to NMR experiments by administration of a mixture containing O$_2$ in medical air (25%/75% v/v at 2 L/min) plus 3% isoflurane (Isoflo, Abbotts Laboratories Ltd) and subsequently 1-2% isoflurane in O$_2$/medical air. They were then placed in a temperature-regulated, dual-tuned ^{13}C/^{1}H volume coil, for ^{13}C transmit and for ^{1}H transmit and receive and a 20 mm diameter surface coil for ^{13}C receive only (Rapid Biomedical, Germany). The core body temperature of the animal was maintained at $\sim 37^\circ$C. The surface coil was placed immediately over the tumour so that it detected signal that was principally from the tumour. Respiratory rate and body temperature were monitored using a Biotrig physiological monitor (Small Animal Instruments, Stony Brook, NY). A cannula was inserted into a tail vein and its patency maintained through the use of heparin diluted in sterile saline (100 U/mL).

The hyperpolarised [1,2-^{13}C$_2$]pyruvate solution (0.2 mL, approx. 80 mM) was injected intravenously over a period of 3-5 s in a low magnetic field of approximately 40 mT. After injection, the mouse and probe assembly were rapidly shuttled into a 7 T horizontal bore magnet (Varian, Palo Alto, CA) for signal acquisition. Spectra were acquired using a non-slice-selective excitation pulse (600 μs sinc-pulse with a nominal bandwidth of 10 kHz) with a flip angle of 10°. A maximum of two injections were given to each mouse.

As a diagnostic of singlet order, in one experiment an animal was injected with singlet-filtered hyperpolarised [1,2-^{13}C$_2$]pyruvate. After dissolution, the pyruvate solution was shaken inside a mu-metal cylinder for approximately 5 s, in order to destroy the longitudinal magnetisation. The

solution was then injected (~ 25 s after dissolution) and spectra acquired as described above.

Data analysis

Data were processed using *Mathematica* (Wolfram Inc, Champaign, IL, USA). NMR signals were zero filled from 6k to 16k (blood) or from 1k to 8k data points (*in vivo*), Fourier transformed and the baselines corrected. The relaxation time constants were estimated by fitting mono-exponential decay curves to the peak integrals:

- For [1-^{13}C]pyruvate, the value of T_1^{HF} refers to the longitudinal decay constant at 9.4 T, while T_1^{LF} corresponds to the decay constant at 1 mT. For measurements at low field multiple samples were maintained at low field for varying periods of time before being inserted into the 9.4 T magnet for measurement.

- For [1,2-^{13}C$_2$]pyruvate, the C1 and the C2 doublets in the first spectrum from each tube were integrated separately and the areas processed according to the sum and difference method (Figure 3.2b). The sum gives the longitudinal magnetisation while the difference gives the singlet order. These values for longitudinal magnetisation and singlet order from successive tubes were fitted to obtain T_1^{LF} and T_S, respectively. Additional estimates of T_1^{LF} and T_S were obtained from the integrals from the second and subsequent spectra from each tube, until the magnetisation had decayed, and these values were then averaged. However, the values quoted are the averages from the specified number of independent experiments. For experiments at high field the integrals of the C1 and C2 doublets were fitted to an exponential decay function to obtain T_1^{HF} for each site. Quoted errors are the standard errors on the mean.

3.4.6 Results

Polarisation, T_S and T_1 of pyruvate in ^{2}H$_2$O at 1 mT and 9.4 T

The longitudinal polarisation was measured to be $P = (26 \pm 1)\%$ at 15 s after dissolution by comparing the integral of the first spectrum of the first tube with the integral of the spectrum of the same sample at thermal equilibrium. Assuming no relaxation losses during transport, Eq. (3.12) gives a predicted singlet polarisation, P_{singlet}, of $\sim 2.3\%$. The singlet order polarisation was measured to be $P_{\text{singlet}} \approx 1.4\%$ at 30 s after dissolution (15 s after the insertion of the first tube).

The relaxation time constants of [1,2-^{13}C$_2$]pyruvate in ^{2}H$_2$O buffer (pH = 7) at 25°C in a low magnetic field strength of $\sim$ 1 mT were measured to be $T_1^{LF} = (36 \pm 1)$ s and $T_S^{LF} = (70 \pm 2)$ s for both C1 and C2. The longitudinal relaxation time constants at 9.4 T were different for each carbon site: $T_1^{HF} = (65.7 \pm 0.3)$ s for C1 and $T_1^{HF} = (40.9 \pm 0.2)$ s for C2.

T_S and T_1 of pyruvate in whole blood at 1 mT and 9.4 T

Figure 3.7a shows an NMR spectrum acquired immediately after addition of hyperpolarised [1,2-^{13}C$_2$]pyruvate to an NMR tube containing oxygenated human blood at 37°C that was already in the 9.4 T spectrometer magnet, the sample being injected via a transfer line. This spectrum comprises two asymmetric doublets, indicating the presence of both hyperpolarised longitudinal magnetisation and singlet order in a ratio of I$_O$: I$_S$ of 16 : 1, with $P \approx 20\%$ and $P_{\text{singlet}} \approx 1.3\%$.

The spectrum shown in Figure 3.7b resulted from addition of hyperpolarised pyruvate to blood with the sample being kept in a low field (1 mT) for 16 s prior to signal acquisition. In this case, the multiplet pattern consists of only the antiphase outer peaks, and indicates that only singlet-derived spin order was present at the time of signal acquisition. This was evidence that the singlet order decayed more slowly relative to the longitudinal magnetisation, i.e. the singlet was 'long-lived', at low field. The data obtained in all the experiments with oxygenated and deoxygenated blood suggested that, at $\sim$ 1 mT, T_1^{LF} was < 5 s (after $\sim$ 20 s only singlet order was detected in the spectra). However, the time interval at which the tubes could be inserted into the acquisition magnet was 15-20 s, so accurate quantification was not possible. The longer lifetime of the singlet order, T_S, was estimated to be $\sim$ 19 s, and no differences in the fitted relaxation times between oxygenated and deoxygenated blood were observed.

The fitted time constants T_1 and T_S for [1-^{13}C]pyruvate and [1,2-^{13}C$_2$]pyruvate in whole human blood are summarised in Table 3. At 9.4 T the values of T_1^{HF} for C1 and C2 in [1,2-^{13}C$_2$]pyruvate were both shorter than those measured for [1-^{13}C]pyruvate. For both isotopologues the ^{13}C T_1^{LF} values at 1 mT were almost an order of magnitude shorter than the respective values of T_1^{HF}. The T_S for [1,2-^{13}C$_2$]pyruvate at 1 mT was approximately 4 times longer than T_1^{LF} of the same system. However, T_S at low field was half T_1^{HF} measured at 9.4 T. Oxygenating the blood had no apparent effect on the measured relaxation times.
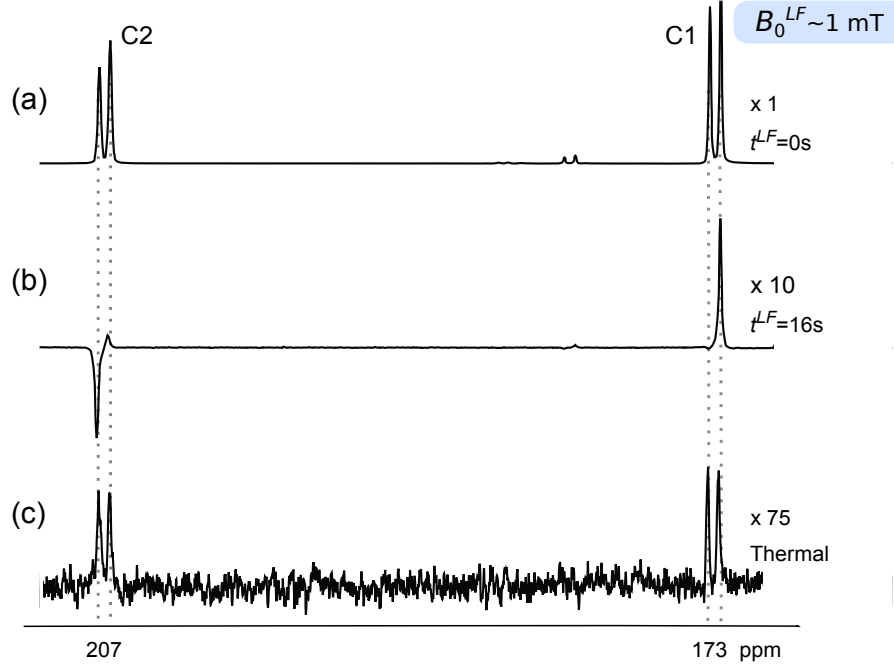
Figure 3.7: ^{13}C-NMR spectra of 13.5 mM hyperpolarised [1,2-^{13}C$_2$]pyruvate in oxygenated, whole human blood (a) immediately after injection (1 scan) and (b) after injection and then storage of the sample at 1 mT for 16 s (1 scan); (c) the same sample at thermal equilibrium (128 scans, T_R=1 s). Spectra were acquired at 9.4 T and 37°C using a 6°-flip angle pulse. Pyruvate hydrate (C1 peak) can be observed at 181 ppm.

	T_1^{LF} [s] at 1 mT	T_S [s] at 1 mT	T_1^{HF} [s] at 9.4 T
[1,2-^{13}C$_2$]pyruvate (non-oxygenated, $n = 3$)	< 5	17 ± 2	(C1) 38.5 ± 0.4 (C2) 30.0 ± 0.2
[1,2-^{13}C$_2$]pyruvate (oxygenated, $n = 4$)	< 5	19 ± 2	(C1) 38.3 ± 0.5 (C2) 30.6 ± 0.3
[1-^{13}C]pyruvate (non-oxygenated, $n = 2$)	8 ± 1	N.A.	45.0 ± 0.5
[1-^{13}C]pyruvate (oxygenated, $n = 2$)	9 ± 2	N.A.	40 ± 2

Table 3.3: ^{13}C relaxation time constants of hyperpolarised [1,2-^{13}C$_2$]pyruvate and [1-^{13}C]pyruvate in whole human blood at 37°C. n is the number of times the measurement was repeated and accounts for the errors quoted.

Experiments in BSA solutions at 1 mT and 9.4 T

The relaxation behaviour of [1,2-^{13}C$_2$]pyruvate in whole blood may be explained by interaction of pyruvate with serum proteins. To investigate this, relaxation time constants for [1,2-^{13}C$_2$]pyruvate in aqueous PBS solutions containing 0, 1, 2, 3 and 5% (w/v) BSA were measured (Table 4) (human blood contains between 3.5 and 5% serum albumin). The decay of the signal in BSA was slower than in blood, and T_1^{HF} could be measured in the same experiment as T_1^{LF} by acquiring 14 spectra at 9.4 T from the same tube with a flip angle of 6° and a repetition time of 1 s. The data show significant shortening of T_1^{LF} at 1% BSA ($\sim$ 50% of T_1^{LF} without BSA), with further decreases at 2, 3 and 5% BSA (at 5% BSA T_1^{LF} was $\sim$ 30% of that at 0% BSA), whereas at high field T_1^{HF} was largely independent of BSA concentration between 0 and 5%. Albeit less dramatic, T_S also decreased as the protein concentration increased. At 5% BSA T_S was $\sim$ 2 times T_1^{LF} and almost as long as T_1^{HF} of the C2 carbon, although still only $\sim$ 60% of T_1^{HF} of the C1 carbon. The change in the inverse relaxation time constants, or relaxation rates ($k_1^{LF} = 1/T_1^{LF}$), with BSA concentration are shown in Figure 3.8. An approximately linear increase of the longitudinal relaxation rates with BSA concentration was observed. Importantly, $1/T_1^{LF}$ increased faster than the singlet relaxation rate, $1/T_S$, demonstrating that the singlet order is less sensitive to relaxation induced by BSA than the longitudinal magnetisation.

Singlet MRS in tumours

Figure 3.9 shows a set of spectra obtained *in vivo* from a murine tumour model following tail vein injection of hyperpolarised [1,2-^{13}C$_2$]pyruvate, where the mice were maintained at $\sim$ 40 mT for different periods of time. The spectra were similar to those observed in blood (Figure 3.7), although an additional feature was the appearance of peaks corresponding to [1,2-^{13}C$_2$]lactate due to metabolism of [1,2-^{13}C$_2$]pyruvate. In the spectrum acquired from the mouse immediately after the injection of [1,2-^{13}C$_2$]pyruvate ($\sim$ 18 s after dissolution; $t^{LF} \sim$ 0 s on Figure 3.9a), singlet order was evident in the asymmetry of the doublets from the pyruvate C1 and C2 carbons. The pyruvate was injected while the animal was outside the magnet and it was then shuttled rapidly into the magnet. The asymmetry in the pyruvate C1 and C2 carbons was also observed in the C1 carbon of lactate at 183 ppm and the C1 carbon of pyruvate hydrate at 181 ppm (Figure 3.9a). The experiment was repeated in the same mouse 1 hour later, except that the animal was maintained at low field for $\sim$ 7 s after injection (Figure 3.9b, $t^{LF} \sim$ 7 s). The resulting pyruvate spectrum from the tumour showed pure singlet order (Figure 3.9b). This indicated that

		0% BSA	1% BSA	2% BSA	3%BSA	5% BSA
T_1^{LF} [s] at 1 mT		43.3 ± 0.6	20.4 ± 0.2	17.3 ± 0.3	14.9 ± 0.4	13 ± 1
T_S [s] at 1 mT		50 ± 3	34 ± 1	28.8 ± 0.5	27 ± 1	26 ± 1
T_1^{HF} [s] at 9.4 T	C1	46.0 ± 0.5	44 ± 4	42 ± 2	40 ± 1	40 ± 1
	C2	32 ± 1	33.5 ± 0.3	36.9 ± 0.4	34 ± 2	30 ± 4

Table 3.4: Relaxation time constants for ^{13}C in hyperpolarised [1,2-^{13}C$_2$]pyruvate at different concentrations of BSA in PBS at pH=7 and 37°C (n=2).
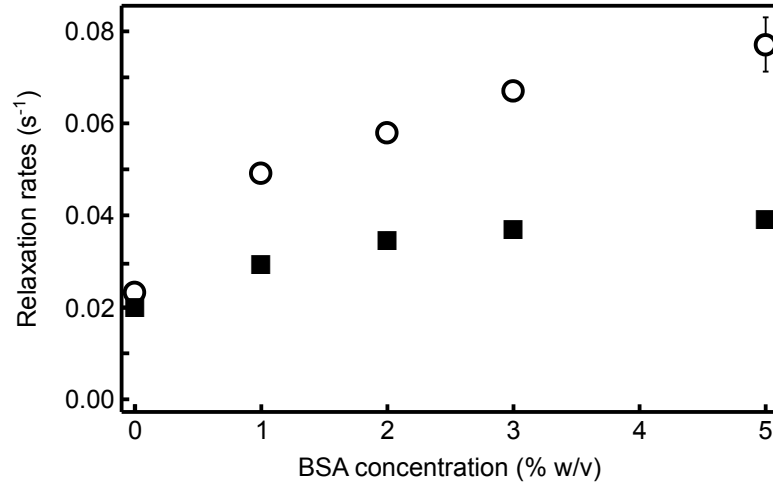
Figure 3.8: Dependence of relaxation rates $R_1^{LF} = 1/T_1^{LF}$ (open circle) and $R_S = 1/T_S$ (black square) on the concentration of BSA in aqueous solution (data from Table 3.4).
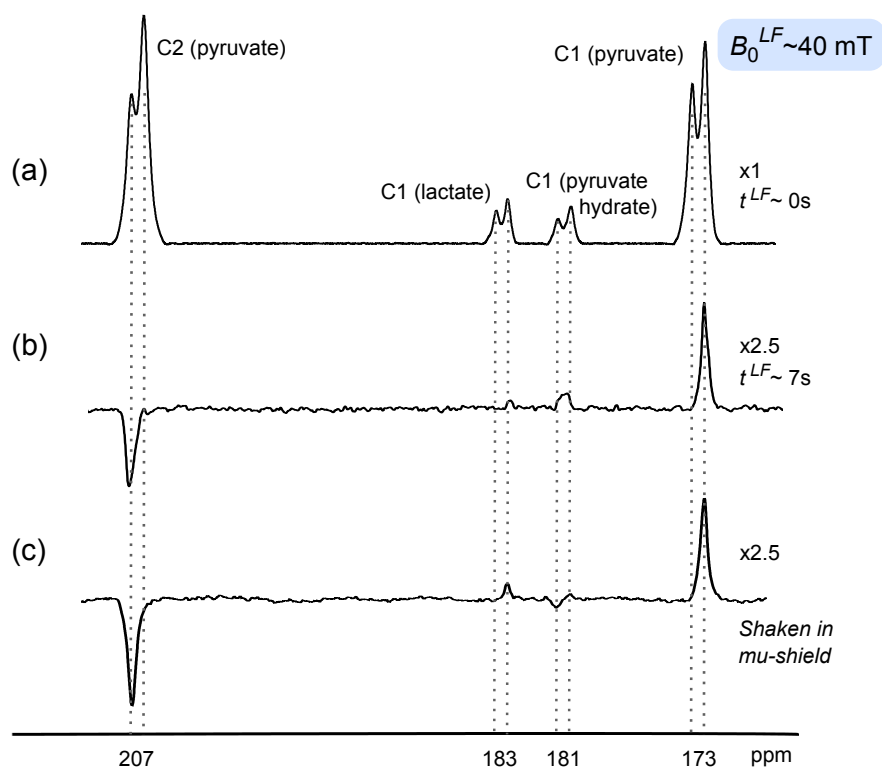
Figure 3.9: ^{13}C-NMR spectra from a mouse tumour *in vivo* at 7.0 T following i.v. injection of hyperpolarised [1,2-^{13}C$_2$]pyruvate. (a) Acquired immediately following injection (18 s after dissolution), (b) after maintaining the animal after injection for 7 s at $\sim$ 40 mT, and (c) following injection of hyperpolarised pyruvate prepared with negative singlet order (30 s after dissolution; the longitudinal magnetisation of the hyperpolarised [1,2-^{13}C$_2$]pyruvate sample was destroyed by shaking the hyperpolarised substrate in a mu-metal chamber immediately after dissolution). In all three experiments the spectra were acquired with a single scan.

the longitudinal magnetisation relaxed much faster at low field than the singlet order and was consistent with the data obtained in whole blood and in BSA solutions at low field. A spectrum acquired after injection of hyperpolarised [1,2-^{13}C$_2$]pyruvate, in which longitudinal magnetisation had been destroyed by shaking the sample of hyperpolarised [1,2-^{13}C$_2$]pyruvate inside a mu-metal chamber prior to injection, again only showed signal from the negative singlet order in pyruvate (Figure 3.9c). In this case the pyruvate was injected 30 s after dissolution.

3.4.7 Discussion

By boosting the polarisation of a pair of coupled spin-1/2 nuclei using DNP, the hyperpolarised signal displays negative singlet order without further manipulation of the spin system.

Peak asymmetry and polarisation

The peak asymmetry arising from the spectrum of a coupled spin-pair has been used previously as a method of estimating longitudinal nuclear polarisation (Hurd *et al.*, 2009, Lau *et al.*, 2013, Tropp, 2010). An asymmetry factor, a, is defined as the relative difference in integrals between the inner and outer peaks of each J-doublet. For instance, for the two carbons of $[1,2\text{-}^{13}C_2]$pyruvate,

$$a_{C1} = \frac{I_{C1}^{inner} - I_{C1}^{outer}}{I_{C1}^{inner} + I_{C1}^{outer}}, \tag{3.19}$$

$$a_{C2} = \frac{I_{C2}^{inner} - I_{C2}^{outer}}{I_{C2}^{inner} + I_{C2}^{outer}}. \tag{3.20}$$

Disregarding relaxation at low field, these asymmetry factors are linearly proportional to the polarisation, P, of the coupled spins and depend on the radiofrequency flip angle, θ_{rf}, used to acquire the spectrum:

$$a_{C1}^{I_O} = -P_2 \cos(\theta_{rf}), \tag{3.21}$$

$$a_{C2}^{I_O} = P_1 \cos(\theta_{rf}). \tag{3.22}$$

However, if the sample is transported through a low field, estimation of the polarisation using the peak asymmetry is problematic considering the variation of T_1 and T_S with magnetic field strength observed in this chapter. The slower relaxing singlet order may distort the asymmetry of the peaks measured at the moment of detection. The asymmetry factors arising from pure singlet order, in which the triplet states are equilibrated, depend only on θ_{rf}:

$$a_{C1}^{I_S} = -\cos(\theta_{rf}), \tag{3.23}$$

$$a_{C2}^{I_S} = \cos(\theta_{rf}). \tag{3.24}$$

Provided the sample remains at low field, where the triplet-singlet are the eigenstates of the spin system, for an interval of time that is shorter than $\sim 4 \times T_1^{LF}$, a spectrum acquired immediately upon insertion into the high field will contain contribution from both longitudinal magnetisation

and singlet order (Figure 3.2b). The asymmetry factors should then account for the percentage of spin order contributing to the NMR signal,

$$a_{C1}(0) = ja_{C1}^{I_O} + ka_{C1}^{I_S} = -(jP_2(0) + k)\cos(\theta_{rf}), \tag{3.25}$$

$$a_{C2}(0) = ja_{C2}^{I_O} + ka_{C2}^{I_S} = (jP_1(0) + k)\cos(\theta_{rf}), \tag{3.26}$$

with j being the fraction of triplet order, and k the percentage of singlet order, expressed in terms of I$_O$ and I$_S$ [Eqs (3.13) and (3.14)]:

$$j = \frac{I_O}{I_O + I_S}, \tag{3.27}$$

$$k = \frac{I_S}{I_O + I_S}, \tag{3.28}$$

which will vary with the time the sample spends at the low field [Eqs (3.15) and (3.16)].

Once at the high field of the spectrometer, the polarisation of each carbon site decays mono-exponentially with the corresponding T_1^{HF} for that nuclear site [e.g. P_1 decays with T_1^{C1} (Figure 3.4)]. The asymmetry factor of each carbon site also decays mono-exponentially but with the T_1^{HF} of the coupled nuclear site:

$$a_{C1}(t) = a_{C1}(0)e^{-t/T_1^{C2}}, \tag{3.29}$$

$$a_{C2}(t) = a_{C2}(0)e^{-t/T_1^{C1}}, \tag{3.30}$$

with $a_{C1(2)}(0)$ being the asymmetry factor at the moment of insertion into the spectrometer given by Eqs (3.25) and (3.26). The relationship between $P_{1(2)}$ and $a_{C2(1)}$ at high field is a linear function independent of T_1^{HF} (Figure 3.10):

$$P_2 = a_{C1}\frac{P_2(0)}{a_{C1}(0)}, \tag{3.31}$$

$$P_1 = a_{C2}\frac{P_1(0)}{a_{C2}(0)}, \tag{3.32}$$

Lau *et al.* (2013) presented an empirical relationship between the asymmetry factors and the polarisation of the spin pair at high field. Keeping the delay at low field constant, the I$_O$ and I$_S$ contributions to the spectra at the moment of insertion into the magnet were the same in all the experiments. They showed a linear correlation between P and a_C (for P between 1 and 20%) using a direct measurement of the pyruvate ^{13}C polarisation involving comparison with the NMR
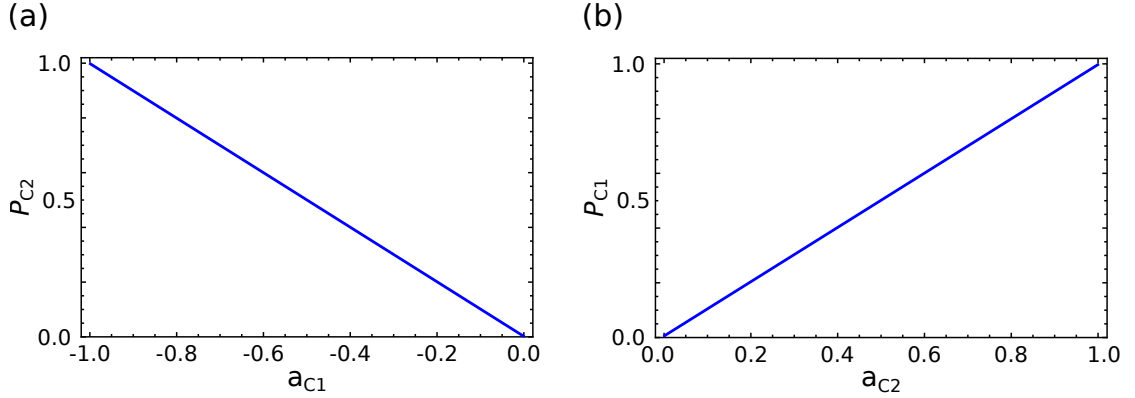
Figure 3.10: Polarisation vs asymmetry factors as defined in (a) Eqs (3.31) and (b) (3.32). The parameters used for these calculations were $P_{1(2)}(0) = 100\%$, $a_{C1}(0) = -1$ and $a_{C2}(0) = 1$.

signals of urea. They observed experimentally that the J-doublets evolve giving rise to asymmetry factors with opposite sign to those predicted by the theory of weakly coupled spin systems shown here, although no theoretical explanation has yet been found. This effect is commonly observed for pyruvate dissolved in blood, whilst less so in aqueous solvents *in vitro*. To ensure the correct measurement, the polarisation values given in our experiments were calculated comparing the sum signal intensity of each doublet with that of its thermal signal [Eq. (1.21)].

Singlet-triplet polarisation

Using a sample of [1,2-^{13}C$_2$]pyruvate in ^{2}H$_2$O buffer polarised to 26% the predicted singlet polarisation was 2.3%. This was observed in the peak asymmetry between the doublets of the first spectrum of the first tube that showed evidence of conversion of longitudinal magnetisation to singlet order in a ratio $I_O : I_S$ of 12 : 1. The signal measured after filtration of singlet order displayed the spectral pattern characteristic of pure singlet order, confirming absence of longitudinal polarisation after being shaken in the mu-shield. The singlet polarisation measured in the second tube was 1.4%. This agrees with the expected result when accounting for decay of the singlet order polarisation at low field during the additional 15 s that the sample remained at 1 mT before being inserted into the spectrometer. The longitudinal polarisation was measured to be $P = 17\%$ at 15 s after dissolution ($P = 26\%$ at the time of dissolution) and $T_S^{LF} = 70$ s, therefore one can calculate that P_{singlet} should be $\sim 1.4\%$ at 30 s after dissolution.

Relaxation of pyruvate in blood and BSA solutions

The change in T_1 between high and low fields may be caused by the dynamics involved in pyruvate binding to blood proteins. To investigate this, the effect of different BSA concentrations on T_1^{LF} and T_S of [1,2-^{13}C$_2$]pyruvate was measured. BSA has almost identical effects to oxyhaemoglobin on the proton T_1 of water (Janick *et al.*, 1991), and for the range of BSA concentrations studied here, the changes in T_1 cannot be attributed to a viscosity effect (Endre and Kuchel, 1986). Similar to the results presented by Pullinger *et al.* (Pullinger *et al.*, 2011) on the T_1 relaxation time of hyperpolarised [1-^{13}C]pyruvate in BSA, we found that at low field (~ 1 mT) T_1^{LF}, and also T_S, decreased markedly in a 1% BSA solution; increasing the BSA concentration further had only modest effects (Table 3.4). A 1% BSA solution corresponds to a protein concentration of ~ 0.2 mM. The smaller decrease in T_1^{LF} and T_S at higher BSA concentrations may reflect partial saturation of the binding sites for pyruvate. At high field (9.4 T) the T_1^{HF} for [1,2-^{13}C$_2$]pyruvate was largely independent of BSA concentration (Table 3.4). Moreno *et al.* reported that at 14.1 T, the T_1^{HF} of [1-^{13}C]pyruvate decreased with increasing BSA concentration, finding T_1s much shorter than those we measured at 9.4 T (Moreno *et al.*, 2010). The discrepancy with what we observed here for [1,2-^{13}C$_2$]pyruvate might be explained by a greater contribution of chemical shift anisotropy to T_1^{HF} at 14.1 T.

T_1^{LF} for [1,2-^{13}C$_2$]pyruvate in 5% BSA was $\sim 2.5 \times$ longer than the T_1^{LF} in whole blood (which contains human serum albumin), whereas T_S was only $\sim 1.3 \times$ longer. The faster T_1^{LF} relaxation in blood may reflect the presence of paramagnetic species (Mieville *et al.*, 2011). However, it appears from our experiments that such an effect cannot be attributed to the presence of deoxyhaemoglobin since the use of partially deoxygenated blood had no significant effect on the measured values of T_1^{LF}, T_S or T_1^{HF}. The oxygenation level of blood and hence the ratio of oxy- to deoxyhaemoglobin, the latter being moderately paramagnetic, has been shown to cause larger changes in T_2 as compared to T_1 (Janick *et al.*, 1991, Silvennoinen *et al.*, 2003). Consistent with our observations, it has been reported previously that water proton T_1 is not affected by haemoglobin oxygenation but that it does change with magnetic field strength (Lin *et al.*, 2012).

The higher T_S/T_1^{LF} ratio measured in blood, as compared to that measured in BSA solutions, may reflect the contribution of other paramagnetic species in blood to T_1^{LF} relaxation, since these have been shown to have a weaker effect on the relaxation of singlet order (Tayler and Levitt, 2011a).

Singlet relaxation *in vivo*

Consistent with the longer values measured for T_S as compared to T_1^{LF} in whole blood and solutions of BSA at ~ 1 mT, our results also show that T_S of [1,2-^{13}C$_2$]pyruvate was longer than T_1^{LF} at ~ 40 mT in a live mouse. If hyperpolarised singlet order [1,2-^{13}C$_2$]pyruvate is injected into a subject and that subject is maintained at low magnetic field, the ^{13}C nuclei of the product of any metabolic reaction will also be expected to be in singlet order configuration, provided that the chemical bond between the two carbons is preserved and that the field is sufficiently low to satisfy the near-equivalence condition (Figure 3.1c). Our observations show that singlet order was not preserved in the product [1,2-^{13}C$_2$]lactate produced at 40 mT from the injected [1,2-^{13}C$_2$]pyruvate. From comparison with the spectral outcomes predicted in Figure 3.5a(ii), we concluded that the lactate signal arises from metabolism at high magnetic field, not low field.

The absence of NMR signals from singlet [1,2-^{13}C$_2$]lactate may be explained by the relatively large chemical shift difference between the carbon sites ($|\delta_2 - \delta_1| \sim 114$ ppm), which at 40 mT corresponds to a frequency difference of 50 Hz. This contrasts with pyruvate where $|\delta_2 - \delta_1|$ is only ~ 15 Hz at 40 mT. The 50 Hz frequency difference is not negligible when compared to the 60 Hz coupling constant, J_{C1C2}, in lactate and means that the singlet and triplet states of lactate are no longer eigenstates of the coherent Hamiltonian. The resulting evolution is an efficient mechanism for singlet leakage; such that one should expect the lifetime T_S of singlet polarised lactate to be similar to the T_1, and shorter than it may potentially be if the singlet were an eigenstate. In addition, the presence of a C2 proton in lactate introduces a strong heteronuclear coupling, as well as an asymmetric relaxation mechanism due to the large difference in the H2-C1 and H2-C2 dipole-dipole couplings, further accelerating the decay of singlet order.

Consequently, if [1,2-^{13}C$_2$]pyruvate is injected at ~ 40 mT and the mouse is maintained at this field while conversion of pyruvate to lactate occurs then singlet polarisation in pyruvate will leak through into non-singlet polarisation in lactate. Therefore, at the moment of detection an apparent reduction in the amount of lactate will be observed in the spectra (Figure 3.9b). Even if one could reduce the field at which the mouse is maintained during injection to 10 mT, the singlet-triplet states would still not be pure eigenstates of the Hamiltonian and singlet polarisation decay would still be accelerated in the lactate product.

Temporal information of reactions from singlet-derived NMR spectra

Similar reasoning can explain the observed spectral patterns for [1,2-^{13}C$_2$]pyruvate hydrate ($|\delta_2 - \delta_1| \sim 85$ ppm). The spectrum shown in Figure 3.9b is characteristic of [1,2-^{13}C$_2$]pyruvate hydrate formed at high field, which is consistent with the relatively rapid injection of [1,2-^{13}C$_2$]pyruvate into the mouse at 40 mT field and spectrum acquisition at 7 T. The spectrum shown in Figure 3.9c, on the other hand, shows signals from pyruvate hydrate formed in both low (negative peak of the doublet) and high fields (positive peak of the doublet). In this experiment the pyruvate solution was shaken in the mu-metal chamber prior to injection into the animal and transport into the 7 T magnet. During this singlet preparation time pyruvate and pyruvate hydrate may undergo chemical exchange at a low field, where the eigenstates of both molecules are in the singlet and triplet states. Thus the singlet order of pyruvate hydrate created at low field is observed when the spectrum is acquired at high field. Note that the signal from the pyruvate hydrate formed at high field in Figure 3.9c is weaker than that observed in Figure 3.9b. This may be due to the longer delay between dissolution and acquisition when the sample was shaken in the mu-metal chamber.

Adiabatic switching of radiofrequency spin-locking

The direct preparation of singlet order after dissolution DNP relies on the adiabatic correlation of the spin system's eigenstates through different regimes as the sample is moved through different magnetic field strengths. During the adiabatic field cycling from high to low magnetic field, the populations of the eigenstates of the weakly coupled regime (high field) are correlated to the eigenstates of the strongly coupled one (low field), in which the singlet may be long-lived. This correlation of states between the two regimes can also be achieved while keeping the sample inside the spectrometer by switching the radiofrequency spin-locking field adiabatically. The spin-locking field brings the pair to chemical equivalence, acting in a similar way as decreasing B_0 does, without the need for, and associated problems with, of field cycling (Figure 3.11). This method has already been used in PHIP experiments (Kiryutin *et al.*, 2013).

3.5   Boosting the singlet signal after DNP with pulse sequences

The sensitivity of the experiment described above could be improved by the use of pulse sequences that involve field cycling to increase the singlet state population.
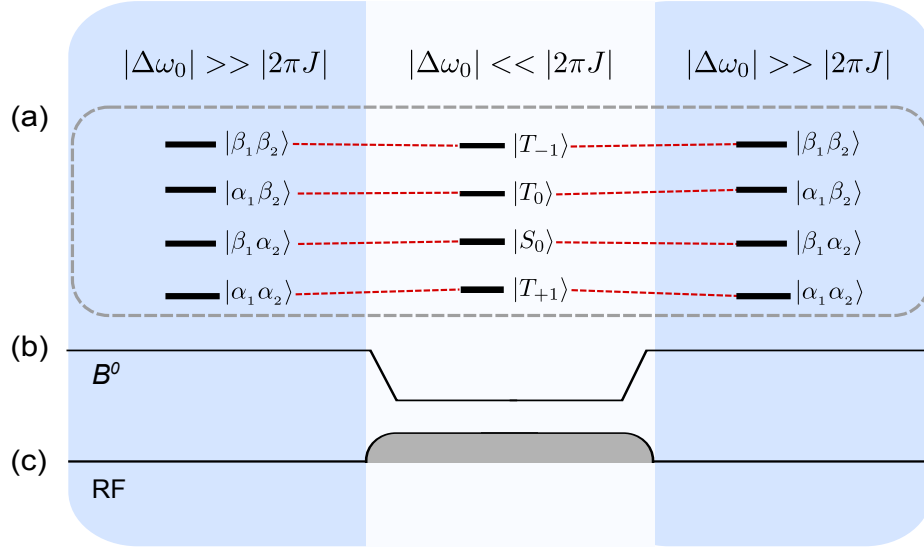
Figure 3.11: Illustration of (a) the adiabatic correlation of Zeeman to triplet-singlet eigenstates, (b) through adiabatic field cycling and (c) adiabatic switching of a radiofrequency spin-locking field.

3.5.1 Inversion method

For instance, another way of generating singlet order would be to transfer the sample to the acquisition magnet immediately after dissolution DNP and invert the doublet at 173 ppm (C1) to exchange the population between $|\alpha_1\alpha_2\rangle$ to $|\beta_1\alpha_2\rangle$ (the singlet pre-cursor) and between $|\beta_1\beta_2\rangle$ and $|\alpha_1\beta_2\rangle$, either by applying a selective 180°-pulse or the sequence $90_0 - \tau - 90_{-90}$. The advantage of the latter is that the pulses are non-selective and inversion occurs if τ is chosen so that $\tau = \pi/|\gamma B_0(\delta_2 - \delta_1)|$. Then, the sample would be shuttled to the low field where the population would be transferred adiabatically from $|\beta_1\alpha_2\rangle$ to $|S_0\rangle$. The inversion sequence $90_0 - \tau - 90_{+90}$ would invert the doublet at 209 ppm (C2), exchanging the population between $|\alpha_1\alpha_2\rangle$ to $|\alpha_1\beta_2\rangle$ and between $|\beta_1\beta_2\rangle$ and $|\beta_1\alpha_2\rangle$. This method, which I call here the inversion method, has been explained in detail for thermal equilibrium polarised samples (Carravetta *et al.*, 2004), and has been tested in dissolution DNP (Bornet *et al.*, 2011). The maximum singlet order polarisation obtained by populating the singlet pre-cursor by inverting C1, and neglecting relaxation effects, is:

$$P_{\text{singlet}}^{\text{inv}} = \frac{P(2+P)}{3}. \tag{3.33}$$

If instead C2 is inverted, the triplet pre-cursor is populated, and the singlet order polarisation is:

$$P_{\text{singlet}}^{\text{inv,neg}} = \frac{P(-2+P)}{3}. \tag{3.34}$$

$P_{\text{singlet}}^{\text{inv}}$ always gives higher singlet order polarisation than $P_{\text{singlet}}^{\text{inv,neg}}$. In the upper limit of $P = 1$, $P_{\text{singlet}}^{\text{inv}} = 1$ while $P_{\text{singlet}}^{\text{inv,neg}} = -0.3$.

The active region of the radiofrequency transmitter coil covers a defined volume, which is usually smaller than the hyperpolarised sample volume. While the sample sits at the low field, after application of the radiofrequency pulse, mixing of the excited spins and the non-excited ones would cause dilution of the excited volume V_{exc}. For example, if the active region of the coil is ~ 1 cm^3 and the sample size is ~ 3 cm^3, only $1/3$ of the population in $|\alpha_1\alpha_2\rangle$ would be transferred to the singlet pre cursor. The non-excited region of the sample, once in the low field, would find itself in the negative singlet-order configuration, as in the case of direct enhancement explained above. One could shake the sample inside the mu-shield to filter the singlet order before moving it back into the spectrometer for acquisition of NMR spectra. Taking into account the dilution effect of the excited proportion of the sample, and recalling that $P_{\text{singlet}}^{\text{direct}} = -P^2/3$ [Eq. (3.12)], the singlet order polarisation obtained with the inversion method is:

$$P^{\text{inv}} = \frac{V_{\text{exc}}}{V_{\text{tot}}} P_{\text{singlet}}^{\text{inv}} + \frac{V_{\text{tot}} - V_{\text{exc}}}{V_{\text{tot}}} P_{\text{singlet}}^{\text{direct}}, \tag{3.35}$$

$$P^{\text{inv,neg}} = \frac{V_{\text{exc}}}{V_{\text{tot}}} P_{\text{singlet}}^{\text{inv,neg}} + \frac{V_{\text{tot}} - V_{\text{exc}}}{V_{\text{tot}}} P_{\text{singlet}}^{\text{direct}}. \tag{3.36}$$

Further loss of polarisation P in the inversion method is caused by spin-lattice relaxation while the sample sits in the spectrometer (T_1^{HF}), during transport to the spectrometer and while the sample remains at low field (T_1^{LF} and T_S).

For the direct enhancement method, the polarisation is lost due to $P_{\text{singlet}}^{\text{direct}}$ relaxing with T_S during the time the pyruvate sample is at low field, but there is no loss caused by dilution.

Comparing the final singlet order polarisation achievable with the inversion method or the direct enhancement method after dissolution DNP, it seems clear that being able to populate the singlet pre-cursor would be desirable (Table 3.5). With this method the singlet order obtained can be up to $(1 + 2P^{-1})$ higher than that obtained with the direct enhancement method. However, care has to be taken in the design of the hardware to make sure that the radiofrequency pulse excites the maximum amount of sample.

V_{exc}	P^{inv} [%]	$P^{\mathrm{inv,neg}}$ [%]	$P_{\mathrm{singlet}}^{\mathrm{direct}}$ [%]
$V_{\mathrm{tot}}/3$	6	-8	-3
V_{tot}	23	-17	-3

Table 3.5: Singlet order polarisations obtained from Eqs (3.12), (3.35) and (3.36) with $P = 30\%$.

3.5.2 M2S at low field

Converting longitudinal polarisation into singlet order may also be done by applying pulse sequences at low field (Pileio *et al.*, 2010). Levitt and co-workers have explained the theory of these experiments in detail (Levitt, 2012, Pileio *et al.*, 2010). For spin pairs with a large chemical shift difference, longitudinal polarisation can be created in the high magnetic field of the spectrometer (thermal polarisation) and singlet order can be accessed by moving the sample to a low field that brings the system into near-equivalence, i.e. the chemical shift difference is now on the order of the J-coupling constant, and apply a pulse sequence that maximises the singlet population (Figure 3.12). The so-called 'Magnetisation-To-Singlet' (M2S) pulse sequence works by applying transverse audio-frequency (AF) fields at the nuclear Larmor frequency in the low-field region, when the two spins are nearly equivalent. The key element of the sequence are the spin echo trains generated by repeating a composite pulse unit $(\tau - [90_{90}240_090_{90}]_\phi - \tau)$ n and $n/2$ times, where $\tau = (4J)^{-1}$ and the phase of the composite pulse runs through a four-step cycle $\phi = \{0, 0, 180°, 180°,...\}$. The number of times n the composite pulse unit is repeated depends on the difference in frequency,

$$n = \mathrm{round} \left| \frac{\pi^2 J}{\Delta \omega_0^{LF}} \right|. \tag{3.37}$$

Retrieving the magnetisation after storage in the singlet state is achieved by applying the M2S pulse sequence in reverse chronological order, known as 'Singlet-To-Magnetisation' (S2M). Further details on how the M2S pulse sequence works will be given in Chapter 4.

This idea could be easily implemented in hyperpolarisation experiments. The only difference to the experiment described above would be the initial polarisation level, which in DNP experiments would be more than 10^4 higher. Technical challenges include having a Helmholtz coil to deliver the radiofrequency pulse sequence while keeping the sample inside a stable magnetic field in which the spins precess at a known Larmor frequency difference.
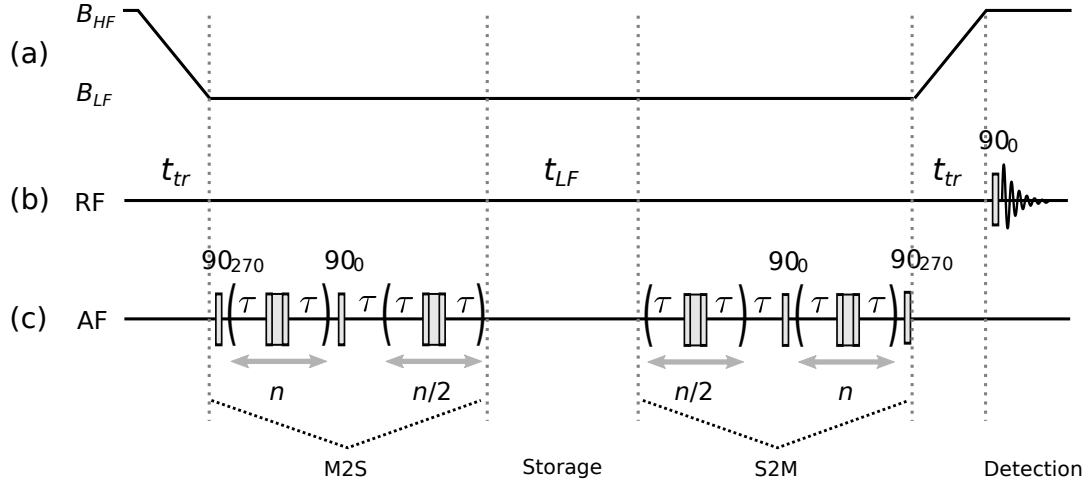
Figure 3.12: Magnetisation-To-Singlet (M2S) and Singlet-To-Magnetisation pulse sequence. (a) Change in the magnetic field experienced by the sample during the transport from the spectrometer (B_{HF}) to the low-field region (B_{LF}). (b) Sampling of the resulting magnetisation after the pulse sequence with a 90° radiofrequency (RF) pulse. t_{tr} are the transport intervals, and t_{LF} is the singlet order storage time. (c) Transverse audio-frequency (AF) fields of the M2S-S2M pulse sequence applied at the nuclear Larmor frequency in B_{LF}. The spin echo trains generated by repeating the composite pulse ($\tau - [90_{90}240_090_{90}]_\phi - \tau$) n and $n/2$ times, where $\tau = (4J)^{-1}$ and $n = \mathrm{round}(\pi^2 J/\Delta\omega_0^{LF})$. The phase of the composite pulse runs through a four-step cycle $\phi = \{0, 0, 180°, 180°,...\}$. Adapted from Pileio *et al.* (2010).

The theoretical limit for the singlet order created with any pulse sequence that converts longitudinal magnetisation into singlet order is $P\sqrt{2/3} \approx 0.82P$. This is about $(2.4P^{-1})$-fold higher than what it is obtained with the direct enhancement method.

While the singlet order obtained by the direct enhancement approach is much lower than that accessible by converting the longitudinal polarisation using a pulse sequence as shown above, the simpler preparation route used here was sufficient for the demonstrations presented in this work. However, conversion of all available spin order into singlet order, with the attendant increase in measured signal, would be an advantage in a clinical setting.

3.6   Suppressing chemical shift difference with decoupling

It has been shown above that the singlet state of $[1,2\text{-}^{13}\text{C}_2]$pyruvate may relax more slowly than the T_1s of the two carbons at a sufficiently low magnetic field, where the two carbons become magnetically equivalent. This was demonstrated with the direct enhancement of nuclear singlet order obtained after hyperpolarisation with dissolution DNP. However, this approach has limitations:

- If T_1 is faster than the time taken for dissolution there will be no significant magnetisation left to transfer into singlet order.

- Moving the [1,2-^{13}C$_2$]pyruvate sample to low field suppresses the frequency difference, but does not remove the J-coupling between ^{13}C and ^{1}H, which can break the magnetic equivalence. In addition, since ^{1}H relaxes very fast, the scalar coupling of ^{13}C with ^{1}H might induce relaxation of the carbon. This scalar relaxation of the second kind would not be avoided by replacing ^{1}H with ^{2}H.

In view of these drawbacks, Overhauser-DNP (O-DNP) and micro-NMR has advantages over dissolution-DNP. It would allow suppression of the ^{13}C chemical shift difference in the high magnetic field of the spectrometer using decoupling, which in turn would effectively remove the coupling with the protons. Moreover, it would allow for repeated hyperpolarisation and spectral acquisition from the same sample.

At higher magnetic fields one can bring the carbons into magnetic equivalence by applying a resonant decoupling field. The strength of the field required, however, is relatively large for most molecules due to the large chemical shift difference of the two carbons ($\sim$ 30 ppm for [1,2-^{13}C$_2$]pyruvate), which would require a decoupling field being of $\sim$ 40 kHz at a B_0 field of 9.4 T. On most hardware, this radiofrequency amplitude is unlikely to be feasible over a few seconds, let alone over a few times T_1. This section focuses on the use of a small radiofrequency coil and a small liquid sample of pyruvate ($\sim$ 1 μL) to measure the singlet relaxation at high field in the presence of on-resonance radiofrequency irradiation.

The experiments presented in this chapter were done in collaboration with Arno Kentgen's laboratory (Radboud University, Solid State NMR Department, Nijmegen, NL) as part of a COST Short Term Scientific Mission (TD1103).

3.6.1 Towards singlet NMR using micro-coils

Each of the following steps has to be accomplished sine qua non to lock and retrieve the singlet state of ^{13}C-pyruvate at high field:

1. Manufacture the hardware needed to perform the experiments (e.g. micro-coil and micro-NMR tubes).
2. Prepare singlet order in ^{13}C.
3. Supress the ^{13}C chemical shift difference using a radiofrequency field.
4. Reconvert to observable magnetisation and acquire a ^{13}C spectrum.

Hardware and sample preparation

The flow of current through a coil generates a magnetic field. For a solenoid of length l with N turns, current i and magnetic moment μ_0,

$$B_1 = \frac{\mu_0 N i}{l} \tag{3.38}$$

Therefore, the shorter the length of the coil, the lower the current needed to generate a certain radiofrequency field. Consequently, since power is proportional to the square of intensity, decreasing the size of the coil lowers the power required.

The micro-coil built for these experiments was 5 mm long and its inner diameter measured 1.2 mm (Figure 3.13). The coil produced a magnetic field with 75% homogeneity and delivered a spectral resolution of 15 Hz linewidth when used in a 9.4 T spectrometer magnet (Figure 3.14). An input power of 0.5 W was sufficient to create a 40 kHz radiofrequency field, whilst using a standard liquid NMR probe the power required is on the order of a kW. An amplifier that can operate in continuous mode was used.

Singlet order preparation via pulse sequence

A pulse sequence that allows preparation of the singlet state in weakly coupled spins pairs, such as [1,2-^{13}C$_2$]pyruvate ($|\omega_1 - \omega_2| \approx 2\pi \times 3.3$ kHz $>> |J_{C1C2}| \approx 60$ Hz), was introduced by Sarkar *et al.* (2007) (Figure 3.15).

The Hamiltonian of a weakly coupled spin pair is composed of the Zeeman Hamiltonian of each nucleus and the secular term of the scalar coupling (if the system is strongly coupled, $I_{x1}I_{x2}$ and $I_{y1}I_{y2}$ cannot be omitted and should also be included in the Hamiltonian):

$$H = \omega_1 I_{1z} + \omega_2 I_{2z} + 2\pi J(I_{1z} \cdot I_{2z}) \tag{3.39}$$

After the first 90°-radiofrequency pulse, which brings the magnetisation into the transverse plane, a spin echo ($|4J^{-1}| - 180° - |4J^{-1}|$) pulse sequence is applied followed by a 45°-flip angle
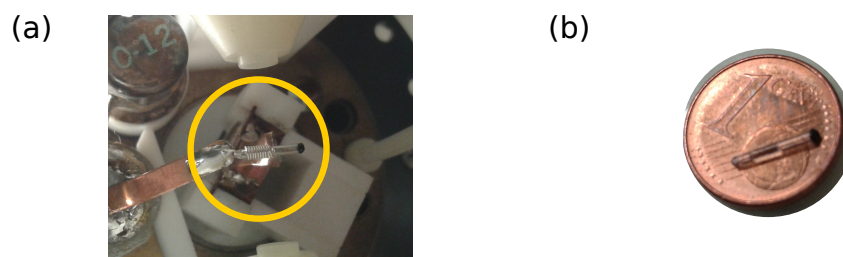
Figure 3.13: (a) Micro-coil (5 mm length and 1.2 mm inner diameter) and tube (1.2 mm outer diameter) in the probe. (b) Display of the NMR tube size used in the experiments in comparison to a coin of 16.25 mm of diameter.
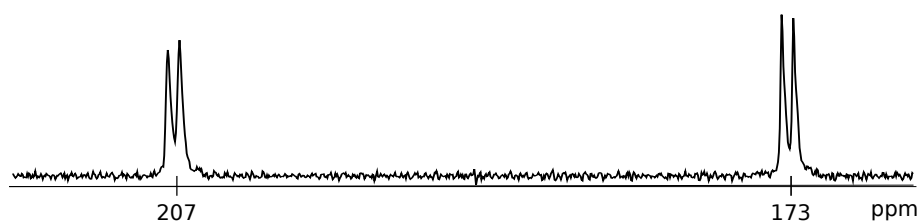
Figure 3.14: Single-scan ^{13}C-NMR pulse-acquire spectrum of neat [1,2-^{13}C$_2$]pyruvic acid acquired with the setup in Figure 3.13 (5 Hz line broadening, zero filled from 1 K to 2 K data points).
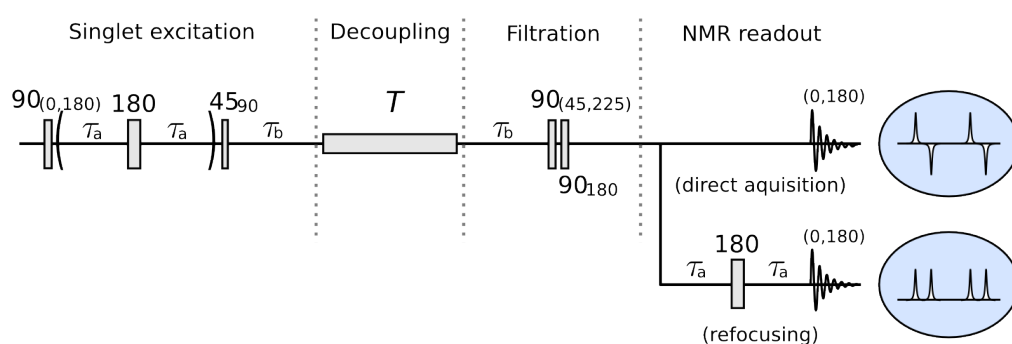
Figure 3.15: Sarkar's pulse sequence for singlet preparation. $\tau_a = |4J|^{-1}$ and $\tau_b = |2\Delta\omega_0|^{-1}$. T is the decoupling duration. The possible NMR spectral outcomes following direct acquisition or refocusing of the signal are shown at the end of each sequence.

pulse:

$$I_{1z} + I_{2z} \xrightarrow{90^\circ} I_{1y} - I_{2y}$$

$$\xrightarrow{\tau_a - 180^\circ - \tau_a} (I_{1y} + I_{2y})\cos(2\pi J\tau_a) + 2(I_{x1}I_{z2} + I_{z1}I_{x2})\sin(2\pi J\tau_a)$$

$$\xrightarrow{\tau_a = |4J|^{-1}} 2(I_{x1}I_{z2} + I_{z1}I_{x2}) \tag{3.40}$$

$$\xrightarrow{45_{90}} 2(I_{x1}I_{x2} - I_{z1}I_{z2}).$$

Then, during a final delay $|2\Delta\omega_0|^{-1}$, the sign of the operator $I_{1x}I_{2x}$ is changed, yielding

$$\text{Eq.(3.41)} \xrightarrow{\tau_b = |2\Delta\omega_0|^{-1}} -2(I_{x1}I_{x2} + I_{z1}I_{z2}), \tag{3.41}$$

which corresponds to 2/3 of the maximum achievable singlet order $(I_{1x}I_{2x} + I_{1y}I_{2y} + I_{1z}I_{2z})$.

Given the large decoupling bandwidth required to lock the singlet state ($\sim$ 3 kHz for [1,2-^{13}C$_2$]pyruvate), this sequence is very sensitive to the transmitter frequency offset and it needs to be carefully selected to be centred between the two ^{13}Cresonances of pyruvate, i.e. $\omega_{\text{tof}} = |\omega_1 - \omega_2|/2$. For pyruvate, $\tau_a \approx 4.17$ ms and $\tau_b \approx 0.150$ ms. These parameters can be optimised experimentally by modifying them around the estimated values and maximising the signal obtained with the pulse sequence.

Once the singlet state is accessed using the pulse sequence given by Sarkar *et al.* (Figure 3.15), a decoupling field that isolates the singlet state from the triplet needs to be applied. The decoupling pulse sequence known as WALTZ-16 has been shown to efficiently store singlet order at high field (Pileio and Levitt, 2009). However, since pyruvate in an aqueous solution also forms pyruvate hydrate, a more broadband decoupling sequence must be applied so that the singlet state of the pyruvate hydrate is also locked.

3.6.2   Results and discussion

The spectrum of 1 μL of a neat pyruvic acid sample (14 M) acquired with the micro-coil setup is shown in Figure 3.14. Neat [1,2-^{13}C$_2$]pyruvic acid has a very high concentration of ^{13}C and ^{1}H and is very acidic (pH = 0.3), which speeds up relaxation, yielding a $T_1 \sim 2$ s. Diluting the sample with ^{2}H$_2$O to 1 M increased the longitudinal relaxation time by a factor of 10. However, the singlet signal was short-lived, with $T_S < 2$ s. The short lifetime of the singlet state was caused by relaxation through the C2 of pyruvate hydrate, which is not efficiently decoupled.

Pyruvate hydration study

The pH and concentration of pyruvic acid in solution gives different amounts of pyruvate hydrate. Since the spin lock effectively acts on a limited spectral range, to preserve the singlet state of [1,2-^{13}C$_2$]pyruvate at high field (C1 peak at 171 ppm and C2 at 207 ppm), reducing the amount of pyruvate hydrate (C2 peak at 181 ppm and C1 peak at 93 ppm) in the solution is required in order to avoid relaxation via the ^{13}C$_2$ singlet state of the pyruvate hydrate, which is not spin locked. This could be achieved by diluting pyruvate in acetone or chloroform. However, we wanted to use a physiological solution.

It is well understood that the hydration and dehydration reactions of pyruvic acid are hydrogen ion-catalysed (Figure 3.16), and that the amount of pyruvate hydrate formation increases with the concentration of water in the solution (Griffiths and Socrates, 1967). Several studies have been reported on the products of pyruvic acid dissolved in an acidic or neutral solution (Griffiths and Socrates, 1967, Hellstrom and Almqvist, 1970, Margolis and Coxon, 1986, Meany, 2007, Pocker *et al.*, 1969), but little has been reported in basic solutions.

Here we studied aqueous solutions with different pyruvate concentrations and pHs (from acidic to basic) to find the optimal values that would minimise pyruvate hydrate formation: ^{13}C natural abundance pyruvic acid (Sigma-Aldrich Company Ltd, Dorset, UK) was diluted with an aqueous solution (9/1 v/v H$_2$O/^{2}H$_2$O) to different pyruvate concentrations (2 M, 1 M, 0.5 M and 0.05 M) and pHs (1.5, 4.5, 7.5, 13.5). The pH of the solutions was adjusted with KOH in water. For each sample, ^{1}H-NMR spectra were acquired at 300 K in a vertical bore 11.0 T magnet (500 MHz proton frequency, Bruker Avance II+, Bruker Corporation, Billerica, MA) using a 5 mm probe and acquiring the spectra with 128 scans, 30°-flip angle, $T_R = 2$ s and SW = 6000 Hz.

The ^{1}H-NMR spectrum of a solution of pyruvic acid shows the pyruvate and the pyruvate hydrate peaks at around 2.3 ppm and 1.4 ppm, respectively (Figure 3.17). The hydrate has a smaller chemical shift because the loss of diamagnetic anisotropy of the carbonyl group in the pyruvate hydrate increasing the screening of the methyl protons (Griffiths and Socrates, 1967).

$$CH_2=C(OH)CO_2^- \xrightleftharpoons{\qquad} CH_3COCO_2^- \underset{- H_2O}{\overset{+ H_2O}{\xrightleftharpoons{\qquad}}} CH_3C(OH)_2CO_2^-$$

enol   keto   hydrate
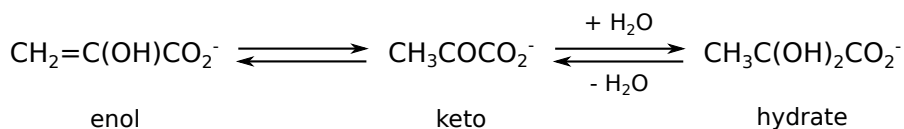
Figure 3.16: Equilibrium between pyruvate and pyruvate hydrate. Adapted from Meany (2007).

Pyruvic acid is unstable in solution at temperatures above $-20°$ C (Margolis and Coxon, 1986), giving rise to derivatives of the acid. In addition to pyruvic acid, pyruvate and hydrate forms, hemihydrates may be formed in concentrated or acidic solutions (Hellstrom and Almqvist, 1970). Furthermore, in strongly acidic or basic solutions aldol consensation occurs (Margolis and Coxon, 1986), resulting in additional peaks being seen in the NMR spectrum (Figure 3.17).

As reported by Hellstrom and Almqvist (1970), a change of pH perturbs the chemical shifts of both species. Figure 3.18 shows the effect of pH and initial pyruvic acid concentration on the difference of chemical shifts between pyruvate and the hydrate form. While the difference in chemical shifts remains almost unaffected against pyruvate concentration, at pH < 7 the difference decreases as the pH becomes more acidic. Therefore, one could conclude that the change in chemical shifts is mainly a pH effect.

The study of the ratio between the area under the methyl group peaks of pyruvate hydrate and pyruvate, denoted here K, indicated that for basic solutions K increases with higher initial pyruvic acid concentrations. K reached a minimum of 0.05 - 0.010 at pHs between 4 and 7 (Figure 3.19). However, pyruvate hydrate was always present and never disappeared completely. These results agree with those presented by Pocker *et al.* (1969).

3.7   Summary

In this chapter I have presented three ways of accessing the singlet state of a weakly coupled spin-pair, with their application in preserving the hyperpolarisation of [1,2-^{13}C$_2$]pyruvate in mind:

- Direct enhancement of nuclear singlet order at low field after dissolution DNP

- Longitudinal magnetisation to singlet order pulse sequences to boost the singlet signal after dissolution-DNP

- Suppressing chemical shift difference with decoupling at high field

Using the direct enhancement of nuclear singlet order after dissolution DNP method, we showed that singlet order in hyperpolarised [1,2-^{13}C$_2$]pyruvate was longer-lived than the longitudinal magnetisation at low field, in ^{2}H$_2$O buffer, in BSA solution, in whole human blood *in vitro* and in a mouse *in vivo*. However, the benefit of creating singlet order in [1,2-^{13}C$_2$]pyruvate is limited by the relatively long T_1 for both carbons at high field, which in blood was between 1.5 and 2 times longer than T_S at low field. Furthermore, we observed that while the T_S for [1,2-^{13}C$_2$]pyruvate
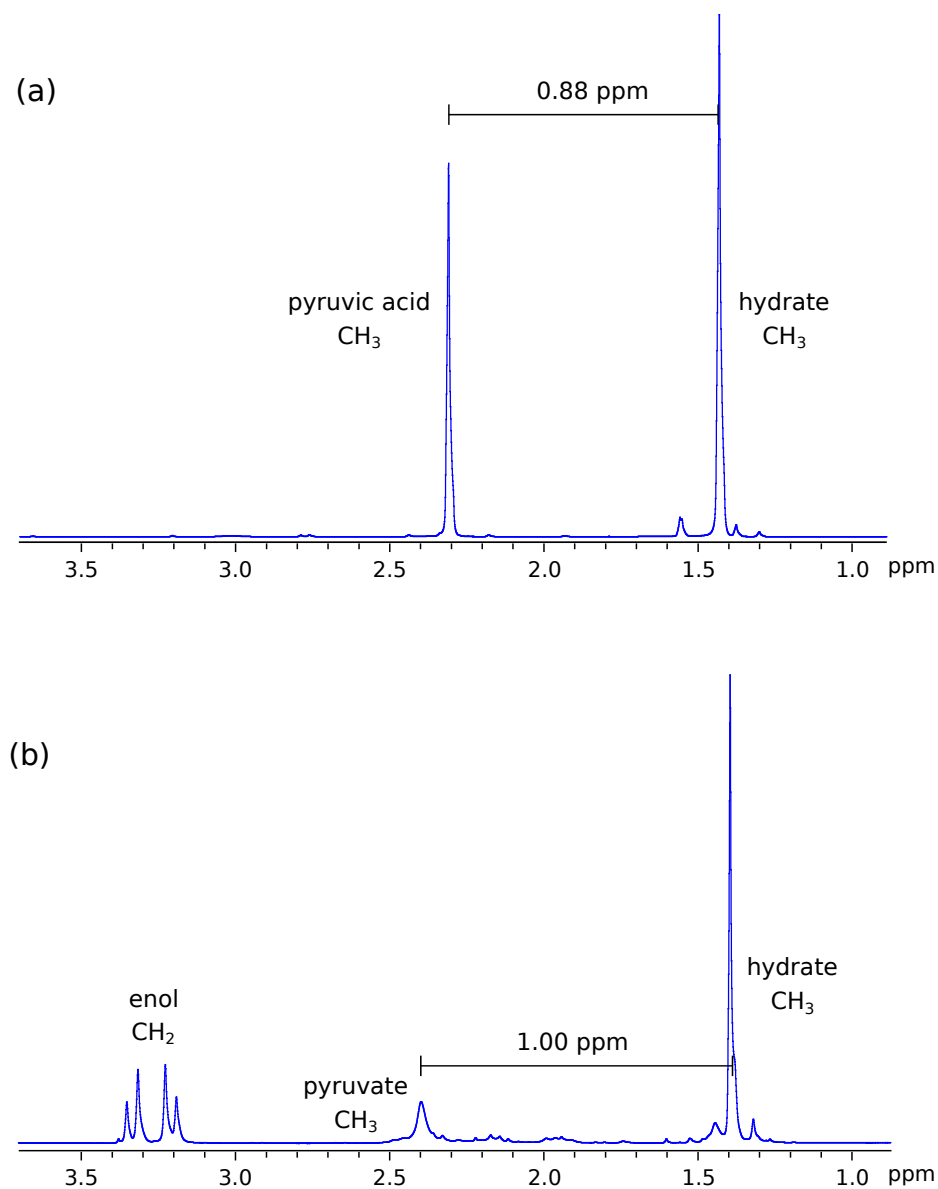
Figure 3.17: Example of ^{1}H-NMR spectra of pyruvic acid in $9/1$ v/v $H_2O/^2H_2O$ at (a) acidic pH (pH $= 1.6$) and (b) basic pH (pH $= 13.5$, with addition of KOH). The spectra shown are for an initial concentration of 1 M of neat pyruvic acid and 128 scans.

(a)

(b)
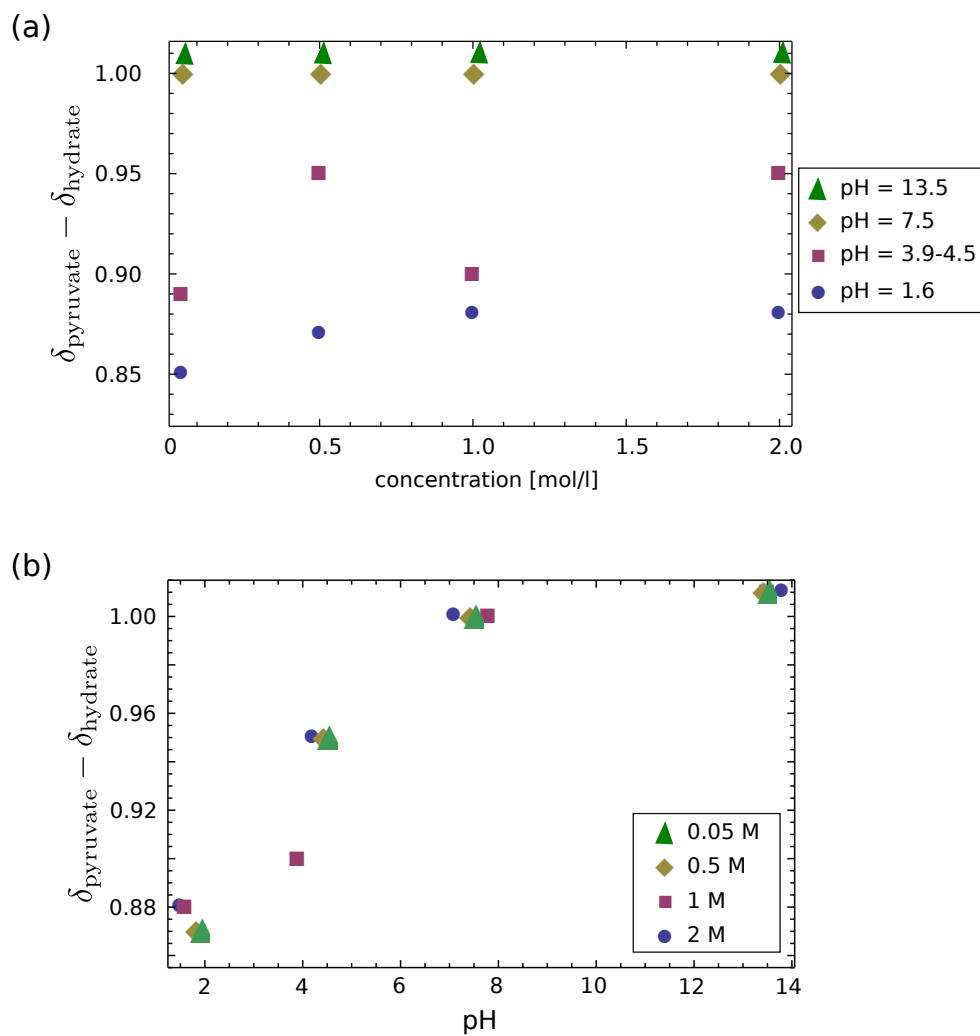
Figure 3.18: Dependence of the difference between pyruvate and pyruvate hydrate chemical shifts on (a) initial pyruvic acid concentration and (b) pH.
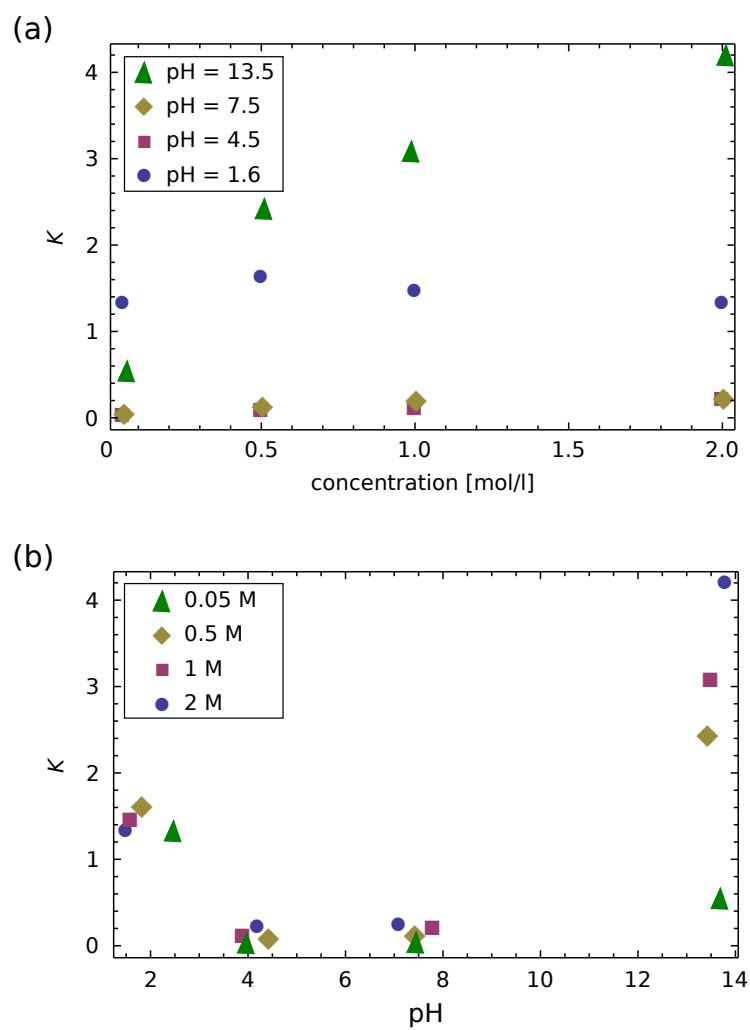
Figure 3.19: Dependence of K = (area under pyruvate hydrate peak / area under pyruvate peak) with (a) initial pyruvic acid concentration and (b) pH.

in ^{2}H$_2$O buffer is approximately twice $T_1{}^{LF}$ of the same molecule, it is not significantly longer than the $T_1{}^{LF}$ of [1-^{13}C]pyruvate. As seen with the hydration reaction from pyruvate to pyruvate hydrate, if the metabolic product of the substrate preserves the pair bond, but has a chemical shift difference of opposite sign and remains in the singlet state, then information on whether the reaction occurred at low or high field can be obtained. However, the long lifetime of the singlet state cannot provide additional information on the metabolic conversion of pyruvate to lactate since the singlet state is not an eigenstate in the high magnetic field.

While the singlet order obtained by the direct enhancement approach is much lower than that accessible by converting the longitudinal polarisation using a pulse sequence, the simpler preparation route used here was sufficient for the demonstrations presented in this work. However, maximum conversion of the available spin order into singlet order, with the corresponding increase in measured signal, would be an advantage in a clinical setting.

First steps towards micro-coil singlet NMR have been taken. Both the hardware and the pulse sequence to prepare the singlet state of a weakly coupled spin-1/2 pair in the high field of the spectrometer magnet were successfully tested. Singlet state of [1,2-^{13}C$_2$]pyruvate was accessed and converted back to observable magnetisation, albeit T_S was shorter than T_1. Since pyruvate hydrate was present in the aqueous solutions used, the singlet state could not be fully isolated by the 40 kHz-radiofrequency field, which was not strong enough to spin lock the C2 carbon of pyruvate hydrate. Further work on this matter will be pursued.

The advantage of generating the singlet state will only be realised for those doubly labelled molecules that possess lifetimes T_S that significantly exceed T_1 of the singly labelled isotopologues at both low and high magnetic fields.

Relaxation lifetimes of [1,4-^{13}C$_2$]fumarate

<div style="text-align: right;">4</div>

Hyperpolarised [1,4-^{13}C$_2$]fumarate has been used to monitor response to cancer treatment. The ratio of fumarate to its metabolic product malate provides information on cell necrosis, which in turn indicates whether the treatment is effective (Gallagher *et al.*, 2009). [1,4-^{13}C$_2$]fumarate is a potential candidate for accessing a long lived singlet state as both the carbon and hydrogen pairs display near magnetic equivalence (AA'XX' system) and near singlet-triplet product eigenstates. The mutual symmetry breaking of each homonuclear spin pair is due to the difference in values of the heteronuclear couplings, and this interaction allows access to singlet state populations. This has been shown previously with [1,2-^{13}C$_2$]diphenylacetylene (Feng *et al.*, 2013), ^{13}C$_2$-diethyl oxalate, 2,2-difluorosuccinic acid and cyclooctyne derivatives (Feng *et al.*, 2012).

This chapter reviews whether the singlet state relaxation times of the ^{13}C or ^{1}H in [1,4-^{13}C$_2$]fumarate are longer or shorter than the corresponding T_1 s. We accessed the singlet state through the asymmetry in the heteronuclear J-couplings using a similar procedure to that adopted by Tayler (2012) and Feng *et al.* (2012). While the pulse sequence is the same, a more careful consideration of the spin dynamics is required because the $^4J_{\mathrm{CC'}}$ and $^3J_{\mathrm{HH'}}$ scalar couplings in fumarate are similar in magnitude. Measured relaxation time constants (T_1, T_2 and T_S), J-coupling constants and singlet-derived NMR spectra of fumarate are presented and discussed. A potential adaptation for exploiting the singlet state of fumarate in combination with DNP is also presented, plus some remarks about potentially longer-lived states that may exist.
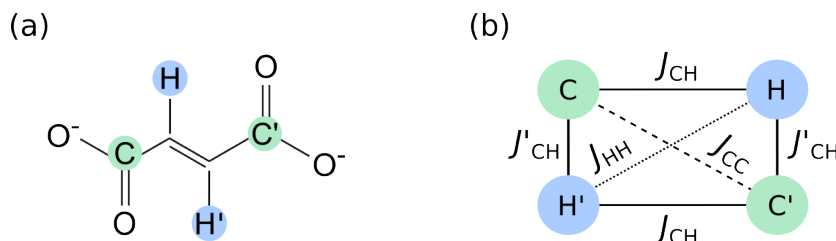
Figure 4.1: (a) molecular structure and (b) spin topology, showing J-couplings, of [1,4-^{13}C$_2$]fumarate.

4.1 Magnetic equivalence symmetry in [1,4-^{13}C$_2$]fumarate

[1,4-^{13}C$_2$]fumaric acid (trans-[1,4-^{13}C$_2$]butenedioic acid; HO$_2$^{13}CCH=CH^{13}CO$_2$H) is a 4-spin-1/2 system containing two ^{13}C nuclei located at the two carboxyl groups, and two ^{1}H nuclei located trans across a C-C double bond (Figure 4.1). Due to the molecular (rotational) symmetry these spin pairs are each chemically equivalent. However, they are magnetically inequivalent because the heteronuclear couplings J_{CH} and J'_{CH} are different from one another (Section 1.6.4). This asymmetry permits access to the singlet state of each pair, provided that the relation $|J_{AA'} \pm J_{XX'}| \gg \Delta J_{AX}$ is satisfied, i.e. that the sum or difference in the homonuclear J-couplings exceeds the difference in J-couplings between the two heteronuclear spin pairs.

4.1.1 NMR spectra and J-couplings

The J-coupling values in fumarate were obtained from the peak splittings in the ^{13}C satellite spectra of [1,4-^{13}C$_2$]fumarate (Figure 4.2) and [2,3-^{13}C$_2$]fumarate (Figure 4.3) and fitting the experimental spectra to simulated spectra generated using the *SpinDynamica* package in *Mathematica* (Wolfram Inc, Champaign, IL, USA). Results are summarised in Table 4.1 and agree reasonably well with those predicted by Braun (1978).

J-couplings [Hz]								
J_{H2H3}	J_{C2H3} J_{C3H2}	J_{C1C2} J_{C3C4}	J_{C1C4}	J_{C2C3}	J_{C2C4} J_{C1C3}	J_{C1H2} J_{C4H3}	J_{C1H3} J_{C4H2}	J_{C2H2} J_{C3H3}
15.7	2.9	64.5	6.8	68.5	1	5.9	3.5	161

Table 4.1: Measured scalar coupling constants for fumarate.
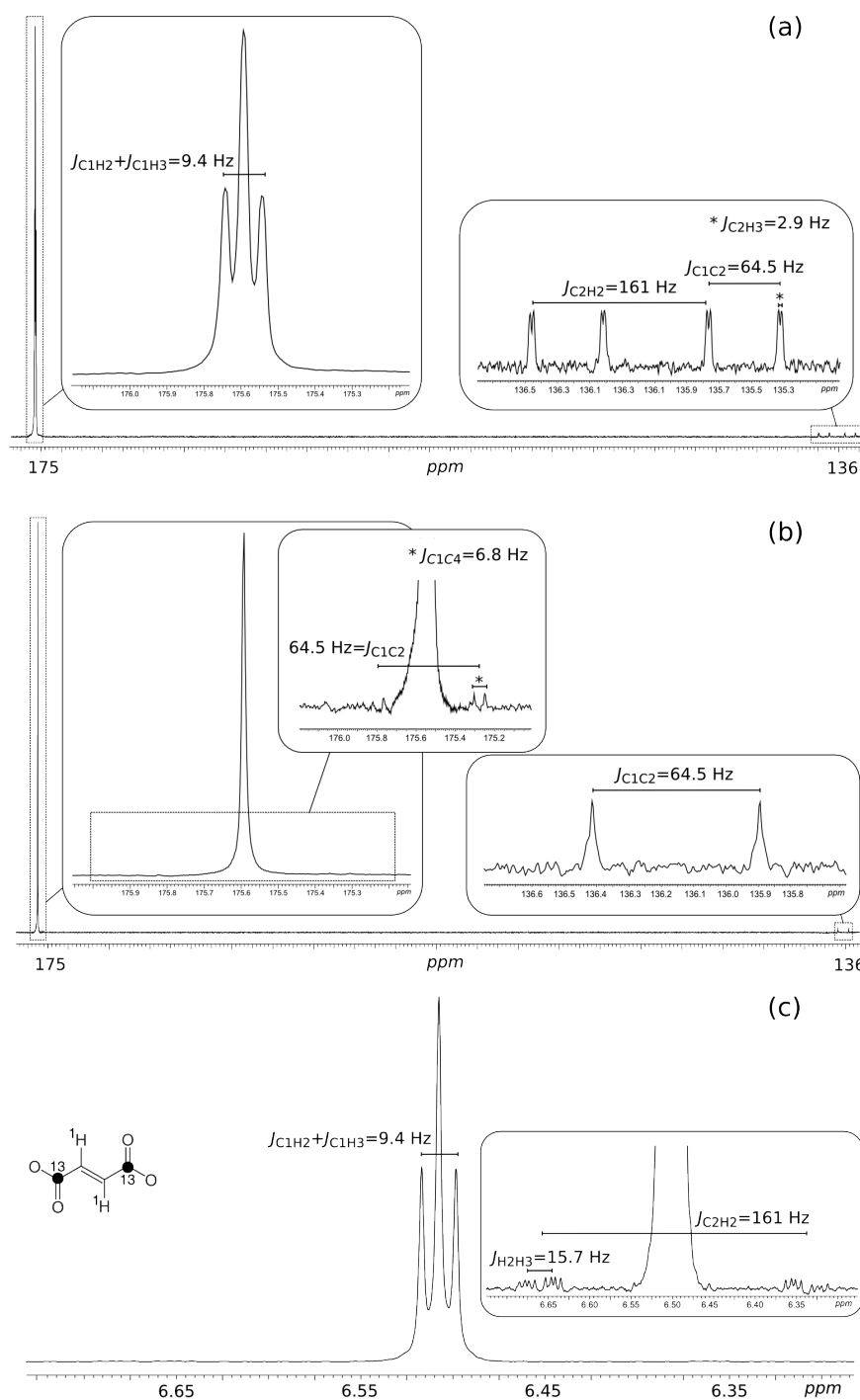
Figure 4.2: 90° pulse-acquire spectra of [1,4-$^{13}C_2$]fumarate (30 mM dissolved in buffered ^2H_2O solution (128 scans, at 11.0 T and 300 K). (a) ^{13}C-NMR spectrum with 1 Hz line broadening, (b) ^1H-decoupled ^{13}C-NMR spectrum with 1 Hz line broadening, and (c) ^1H-NMR spectrum with 0.5 Hz line broadening.
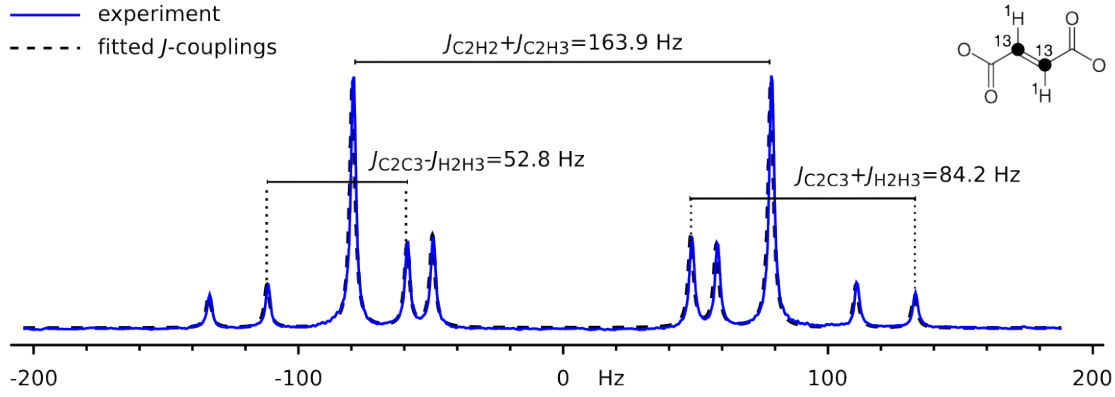
Figure 4.3: ^{1}H-NMR spectrum of 30 mM [2,3-^{13}C$_2$]fumarate (sodium salt) in ^{2}H$_2$O at 11.0 T and 300 K (64 scans scans). ^{13}C spectrum displays the same peak pattern.

4.1.2   Hamiltonian and eigenstates of the system

The Hamiltonian of the 4-spin system ([1,4-^{13}C$_2$]fumarate) with chemical equivalence within the ^{13}C-pair and the ^{1}H-pair is given by:

$$
\begin{aligned}
H = \;& \omega_{\mathrm{C}}(I_z^{\mathrm{C}} + I_z^{\mathrm{C}'}) + \omega_{\mathrm{H}}(I_z^{\mathrm{H}} + I_z^{\mathrm{H}'}) + 2\pi J_{\mathrm{CC}'} I^{\mathrm{C}} \cdot I^{\mathrm{C}'} + 2\pi J_{\mathrm{HH}'} I^{\mathrm{H}} \cdot I^{\mathrm{H}'} + \\
& \pi J_{\mathrm{CH}}(2I_z^{\mathrm{C}} I_z^{\mathrm{H}} + 2I_z^{\mathrm{C}'} I_z^{\mathrm{H}'}) + \pi J'_{\mathrm{CH}}(2I_z^{\mathrm{C}} I_z^{\mathrm{H}'} + 2I_z^{\mathrm{C}'} I_z^{\mathrm{H}}),
\end{aligned} \tag{4.1}
$$

where ω_{C} and ω_{H} are the precession frequencies of the respective nuclei at the acquisition field ($\omega_j = -\gamma_j B_0$). I^{C}, $I^{\mathrm{C}'}$, I^{H} and $I^{\mathrm{H}'}$ are the total spin angular momentum operator of each ^{13}C or ^{1}H site, which can be decomposed into their Cartesian components

$$
I^j = (I_x^j, I_y^j, I_z^j). \tag{4.2}
$$

And the $I^j \cdot I^k$ product is

$$
I^j \cdot I^k = I_x^j I_x^k + I_y^j I_y^k + I_z^j I_z^k. \tag{4.3}
$$

The J-coupling constants between each spin pair in the system are represented with J and the subscript of the corresponding pair. Here, $J_{\mathrm{CH}} = J_{\mathrm{C}'\mathrm{H}'} = 5.9$ Hz and $J'_{\mathrm{CH}} \equiv J_{\mathrm{CH}'} = J_{\mathrm{C}'\mathrm{H}} = 3.5$ Hz. The pairs of nuclei are magnetically inequivalent because J_{CH} and J'_{CH} have different magnitude, i.e $|J_{\mathrm{CH}}| \neq |J'_{\mathrm{CH}}|$, since the Hamiltonian is no longer symmetric on permutation of the pair.

The Zeeman and singlet-triplet state bases of a spin-1/2 pair correlate as shown earlier in Eq. (1.44). The 4-spin system of $[1,4\text{-}^{13}C_2]$fumarate contains 16 states ($=2^4$). These can be written as products of the singlet and the triplet states of each homonuclear spin pair (i.e. CC' and HH'):

- States involving $\left|T_{+1}^{C}\right\rangle \otimes \left|\phi^{H}\right\rangle$:

$$
\begin{aligned}
\left|T_{+1}^{C}T_{+1}^{H}\right\rangle &= \left|\alpha^{C}\alpha^{C'}\alpha^{H}\alpha^{H'}\right\rangle, \\
\left|T_{+1}^{C}T_{0}^{H}\right\rangle &= \frac{1}{\sqrt{2}}\left(\left|\alpha^{C}\alpha^{C'}\alpha^{H}\beta^{H'}\right\rangle + \left|\alpha^{C}\alpha^{C'}\beta^{H}\alpha^{H'}\right\rangle\right), \\
\left|T_{+1}^{C}T_{-1}^{H}\right\rangle &= \left|\alpha^{C}\alpha^{C'}\beta^{H}\beta^{H'}\right\rangle, \\
\left|T_{+1}^{C}S_{0}^{H}\right\rangle &= \frac{1}{\sqrt{2}}\left(\left|\alpha^{C}\alpha^{C'}\alpha^{H}\beta^{H'}\right\rangle - \left|\alpha^{C}\alpha^{C'}\beta^{H}\alpha^{H'}\right\rangle\right).
\end{aligned}
\tag{4.4}
$$

- States involving $\left|T_{-1}^{C}\right\rangle \otimes \left|\phi^{H}\right\rangle$:

$$
\begin{aligned}
\left|T_{-1}^{C}T_{+1}^{H}\right\rangle &= \left|\beta^{C}\beta^{C'}\alpha^{H}\alpha^{H'}\right\rangle, \\
\left|T_{-1}^{C}T_{0}^{H}\right\rangle &= \frac{1}{\sqrt{2}}\left(\left|\beta^{C}\beta^{C'}\alpha^{H}\beta^{H'}\right\rangle + \left|\beta^{C}\beta^{C'}\beta^{H}\alpha^{H'}\right\rangle\right), \\
\left|T_{-1}^{C}T_{-1}^{H}\right\rangle &= \left|\beta^{C}\beta^{C'}\beta^{H}\beta^{H'}\right\rangle, \\
\left|T_{-1}^{C}S_{0}^{H}\right\rangle &= \frac{1}{\sqrt{2}}\left(\left|\beta^{C}\beta^{C'}\alpha^{H}\beta^{H'}\right\rangle - \left|\beta^{C}\beta^{C'}\beta^{H}\alpha^{H'}\right\rangle\right).
\end{aligned}
\tag{4.5}
$$

- States involving $\left|T_{0}^{C}\right\rangle \otimes \left|\phi^{H}\right\rangle$:

$$
\begin{aligned}
\left|T_{0}^{C}T_{+1}^{H}\right\rangle &= \frac{1}{\sqrt{2}}\left(\left|\beta^{C}\alpha^{C'}\alpha^{H}\alpha^{H'}\right\rangle + \left|\alpha^{C}\beta^{C'}\alpha^{H}\alpha^{H'}\right\rangle\right), \\
\left|T_{0}^{C}T_{0}^{H}\right\rangle &= \frac{1}{2}(\left|\beta^{C}\alpha^{C'}\alpha^{H}\beta^{H'}\right\rangle + \left|\alpha^{C}\beta^{C'}\beta^{H}\alpha^{H'}\right\rangle + \\
&\quad \left|\beta^{C}\alpha^{C'}\beta^{H}\alpha^{H'}\right\rangle + \left|\alpha^{C}\beta^{C'}\alpha^{H}\beta^{H'}\right\rangle), \\
\left|T_{0}^{C}T_{-1}^{H}\right\rangle &= \frac{1}{\sqrt{2}}\left(\left|\beta^{C}\alpha^{C'}\beta^{H}\beta^{H'}\right\rangle + \left|\alpha^{C}\beta^{C'}\beta^{H}\beta^{H'}\right\rangle\right), \\
\left|T_{0}^{C}S_{0}^{H}\right\rangle &= \frac{1}{2}(\left|\beta^{C}\alpha^{C'}\alpha^{H}\beta^{H'}\right\rangle - \left|\alpha^{C}\beta^{C'}\beta^{H}\alpha^{H'}\right\rangle + \\
&\quad \left|\beta^{C}\alpha^{C'}\beta^{H}\alpha^{H'}\right\rangle + \left|\alpha^{C}\beta^{C'}\alpha^{H}\beta^{H'}\right\rangle).
\end{aligned}
\tag{4.6}
$$

- States involving $\left|S_0^{\mathrm{C}}\right\rangle \otimes \left|\phi^{\mathrm{H}}\right\rangle$:

$$
\begin{aligned}
\left|S_0^{\mathrm{C}}T_{+1}^{\mathrm{H}}\right\rangle &= \frac{1}{\sqrt{2}}\left(\left|\alpha^{\mathrm{C}}\beta^{\mathrm{C'}}\alpha^{\mathrm{H}}\alpha^{\mathrm{H'}}\right\rangle - \left|\beta^{\mathrm{C}}\alpha^{\mathrm{C'}}\alpha^{\mathrm{H}}\alpha^{\mathrm{H'}}\right\rangle\right), \\
\left|S_0^{\mathrm{C}}T_0^{\mathrm{H}}\right\rangle &= \frac{1}{2}(-\left|\beta^{\mathrm{C}}\alpha^{\mathrm{C'}}\alpha^{\mathrm{H}}\beta^{\mathrm{H'}}\right\rangle + \left|\alpha^{\mathrm{C}}\beta^{\mathrm{C'}}\beta^{\mathrm{H}}\alpha^{\mathrm{H'}}\right\rangle - \\
&\quad \left|\beta^{\mathrm{C}}\alpha^{\mathrm{C'}}\beta^{\mathrm{H}}\alpha^{\mathrm{H'}}\right\rangle + \left|\alpha^{\mathrm{C}}\beta^{\mathrm{C'}}\alpha^{\mathrm{H}}\beta^{\mathrm{H'}}\right\rangle), \\
\left|S_0^{\mathrm{C}}T_{-1}^{\mathrm{H}}\right\rangle &= \frac{1}{\sqrt{2}}\left(\left|\alpha^{\mathrm{C}}\beta^{\mathrm{C'}}\beta^{\mathrm{H}}\beta^{\mathrm{H'}}\right\rangle - \left|\beta^{\mathrm{C}}\alpha^{\mathrm{C'}}\beta^{\mathrm{H}}\beta^{\mathrm{H'}}\right\rangle\right), \\
\left|S_0^{\mathrm{C}}S_0^{\mathrm{H}}\right\rangle &= \frac{1}{2}(-\left|\beta^{\mathrm{C}}\alpha^{\mathrm{C'}}\alpha^{\mathrm{H}}\beta^{\mathrm{H'}}\right\rangle - \left|\alpha^{\mathrm{C}}\beta^{\mathrm{C'}}\beta^{\mathrm{H}}\alpha^{\mathrm{H'}}\right\rangle + \\
&\quad \left|\beta^{\mathrm{C}}\alpha^{\mathrm{C'}}\beta^{\mathrm{H}}\alpha^{\mathrm{H'}}\right\rangle + \left|\alpha^{\mathrm{C}}\beta^{\mathrm{C'}}\alpha^{\mathrm{H}}\beta^{\mathrm{H'}}\right\rangle).
\end{aligned} \tag{4.7}
$$

4.1.3 Mixing of states: subspaces

The matrix representation of Eq. (4.1) is approximately diagonal in the singlet-triplet product basis [Eqs (4.4)-(4.7)]. Of the 16 states, 12 are eigenstates (that have off-diagonal elements that are all zero) while the remaining four form two isolated pairs.

The sets of connected states correspond to products of the singlet and triplet states $\left|T_0\right\rangle$ and $\left|S_0\right\rangle$ of each homonuclear pair. The matrix representation of the Hamiltonian for these subspaces, assuming $\omega_{\mathrm{C}} = \omega_{\mathrm{C'}}$ and $\omega_{\mathrm{H}} = \omega_{\mathrm{H'}}$, are as follows:

- Subspace $\left|T_0^{\mathrm{C}}T_0^{\mathrm{H}}\right\rangle \leftrightarrow \left|S_0^{\mathrm{C}}S_0^{\mathrm{H}}\right\rangle$:

$$
\begin{pmatrix}
\langle T_0^{\mathrm{C}}T_0^{\mathrm{H}}|H|T_0^{\mathrm{C}}T_0^{\mathrm{H}}\rangle & \langle T_0^{\mathrm{C}}T_0^{\mathrm{H}}|H|S_0^{\mathrm{C}}S_0^{\mathrm{H}}\rangle \\
\langle S_0^{\mathrm{C}}S_0^{\mathrm{H}}|H|T_0^{\mathrm{C}}T_0^{\mathrm{H}}\rangle & \langle S_0^{\mathrm{C}}S_0^{\mathrm{H}}|H|S_0^{\mathrm{C}}S_0^{\mathrm{H}}\rangle
\end{pmatrix} = \pi
\begin{pmatrix}
1/2(J_{\mathrm{CC'}} + J_{\mathrm{HH'}}) & (J_{\mathrm{CH}} - J'_{\mathrm{CH}}) \\
(J_{\mathrm{CH}} - J'_{\mathrm{CH}}) & -3/2(J_{\mathrm{CC'}} + J_{\mathrm{HH'}})
\end{pmatrix}. \tag{4.8}
$$

- Subspace $\left|T_0^{\mathrm{C}}S_0^{\mathrm{H}}\right\rangle \leftrightarrow \left|S_0^{\mathrm{C}}T_0^{\mathrm{H}}\right\rangle$:

$$
\begin{pmatrix}
\langle T_0^{\mathrm{C}}S_0^{\mathrm{H}}|H|T_0^{\mathrm{C}}S_0^{\mathrm{H}}\rangle & \langle T_0^{\mathrm{C}}S_0^{\mathrm{H}}|H|S_0^{\mathrm{C}}T_0^{\mathrm{H}}\rangle \\
\langle S_0^{\mathrm{C}}T_0^{\mathrm{H}}|H|T_0^{\mathrm{C}}S_0^{\mathrm{H}}\rangle & \langle S_0^{\mathrm{C}}T_0^{\mathrm{H}}|H|S_0^{\mathrm{C}}T_0^{\mathrm{H}}\rangle
\end{pmatrix} = \pi
\begin{pmatrix}
1/2(J_{\mathrm{CC'}} - 3J_{\mathrm{HH'}}) & (J_{\mathrm{CH}} - J'_{\mathrm{CH}}) \\
(J_{\mathrm{CH}} - J'_{\mathrm{CH}}) & 1/2(-3J_{\mathrm{CC'}} + J_{\mathrm{HH'}})
\end{pmatrix}. \tag{4.9}
$$

By making the subspaces traceless, only their anisotropic part is left:

- Subspace $\left|T_0^{\mathrm{C}}T_0^{\mathrm{H}}\right\rangle \leftrightarrow \left|S_0^{\mathrm{C}}S_0^{\mathrm{H}}\right\rangle$:

$$
\text{Eq.}(4.8) \xrightarrow{\text{iso}} \pi
\begin{pmatrix}
J_{\mathrm{CC'}} + J_{\mathrm{HH'}} & J_{\mathrm{CH}} - J'_{\mathrm{CH}} \\
J_{\mathrm{CH}} - J'_{\mathrm{CH}} & -J_{\mathrm{CC'}} - J_{\mathrm{HH'}}
\end{pmatrix}. \tag{4.10}
$$

- Subspace $\left|T_0^{\mathrm{C}} S_0^{\mathrm{H}}\right\rangle \leftrightarrow \left|S_0^{\mathrm{C}} T_0^{\mathrm{H}}\right\rangle$:

$$\text{Eq.(4.9)} \xrightarrow{\text{iso}} \pi \begin{pmatrix} J_{\mathrm{CC'}} - J_{\mathrm{HH'}} & J_{\mathrm{CH}} - J'_{\mathrm{CH}} \\ J_{\mathrm{CH}} - J'_{\mathrm{CH}} & -J_{\mathrm{CC'}} + J_{\mathrm{HH'}} \end{pmatrix}. \tag{4.11}$$

The above shows clearly that $J_{\mathrm{CH}} \neq J'_{\mathrm{CH}}$ mutually breaks the magnetic equivalence symmetry of each homonuclear spin pair, since each off-diagonal element is a multiple of $(J_{\mathrm{CH}} - J'_{\mathrm{CH}})$. If all the heteronuclear couplings are equal or zero, the subspaces in Eqs (4.10) and (4.11) become diagonal and there is no mixing of the states under free evolution.

The matrix representation of the Hamiltonian is given in the Appendix (Section 4.7).

4.2 Preparation of singlet order in [1,4-^{13}C$_2$]fumarate

4.2.1 Bloch sphere representation

The two isolated subspaces can each be visualised using the Bloch sphere representation (equivalent to 1-spin-1/2). The situation of near magnetic equivalence is demonstrated by Figure 4.4, which shows a geometric representation of the subsystems connected by the symmetry breaking interaction ΔJ_{CH}. When $|\Delta J_{\mathrm{CH}}| << |J_{\mathrm{CC'}} \pm J_{\mathrm{HH'}}|$, the effective field is close to the z-axis of the sphere, so the singlet-triplet states are approximate eigenstates under these conditions. The subspace illustrates that a population difference between each pair of states is isolated during free evolution.

In this Bloch sphere representation, the Hamiltonian for the subspace $\left|T_0^{\mathrm{C}} T_0^{\mathrm{H}}\right\rangle \leftrightarrow \left|S_0^{\mathrm{C}} S_0^{\mathrm{H}}\right\rangle$ is the following:

$$H_{SS} = 2\pi(J_{\mathrm{CH}} - J'_{\mathrm{CH}})I_x + 2\pi(J_{\mathrm{CC'}} + J_{\mathrm{HH'}})I_z - \frac{\pi}{2}(J_{\mathrm{CC'}} + J_{\mathrm{HH'}})\mathbb{1}. \tag{4.12}$$

And for the subspace $\left|T_0^{\mathrm{C}} S_0^{\mathrm{H}}\right\rangle \leftrightarrow \left|S_0^{\mathrm{C}} T_0^{\mathrm{H}}\right\rangle$:

$$H_{ST} = 2\pi(J_{\mathrm{CH}} - J'_{\mathrm{CH}})I_x + 2\pi(J_{\mathrm{CC'}} - J_{\mathrm{HH'}})I_z - \frac{\pi}{2}(J_{\mathrm{CC'}} + J_{\mathrm{HH'}})\mathbb{1}. \tag{4.13}$$

with $\mathbb{1}$ being the identity matrix, and the I_x and I_z terms being the anisotropic components along the x- and z-axis that allow the mixing of states. This can be understood by analogy with an isolated spin-1/2 irradiated with a radiofrequency field of amplitude ω_{rf} with the transmitter offset
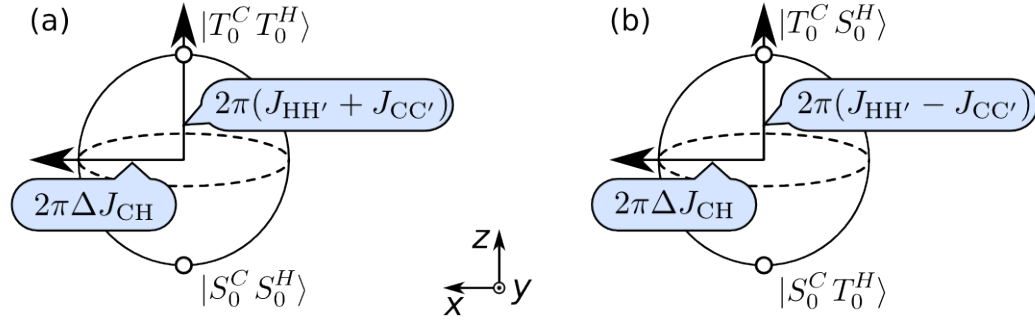
Figure 4.4: Bloch sphere representation of the subsystems connected by the symmetry breaking interaction $\Delta J_{CH} = (J_{CH} - J'_{CH})$.: (a) $\left|T_0^H T_0^C\right\rangle \leftrightarrow \left|S_0^H S_0^C\right\rangle$ and (b) $\left|T_0^H S_0^C\right\rangle \leftrightarrow \left|S_0^H T_0^C\right\rangle$. Provided $|\Delta J_{CH}| << |J_{CC'} \pm J_{HH'}|$, a population difference between each pair of states is isolated during free evolution, and the x and z components that allow the mixing of states when a radiofrequency spin-echo train is applied. Adapted from Tayler (2012).
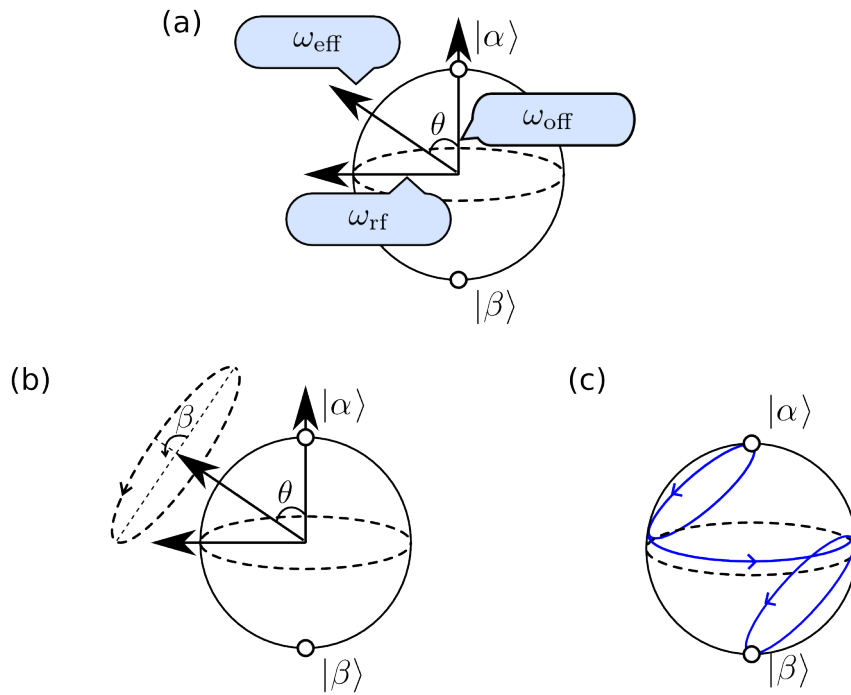
Figure 4.5: Bloch sphere representation of a single spin-1/2. (a) Magnetic fields present when a radiofrequency field with amplitude ω_{rf} is applied off-resonance, with the transmitter offset producing a field along the z-axis ω_{off}. (b) Mixing of the states under free evolution illustrated for off-resonance radiofrequency irradiation. The maximum departure of the magnetisation from its equilibrium is found at 2θ from the longitudinal axis. (c) Schematic representation of the accumulative evolution under n cycles of phase inversion after each radiofrequency pulse.

producing a field along the z-axis with amplitude ω_{off} (Figure 4.5) (Shaka, 1985). The Hamiltonian in the rotating frame of this single spin-$1/2$,

$$H = \omega_{\mathrm{rf}} I_x + \omega_{\mathrm{off}} I_z, \tag{4.14}$$

resembles that presented in Eqs (4.12) and (4.13), since there is a perturbing force along the z-axis and another one perpendicular to it.

The effective field experienced by the spin is

$$\omega_{\mathrm{eff}} = \sqrt{\omega_{\mathrm{off}}^2 + \omega_{\mathrm{rf}}^2}, \tag{4.15}$$

at an angle θ from the z-axis, where $\tan\theta = \omega_{\mathrm{rf}}/\omega_{\mathrm{off}}$. In the off-resonance limit, where $\omega_{\mathrm{off}} \gg \omega_{\mathrm{rf}}$, the effective field is close to the z-axis of the Bloch sphere and the states $|\alpha\rangle$ and $|\beta\rangle$ are the approximate eigenstates. The angular position on the perpendicular plane to that defined by ω_{eff}, β, is determined by the delay time that the radiofrequency field is applied for:

$$\beta = \omega_{\mathrm{eff}} \tau_{\mathrm{rf}}. \tag{4.16}$$

The maximum departure of the magnetisation from its equilibrium position (i.e. maximum mixing of the states $|\alpha\rangle$ and $|\beta\rangle$) occurs at $\beta = 2\theta$, or equivalently, at

$$\beta = 2\arctan\left(\frac{\omega_{\mathrm{rf}}}{\omega_{\mathrm{off}}}\right) \tag{4.17}$$

after an irradiation time of

$$\tau = \frac{\pi}{\omega_{\mathrm{eff}}}. \tag{4.18}$$

Irradiation for a duration longer than τ rotates the magnetisation back to its starting point (Figure 4.5b). Full inversion of the population is possible by reversing the phase of the radiofrequency pulse (shifting by $180°$) at intervals of τ, so that rotation in the plane perpendicular to the radiofrequency field axis accumulates. To achieve full inversion, the phase shifting is repeated n cycles ($n2\theta = \pi$):

$$n = \mathrm{round}\left(\frac{2}{\pi}\arctan\left|\frac{\omega_{\mathrm{rf}}}{\omega_{\mathrm{off}}}\right|\right)^{-1}. \tag{4.19}$$

This is known formally as 'double resonance'.

Using the above as an analogy to the isolated subspaces of fumarate [Eqs (4.11) and (4.12)],

the heteronuclear J-coupling difference ΔJ_{CH} corresponds to ω_{rf}, and $(J_{\mathrm{CC'}} \pm J_{\mathrm{HH'}})$ corresponds to ω_{off}. Under conditions of near magnetic equivalence, $|J_{\mathrm{CC'}} \pm J_{\mathrm{HH'}}| >> |\Delta J_{\mathrm{CH}}|$, so the effective perturbation field is approximately parallel to the longitudinal axis and the singlet-triplet states are approximately the eigenstates. For [1,4-^{13}C$_2$]fumarate, $J_{\mathrm{HH'}} + J_{\mathrm{CC'}} = 15.7 + 6.8 = 22.5$ Hz, $|J_{\mathrm{HH'}} - J_{\mathrm{CC'}}| = 8.9$ Hz and $|\Delta J_{\mathrm{CH}}| = 2.4$ Hz.

The analogous situation for phase reversal is a 180°-pulse on either nuclear spin pair. A 180°-pulse applied to each pair changes the sign of $|T_0\rangle$, while when applied to $|S_0\rangle$ it leaves it unchanged:

$$
\begin{aligned}
|T_0\rangle &\xrightarrow{180°} -|T_0\rangle, \\
|S_0\rangle &\xrightarrow{180°} +|S_0\rangle.
\end{aligned}
\tag{4.20}
$$

Therefore, a 180°-pulse applied for instance to the carbon pair has the following effect on the states:

$$
\begin{aligned}
\left|T_0^{\mathrm{C}} T_0^{\mathrm{H}}\right\rangle &\xrightarrow{180°(C)} -\left|T_0^{\mathrm{C}} T_0^{\mathrm{H}}\right\rangle, \\
\left|S_0^{\mathrm{C}} S_0^{\mathrm{H}}\right\rangle &\xrightarrow{180°(C)} +\left|S_0^{\mathrm{C}} S_0^{\mathrm{H}}\right\rangle, \\
\left|T_0^{\mathrm{C}} S_0^{\mathrm{H}}\right\rangle &\xrightarrow{180°(C)} -\left|T_0^{\mathrm{C}} S_0^{\mathrm{H}}\right\rangle, \\
\left|S_0^{\mathrm{C}} T_0^{\mathrm{H}}\right\rangle &\xrightarrow{180°(C)} +\left|S_0^{\mathrm{C}} T_0^{\mathrm{H}}\right\rangle.
\end{aligned}
\tag{4.21}
$$

This is actually performed as a spin echo, so that the chemical shift evolution of $|T_{+1}\phi\rangle$ and $|T_{-1}\phi\rangle$ is refocused (Figure 4.6). Here, the 'double resonance' parameters (the number of cycles n and the delay τ) depend on the heteronuclear J-couplings difference and either the sum or the difference of the homonuclear J-couplings:

$$
\left|T_0^{\mathrm{C}} T_0^{\mathrm{H}}\right\rangle \leftrightarrow \left|S_0^{\mathrm{C}} S_0^{\mathrm{H}}\right\rangle \quad : \quad
\begin{cases}
\tau_{SS} = 1/\left(2\sqrt{(J_{\mathrm{CC'}} + J_{\mathrm{HH'}})^2 + (J_{\mathrm{CH}} - J'_{\mathrm{CH}})^2}\right), \\
n_{SS} = \mathrm{round}\left(\frac{2}{\pi} \arctan\left|\frac{J_{\mathrm{CH}} - J'_{\mathrm{CH}}}{J_{\mathrm{CC'}} + J_{\mathrm{HH'}}}\right|\right)^{-1}.
\end{cases}
\tag{4.22}
$$

$$
\left|T_0^{\mathrm{C}} S_0^{\mathrm{H}}\right\rangle \leftrightarrow \left|S_0^{\mathrm{C}} T_0^{\mathrm{H}}\right\rangle \quad : \quad
\begin{cases}
\tau_{ST} = 1/\left(2\sqrt{(J_{\mathrm{CC'}} - J_{\mathrm{HH'}})^2 + (J_{\mathrm{CH}} - J'_{\mathrm{CH}})^2}\right), \\
n_{ST} = \mathrm{round}\left(\frac{2}{\pi} \arctan\left|\frac{J_{\mathrm{CH}} - J'_{\mathrm{CH}}}{J_{\mathrm{CC'}} - J_{\mathrm{HH'}}}\right|\right)^{-1}.
\end{cases}
\tag{4.23}
$$

If one of the homonuclear couplings is much larger than the other (including the case where $J_{\mathrm{HH'}} = 0$ or $J_{\mathrm{CC'}} = 0$), the optimal conditions to access the singlet state are the same for both

subspaces, maximising the amount of signal preservation in the singlet order. This is the case presented previously by Feng *et al.* (2012).

4.2.2 Notes on the M2S pulse sequence at high field

In the nearly-equivalent regime, e.g. [1,4-^{13}C$_2$]fumarate, migration of spin populations within the subspaces represented in Figure 4.4 may be created by stimulating transitions between $\left|T_0^{H(C)}\right\rangle$ and $\left|S_0^{H(C)}\right\rangle$ using the M2S pulse sequence introduced in Section 3.5.2. The Magnetisation-To-Singlet (M2S) pulse sequence was suggested as a method to access the singlet state of the strongly coupled ^{13}C-pair in [1,2-^{13}C$_2$]pyruvate at millitesla fields. [1,2-^{13}C$_2$]pyruvate was regarded as a two-spin system in which the symmetry-breaking interaction responsible for the mixing of the states was the small chemical shift frequency difference in the low field, with the pulses applied at the corresponding Larmor audio-frequency. Here, we deal with a four-spin system with pairs of chemically equivalent spins at high field, and therefore the parameters involved in the M2S sequence depend on the difference in heteronuclear *J*-couplings [Eqs (4.22) and (4.23)] and the radiofrequency pulses are applied at either the ^{13}C or the ^{1}H Larmor frequency. Accumulation of $\left|T_0^{H(C)}\right\rangle \leftrightarrow \left|S_0^{H(C)}\right\rangle$ mixing is allowed for by the spin echo trains of the M2S sequence (Figure 4.6).

The density matrix evolution under the M2S sequence given below assumes that pulses are applied on resonance with ^{13}C, but the same result can be found if they are applied to ^{1}H by swapping the spin labels.

The pulse sequence starts with the initial thermal equilibrium magnetisation of the ^{13}C-pair,

$$I_z^C \cong \left(\left|T_{+1}^C\right\rangle \left\langle T_{+1}^C\right| - \left|T_{-1}^C\right\rangle \left\langle T_{-1}^C\right|\right) \mathbb{1}^H, \tag{4.24}$$

where $\mathbb{1}^H$ is the identity matrix of the proton-pair,

$$\mathbb{1}^H = \left|T_{+1}^H\right\rangle \left\langle T_{+1}^H\right| + \left|T_0^H\right\rangle \left\langle T_0^H\right| + \left|S_0^H\right\rangle \left\langle S_0^H\right| + \left|T_{-1}^H\right\rangle \left\langle T_{-1}^H\right|. \tag{4.25}$$

The first 90°-radiofrequency pulse brings longitudinal magnetisation into triplet-triplet single-quantum coherences,

$$\text{Eq.}(4.24) \xrightarrow{90_{90}} \cong \left(\left|T_{+1}^C\right\rangle \left\langle T_0^C\right| + \left|T_0^C\right\rangle \left\langle T_{-1}^C\right|\right) \mathbb{1}^H + c.c. \tag{4.26}$$

c.c. are the complex conjugates of the coherences presented in the expression above, those with opposite coherence order.
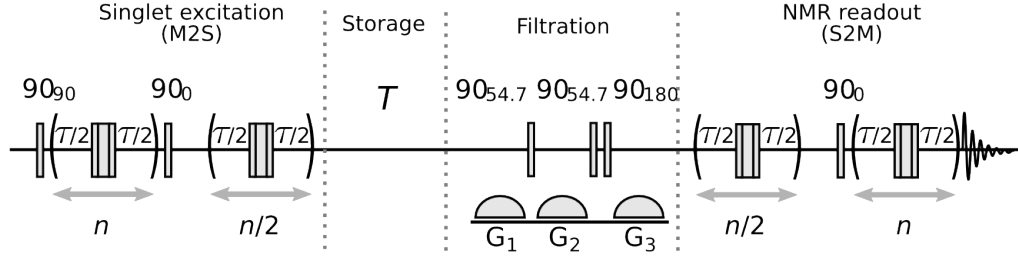
Figure 4.6: M2S-S2M pulse sequence used to access the population differences $|S_0 S_0\rangle \langle S_0 S_0| - |T_0 T_0\rangle \langle T_0 T_0|$ and $|S_0 T_0\rangle \langle S_0 T_0| - |T_0 S_0\rangle \langle T_0 S_0|$ of [1,4-^{13}C$_2$]fumarate. At the M2S and S2M parts of the sequence, the spin echo trains are generated by the composite pulse $(\tau - [90_{90} - 180_0 - 90_{90}] - \tau)$ repeated n and $n/2$ times. n and τ are defined in Eqs (4.22) and (4.23). During the interval between singlet excitation and NMR signal readout, in which polarisation is preserved in the singlet state, a set of 90° radiofrequency pulses together with gradients along z may be applied to filter any non-singlet order.

In order to reach a full inversion within the triplet-triplet and singlet-triplet product subspaces, i.e. complete inversion of the population of the two states, a set of n 180°-equivalent radiofrequency pulses separated by a delay τ must be applied on resonance with either carbons or protons (Figure 4.6). Composite pulses $[90_{90} - 180_0 - 90_{90}]$ are used to ensure accurate 180 rotations during the spin echo train, by compensating field offset and radiofrequency amplitude inhomogeneity (Levitt, 1986). Magnetisation is converted into singlet order (M2S), and retrieved (S2M), by using the appropriate values of n and τ given in Eqs (4.22) and (4.23).

For the purpose of simplicity, in the remainder of the analysis, let us assume $J_{\mathrm{HH}'} = 0$ so both $|T_0^{\mathrm{H}} T_0^{\mathrm{C}}\rangle \leftrightarrow |S_0^{\mathrm{H}} S_0^{\mathrm{C}}\rangle$ and $|T_0^{\mathrm{H}} S_0^{\mathrm{C}}\rangle \leftrightarrow |S_0^{\mathrm{H}} T_0^{\mathrm{C}}\rangle$ subspaces are inverted using the same n and τ. The first echo train of the M2S sequence (repeated n times), exchanges the populations between $|T_0\rangle$ and $|S_0\rangle$ of both ^{1}H and ^{13}C:

$$\text{Eq.(4.26)} \quad \xrightarrow{\text{echo train}}$$

$$\cong \frac{\sqrt{2}}{2} \left(|T_{+1}^{\mathrm{C}}\rangle \langle T_0^{\mathrm{C}}| + |T_0^{\mathrm{C}}\rangle \langle T_{-1}^{\mathrm{C}}| \right) \left(|T_{+1}^{\mathrm{H}}\rangle \langle T_{+1}^{\mathrm{H}}| + |T_{-1}^{\mathrm{H}}\rangle \langle T_{-1}^{\mathrm{H}}| \right) +$$

$$i \frac{\sqrt{2}}{2} \left(|T_{+1}^{\mathrm{C}}\rangle \langle S_0^{\mathrm{C}}| + |S_0^{\mathrm{C}}\rangle \langle T_{-1}^{\mathrm{C}}| \right) \left(|T_0^{\mathrm{H}}\rangle \langle S_0^{\mathrm{H}}| + |S_0^{\mathrm{H}}\rangle \langle T_0^{\mathrm{H}}| \right) + c.c. \qquad (4.27)$$

The coherences that involve $|T_{\pm 1}^{\mathrm{H}}\rangle$, first line of Eq. (4.27), are not affected by the multiple echo train and are left out below.

The 90°-radiofrequency pulse after the first multiple echo train, phase-shifted 90° from the starting pulse, converts the single-quantum triplet-singlet coherences into triplet-singlet zero-quantum coherences.

$$\text{Eq.}(4.27) \quad \xrightarrow{90_{90}} \quad (4.28)$$
$$\cong \frac{\sqrt{2}}{2} \left(\left| T_0^{\mathrm{C}} \right\rangle \left\langle S_0^{\mathrm{C}} \right| + \left| S_0^{\mathrm{C}} \right\rangle \left\langle T_0^{\mathrm{C}} \right| \right) \left(\left| T_0^{\mathrm{H}} \right\rangle \left\langle S_0^{\mathrm{H}} \right| + \left| S_0^{\mathrm{H}} \right\rangle \left\langle T_0^{\mathrm{H}} \right| \right) + c.c.$$

The second echo train (repeated $n/2$ times) finally rotates the states 90° within the subspaces, and converts triplet-singlet zero-quantum coherences into populations:

$$\text{Eq.}(4.28) \quad \xrightarrow{\text{echo train}}$$
$$\cong \left(\left| T_0 \right\rangle^{\mathrm{C}} \left\langle T_0 \right|^{\mathrm{C}} - \left| S_0 \right\rangle^{\mathrm{C}} \left\langle S_0 \right|^{\mathrm{C}} \right) \left(\left| T_0 \right\rangle^{\mathrm{H}} \left\langle T_0 \right|^{\mathrm{H}} + \left| S_0 \right\rangle^{\mathrm{H}} \left\langle S_0 \right|^{\mathrm{H}} \right) =$$
$$\left| T_0 T_0 \right\rangle \left\langle T_0 T_0 \right| - \left| S_0 T_0 \right\rangle \left\langle S_0 T_0 \right| + \left| T_0 S_0 \right\rangle \left\langle T_0 S_0 \right| - \left| S_0 S_0 \right\rangle \left\langle S_0 S_0 \right|. \quad (4.29)$$

A sequence of 90°-radiofrequency pulses applied together with three successive gradients along the laboratory z-axis serves as a filter for coherences and populations other than the ones in Eq. (4.29) (Tayler, 2012).

4.2.3   Transitions observed in the NMR spectrum

The peaks observed in the NMR spectrum correspond to single-quantum transitions between states. However, not all single-quantum transitions are observable: firstly, the allowed transitions do not involve a change of state in the passive spin pair. Furthermore, the transition between $\left| T_{\pm 1} \right\rangle \leftrightarrow \left| S_0 \right\rangle$ is symmetry forbidden. This means that in a pulse-acquire ^{1}H-NMR spectrum, for example, 8 peaks will be detected: the combination of 2 dipole-allowed single-quantum transitions from the ^{1}H-pair with identity operator of the ^{13}C-pair (Figure 4.7).

The middle peak is the only one that has a contribution from the zero-quantum subspaces mentioned above. It is consequently a means to determine the optimal parameters for the M2S pulse sequence: a 90°-pulse followed by a spin echo train, before acquisition, will result in a spectrum where the intensity of the peak depends on the spin echo delay and number of echoes. This was confirmed experimentally, as shown later in Figure 4.10.
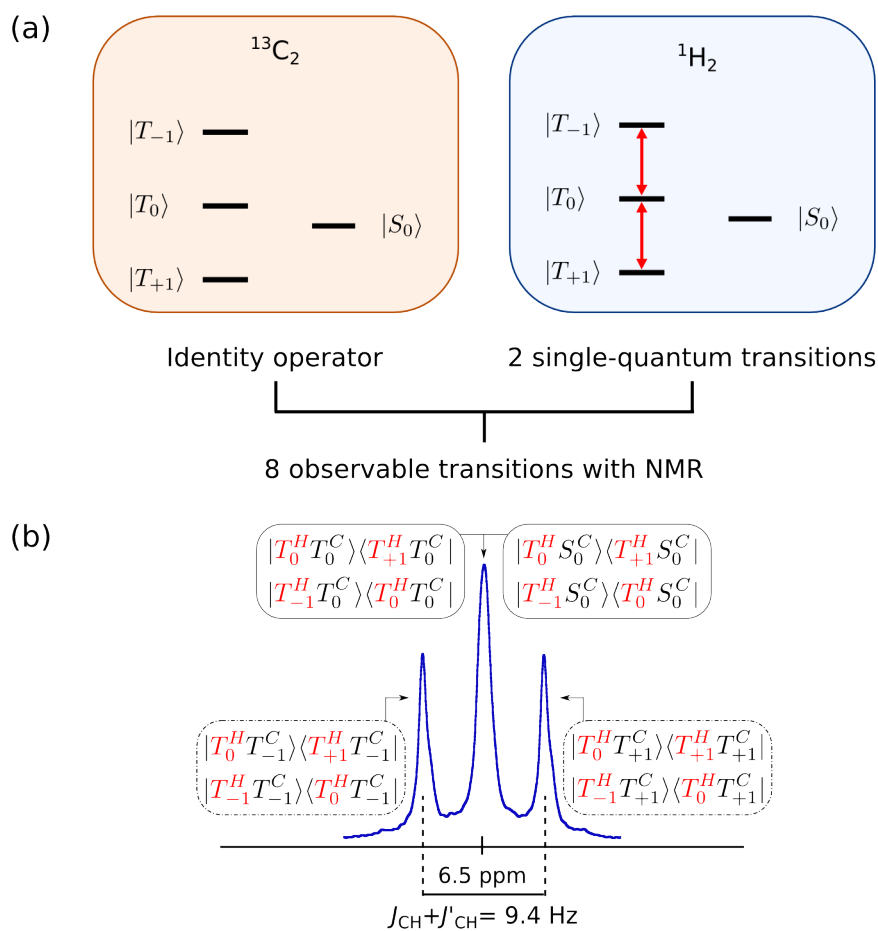
Figure 4.7: (a) Scheme showing the observable ^{1}H transitions in the HH'CC' system. (b) 90°-acquire ^{1}H-NMR spectrum of [1,4-^{13}C$_2$]fumarate labelled with identities of the transitions between spin states. Only single-quantum transitions of the hydrogen pair, in which the spin state of the carbon pair are left unchanged, are observed in the spectrum.

4.2.4 Resonance parameter simulations

The influence of the chemical shift differences and J-coupling constants was investigated by simulation of the ^{1}H-NMR and ^{13}C-NMR signal evolution during optimisation of τ and n in the triplet-triplet and triplet-singlet product state subspaces and monitoring the changes in relative peak intensities. The optimisation of τ and n was done with the first echo train of the M2S sequence (Figure 4.8).

^{1}H-NMR signal was simulated using the scalar coupling constant values of $J_{\mathrm{HH'}} = 24$ Hz, $J_{\mathrm{CH}} = 4.8$ Hz and $J'_{\mathrm{CH}} = 4$ Hz, neglecting relaxation and assuming chemical equivalence unless stated otherwise (Figure 4.9). ^{13}C-NMR simulations presented the same evolution pattern as ^{1}H-NMR signal and are not shown here.

The main observations that arise from Figure 4.9 are that:

- Provided the equivalence is broken by the scalar couplings, only the central peak is modulated (Figure 4.9a and b).

- If there is chemical inequivalence, the outer peaks are also modulated (Figure 4.9e).

- As predicted by Eqs (4.22) and (4.23), if $J_{\mathrm{HH'}} \neq 0$ and $J_{\mathrm{CC'}} = 0$ both subspaces are fully inverted simultaneously when the optimal value of n and τ is used, and this leads to an inversion of the central peak (Figure 4.9a).

- If $J_{\mathrm{HH'}} \neq 0$ and $J_{\mathrm{CC'}} \neq 0$, multiple resonances may be observed during the optimisation of the parameters due to the optimal values for each of the subspaces and subsequent combination of those (Figure 4.9c). The singlet state is not accessed simultaneously in both subspaces and, therefore, full inversion of one of the subspaces implies disappearance of the central peak instead of inversion of the peak. This translates into reduced efficiency of the M2S sequence, since the signal retrieved is 50% of that in Figure 4.9a.
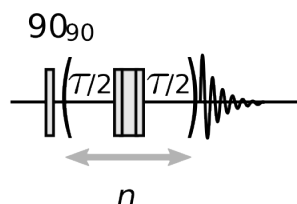
Figure 4.8: Pulse sequence used for optimising the parameters n and τ of the M2S experiment.
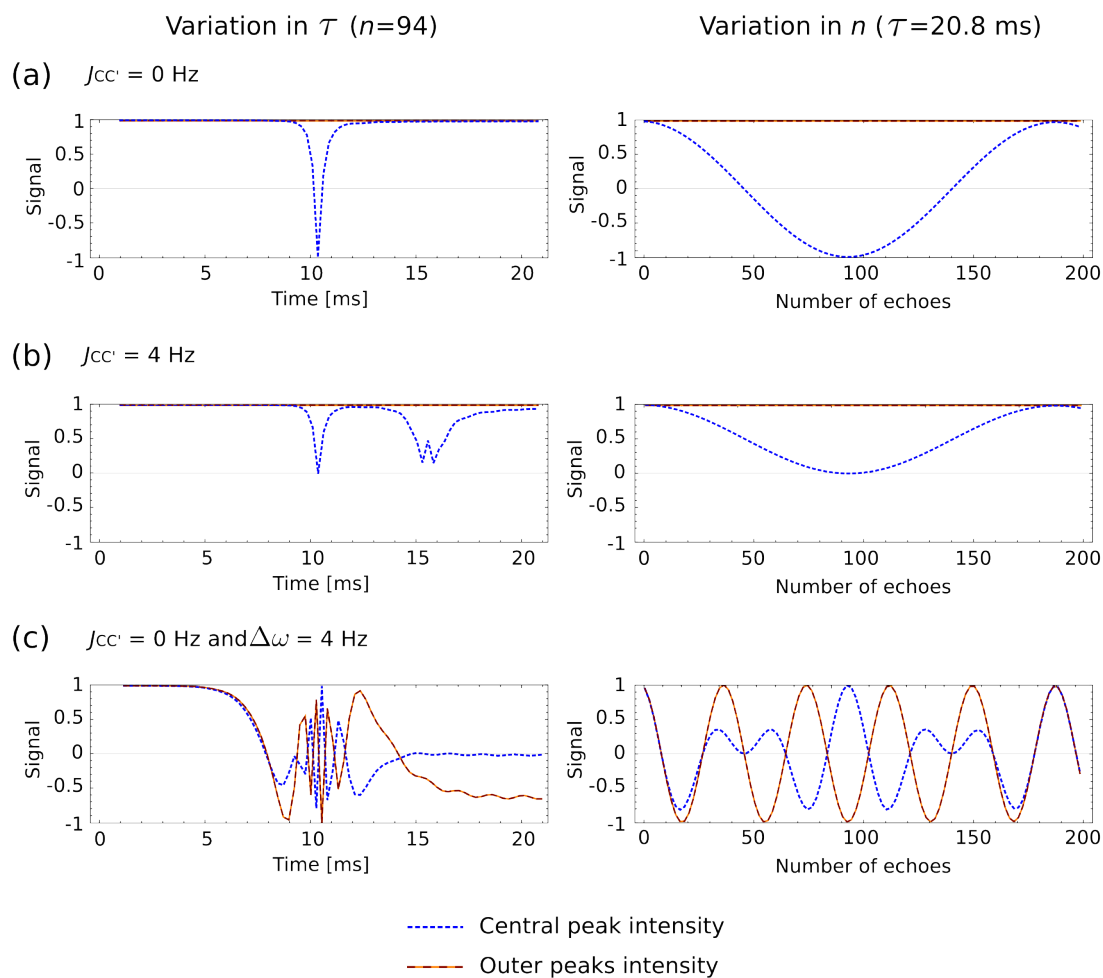
Figure 4.9: Calculated intensities (normalised) of the central and outer-J ^{1}H-NMR resonances with respect to variation in n and τ, following the pulse sequence displayed in Figure 4.8. The profiles were modelled assuming no relaxation and spins with parameters: (a) $J_{CC'} = 0$ Hz and $\Delta\omega = 0$ rad/s, (b) $J_{CC'} = 4$ Hz and $\Delta\omega = 0$ rad/s, and (c) $J_{CC'} = 0$ Hz and $\Delta\omega = 8\pi$ rad/s. The scalar coupling constants used were $J_{HH'} + J_{CC'} = 24$ Hz, $J_{CH} = 4.8$ Hz and $J'_{CH} = 4$ Hz.

4.3   Methods

4.3.1   Sample preparation

Samples of 30 mM fumaric acid (MW=116) were prepared in 90%/10% H_2O/^2H_2O solution (pH=2.3), 100% ^2H_2O solution (pH=2.3) and 40 mM phosphate buffer solutions containing 50 mM NaCl, 40 mM NaOH and 100 mg/L EDTA in either 90%/10% H_2O/^2H_2O or 100% ^2H_2O (pH=7.4). The fumarate isotopologues used in these solutions were: ^{13}C-natural abundance fumaric acid, 99% [1,4-$^{13}C_2$]fumaric acid, 99% [1,4-$^{13}C_2$, 2,3-^2H]fumaric acid and 99% [2,3-$^{13}C_2$]fumarate sodium salt (Cambridge Isotope Laboratories Inc, Ibstock, UK). The concentration was chosen to match the typical concentration of fumaric acid obtained after a dissolution-DNP experiment.

4.3.2   Spectra acquisition and measurement of relaxation time constants

T_1 measurements were made with an inversion recovery sequence, T_2 measurements were made with a CPMG sequence, and T_S measurements with the M2S pulse sequence (Section 4.2.2). All experiments were done with fully relaxed spectra, i.e. $T_R = 5T_1$. Measurements were made with a vertical wide-bore (a) 11.0 T-magnet (Bruker 500 MHz ^1H frequency spectrometer) or/and (b) 14.1 T-magnet (Bruker 600 MHz ^1H frequency spectrometer). Relaxation time constants were fitted with the software *TOP SPIN 2.1*.

4.4   Results

4.4.1 T_1 and T_2 relaxation time constants of fumarate isotopologues

Table 4.2 shows the measured ^{13}C and ^1H longitudinal and transverse relaxation time constants for 30 mM fumarate solutions in a 11.0 T-magnet and at 300 K. The longest relaxation time constants are those for fumarate dissolved in ^2H_2O buffer, whilst the shortest are the ones for fumaric acid dissolved in non-buffered H_2O.

4.4.2   Experimental optimisation of the resonance parameters

The conditions of 'double resonance' in the $|S_0S_0\rangle \leftrightarrow |T_0T_0\rangle$ and $|T_0S_0\rangle \leftrightarrow |S_0T_0\rangle$ subspaces [Eqs (4.22) and (4.23)] may be verified against the changes in the NMR spectrum acquired after a single train of spin echoes, with respect to variation of the parameters n and τ (Figure 4.10). The central peak intensity is modulated upon variation of n and τ as the echoes convert observable

Isotopologues	T_1 [s]		T_2 [s]	
of fumaric acid	^{1}H	^{13}C	^{1}H	^{13}C
Non-labelled (in H$_2$O)	6.2	-	2.0	-
Non-labelled (in ^{2}H$_2$O)	12.9	-	5.3	-
Non-labelled (in H$_2$O buffer)	6.3	-	2.1	-
Non-labelled (in ^{2}H$_2$O buffer)	15.6	-	5.1	-
[2,3-^{13}C$_2$] (sodium salt, ^{2}H$_2$O)	3.5	4.2		
[1,4-^{13}C$_2$] (in ^{2}H$_2$O)	13.5	16.4	10.2	3.4
[1,4-^{13}C$_2$] (in H$_2$O buffer)	5.2	25.1	1.6	2.8
[1,4-^{13}C$_2$] (in ^{2}H$_2$O buffer)	13.1	29.2	6.1	12.6
[1,4-^{13}C$_2$, 1,2-^{2}H] (in ^{2}H$_2$O)	-	18.1	-	2.1
[1,4-^{13}C$_2$, 1,2-^{2}H] (in H$_2$O buffer)	-	28.5	-	5.7
[1,4-^{13}C$_2$, 1,2-^{2}H] (in ^{2}H$_2$O buffer)	-	34.5	-	7.7

Table 4.2: Longitudinal (T_1) and transverse (T_2) relaxation time constants at 11.0 T and 300 K measured in various samples of 30 mM of fumaric acid isotopologues dissolved in different solvents. The maximum error of the measurements was ± 1 s.

coherences, such as those of the form $|T_0 T_0\rangle \langle T_{+1} T_0|$, into non-observable coherences, for instance $|S_0 S_0\rangle \langle T_{+1} T_0|$.

Figure 4.10 illustrates the spins' behaviour after n trains of echoes $[\tau/2 - 180 - \tau/2]$. The curves show the areas under each transition in the proton NMR spectrum of 30 mM $[1,4\text{-}^{13}\text{C}_2]$fumaric acid and 0.5 mM TEMPOL dissolved in $^2\text{H}_2\text{O}$ buffer (at 11.0 T and 300 K). The following conditions were analysed:

- Variation in the interval τ for a constant number of echoes: $n_{ST} = 12$ corresponds to the inversion in the subspace $|T_0 S_0\rangle \leftrightarrow |S_0 T_0\rangle$ (Figure 4.10a) and $n_{SS} = 4$ to the inversion in the subspace $|T_0 T_0\rangle \leftrightarrow |S_0 S_0\rangle$ (Figure 4.10c), according to Eqs (4.23) and (4.22) and the measured values of the scalar couplings (Table 4.1).

- Variation in n at fixed $\tau_{ST} = 22$ ms (Figure 4.10b) and $\tau_{SS} = 56$ ms (Figure 4.10d) as per Eqs (4.23) and (4.22), respectively.

The observed variation in signal intensity is very close to the calculated behaviour using the measured coupling constants (Figure 4.10, solid black line). The outer two multiplet peaks are always refocused and have constant area, with the exception of decay due to spin relaxation. These observations are consistent with chemical equivalence of each pair of spins, as one would expect from arguments of the molecular symmetry, i.e. there is no chemical shift difference of either pair.

The parameters of the 'double resonance' are then $\tau_{SS} = 56.0$ ms and $n_{SS} = 4 - 5$ for the $|S_0 S_0\rangle \leftrightarrow |T_0 T_0\rangle$ subspace and $\tau_{ST} = 22.0$ ms and $n_{ST} = 12$ for the $|T_0 S_0\rangle \leftrightarrow |S_0 T_0\rangle$ subspace.

4.4.3 Singlet relaxation in $[1,4\text{-}^{13}\text{C}_2]$fumarate

The longitudinal, transverse and singlet relaxation time constants for both ^{13}C and ^1H in 30 mM $[1,4\text{-}^{13}\text{C}_2]$fumaric acid dissolved in $^2\text{H}_2\text{O}$ buffer and both with and without the addition of 0.5 mM TEMPOL in two different magnet strengths (11.0 T and 14.1 T) and at 300 K are presented in Tables 4.3 and 4.4.

The addition of TEMPOL accelerates the relaxation. This was most pronounced for the hydrogens. The ^{13}C relaxation was most accelerated by the increase in the magnetic field strength. The increase in relaxation rate with field suggests that CSA is a major contributor towards relaxation of the carbon nuclei in $[1,4\text{-}^{13}\text{C}_2]$fumarate.

Optimisation of τ Optimisation of n

(a) T$_0$S$_0$-S$_0$T$_0$ subspace (n=12)   (b) T$_0$S$_0$-S$_0$T$_0$ subspace (τ=22 ms)

(c) T$_0$T$_0$-S$_0$S$_0$ subspace (n=4)   (d) T$_0$T$_0$-S$_0$S$_0$ subspace (τ=56 ms)

——— Simulated central peak intensity

•–•–• Observed central peak intensity

•–•–• Outer peaks intensity
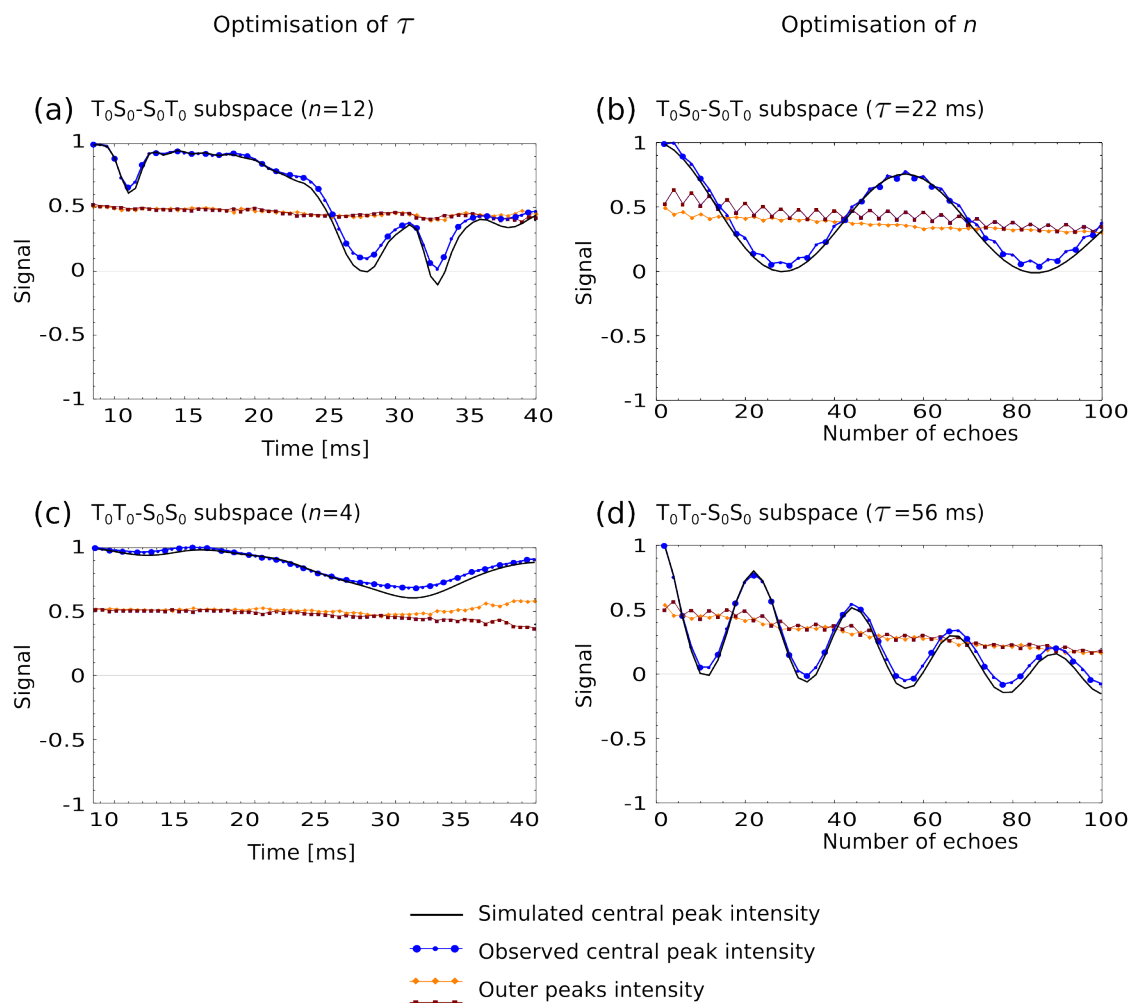
Figure 4.10: Experimental ^{1}H-NMR signal of the central (blue) and outer peaks (red and orange) during variation of τ and n in the pulse sequence shown in Fig. 4.8. The calculated modulation of the peaks was based upon the measured values of the J-couplings $J_{CC'}$, $J_{HH'}$ and ΔJ_{CH} and T_2 (Table 4.1; $T_2 = 4$ s, $J_{CC'} = 6.86$ Hz, $J_{HH'} = 15.84$ Hz, and $\Delta J_{CH} = 2.51$ Hz). Data were recorded at 11.0 T and 300 K.

B_0 [T]	^{13}C-Fumarate	T_1 [s]	T_2 [s]	T_S [s] ($\tau_{ST} = 22$ ms, $n_{ST} = 12$)	T_S [s] ($\tau_{SS} = 56$ ms, $n_{SS} = 5$)
11.0	-	13.1 ± 0.6	6.1 ± 0.4	15.7 ± 0.2	14.5 ± 0.3
	+TEMPOL	7.7 ± 0.1	3.1 ± 0.1	13.1 ± 0.1	10.6 ± 0.5
14.1	-	13.3 ± 0.1	5.7 ± 0.1	14.7 ± 0.2	15.9 ± 0.8
	+TEMPOL	7.6 ± 0.1	2.9 ± 0.1	12.4 ± 0.1	14.1 ± 1.5

Table 4.3: ^{1}H relaxation time constants measurements of 30 mM of [1,4-^{13}C$_2$]fumaric acid dissolved in a ^{2}H$_2$O buffered solution with and without the addition of 0.5 mM of TEMPOL in magnetic field strength of 11.0 T or 14.1 T and at 300 K. Quoted errors are the SD of the repeated measurements.

B_0 [T]	^{13}C-Fumarate	T_1 [s]	T_2 [s]	T_S [s] ($\tau_{ST} = 22$ ms, $n_{ST} = 12$)	T_S [s] ($\tau_{SS} = 56$ ms, $n_{SS} = 5$)
11.0	-	29.2 ± 0.6	12.6 ± 0.1	16.2 ± 0.7	15.4 ± 0.9
	+TEMPOL	25.9 ± 0.4	11.1 ± 0.8	13.0 ± 0.8	10.7 ± 0.5
14.1	-	21.7 ± 0.7	9.4 ± 0.2	15.1 ± 0.5	14.7 ± 1.4
	+TEMPOL	19.5 ± 0.9	8.3 ± 0.1	12.3 ± 2.1	11.1 ± 4.1

Table 4.4: ^{13}C relaxation time constants measurements of 30 mM of [1,4-^{13}C$_2$]fumaric acid dissolved in a ^{2}H$_2$O buffered solution with and without the addition of 0.5 mM of TEMPOL in magnetic field strength of 11.0 T or 14.1 T and at 300 K. Quoted errors are the SD of the repeated measurements.

4.4.4   Singlet-derived signal in [1,4-^{13}C$_2$]fumarate

Taking into account that the singlet state is populated in only one of the subspaces every time one set of resonance parameters (τ and n) are used, the maximum signal stored in the singlet state is already 50% of the initial signal of the central peak. Additional signal loss occurs due to the short T_2 and the intrinsic 2/3 efficiency of the M2S-S2M sequence. Comparing the integral values of the middle peak of [1,4-^{13}C$_2$]fumarate acquired with a 90°-flip angle and after the M2S-S2M sequence (Figure 4.11), the singlet signal is $\sim$ 20-30% of the initial signal. These results agree with the simulations performed using $T_2 = 3$ s for ^{1}H and $T_2 = 11$ s for ^{13}C (Table 4.5).

4.5   Discussion

4.5.1   Signal preservation

The measured relaxation time constants were longer in the buffered solutions than in the non-buffered solutions (Table 4.2). The longest measured lifetime of the system was for ^{13}C in the buffered ^{2}H$_2$O solution, where the T_1 was $\sim$ 30 s. The lifetime in the non-buffered solution was significantly shorter, $T_1 \approx 16$ s, which implies that the buffer is an important component for preserving spin polarisation. The reason for this is not clear.

Accessing the singlet state of the two homonuclear spin-pairs simultaneously, $|S_0 S_0\rangle$, does not guarantee a long-lived state. In the case presented here, the singlet relaxation time constant was longer than the T_1 of protons, but shorter than the T_1 of carbon. The singlet relaxation time constant of $\left|S_0^{\mathrm{H}} S_0^{\mathrm{C}}\right\rangle \left\langle S_0^{\mathrm{H}} S_0^{\mathrm{C}}\right| - \left|T_0^{\mathrm{H}} T_0^{\mathrm{C}}\right\rangle \left\langle T_0^{\mathrm{H}} T_0^{\mathrm{C}}\right|$, $T_S(56$ ms$)$, did not depend on whether the experiment was performed acquiring proton or carbon signals. The relaxation time constant for the other subspace, $T_S(22$ ms$)$, was also found to be the same when acquiring proton or carbon signals. A major hindrance to the utility of singlet populations in [1,4-^{13}C$_2$]fumarate is the fact that the M2S populates only one of the subspaces, either $|T_0 T_0\rangle \leftrightarrow |S_0 S_0\rangle$ or $|T_0 S_0\rangle \leftrightarrow |S_0 T_0\rangle$, and therefore the maximum signal stored in the singlet state is at best 50% of the initial signal regardless of whether the state is shorter or longer-lived. As illustrated in Figure 4.7, there are four transitions contributing to the middle peak of the [1,4-^{13}C$_2$]fumarate spectrum, and after the M2S-S2M pulse sequence only two of these transitions are preserved. Additional signal loss occurs due to the short T_2 and the intrinsic 2/3 efficiency of the M2S sequence. These losses are consistent with the observed ratio of approximately 20-30% between the intensity of the signal acquired after the M2S-S2M sequence and that after a 90° pulse.

Magnetisation after M2S+S2M	$S_{\text{singlet}}/S_{\text{central}}$ ($\tau_{ST} = 22$ ms, $n_{ST} = 12$)		$S_{\text{singlet}}/S_{\text{central}}$ ($\tau_{SS} = 56$ ms, $n_{SS} = 5$)	
	^{1}H	^{13}C	^{1}H	^{13}C
Simulated	26%	31%	25%	31%
Experimental	27%	29%	23%	23%
Max theoretical	33%	33%	33%	33%

Table 4.5: Ratio between the integral of the central ^{1}H peak in fumarate after the M2S-S2M sequence (delay between M2S and S2M of 1 μs, 90° pulse width of 11.6 μs) and that after a 90°-acquire. The theoretical maxima, 'Max theoretical', were calculated assuming no T_2 relaxation.
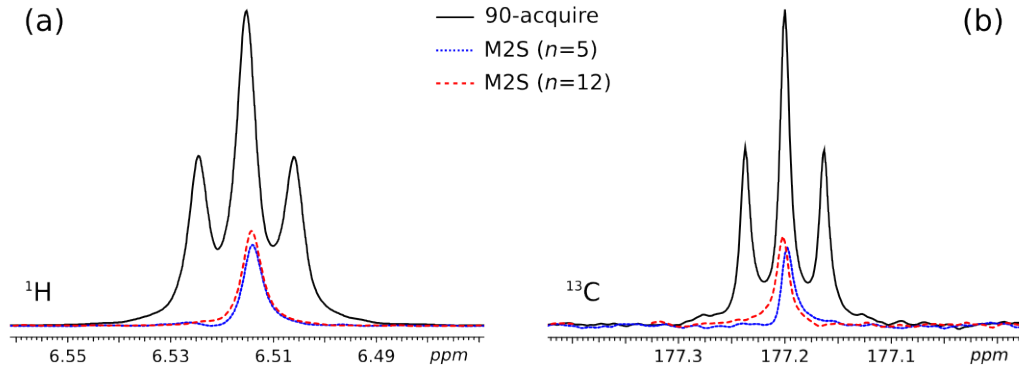
Figure 4.11: Spectrum of 30 mM of [1,4-^{13}C$_2$]fumarate in ^{2}H$_2$O buffer with 0.5 mM TEMPOL after a 90-acquire or the M2S sequence to access each of the subspaces (either $\tau_{SS} = 56$ ms and $n_{SS} = 5$, or $\tau_{ST} = 22$ ms and $n_{ST} = 12$). (a) ^{1}H spectrum (4 scans, 0.5 Hz line broadening), and (b) ^{13}C spectrum (16 scans, 1 Hz line broadening).

4.5.2   Field dependent studies of the relaxation

The main relaxation mechanisms that affect the longitudinal relaxation rate of [1,4-^{13}C$_2$]fumarate, $R_1 = 1/T_1$, are the intra- and intermolecular dipolar relaxation, R_1^{d}, the paramagnetic relaxation if the nitroxide radical TEMPOL is added, R_1^{TEMPOL}, and the CSA relaxation, R_1^{CSA}, (Section 1.4.2):

$$R_1 = R_1^{\mathrm{d}} + R_1^{\mathrm{TEMPOL}} + R_1^{\mathrm{CSA}}. \tag{4.30}$$

The field-dependent CSA may be defined in turn with the CSA-factor ε (Ardenkjaer-Larsen *et al.*, 2011) as

$$R_1^{\mathrm{CSA}} = B_0^2 \varepsilon. \tag{4.31}$$

Knowing R_1 of the same sample at two different magnetic fields, ε may be determined both for ^{1}H and ^{13}C using the relaxation time constants measured for [1,4-^{13}C$_2$]fumarate dissolved in ^{2}H$_2$O buffer at 11.0 T and 14.1 T (Tables 4.3 and 4.4):

$$\varepsilon = \frac{R_1(B_0^{(1)}) - R_1(B_0^{(2)})}{(B_0^{(1)})^2 - (B_0^{(2)})^2}. \tag{4.32}$$

Once the CSA term is quantified, the dipolar relaxation contribution can be calculated from the T_1 values of [1,4-^{13}C$_2$]fumarate dissolved in H$_2$O buffer or ^{2}H$_2$O buffer at 11.0 T (Table 4.2):

$$R_1^{\mathrm{d}} = R_1 - R_1^{\mathrm{CSA}}. \tag{4.33}$$

The paramagnetic relaxation term may be characterised by subtracting the relaxation rate constants of the same sample dissolved in the same buffer with and without TEMPOL displayed in Tables 4.3 and 4.4:

$$R_1^{\mathrm{TEMPOL}} = R_1^{\mathrm{with}} + R_1^{\mathrm{without}}. \tag{4.34}$$

Using the measurements presented in Table 4.3, the terms contributing to ^{1}H relaxation of [1,4-^{13}C$_2$]fumarate can be calculated: $\varepsilon = 1.1 \cdot 10^{-5}$ and $T_1^{\mathrm{CSA}} = 744$ s at 11.0 T and 453 s at 14.1 T. The dipolar term in ^{2}H$_2$O buffer is $T_1^{\mathrm{d}} = 12.9$ s, while in H$_2$O buffer it is 5.2 s. And the paramagnetic relaxation induced by the addition of TEMPOL is $T_1^{\mathrm{TEMPOL}} = 18.4$ s at 11.0 T and 17.6 s at 14.1 T.

The same can be calculated for ^{13}C with the measurements in Table 4.4: $\varepsilon = 1.5 \cdot 10^{-4}$ and

$T_1^{\text{CSA}} = 54.4$ s at 11.0 T and 33.1 s at 14.1T. The dipolar term in $^2\text{H}_2\text{O}$ buffer is $T_1^{\text{d}} = 62.8$ s, while in H_2O buffer it is 46.6 s. And the paramagnetic relaxation induced by the addition of TEMPOL is $T_1^{\text{TEMPOL}} = 234$ s at 11.0 T and 191 s at 14.1 T.

These findings support the hypothesis that CSA relaxation is the dominant relaxation mechanism of the carbon pair in [1,4-$^{13}\text{C}_2$]fumarate, while dipolar and paramagnetic relaxation are more important for the relaxation of the proton pair.

The T_S measurements at 11.0 T and 14.1 T presented in tables 4.3 and 4.4 were unaffected by the magnetic field increase, which implies that CSA is not the dominant relaxation mechanism of the singlet subspaces of [1,4-$^{13}\text{C}_2$]fumarate. On the other hand, adding TEMPOL to the sample decreases T_S. It affects the subspace with $\tau_{SS} = 56$ ms at least twice as much as the subspace with $\tau_{ST} = 22$ ms, with $T_S^{\text{TEMPOL}}(56 \text{ ms}) \approx 40$ s for both ^1H and ^{13}C , and $T_S^{\text{TEMPOL}}(22 \text{ ms}) \approx 80$ s for ^1H $T_S^{\text{TEMPOL}}(22 \text{ ms}) \approx 65$ s for ^{13}C. $T_S^{\text{TEMPOL}}(56 \text{ ms})$ for ^1H at 14.0 T differs from the other $T_S^{TEMPOL}(56 \text{ ms})$ measurements, both for ^1H and ^{13}C, by being about 4 times less affected by the radical addition, with $T_S^{\text{TEMPOL}}(56 \text{ ms}) \approx 128$ s. However, such discrepancy may be attributed to the large error of the measurement.

4.5.3   [2,3-$^{13}\text{C}_2$]fumarate

[2,3-$^{13}\text{C}_2$]fumarate does not support singlet and triplet eigenstates under free evolution due to the large one-bond coupling between C2 and H2 ($J_{\text{C2H2}} = 161$ Hz). The difference $|\Delta J_{\text{CH}}| = 158.1$ Hz is much larger than the sum $|J_{\text{CC}'} + J_{\text{HH}'}| = 84.2$ Hz and difference $|J_{\text{CC}'} - J_{\text{HH}'}| = 52.8$ Hz (Table 4.1, Figure 4.3). A long-lived singlet-state is not expected, as result. In principle, one can force isolation between the singlet and triplet states by applying a spin lock on either nucleus, suppressing the heteronuclear J-couplings, although the relaxation is likely to be much faster due to the strong one-bond CH dipole-dipole coupling. Additionally, since T_2 relaxation of [2,3-$^{13}\text{C}_2$]fumarate is faster than for the other isotoplogues of ^{13}C-fumarate, there would be an important loss of signal during the M2S pulse sequence.

4.6   Summary and future perspectives

In this chapter it has been shown that accessing the singlet state of both carbon and proton pairs of [1,4-$^{13}\text{C}_2$]fumarate is made possible by the M2S pulse sequence.

The situation $|J_{\text{CC}'} \pm J_{\text{HH}'}| >> |J_{\text{CH}} - J_{\text{CH}}'|$ in [1,4-$^{13}\text{C}_2$]fumarate eliminates the need to sustain the singlet-triplet population difference, unlike [2,3-$^{13}\text{C}_2$]fumarate where the opposite is found.

It has been noted that although ^{1}H-NMR could benefit from the slower relaxing singlet, for ^{13}C-NMR it would be detrimental. Therefore, having both ^{1}H$_2$ and ^{13}C$_2$ spin-pairs in the singlet state does not guarantee a longer lifetime, which is worth considering when choosing a contrast agent in which the singlet state is to be exploited.

The singlet relaxation measurements reported in this chapter on [1,4-^{13}C$_2$]fumarate prove that the singlet state can be accessed even in chemically equivalent molecules in which all the J-couplings are of the same order of magnitude. Although the non-trivial resonance pattern makes it more difficult to find the right n and τ from the optimisation curves, it gives useful information about the relative magnitude of the homonuclear couplings and the chemical equivalence of the spin pairs. Unfortunately, the fact that $J_{CC'}$ and $J_{HH'}$ are of similar magnitude means the magnetisation-singlet conversion is rather inefficient using the M2S pulse sequence, generating about 50% of the maximum singlet order available when either $|J_{CC'}| << |J_{HH'}|$, or $|J_{CC'}| >> |J_{HH'}|$.

4.6.1   Adaptation for a DNP experiment

In the presence of the enzyme fumarase, fumarate undergoes a reversible conversion into malate (Figure 4.12a). The OH- group in C2 of malate results in the lower molecular symmetry and the chemical inequivalence of the hydrogen and carbon nuclei. The ^{13}C-NMR peaks of fumarate are found at 177.2 ppm (C1 and C4) and 138.0 ppm (C2 and C3); malate's peaks are found at 183.5 ppm (C1), 182.4 ppm (C2), 73.1 ppm (C3) and 45.3 ppm (C4).

In a typical DNP experiment, [1,4-^{13}C$_2$]fumarate is injected into a test tube with cells/enzyme immediately after dissolution. As shown in Figure 4.12b, ^{13}C-NMR signal is sampled every second and decay of the fumarate polarisation is observed while malate's signal builds up as it is being produced, before later decaying.

A proposed experiment that combines DNP and the singlet state would involve addition of cells/enzyme after the polarisation of fumarate has been stored in the singlet state using the M2S pulse sequence. Signal acquisition would then be performed in the conventional way, sampling every second with a small flip-angle radiofrequency pulse. Since fumarate is locked in the non-magnetic singlet state, only malate would be observed in the NMR spectra. The malate signal would increase as the metabolite pool built up, until it reached a plateau when equilibrium was established (Figure 4.12c). In an idealised situation, where the polarisation of fumarate is long-lived in the singlet state, malate signal could be observed for a longer time than it would be in a typical DNP experiment. When information on fumarate's signal was required, the S2M pulse sequence could be applied to bring the remaining polarisation back to observable magnetisation.

The relatively short singlet relaxation time constant and weak singlet-derived signal measured in this work for $[1,4\text{-}^{13}C_2]$fumarate makes the combination of DNP and singlet state non-advantageous for this particular metabolite. However, this idea could be used for chemically equivalent substrates with long singlet relaxation lifetimes and whose symmetry is broken after a chemical reaction.
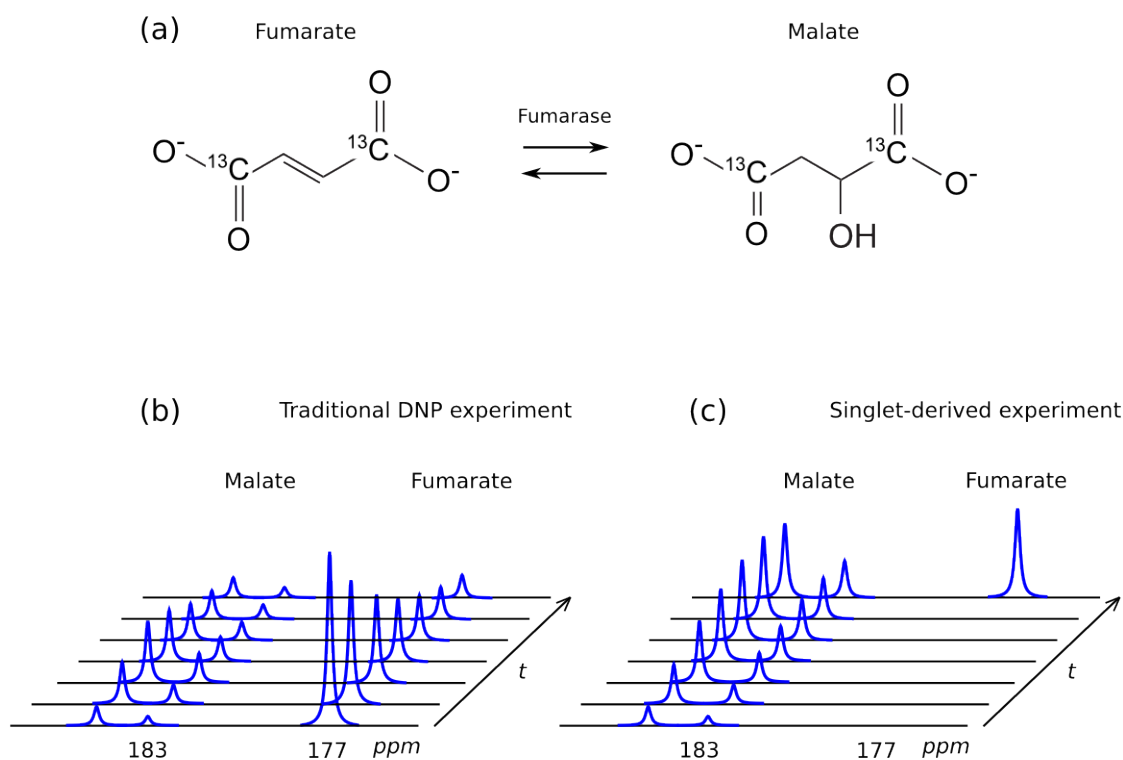
Figure 4.12: (a) Fumarate-malate enzymatic exchange reaction. (b) Representation of the ^{13}C-NMR spectra of a typical time-evolution DNP experiment of $[1,4\text{-}^{13}C_2]$fumarate in presence of fumarase. Hyperpolarised fumarate signal decays while malate's signal builds up and then decays. (c) Experiment that combines DNP and singlet NMR. Polarisation of $[1,4\text{-}^{13}C_2]$fumarate is stored in the spin-0 state (M2S sequence) before the enzyme is added to the sample. Malate's peaks are the only ones observed in the ^{13}C-NMR spectra until fumarate's polarisation is converted back into observable magnetisation with the S2M pulse sequence.

4.6.2   Longer-lived states

Regarding symmetric properties of the states under swapping of spin labels, the eigenbasis of the Hamiltonian of a strongly coupled pair of spins-1/2 contains three symmetric states (triplet) and one anti-symmetric state (singlet). The longest lived spin order is that corresponding to population difference between states that are symmetric and antisymmetric with respect to permuting the nuclei of the pair, since the dipolar Hamiltonian cannot induce transitions across this symmetry.

As we have shown here, the eigenbasis of the Hamiltonian of an AA'XX' system of four spins-1/2 is composed of 16 eigenstates. We have evaluated the singlet relaxation taking the singlet states of each pair. However, a new symmetry may be defined by swapping the spin labels of both the carbon and proton pairs simultaneously. If the sign of the states under permutation of the spin label remains the same, the states are said to be symmetric. If the sign changes, they are anti-symmetric. A symmetric Hamiltonian under these conditions cannot induce transitions between symmetric and anti-symmetric states. J-coupling relaxation is always a symmetric interaction under simultaneous permutation of AA' and XX', denoted (AA')(XX'), since it does not depend on the molecular geometry. The symmetry under (AA')(XX') of the dipolar Hamiltonian, on the other hand, relies on the centre of inversion in the molecule. In fumarate, dipolar relaxation is a symmetric interaction under (AA')(XX') because the CH dipolar couplings are parallel.Transitions between symmetric and anti-symmetric states are forbidden under symmetric perturbations (Figure 4.13). However, symmetric perturbations may relax the states within each symmetry group. A potentially longer relaxation rate could be found between the block of symmetric states and the block of anti-symmetric states. Of the 16 states only 6 are anti-symmetric: $|T_{+1}S_0\rangle$, $|T_{-1}S_0\rangle$, $|T_0S_0\rangle$, $|S_0T_0\rangle$, $|S_0T_{+1}\rangle$ and $|S_0T_{-1}\rangle$. It is noteworthy that is $|S_0S_0\rangle$ symmetric under simultaneous permutation of both carbon and proton labels.
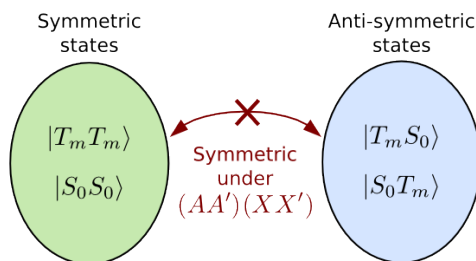
Figure 4.13: Symmetry-allowed transitions between spin states. Transitions between symmetric and anti-symmetric states are symmetry-forbidden.

4.7   Appendix

The matrix representation of the Hamiltonian in the **_Zeeman eigenbasis_**

$$\left\{ |\alpha\alpha\alpha\alpha\rangle, |\beta\alpha\alpha\alpha\rangle, |\alpha\beta\alpha\alpha\rangle, |\beta\beta\alpha\alpha\rangle, |\alpha\alpha\beta\alpha\rangle, |\beta\alpha\beta\alpha\rangle, |\alpha\beta\beta\alpha\rangle, |\beta\beta\beta\alpha\rangle, \right.$$
$$\left. |\alpha\alpha\alpha\beta\rangle, |\beta\alpha\alpha\beta\rangle, |\alpha\beta\alpha\beta\rangle, |\beta\beta\alpha\beta\rangle, |\alpha\alpha\beta\beta\rangle, |\beta\alpha\beta\beta\rangle, |\alpha\beta\beta\beta\rangle, |\beta\beta\beta\beta\rangle \right\}$$

is the following:

$$H^{Zeeman} = \pi \begin{pmatrix}
H_1 & 0 & 0 & 0 & 0 & 0 & 0 & 0 & 0 & 0 & 0 & 0 & 0 & 0 & 0 & 0 \\
0 & H_2 & J_{\mathrm{HH'}} & 0 & 0 & 0 & 0 & 0 & 0 & 0 & 0 & 0 & 0 & 0 & 0 & 0 \\
0 & J_{\mathrm{HH'}} & H_3 & 0 & 0 & 0 & 0 & 0 & 0 & 0 & 0 & 0 & 0 & 0 & 0 & 0 \\
0 & 0 & 0 & H_4 & 0 & 0 & 0 & 0 & 0 & 0 & 0 & 0 & 0 & 0 & 0 & 0 \\
0 & 0 & 0 & 0 & H_5 & 0 & 0 & 0 & J_{\mathrm{CC'}} & 0 & 0 & 0 & 0 & 0 & 0 & 0 \\
0 & 0 & 0 & 0 & 0 & H_6 & J_{\mathrm{HH'}} & 0 & 0 & J_{\mathrm{CC'}} & 0 & 0 & 0 & 0 & 0 & 0 \\
0 & 0 & 0 & 0 & 0 & J_{\mathrm{HH'}} & H_7 & 0 & 0 & 0 & J_{\mathrm{CC'}} & 0 & 0 & 0 & 0 & 0 \\
0 & 0 & 0 & 0 & 0 & 0 & 0 & H_8 & 0 & 0 & 0 & J_{\mathrm{CC'}} & 0 & 0 & 0 & 0 \\
0 & 0 & 0 & 0 & J_{\mathrm{CC'}} & 0 & 0 & 0 & H_9 & 0 & 0 & 0 & 0 & 0 & 0 & 0 \\
0 & 0 & 0 & 0 & 0 & J_{\mathrm{CC'}} & 0 & 0 & 0 & H_{10} & J_{\mathrm{HH'}} & 0 & 0 & 0 & 0 & 0 \\
0 & 0 & 0 & 0 & 0 & 0 & J_{\mathrm{CC'}} & 0 & 0 & J_{\mathrm{HH'}} & H_{11} & 0 & 0 & 0 & 0 & 0 \\
0 & 0 & 0 & 0 & 0 & 0 & 0 & J_{\mathrm{CC'}} & 0 & 0 & 0 & H_{12} & 0 & 0 & 0 & 0 \\
0 & 0 & 0 & 0 & 0 & 0 & 0 & 0 & 0 & 0 & 0 & 0 & H_{13} & 0 & 0 & 0 \\
0 & 0 & 0 & 0 & 0 & 0 & 0 & 0 & 0 & 0 & 0 & 0 & 0 & H_{14} & J_{\mathrm{HH'}} & 0 \\
0 & 0 & 0 & 0 & 0 & 0 & 0 & 0 & 0 & 0 & 0 & 0 & 0 & J_{\mathrm{HH'}} & H_{15} & 0 \\
0 & 0 & 0 & 0 & 0 & 0 & 0 & 0 & 0 & 0 & 0 & 0 & 0 & 0 & 0 & H_{16}
\end{pmatrix}.$$

with

$$H_1 = \frac{1}{2}(J_{\mathrm{CC'}} + J_{\mathrm{HH'}}) + \pi(J_{\mathrm{CH}} + J'_{\mathrm{CH}}) + \omega_{\mathrm{H}} + \omega_{\mathrm{H}},$$

$$H_2 = \frac{1}{2}(J_{\mathrm{CC'}} - J_{\mathrm{HH'}}) + \omega_{\mathrm{C}},$$

$$H_3 = H2,$$

$$H_4 = \frac{1}{2}(J_{\mathrm{CC'}} + J_{\mathrm{HH'}}) - \pi(J_{\mathrm{CH}} + J'_{\mathrm{CH}}) + \omega_{\mathrm{C}} - \omega_{\mathrm{H}},$$

$$H_5 = \frac{-1}{2}(J_{\mathrm{CC'}} - J_{\mathrm{HH'}}) + \omega_{\mathrm{H}},$$

$$H_6 = \frac{-1}{2}(J_{\mathrm{CC'}} + J_{\mathrm{HH'}}) + \pi(J_{\mathrm{CH}} - J'_{\mathrm{CH}}),$$

$$H_7 = \frac{-1}{2}(J_{\mathrm{CC'}} + J_{\mathrm{HH'}}) - \pi(J_{\mathrm{CH}} - J'_{\mathrm{CH}}),$$

$$H_8 = \frac{-1}{2}(J_{\mathrm{CC'}} - J_{\mathrm{HH'}}) - \omega_{\mathrm{H}},$$

$$H_9 = H_5,$$

$$H_{10} = \frac{-1}{2}(J_{\mathrm{CC'}} + J_{\mathrm{HH'}}) - \pi(J_{\mathrm{CH}} - J'_{\mathrm{CH}}),$$

$$H_{11} = \frac{-1}{2}(J_{\mathrm{CC'}} + J_{\mathrm{HH'}}) + \pi(J_{\mathrm{CH}} - J'_{\mathrm{CH}}),$$

$$H_{12} = H_8,$$

$$H_{13} = \frac{1}{2}(J_{\mathrm{CC'}} + J_{\mathrm{HH'}}) - \pi(J_{\mathrm{CH}} + J'_{\mathrm{CH}}) - \omega_{\mathrm{C}} + 2\omega_{\mathrm{H}},$$

$$H_{14} = \frac{1}{2}(J_{\mathrm{CC'}} - J_{\mathrm{HH'}}) - \omega_{\mathrm{C}},$$

$$H_{15} = H_{14},$$

$$H_{16} = \frac{1}{2}(J_{\mathrm{CC'}} + J_{\mathrm{HH'}}) + \pi(J_{\mathrm{CH}} + J'_{\mathrm{CH}}) - \omega_{\mathrm{C}} - \omega_{\mathrm{H}}.$$

The matrix representation of the Hamiltonian in the **singlet-triplet eigenbasis**

$$\left\{ \left|S_0^{\mathrm{C}}T_0^{\mathrm{H}}\right\rangle, \left|S_0^{\mathrm{C}}T_{-1}^{\mathrm{H}}\right\rangle, \left|T_0^{\mathrm{C}}S_0^{\mathrm{H}}\right\rangle, \left|S_0^{\mathrm{C}}T_{+1}^{\mathrm{H}}\right\rangle, \left|S_0^{\mathrm{C}}S_0^{\mathrm{H}}\right\rangle, \left|T_0^{\mathrm{C}}T_{-1}^{\mathrm{H}}\right\rangle, \left|T_0^{\mathrm{C}}T_0^{\mathrm{H}}\right\rangle, \left|T_0^{\mathrm{C}}T_{+1}^{\mathrm{H}}\right\rangle, \right.$$

$$\left. \left|T_{-1}^{\mathrm{C}}S_0^{\mathrm{H}}\right\rangle, \left|T_{+1}^{\mathrm{C}}S_0^{\mathrm{H}}\right\rangle, \left|T_{-1}^{\mathrm{C}}T_{-1}^{\mathrm{H}}\right\rangle, \left|T_{-1}^{\mathrm{C}}T_0^{\mathrm{H}}\right\rangle, \left|T_{-1}^{\mathrm{C}}T_{+1}^{\mathrm{H}}\right\rangle, \left|T_{+1}^{\mathrm{C}}T_{-1}^{\mathrm{H}}\right\rangle, \left|T_{+1}^{\mathrm{C}}T_0^{\mathrm{H}}\right\rangle, \left|T_{+1}^{\mathrm{C}}T_{+1}^{\mathrm{H}}\right\rangle \right\}$$

is the following:

$$H^{ST} = \begin{pmatrix}
H_1 & 0 & \pi\Delta J_{\mathrm{CH}} & 0 & 0 & 0 & 0 & 0 & 0 & 0 & 0 & 0 & 0 & 0 & 0 & 0 \\
0 & H_2 & 0 & 0 & 0 & 0 & 0 & 0 & 0 & 0 & 0 & 0 & 0 & 0 & 0 & 0 \\
\pi\Delta J_{\mathrm{CH}} & 0 & H_3 & 0 & 0 & 0 & 0 & 0 & 0 & 0 & 0 & 0 & 0 & 0 & 0 & 0 \\
0 & 0 & 0 & H_4 & 0 & 0 & 0 & 0 & 0 & 0 & 0 & 0 & 0 & 0 & 0 & 0 \\
0 & 0 & 0 & 0 & H_5 & 0 & \pi\Delta J_{\mathrm{CH}} & 0 & 0 & 0 & 0 & 0 & 0 & 0 & 0 & 0 \\
0 & 0 & 0 & 0 & 0 & H_6 & 0 & 0 & 0 & 0 & 0 & 0 & 0 & 0 & 0 & 0 \\
0 & 0 & 0 & 0 & \pi\Delta J_{\mathrm{CH}} & 0 & H_7 & 0 & 0 & 0 & 0 & 0 & 0 & 0 & 0 & 0 \\
0 & 0 & 0 & 0 & 0 & 0 & 0 & H_8 & 0 & 0 & 0 & 0 & 0 & 0 & 0 & 0 \\
0 & 0 & 0 & 0 & 0 & 0 & 0 & 0 & H_9 & 0 & 0 & 0 & 0 & 0 & 0 & 0 \\
0 & 0 & 0 & 0 & 0 & 0 & 0 & 0 & 0 & H_{10} & 0 & 0 & 0 & 0 & 0 & 0 \\
0 & 0 & 0 & 0 & 0 & 0 & 0 & 0 & 0 & 0 & H_{11} & 0 & 0 & 0 & 0 & 0 \\
0 & 0 & 0 & 0 & 0 & 0 & 0 & 0 & 0 & 0 & 0 & H_{12} & 0 & 0 & 0 & 0 \\
0 & 0 & 0 & 0 & 0 & 0 & 0 & 0 & 0 & 0 & 0 & 0 & H_{13} & 0 & 0 & 0 \\
0 & 0 & 0 & 0 & 0 & 0 & 0 & 0 & 0 & 0 & 0 & 0 & 0 & H_{14} & 0 & 0 \\
0 & 0 & 0 & 0 & 0 & 0 & 0 & 0 & 0 & 0 & 0 & 0 & 0 & 0 & H_{15} & 0 \\
0 & 0 & 0 & 0 & 0 & 0 & 0 & 0 & 0 & 0 & 0 & 0 & 0 & 0 & 0 & H_{16}
\end{pmatrix}.$$

with

$$\Delta J_{\mathrm{CH}} = (J_{\mathrm{CH}} - J'_{\mathrm{CH}}),$$

and

$$
\begin{aligned}
H_1 &= \frac{-\pi}{2}(3J_{\mathrm{CC'}} - J_{\mathrm{HH'}}), \\
H_2 &= \frac{\pi}{2}(J_{\mathrm{CC'}} - 3J_{\mathrm{HH'}}) - \omega_{\mathrm{C}}, \\
H_3 &= \frac{\pi}{2}(J_{\mathrm{CC'}} - 3J_{\mathrm{HH'}}), \\
H_4 &= \frac{\pi}{2}(J_{\mathrm{CC'}} - 3J_{\mathrm{HH'}}) + \omega_{\mathrm{C}}, \\
H_5 &= \frac{-3\pi}{2}(J_{\mathrm{CC'}} + J_{\mathrm{HH'}}), \\
H_6 &= \frac{\pi}{2}(J_{\mathrm{CC'}} + J_{\mathrm{HH'}}) - \omega_{\mathrm{C}}, \\
H_7 &= \frac{\pi}{2}(J_{\mathrm{CC'}} + J_{\mathrm{HH'}}), \\
H_8 &= \frac{\pi}{2}(J_{\mathrm{CC'}} + J_{\mathrm{HH'}}) + \omega_{\mathrm{C}}, \\
H_9 &= \frac{\pi}{2}(-3J_{\mathrm{CC'}} + J_{\mathrm{HH'}}) - \omega_{\mathrm{C}}, \\
H_{10} &= \frac{-\pi}{2}(3J_{\mathrm{CC'}} - J_{\mathrm{HH'}}) + \omega_{\mathrm{H}}, \\
H_{11} &= \frac{\pi}{2}(J_{\mathrm{CC'}} + J_{\mathrm{HH'}}) + \pi(J_{\mathrm{CH}} + J'_{\mathrm{CH}}) - \omega_{\mathrm{C}} - \omega_{\mathrm{H}}, \\
H_{12} &= \frac{\pi}{2}(J_{\mathrm{CC'}} + J_{\mathrm{HH'}}) - \omega_{\mathrm{H}}, \\
H_{13} &= \frac{\pi}{2}(J_{\mathrm{CC'}} + J_{\mathrm{HH'}}) - \pi(J_{\mathrm{CH}} + J'_{\mathrm{CH}}) + \omega_{\mathrm{C}} - \omega_{\mathrm{H}}, \\
H_{14} &= \frac{\pi}{2}(J_{\mathrm{CC'}} + J_{\mathrm{HH'}}) - \pi(J_{\mathrm{CH}} + J'_{\mathrm{CH}}) - \omega_{\mathrm{C}} + \omega_{\mathrm{H}}, \\
H_{15} &= \frac{\pi}{2}(J_{\mathrm{CC'}} + J_{\mathrm{HH'}}) + \omega_{\mathrm{H}}, \\
H_{16} &= \frac{\pi}{2}(J_{\mathrm{CC'}} + J_{\mathrm{HH'}}) + \pi(J_{\mathrm{CH}} + J'_{\mathrm{CH}}) + \omega_{\mathrm{C}} + \omega_{\mathrm{H}}.
\end{aligned}
$$

Conclusions

<div align="right">

5

</div>

In this work, we aimed to preserve hyperpolarised spin order in substrates used for cancer metabolism studies. Two methods were explored, with the theory and experiments being presented in this thesis: Spin Polarisation Induced NOE (SPINOE) and potentially long-lived singlet states.

The main outcomes of this work are as follows:

5.1 Summary of Chapter 2

- The SPINOE depends on the ratio of solute (^{13}C) and proton solvent spins. Using partially deuterated solvent would increase the SPINOE magnitude, albeit at the cost of reducing the ^{1}H-NMR signal intensity arising from the solvent.

- The SPINOE also depends on the ratio of the cross-relaxation rate constant between solute (^{13}C) and solvent spins to the longitudinal relaxation time constant of solvent protons, which is itself dependent on the magnetic field strength.

- Since SPINOE increases at lower field strengths, at the magnetic field strengths used in the clinic (1.5-3 T) the effect is expected to be easily detectable.

- We propose using the SPINOE effect, directly linked to the inevitable loss of ^{13}C polarisation caused by cross-relaxation, to follow the progress of a bolus of hyperpolarised ^{13}C-labeled material in the bloodstream by acquiring ^{1}H-NMR signal from solvent protons. The ^{13}C

polarisation would then be preserved until it reaches the site of interest, when signal would be acquired to probe the metabolic reaction pathway.

- The SPINOE effect was demonstrated with $[1,4\text{-}^{13}\text{C}_2]$fumarate dissolved in an aqueous buffer.

5.2 Summary of Chapter 3

Pyruvate is the most-widely used substrate in DNP studies of cancer metabolism. Accessing the singlet state of the weakly coupled ^{13}C-spin pair of $[1,2\text{-}^{13}\text{C}_2]$pyruvate was studied with three approaches:

1. Direct enhancement of nuclear singlet order at low field

- Singlet order in hyperpolarised $[1,2\text{-}^{13}\text{C}_2]$pyruvate was shown to be longer-lived than the longitudinal magnetisation at low field, in $^2\text{H}_2\text{O}$ buffer, in BSA solution, in whole human blood *in vitro* and in a mouse *in vivo*.

- Comparing T_S at low field with T_1 at high field in blood revealed that T_1 for both carbons at high field was between 1.5 and 2 times longer than T_S at low field. Therefore, minimising the time the pyruvate sample experiences a low field is recommended.

- Furthermore, using $[1,2\text{-}^{13}\text{C}_2]$pyruvate instead of $[1\text{-}^{13}\text{C}]$pyruvate offers no advantage in terms of preservation of the polarisation; while the T_S for $[1,2\text{-}^{13}\text{C}_2]$pyruvate in $^2\text{H}_2\text{O}$ buffer is approximately twice T_1^{LF} of the same molecule, it is not significantly longer than the T_1^{LF} of $[1\text{-}^{13}\text{C}]$pyruvate. Conversely, in blood at low field there is a distinct benefit of using $[1,2\text{-}^{13}\text{C}_2]$pyruvate.

- During metabolic studies, information on whether the reaction occurred at low or high field can be obtained as long as the metabolic product of the substrate preserves the pair bond and the chemical shift difference of the pair has opposite sign to that of the substrate. This is the case of the hydration reaction from pyruvate to pyruvate hydrate. However, the long lifetime cannot provide additional information on the metabolic conversion of pyruvate to lactate since the singlet state is not preserved in the high magnetic field, due to the large C1-C2 chemical shift difference.

2. Pulse sequences after DNP

- Converting the longitudinal polarisation using a pulse sequence with suitable hardware may access larger amounts of singlet order.

- Conversion of all available spin order into singlet order, with the attendant increase in measured signal, would be an advantage in a clinical setting.

3. Suppressing chemical shift difference with decoupling at high field

- Accessing the singlet state of [1,2-^{13}C$_2$]pyruvate at high field and storing it while applying a decoupling sequence to bring the ^{13}C-pair into chemical equivalence. The decoupling field would also remove the scalar coupling of ^{13}C to the nearby protons and a longer T_S may be found.

- Since a decoupling radiofrequency field of 40 kHz needed to be applied for a few minutes, micro-coil NMR was the approach chosen.

- Singlet state of [1,2-^{13}C$_2$]pyruvate was accessed and converted back to observable magnetisation, albeit T_S was shorter than T_1. This was a consequence of pyruvate hydrate being present in the aqueous solutions used; the singlet state could not be fully isolated by the 40 kHz-radiofrequency field, which could not decouple C2 of pyruvate hydrate.

5.3   Summary of Chapter 4

- The singlet states of both carbon and proton pairs of [1,4-^{13}C$_2$]fumarate were accessed using the M2S pulse sequence at high-field and their relaxation time constant T_S measured.

- Since $|J_{CC'} \pm J_{HH'}| >> |J_{CH} - J'_{CH}|$ in [1,4-^{13}C$_2$]fumarate, there is no need to sustain the singlet-triplet population difference, unlike [2,3-^{13}C$_2$]fumarate where the carbon and hydrogen spin pairs are both far from magnetic equivalence due to the strong $^1J_{CH}$ coupling.

- Having both ^{1}H$_2$ and ^{13}C$_2$ spin-pairs in the singlet state does not guarantee the longest lived lifetime: although the singlet relaxation time constant is about twice the longitudinal relaxation time constant of the protons ($T_S \simeq 2 \times T_1^H$), it is half that of the carbons ($T_S \simeq 0.5 \times T_1^C$).

- Despite the disappointing lifetime of the states accessed in this work, we have shown for the first time that the singlet state can be accessed even in chemically equivalent molecules in which all the J-couplings are of the same order of magnitude.

- The resonance pattern observed during the optimisation of the M2S parameters n and τ provides useful information on the relative magnitude of the homonuclear couplings and the chemical equivalence of the spin pairs. To highlight two: (i) if each pair is composed of chemically equivalent spins, only the central peak resonates; (ii) if one of the homonuclear couplings is zero, both the triplet-triplet and the singlet-triplet product state subspaces resonate under the same conditions, and inversion of the central peak is observed in the optimisation curve.

- A drawback of the fact that $|J_{CC'}|$ and $|J_{HH'}|$ are of similar magnitude in $[1,4\text{-}^{13}C_2]$fumarate means the magnetisation-singlet conversion is rather inefficient using the M2S pulse sequence, generating about 50% of the maximum singlet order possible when either $|J_{CC'}| << |J_{HH'}|$, or $|J_{CC'}| >> |J_{HH'}|$.

5.4 Future perspectives

Preserving hyperpolarisation of endogenous metabolites using singlet order does not seem to be the solution to the fast decay of the DNP signal. Long-lived singlet states have been found in molecules with high pair-symmetry in which the symmetry-breaking element was far from the pair and in isolated spin-pairs with no other spins interacting with the pair (Tayler, 2012), e.g. no protons coupled with the ^{13}C pair of interest. Since the opportunities to modify endogenous metabolites are limited, in most cases restricted to deuteration of the substrate and the solvent, satisfying the high-symmetry requirement is unlikely.

Work towards synthetic molecules that satisfy all the properties required for a long-lived spin order has already led to very impressive results for singlet relaxation time constants, such as acetylene derivatives with $T_S \approx 15$ min (Pileio *et al.*, 2012) or $^{15}N_2O$ with $T_S \approx 20$ min (Ghosh *et al.*, 2011). These substrates, however, are either toxic to the human body or do not undergo reactions, so provide at best information on perfusion kinetics. The challenge of obtaining a slow-relaxing substrate that can provide information on metabolic reactions still remains.

References

Abragam, A. and Goldman, M. 1978. *Principles of dynamic nuclear polarization.* Rep. Progr. Phys., 41, 70.

Albers, M. J., Bok, R., Chen, A. P., Cunningham, C. H., Zierhut, M. L., Zhang, V. Y., Kohler, S. J., Tropp, J., Hurd, R. E., Yen, Y. F., Nelson, S. J., Vigneron, D. B. and Kurhanewicz, J. 2008. *Hyperpolarized ^{13}C lactate, pyruvate, and alanine: noninvasive biomarkers for prostate cancer detection and grading.* Cancer Res., 68, 8607-15.

Allouche-Arnon, H., Wade, T., Waldner, L. F., Miller, V. N., Gomori, J. M., Katz-Brull, R. and McKenzie, C. A. 2013. *In vivo magnetic resonance imaging of glucose - initial experience.* Contrast Media Mol. I., 8, 72-82.

Ardenkjaer-Larsen, J. H., Fridlund, B., Gram, A., Hansson, G., Hansson, L., Lerche, M. H., Servin, R., Thaning, M. and Golman, K. 2003. *Increase in signal-to-noise ratio of > 10,000 times in liquid-state NMR.* Proc. Natl. Acad. Sci. USA, 100, 10158-10163.

Ardenkjaer-Larsen, J. H., Johannesson, H., Petersson, J. S. and Wolber, J. 2011. *Hyperpolarized molecules in solution.* In: SCHRODER, L. and FABER, C. (eds.) In vivo NMR imaging: Methods in molecular biology. 2011/08/30 ed.: Springer Science+Business Media.

Augath, M., Heiler, P., Kirsch, S. and Schad, L. R. 2009. *In vivo ^{39}K, ^{23}Na and ^{1}H MR imaging using a triple resonant RF coil setup.* J. Magn. Reson., 200, 134-6.

Bart, J., Janssen, J. W., van Bentum, P. J., Kentgens, A. P. and Gardeniers, J. G. 2009. *Optimization of stripline-based microfluidic chips for high-resolution NMR.* J. Magn. Reson., 201, 175-85.

Bastiaansen, J. A., Cheng, T., Mishkovsky, M., Duarte, J. M., Comment, A. and Gruetter, R. 2013. *In vivo enzymatic activity of acetylCoA synthetase in skeletal muscle revealed by ^{13}C turnover from hyperpolarized [1-^{13}C]acetate to [1-^{13}C]acetylcarnitine.* Biochim. Biophys. Acta, 1830, 4171-8.

Berg, J. M., Tymoczko, J. L. and Stryer, L. 2007. Biochemistry, New York, US, W.H. Freeman and Company.

Bloch, F. 1946. *Nuclear induction.* Phys. Rev., 70, 460-474.

Bloch, F., Hansen, W. W. and Packard, M. 1946. *The nuclear induction experiment.* Phys. Rev., 70, 474-485.

Bohndiek, S. E., Kettunen, M. I., Hu, D.-E., Kennedy, B. W., Boren, J., Gallagher, F. A. and Brindle, K. M. 2011. *Hyperpolarized [1-^{13}C]ascorbic and dehydroascorbic acid: vitamin C as a probe for imaging redox status in vivo.* J. Am. Chem. Soc., 133, 11795-801.

Bohndiek, S. E., Kettunen, M. I., Hu, D.-E., Witney, T. H., Kennedy, B. W. C., Gallagher, F. A. and Brindle, K. M. 2010. *Detection of tumor response to a vascular disrupting agent by hyperpolarized ^{13}C magnetic resonance spectroscopy.* Mol. Cancer Ther., 9, 3278-3288.

Bornet, A., Jannin, S. and Bodenhausen, G. 2011. *Three-field NMR to preserve hyperpolarized proton magnetization as long-lived states in moderate magnetic fields.* Chem. Phys. Letters, 512, 151-154.

Bowen, S. and Hilty, C. 2010. *Rapid sample injection for hyperpolarized NMR spectroscopy.* Phys. Chem. Chem. Phys., 12, 5766-70.

Braun, S. 1978. *High resolution ^{13}C NMR spectroscopy. IV - Stereochemical assignements in butenedioic acid and 3-pentene-2-ones.* Org. Magn. Resonance, 11, 197-203.

Brindle, K. 2008. *New approaches for imaging tumour responses to treatment.* Nat. Rev. Cancer., 8, 94-107.

Brindle, K. M., Bohndiek, S. E., Gallagher, F. A. and Kettunen, M. I. 2011. *Tumor imaging using hyperpolarized ^{13}C magnetic resonance spectroscopy.* Magn. Reson. Med., 66, 505-519.

Buljubasich, L., Franzoni, M. B., Spiess, H. W. and Munnemann, K. 2012. *Level anti-crossings in ParaHydrogen Induced Polarization experiments with Cs-symmetric molecules.* J. Magn. Reson., 219, 33-40.

Carravetta, M., Johannessen, O. and Levitt, M. 2004. *Beyond the T_1 limit: singlet nuclear spin states in low magnetic fields.* Phys. Rev. Lett., 92, 153003.

Carravetta, M. and Levitt, M. H. 2004. *Long-lived nuclear spin states in high-field solution NMR.* J. Am. Chem. Soc., 126, 6228-6229.

Carravetta, M. and Levitt, M. H. 2005. *Theory of long-lived nuclear spin states in solution nuclear magnetic resonance.* I. Singlet states in low magnetic field. J. Chem. Phys., 122, 214505.

Chattergoon, N. N., Martinez-Santiesteban, F., Handler, W. B., Ardenkjaer-Larsen, J. H. and Scholl, T. J. 2013. *Field dependence of T_1 for hyperpolarized [1-^{13}C]pyruvate.* Contrast Media Mol. I., 8, 57-62.

Chekmenev, E. Y., Hovener, J., Norton, V. A., Harris, K., Batchelder, L. S., Bhattacharya, P., Ross, B. D. and Weitekamp, D. P. 2008. *PASADENA hyperpolarization of succinic acid for MRI and NMR spectroscopy.* J. Am. Chem. Soc., 130, 4212-3.

Chen, A. P., Chu, W., Gu, Y. P. and Cunnhingham, C. H. 2013. *Probing early tumor response to radiation therapy using hyperpolarized [1-^{13}C]pyruvate in MDA-MB-231 xenografts.* PLoS One, 8, e56551.

Chen, A. P., Hurd, R. E., Gu, Y. P., Wilson, D. M. and Cunningham, C. H. 2011. ^{13}C *MR reporter probe system using dynamic nuclear polarization.* NMR Biomed., 24, 514-20.

Cheng, T., Mishkovsky, M., Bastiaansen, J. A., Ouari, O., Hautle, P., Tordo, P., van den Brandt, B. and Comment, A. 2013. *Automated transfer and injection of hyperpolarized molecules with polarization measurement prior to in vivo NMR.* NMR Biomed.

Comment, A., Uffmann, K., Jannin, S., Kurdzesau, F., van Heseswijk, R. B., Frenkel, H., Hautle, P., Konter, J. A., van den Brandt, B., Gruetter, R. and van der Klink, J. J. 2007. *In vivo DNP-enhanced ^{13}C labeled acetate brain studies in a 9.4 T animal scanner.* Proc. Intl. Soc. Mag. Reson. Med., 369.

Damadian, R. 1971. *Tumor detection by nuclear magnetic resonance.* Science, 171, 1151-1153.

Day, S. E., Kettunen, M. I., Cherukuri, M. K., Mitchell, J. B., Lizak, M. J., Morris, H. D., Matsumoto, S., Koretsky, A. P. and Brindle, K. M. 2011. *Detecting response of rat C6 glioma tumors to radiotherapy using hyperpolarized [1-^{13}C]pyruvate and ^{13}C magnetic resonance spectroscopic imaging.* Magn. Reson. Med., 65, 557-563.

Day, S. E., Kettunen, M. I., Gallagher, F. A., Hu, D.-E., Lerche, M., Wolber, J., Golman, K., Ardenkjaer-Larsen, J. H. and Brindle, K. M. 2007. *Detecting tumor response to treatment using hyperpolarized ^{13}C magnetic resonance imaging and spectroscopy.* Nat. Med., 13, 1382-1387.

de Graaf, A. A., Maathuis, A., de Waard, P., Deutz, N. E. P., Dijkema, C., de Vos, W. M. and Venema, K. 2009. *ProÞling human gut bacterial metabolism and its kinetics using [U-^{13}C]glucose and NMR.* NMR Biomed.

de Graaf, R. A., Brown, P. B., McIntyre, S., Nixon, T. W., Behar, K. L. and Rothman, D. L. 2006. *High magnetic field water and metabolite proton T_1 and T_2 relaxation in rat brain in vivo.* Magn. Reson. Med., 56, 386-94.

Du, W., Xiaobing, F., Foxley, S., Zamora, M., River, J. N., Culp, R. M. and Karczmar, G. S. 2004.

Comparison of high-resolution echo-planar spectroscopic imaging with conventional MR imaging of prostate tumors in mice. NMR Biomed., 18, 285-292.

Duchin, Y., Abosch, A., Yacoub, E., Sapiro, G. and Harel, N. 2012. *Feasibility of using ultra-high field (7 T) MRI for clinical surgical targeting.* PLoS One, 7, e37328.

Dumez, J. N. and Frydman, L. 2013. *Multidimensional excitation pulses based on spatiotemporal encoding concepts.* J. Magn. Reson., 226, 22-34.

Dzien, P., Kettunen, M. I., Marco-Rius, I., Serrao, E. M., Rodrigues, T. B., Larkin, T. J., Timm, K. N. and Brindle, K. M. 2014. ^{13}C *magnetic resonance spectroscopic imaging of hyperpolarized [1-^{13}C, U-$^2H_5$]ethanol oxidation in vivo can be used to assess aldehyde dehydrogenase activity.* Magn. Reson. Med.

Eichhorn, T. R., Takado, Y., Salameh, N., Capozzi, A., Cheng, T., Hyacinthe, J. N., Mishkovsky, M., Roussel, C. and Comment, A. 2013. *Hyperpolarization without persistent radicals for in vivo real-time metabolic imaging.* Proc. Natl. Acad. Sci. USA, 110, 18064-9.

Endre, Z. H. and Kuchel, P. W. 1986. *Viscosity of concentrated solutions and of human erythrocyte cytoplasm determined from NMR measurement of molecular correlation times. The dependence of viscosity on cell volume.* Biophys. Chem., 24, 337-355.

Fan, T. W.-M. and Lane, A. N. 2008. Structure-based profiling of metabolites and isotopomers by NMR. Prog. Nucl. Mag. Res. Sp., 52.

Feng, Y., Davis, R. M. and Warren, W. S. 2012. *Acessing long-lived nuclear singlet states between chemically equivalent spins without breaking symmetry.* Nature Physics, 2425.

Feng, Y., Theis, T., Liang, X., Wang, Q., Zhou, P. and Warren, W. S. 2013. *Storage of hydrogen spin polarization in long-lived $^{13}C_2$ singlet order and implications for hyperpolarized MRI.* J. Am. Chem. Soc.

Fitzgerald, R. J., Sauer, K. L. and Happer, W. 1998. *Cross-relaxation in laser-polarized liquid*

xenon. Chem. Phys. Letters, 284, 87-92.

Franzoni, M. B., Buljubasich, L., Spiess, H. W. and Munnemann, K. 2012. Long-lived ^{1}H singlet spin states originating from para-hydrogen in Cs-symmetric molecules stored for minutes in high magnetic fields. J. Am. Chem. Soc., 134, 10393-6.

Gallagher, F., Kettunen, M., Day, S., Hu, D.-E., Ardenkjaer-Larsen, J., in Ôt Zandt, R., Jensen, P., Karlsson, M., Golman, K., Lerche, M. and Brindle, K. 2008a. *Magnetic resonance imaging of pH in vivo using hyperpolarized ^{13}C-labeled bicarbonate.* Nature, 453, 940-943.

Gallagher, F. A., Bohndiek, S. E., Kettunen, M. I., Lewis, D. Y., Soloviev, D. and Brindle, K. M. 2011a. *Hyperpolarized ^{13}C MRI and PET: in vivo tumor biochemistry.* J. Nucl. Med., 52, 1333-6.

Gallagher, F. A., Kettunen, M. I., Day, S. E., Hu, D.-E., Ardenkjaer-Larsen, J. H., Zandt, R. i. t., Jensen, P. R., Karlsson, M., Golman, K., Lerche, M. H. and Brindle, K. M. 2008b. *Magnetic resonance imaging of pH in vivo using hyperpolarized ^{13}C-labelled bicarbonate.* Nature, 453, 940-943.

Gallagher, F. A., Kettunen, M. I., Day, S. E., Hu, D. E., Karlsson, M., Gisselsson, A., Lerche, M. H. and Brindle, K. M. 2011b. *Detection of tumor glutamate metabolism in vivo using ^{13}C magnetic resonance spectroscopy and hyperpolarized [1-^{13}C]glutamate.* Magn. Reson. Med., 66, 18-23.

Gallagher, F. A., Kettunen, M. I., Day, S. E., Lerche, M. and Brindle, K. M. 2008c. *^{13}CMR spectroscopy measurements of glutaminase activity in human hepatocellular carcinoma cells using hyperpolarized ^{13}C-labeled glutamine.* Magn. Reson. Med., 60, 253-7.

Gallagher, F. A., Kettunen, M. I., Hu, D.-E., Jensen, P. R., in 't Zandt, R., Karlsson, M., Gisselsson, A., Nelson, S. K., Witney, T. H., Bohndiek, S. E., Hansson, G., Peitersen, T., Lerche, M. H. and Brindle, K. M. 2009. *Production of hyperpolarized [1,4-$^{13}C_2$]malate from [1,4-$^{13}C_2$]fumarate is a marker of cell necrosis and treatment response in tumors.* Proc. Natl. Acad. Sci. USA, 106, 19801-19806.

Golman, K., Ardenkjaer-Larsen, J. H., Petersson, J. S., Mansson, S. and Leunbach, I. 2003. *Molecular imaging with endogenous substances.* Proc. Natl. Acad. Sci. USA, 100, 10435-9.

Gore, J. C. and Kennan, R. P. 1999. *Physical an physiological basis of magnetic relaxation.* In: STARKDD, B. (ed.) Magnetic Resonance Imaging. St. Louis: Mosby.

Griffiths, V. S. and Socrates, G. 1967. *N.M.R. study of the hydration of pyruvic acid.* Trans. Faraday Soc., 63, 673-677.

Harris, T., Szekely, O. and Frydman, L. 2014. *On the potential of radical-based, fast-dissolution DNP for protein NMR studies.* J. Phys. Chem. B, doi: 10.1021/jp4102916

Hellstrom, N. and Almqvist, S.-O. 1970. *Hydration and dehydration of pyruvic acid.* J. Chem. Soc., B, 1396-1400.

Hielscher, A. H., Bluestone, A. Y., Abdoulaev, G. S., Klose, A. D., Lasker, J., Stewart, M., Netz, U. and Beuthan, J. 2002. *Near-infrared diffuse optical tomography.* Dis. Markers, 18, 313-37.

Hurd, R. E., Chen, A., Cunningham, C. H. and Tropp, J. *Scalar coupling patterns in hyperpolarized spin systems: J_{CC} spectral pattern in hyperpolarized 1,2-[^{13}C]-pyruvate. A potential indirect measure of polarization.* Exp. Nuc. Magn. Res. Conference, 2009 Asilomar Conference Grounds, Pacific Grove, California.

Hurd, R. E., Yen, Y. F., Chen, A. and Ardenkjaer-Larsen, J. H. 2012. *Hyperpolarized ^{13}C metabolic imaging using dissolution dynamic nuclear polarization.* J. Magn. Reson. Imaging, 36, 1314-28.

Hurd, R. E., Yen, Y. F., Mayer, D., Chen, A., Wilson, D., Kohler, S., Bok, R., Vigneron, D., Kurhanewicz, J., Tropp, J., Spielman, D. and Pfefferbaum, A. 2010. *Metabolic imaging in the anesthetized rat brain using hyperpolarized [1-^{13}C] pyruvate and [1-^{13}C] ethyl pyruvate.* Magn. Reson. Med., 63, 1137-43.

Janick, P. A., Hackney, D. B., Grossman, R. I. and Asakura, T. 1991. *MR imaging of various oxidation states of intracellular and extracellular hemoglobin.* AJNR Am. J. Neuroradiol., 12, 891-7.

Jannin, S., Bornet, A., Melzi, R. and Bodenhausen, G. 2012. *High field dynamic nuclear polariza-

tion at 6.7 T: Carbon-13 polarization above 70% within 20 min. Chem. Phys. Letters, 549, 99-102.

Jannin, S., Mieville, P., Bornet, A. and Bodenhausen, G. 2011. *Dynamic nuclear polarization for NMR spectroscopy.* DNP Workshop. Ecole Doctorale de Chemie (EDCH), EPFL-SB-ISIC, Switzerland.

Jeffries, R. E., Gamcsik, M. P., Keshari, K., Pediaditakis, P., Tikunov, A. P., Young, G. B., Lee, H., Watkins, P. B. and Macdonald, J. 2012. *Effect of oxygen concentration on viability and metabolism in a fluidized-bed bioartificial liver using ^{31}P and ^{13}C NMR spectroscopy.* Tissue Eng. Pt. C-Meth., 19, 93-100.

Jensen, P. R., Karlsson, M., Meier, S., Duus, J. O. and Lerche, M. H. 2009. *Hyperpolarized amino acids for in vivo assays of transaminase activity.* Chemistry, 15, 10010-2.

Johansson, E., Mansson, S., Wirestam, R., Svensson, J., Petersson, J. S., Golman, K. and Stahlberg, F. 2004. *Cerebral perfusion assessment by bolus tracking using hyperpolarized ^{13}C.* Magn. Reson. Med., 51, 464-72.

Karlsson, M., Jensen, P. R., in 't Zandt, R., Gisselsson, A., Hansson, G., Duus, J. O., Meier, S. and Lerche, M. H. 2010. *Imaging of branched chain amino acid metabolism in tumors with hyperpolarized ^{13}C ketoisocaproate.* Int. J. Cancer, 127, 729-36.

Kennedy, B. W., Kettunen, M. I., Hu, D. E. and Brindle, K. M. 2012. *Probing lactate dehydrogenase activity in tumors by measuring hydrogen/deuterium exchange in hyperpolarized l-[1-^{13}C,U-^{2}H]lactate.* J. Am. Chem. Soc., 134, 4969-77.

Kentgens, A. P., Bart, J., van Bentum, P. J., Brinkmann, A., van Eck, E. R., Gardeniers, J. G., Janssen, J. W., Knijn, P., Vasa, S. and Verkuijlen, M. H. 2008. *High-resolution liquid- and solid-state nuclear magnetic resonance of nanoliter sample volumes using microcoil detectors.* J. Chem. Phys., 128, 052202.

Keshari, K. R., Kurhanewicz, J., Bok, R., Larson, P. E., Vigneron, D. B. and Wilson, D. M. 2011. *Hyperpolarized ^{13}C dehydroascorbate as an endogenous redox sensor for in vivo metabolic imaging.*

Proc. Natl. Acad. Sci. USA, 108, 18606-11.

Keshari, K. R., Wilson, D. M., Chen, A. P., Bok, R., Larson, P. E., Hu, S., Van Criekinge, M., Macdonald, J. M., Vigneron, D. B. and Kurhanewicz, J. 2009. *Hyperpolarized [2-^{13}C]-fructose: a hemiketal DNP substrate for in vivo metabolic imaging.* J. Am. Chem. Soc., 131, 17591-6.

Kiryutin, A. S., Ivanov, K. L., Yurkovskaya, A. V., Vieth, H. M. and Lukzen, N. N. 2013. *Manipulating spin hyper-polarization by means of adiabatic switching of a spin-locking RF-field.* Phys. Chem. Chem. Phys., 15, 14248-55.

Kowalewski, J. and Maler, L. 2006. *Nuclear spin relaxation in liquids: theory, experiments, and applications*, New York, London, Taylor and Francis.

Krahn, A., Lottmann, P., Marquardsen, T., Tavernier, A., Turke, M. T., Reese, M., Leonov, A., Bennati, M., Hoefer, P., Engelke, F. and Griesinger, C. 2010. *Shuttle DNP spectrometer with a two-center magnet.* Phys. Chem. Chem. Phys., 12, 5830-40.

Krishnan, V. V. and Murali, N. 2013. *Radiation damping in modern NMR experiments: progress and challenges.* Prog. Nucl. Magn. Reson. Spectrosc., 68, 41-57.

Kurhanewicz, J., Vigneron, D. B., Brindle, K., Chekmenev, E. Y., Comment, A., Cunningham, C. H., DeBerardinis, R. J., Green, G. G., Leach, M. O., Rajan, S. S., Rizi, R. R., Ross, B. D., Warren, W. S. and Malloy, C. R. 2011. *Analysis of cancer metabolism by imaging hyperpolarized nuclei: prospects for translation to clinical research.* Neoplasia, 13, 81-97.

Lau, J. Y., Chen, A. P., Gu, Y. P. and Cunningham, C. H. 2013. *A calibration-based approach to real-time in vivo monitoring of pyruvate C1 and C2 polarization using the J_{CC} spectral asymmetry.* NMR Biomed., 26, 1233-41.

Laustsen, C., Pileio, G., Tayler, M. C., Brown, L. J., Brown, R. C., Levitt, M. H. and Ardenkjaer-Larsen, J. H. 2012. *Hyperpolarized singlet NMR on a small animal imaging system.* Magn. Reson. Med., 68, 1262-5.

Le, A., Lane, A. N., Hamaker, M., Bose, S., Gouw, A., Barbi, J., Tsukamoto, T., Rojas, C. J., Slusher, B. S., Zhang, H., Zimmerman, L. J., Liebler, D. C., Slebos, R. J., Lorkiewicz, P. K., Higashi, R. M., Fan, T. W. and Dang, C. V. 2012. *Glucose-independent glutamine metabolism via TCA cycling for proliferation and survival in B cells.* Cell Metab., 15, 110-21.

Levin, Y. S., Mayer, D., Yen, Y. F., Hurd, R. E. and Spielman, D. M. 2007. *Optimization of fast spiral chemical shift imaging using least squares reconstruction: application for hyperpolarized ^{13}C metabolic imaging.* Magn. Reson. Med., 58, 245-52.

Levitt, M. H. 1986. *Composite pulses.* Prog. Nucl. Mag. Res. Sp., 18, 61-122.

Levitt, M. H. 1997. *The signs of frequencies and phases in NMR.* J. Magn. Reson., 126, 164-182.

Levitt, M. H. 2008. *Spin dynamics: basics of nuclear magnetic resonance*, John Wiley and Sons Ltd.

Levitt, M. H. 2010. *Singlet and other states with extended lifetimes.* In: WASYLISHEN, R. K. and HARRIS, R. E. (eds.) Encyclopedia of Nuclear Magnetic Resonance. Chichester: John Wiley.

Levitt, M. H. 2012a. *Singlet NMR*, conference presentation at Euromar 2012. University College Dublin, Ireland.

Levitt, M. H. 2012b. *Singlet nuclear magnetic resonance.* Annu. Rev. Phys. Chem., 63, 89-105.

Lin, A. L., Qin, Q., Zhao, X. and Duong, T. Q. 2012. *Blood longitudinal (T1) and transverse (T2) relaxation time constants at 11.7 Tesla.* Magn. Reson. Mater Phy., 25, 245-9. Lin, Y. Y., Lisitza, N., Ahn, S. and Warren, W. S. 2000. *Resurrection of crushed magnetization and chaotic dynamics in solution NMR spectroscopy.* Science, 290, 118-22.

MacNamara, E., Rice, C. V., Smith, J., Smith, L. J. and Raftery, D. 2000. *Cross-relaxation dynamics between laser-polarized xenon and surface species using a simple three-spin model.* Chem. Phys. Letters, 317, 165-173.

Marco-Rius, I., Tayler, M. C., Kettunen, M. I., Larkin, T. J., Timm, K. N., Serrao, E. M., Rodrigues, T. B., Pileio, G., Ardenkjaer-Larsen, J. H., Levitt, M. H. and Brindle, K. M. 2013. *Hyperpolarized singlet lifetimes of pyruvate in human blood and in the mouse.* NMR Biomed., 26, 1696-1704.

Margolis, S. A. and Coxon, B. 1986. *Identification and quantitation of the impurities in sodium pyruvate.* Anal. Chem., 58, 2504-2510.

Mayer, D., Levin, Y. S., Hurd, R. E., Glover, G. H. and Spielman, D. M. 2006. *Fast metabolic imaging of systems with sparse spectra: application for hyperpolarized ^{13}C imaging.* Magn. Reson. Med., 56, 932-7.

Meany, J. E. 2007. *Lactate dehydrogenase catalysis: roles of keto, hydrated, and enol pyruvate.* J. Chem. Educ., 84, 1520-1523.

Menzel, M. I., Farrell, E. V., Janich, M. A., Khegai, O., Wiesinger, F., Nekolla, S., Otto, A. M., Haase, A., Schulte, R. F. and Schwaiger, M. 2013. *Multimodal assessment of in vivo metabolism with hyperpolarized [1-^{13}C]MR spectroscopy and ^{18}F-FDG PET imaging in hepatocellular carcinoma tumor-bearing rats.* J. Nucl. Med.

Mieville, P., Ahuja, P., Sarkar, R., Jannin, S., Vasos, P. R., Gerber-Lemaire, S., Mishkovsky, M., Comment, A., Gruetter, R., Ouari, O., Tordo, P. and Bodenhausen, G. 2010. Scavenging free radicals to preserve enhancement and extend relaxation times in NMR using dynamic nuclear polarization. Angew. Chem. Int. Ed., 49, 6182-6185.

Mieville, P., Jannin, S. and Bodenhausen, G. 2011. *Relaxometry of insensitive nuclei: optimizing dissolution dynamic nuclear polarization.* J. Magn. Reson., 210, 137-40.

Mishkovsky, M., Comment, A. and Gruetter, R. 2012. *In vivo detection of brain Krebs cycle intermediate by hyperpolarized magnetic resonance.* J. Cereb. Blood Flow Metab., 32, 2108-13.

Moreno, K. X., Harrison, C., Dean Sherry, A., Malloy, C. R. and Merritt, M. E. 2011. *Transfer of hyperpolarization from long T1 storage nuclei to short T1 neighbors using FLOPSY-8.* J. Magn.

Reson., 213, 187-91.

Moreno, K. X., Sabelhaus, S. M., Merritt, M. E., Sherry, A. D. and Malloy, C. R. 2010. *Competition of pyruvate with physiological substrates for oxidation by the heart: implications for studies with hyperpolarized [1-^{13}C]pyruvate.* Am. J. Physiol. Heart Circ. Physiol., 298, H1556-64.

Navon, G., Song, Y.-Q., Room, T., Appelt, S., Taylor, R. E. and Pines, A. 1996. *Enhancement of solution NMR and MRI with laser-polarized xenon.* Science, 271, 1848-1851.

Nelson, S. J., Kurhanewicz, J., Vigneron, D. B., Larson, P., Harzstarck, A., Ferrone, M., van Criekinge, M., Chang, J., Bok, R., Park, I., Reed, G., Carvajal, L., Crane, J., Ardenkjaer-Larsen, J. H., Chen, A., Hurd, R., Odegardstuen, L.-I. and Tropp, J. 2012. *Proof of concept clinical trial of hyperpolarized C-13 pyruvate in patients with prostate cancer.* Proc. Intl. Soc. Mag. Reson. Med., 274.

Nelson, S. J., Kurhanewicz, J., Vigneron, D. B., Larson, P. E., Harzstark, A. L., Ferrone, M., van Criekinge, M., Chang, J. W., Bok, R., Park, I., Reed, G., Carvajal, L., Small, E. J., Munster, P., Weinberg, V. K., Ardenkjaer-Larsen, J. H., Chen, A. P., Hurd, R. E., Odegardstuen, L. I., Robb, F. J., Tropp, J. and Murray, J. A. 2013. *Metabolic imaging of patients with prostate cancer using hyperpolarized [1-^{13}C]pyruvate.* Sci. Transl. Med., 5, 198ra108.

Neuhaus, D., Williamson, M. P. 2000. *The Nuclear Overhauser Effect in structural and conformational analysis*, New York, Wiley-VCH, Inc.

Noggle, J. H. and Schirmer, R. E. 1971. *The nuclear Overhauser effect; chemical applications*, New York, Academic Press, Inc.

Oppelt, A. 2005. *Imaging systems for medical diagnostics*, Erlangen, Germany, Publicis Corporate Publishing.

Ouwerkerk, R. 2007. *Sodium magnetic resonance imaging: from research to clinical use.* J. Am. Coll. Radiol., 4, 739-41.

Oxford-Instruments. *HyperSense¨ - the in-vitro DNP polariser* [Online]. Available: http://www.oxford-instruments.com/products/dnp/hyperSense/Pages/hyperSense.aspx 2012].

Petiet, A. and Johnson, G. A. 2010. *Active staining of mouse embryos for magnetic resonance microscopy.* Methods Mol. Biol., 611, 141-9.

Petit, C. and Lee, A. 2014. *Monitoring side-chain dynamics of proteins using H relaxation.* In: LIVESAY, D. R. (ed.) Protein Dynamics. Humana Press.

Pileio, G., Carravetta, M., Hughes, E. and Levitt, M. H. 2008. *The long-lived nuclear singlet state of ^{15}N-nitrous oxide in solution.* J. Am. Chem. Soc., 130, 12582-12583.

Pileio, G., Carravetta, M. and Levitt, M. H. 2010. *Storage of nuclear magnetization as long-lived singlet order in low magnetic field.* Proc. Natl. Acad. Sci. USA, 107, 17135-17139.

Pileio, G. and Levitt, M. H. 2009. *Theory of long-lived nuclear spin states in solution nuclear magnetic resonance. II. Singlet spin locking.* J. Chem. Phys., 130, 214501.

Pocker, Y., Meany, J. E., Nist, B. J. and Zadorojny, C. 1969. *The reversible hydration of pruvic acid. I. Equilibrium studies.* J. Phys. Chem., 73, 2879-2882.

Preston, A. 2010. *The masters of our minds: Meet the brain scientists battling to preserve sanity* [Online]. http://www.dailymail.co.uk/home/moslive/article-1330570/Brain-scientists-battling-preserve-sanity-MS-Alzheimers-Parkinsons.html: MailOnline. Accessed 25/11/2013.

Pullinger, B. M., Kadlecek, S. J., Kuzma, N. N. and Rizi, R. R. 2011. *The influence of bovine serum albumin on the T_1 relaxation of $[1-^{13}C]$pyruvate - A study at low fields.* Proc. Intl. Soc. Mag. Reson. Med., 1514.

Purcell, E. M., Torrey, H. C. and Pound, R. V. 1946. *Resonance absorption by nuclear magnetic moments in a solid.* Phys. Rev., 69, 37-38.

Reeder, S. B., Brittain, J. H., Grist, T. M. and Yen, Y. F. 2007. *Least-squares chemical shift*

separation for ^{13}C metabolic imaging. J. Magn. Reson. Imaging, 26, 1145-52.

Reynolds, S., Bucur, A., Port, M., Alizadeh, T., Kazan, S. M., Tozer, G. M. and Paley, M. N. J. 2014. *A system for accurate and automated injection of hyperpolarized substrate with minimal dead time and scalable volumes over a large range.* J. Magn. Reson., 239, 1-8.

Richter, W., Richter, M., Warren, W. S., Merkle, H., Andersen, P., Adriany, G. and Ugurbil, K. 2000. *Functional magnetic resonance imaging with intermolecular multiple-quantum coherences.* Magn. Reson. Imaging., 18, 489-94.

Rodrigues, T. B., Serrao, E. M., Kennedy, B. W., Hu, D. E., Kettunen, M. I. and Brindle, K. M. 2014. *Magnetic resonance imaging of tumor glycolysis using hyperpolarized ^{13}C-labeled glucose.* Nat. Med., 20, 93-97.

Sarkar, R., Vasos, P. R. and Bodenhausen, G. 2007. *Singlet-state exchange NMR spectroscopy for the study of very slow dynamic processes.* J. Am. Chem. Soc., 129, 328-34.

Sarkar, S., Heberlein, K., Metzger, G. J., Zhang, X. and Hu, X. 1999. *Applications of high-resolution echoplanar spectroscopic imaging for structural imaging.* J. Magn. Reson. Imaging, 10, 1-7.

Schmidt, R., Baishya, B., Ben-Eliezer, N., Seginer, A. and Frydman, L. 2013. *Super-resolved parallel MRI by spatiotemporal encoding.* Magn Reson Imaging, 32, 60-70.

Schmidt, R. and Frydman, L. 2013. *Alleviating artifacts in ^{1}H MRI thermometry by single scan spatiotemporal encoding.* MAGMA, 26, 477-90.

Schroeder, M. A., Atherton, H. J., Ball, D. R., Cole, M. A., Heather, L. C., Griffin, J. L., Clarke, K., Radda, G. K. and Tyler, D. J. 2009. *Real-time assessment of Krebs cycle metabolism using hyperpolarized ^{13}C magnetic resonance spectroscopy.* FASEB J., 23, 2529-38.

Shaka, A. J. 1985. *Composite pulses for utra-broadband spin inversion.* Chem. Phys. Letters, 120, 201-5.

Shapiro, E. M., Skrtic, S., Sharer, K., Hill, J. M., Dunbar, C. E. and Koretsky, A. P. 2004. *MRI detection of single particles for cellular imaging.* Proc. Natl. Acad. Sci. USA, 101, 10901-6.

Silvennoinen, M. J., Kettunen, M. I. and Kauppinen, R. A. 2003. *Effects of hematocrit and oxygen saturation level on blood spin-lattice relaxation.* Magn. Reson. Med., 49, 568-71.

Solomon, I. 1955. *Relaxation processes in a system of two spins.* Phys. Rev., 99, 559-65.

Song, Y.-Q. 2000. *Spin polarization-induced nuclear Overhauser effect: an application of spin-polarized xenon and helium.* Concept. Magnetic Res., 12, 6-20.

Tal, A. and Frydman, L. 2010. *Single-scan multidimensional magnetic resonance.* Prog. Nuc. Mag. Res. Sp., 57, 241-92.

Tayler, M. C. D. 2012. *Theory and practice of singlet nuclear magnetic resonance.* Doctor of Philosophy, University of Southampton.

Tayler, M. C. D. and Levitt, M. H. 2011a. *Paramagnetic relaxation of nuclear singlet states.* Phys. Chem. Chem. Phys., 13, 9128-30.

Tayler, M. C. D. and Levitt, M. H. 2011b. *Singlet nuclear magnetic resonance of nearly-equivalent spins.* Phys. Chem. Chem. Phys., 13, 5556-60.

Tayler, M. C. D., Marco-Rius, I., Kettunen, M. I., Brindle, K. M., Levitt, M. H. and Pileio, G. 2012. *Direct enhancement of nuclear singlet order by dynamic nuclear polarization.* J. Am. Chem. Soc., 134, 7668-7671.

Tennant, D. A., Duran, R. V. and Gottlieb, E. 2010. *Targeting metabolic transformation for cancer therapy.* Nat. Rev. Cancer, 10, 267-77.

Tropp, J. 2010. *Multiplet asymmetry and multip-spin order in liquid-state NMR spectra of hyperpolarized compounds.* Proc. Intl. Soc. Mag. Reson. Med., 1026.

Unnikrishnan, S. and Klibanov, A. L. 2012. *Microbubbles as ultrasound contrast agents for molec-*

ular imaging: preparation and application. Am. J. Roentgenol., 199, 292-9.

van Bentum, P. J., van der Heijden, G. H., Villanueva-Garibay, J. A. and Kentgens, A. P. 2011. *Quantitative analysis of high field liquid state dynamic nuclear polarization.* Phys. Chem. Chem. Phys., 13, 17831-40.

Waldner, L. F., Scholl, T. J., Chen, A., Rutt, B. and McKenzie, C. 2010. *The effects of contrast agents on hyperpolarised [1-^{13}C]pyruvic acid.* Proc. Intl. Soc. Mag. Reson. Med., 3263.

Warren, W. S. 1998. *Rethinking solution NMR.* Science, 280, 398-399.

Warren, W. S., Ahn, S., Mescher, M., Garwood, M., Ugurbil, K., Richter, W., Rizi, R. R., Hopkins, J. and Leigh, J. S. 1998. *MR imaging contrast enhancement based on intermolecular zero quantum coherences.* Science, 281, 247-251.

Warren, W. S., Jenista, E., Branca, R. T. and Chen, X. 2009. *Increasing hyperpolarized spin lifetimes through true singlet eigenstates.* Science, 323, 1711-4.

Wen, H. 2001. *Mapping the velocity vector onto the spin vector: two-dimensional velocity-selective spin excitation for MR flow imaging.* Magn. Reson. Med., 46, 767-72.

Wilson, D. M., Hurd, R. E., Keshari, K., Van Criekinge, M., Chen, A. P., Nelson, S. J., Vigneron, D. B. and Kurhanewicz, J. 2009. *Generation of hyperpolarized substrates by secondary labeling with [1,1-^{13}C]acetic anhydride.* Proc. Natl. Acad. Sci. USA, 106, 5503-7.

Wilson, D. M., Keshari, K. R., Larson, P. E., Chen, A. P., Hu, S., Van Criekinge, M., Bok, R., Nelson, S. J., Macdonald, J. M., Vigneron, D. B. and Kurhanewicz, J. 2010. *Multi-compound polarization by DNP allows simultaneous assessment of multiple enzymatic activities in vivo.* J. Magn. Reson., 205, 141-7.

Witney, T. H., Kettunen, M. I. and Brindle, K. M. 2011. *Kinetic modeling of hyperpolarized ^{13}C label exchange between pyruvate and lactate in tumor cells.* J. Biol. Chem., 286, 24572-80.

Witney, T. H., Kettunen, M. I., Day, S. E., Hu, D.-E., Neves, A. A., Gallagher, F. A., Fulton, S. M. and Brindle, K. M. 2009. *A comparison between radiolabeled fluorodeoxyglucose uptake and hyperpolarized ^{13}C-labeled pyruvate utilization as methods for detecting tumor response to treatment.* Neoplasia, 11, 574-582.

Witney, T. H., Kettunen, M. I., Hu, D.-E., Gallagher, F. A., Bohndiek, S. E., Napolitano, R. and Brindle, K. M. 2010. *Detecting treatment response in a model of human breast adenocarcinoma using hyperpolarised [1-^{13}C]pyruvate and [1,4-$^{13}C_2$]fumarate.* Br. J. Canc., 103, 1400-1406.

Yoshida, K., Wakai, C., Matubayasi, N. and Nakahara, M. 2005. *A new high-temperature multinuclear-magnetic-resonance probe and the self-diffusion of light and heavy water in sub- and supercritical conditions.* J. Chem. Phys., 123, 164506.

Zhao, L., Walls, J. D., Huang, S. Y. and Lin, Y. Y. 2013. *^{13}C MR molecular imaging by indirect detection and spin amplification.* Proc. Intl. Soc. Mag. Reson. Med., 530.